HELLENIC REPUBLIC
UNIVERSITY OF IOANNINA
SCHOOL OF ENGINEERING
DEPARTMENT OF MATERIALS SCIENCE AND ENGINEERING

COMPUTATIONAL DESIGN OF FUNCTIONAL Fe-X (X=Cu, Co, Mn) COATINGS AND NANOCLUSTERS FOR ENVIRONMENTALLY SUSTAINABLE APPLICATIONS

CARLA CUTRANO

PhD These

IOANNINA 2020

ΕΛΛΗΝΙΚΗ ΔΗΜΟΚΡΑΤΙΑ
ΠΑΝΕΠΙΣΤΗΜΙΟ ΙΩΑΝΝΙΝΩΝ
ΠΟΛΥΤΕΧΝΙΚΗ ΣΧΟΛΗ
ΤΜΗΜΑ ΜΗΧΑΝΙΚΩΝ ΕΠΙΣΤΗΜΗΣ ΥΛΙΚΩΝ

ΥΠΟΛΟΓΙΣΤΙΚΗ ΜΕΛΕΤΗ ΛΕΙΤΟΥΡΓΙΚΩΝ Fe-X (X=Cu, Co, Mn) ΕΠΙΣΤΡΩΣΕΩΝ ΚΑΙ ΝΑΝΟ-ΣΥΣΣΩΜΑΤΩΜΑΤΩΝ ΓΙΑ ΠΕΡΙΒΑΛΛΟΝΤΙΚΑ ΒΙΩΣΙΜΕΣ ΕΦΑΡΜΟΓΕΣ

ΔΙΔΑΚΤΟΡΙΚΗ ΔΙΑΤΡΙΒΗ

ΙΩΑΝΝΙΝΑ 2020

«Η έγκριση της διδακτορικής διατριβής από το Τμήμα Μηχανικών Επιστήμης Υλικών της Πολυτεχνικής Σχολής του Πανεπιστημίου Ιωαννίνων δεν υποδηλώνει αποδοχή των γνωμών του συγγραφέα Ν. 5343/32, άρθρο 202, παράγραφος 2»

Date of application of Mrs Carla Cutrano: 07.09.2015

Date of Appointment of PhD Advisory Committee: 07.10.2015
Members of 3 Member Advisory Committee

Thesis Advisor
Χριστίνα Λέκκα, Associate Professor, Department of Materials Science & Engineering, School of Engineering, University of Ioannina

Members
Dimitrios Papageorgiou, Associate Professor, Department of Materials Science & Engineering, School of Engineering, University of Ioannina
Georgos Evangelakis, Professor, Department of Physics, School of Science, University of Ioannina

Date of Thesis Definition: 07.10.2015
«Computational design of functional Fe- and Cu-based coatings for environmentally sustainable applications».

Date of Thesis Modification: 27.03.2019
«Computational design of functional Fe-X (X=Cu, Co, Mn) coatings and nanoclusters for environmentally sustainable applications».

DATE OF APPOINTMENT OF THE MEMBER EXAMINATION COMMITTEE : 05.06.2019

1. Χριστίνα Λέκκα, Associate Professor, Department of Materials Science & Engineering, School of Engineering, University of Ioannina,
2. Dimitrios Papageorgiou, Associate Professor, Department of Materials Science & Engineering, School of Engineering, University of Ioannina,
3. Georgos Evangelakis, Professor, Department of Physics, School of Science, University of Ioannina,
4.Eleutherios Lidorikis, Professor, Department of Materials Science & Engineering, School of Engineering, University of Ioannina,
5. Filomela Komninou, Professor, Department of Physics, S.Th.E. of A.U.Th.,
6. Iosif Kioseoglou, Associate Professor, Department of Physics, S.Th.E. of A.U.Th.,,
7.Leonidas Gergidis, Assistant Professor, Department of Materials Science & Engineering, School of Engineering, University of Ioannina.

The PhD Thesis is approved with **«Excellent »** on **11.05.2020**

The Chairman of the Department

Alkiviadis Paipetis
Professor

The Secretary of the Department

Maria Kontou

Ημερομηνία αίτησης της κ. Carla Cutrano: 07.09.2015

Ημερομηνία ορισμού Τριμελούς Συμβουλευτικής Επιτροπής: 07.10.2015

Μέλη Τριμελούς Συμβουλευτικής Επιτροπής:

Επιβλέπουσα
Χριστίνα Λέκκα, Αναπληρώτρια Καθηγήτρια του Τμήματος Μηχανικών Επιστήμης Υλικών της Πολυτεχνικής Σχολής του Πανεπιστημίου Ιωαννίνων

Μέλη
Δημήτριος Παπαγεωργίου, Αναπληρωτής Καθηγητής του Τμήματος Μηχανικών Επιστήμης Υλικών της Πολυτεχνικής Σχολής του Πανεπιστημίου Ιωαννίνων,
Γεώργιος Ευαγγελάκης, Καθηγητής του Τμήματος Φυσικής της Σ.Θ.Ε. του Πανεπιστημίου Ιωαννίνων.

Ημερομηνία ορισμού θέματος: 07.10.2015
«Computational design of functional Fe- and Cu-based coatings for environmentally sustainable applications».

Ημερομηνία τροποποίησης θέματος: 27.03.2019
«Computational design of functional Fe-X (X=Cu, Co, Mn) coatings and nanoclusters for environmentally sustainable applications».

ΔΙΟΡΙΣΜΟΣ ΕΠΤΑΜΕΛΟΥΣ ΕΞΕΤΑΣΤΙΚΗΣ ΕΠΙΤΡΟΠΗΣ : 05.06.2019

1.Χριστίνα Λέκκα, Αναπληρώτρια Καθηγήτρια του Τμήματος Μηχανικών Επιστήμης Υλικών της Πολυτεχνικής Σχολής του Πανεπιστημίου Ιωαννίνων,
2.Δημήτριος Παπαγεωργίου, Αναπληρωτής Καθηγητής του Τμήματος Μηχανικών Επιστήμης Υλικών της Πολυτεχνικής Σχολής του Πανεπιστημίου Ιωαννίνων,
3.Γεώργιος Ευαγγελάκης, Καθηγητής του Τμήματος Φυσικής της Σ.Θ.Ε. του Πανεπιστημίου Ιωαννίνων,
4.Ελευθέριος Λοιδωρίκης, Καθηγητής του Τμήματος Μηχανικών Επιστήμης Υλικών της Πολυτεχνικής Σχολής του Πανεπιστημίου Ιωαννίνων,
5. Φιλομήλα Κομνηνού, Καθηγήτρια του Τμήματος Φυσικής της Σ.Θ.Ε. του Α.Π.Θ.,
6. Ιωσήφ Κιοσέογλου, Αναπληρωτής Καθηγητής του Τμήματος Φυσικής της Σ.Θ.Ε. του Α.Π.Θ.,
7.Λεωνίδας Γεργίδης, Επίκουρος Καθηγητής του Τμήματος Μηχανικών Επιστήμης Υλικών της Πολυτεχνικής Σχολής του Πανεπιστημίου Ιωαννίνων.

Έγκριση Διδακτορικής Διατριβής με βαθμό **«ΑΡΙΣΤΑ»** στις **11.05.2020**

Ο Πρόεδρος του Τμήματος

Αλκιβιάδης Παϊπέτης
Καθηγητής

Η Γραμματέας του Τμήματος

Μαρία Κόντου

ΠΕΡΙΛΗΨΗ

Το ενδιαφέρον για τους φιλικά προς το περιβάλλον και βιώσιμα Fe-X (X = Cu, Co, Mn) νανοσυσσωματώματα και επικαλύψεις αυξάνεται σήμερα λόγω των πιθανών ανώτερων μαγνητικών ιδιοτήτων τους που μπορούν να οδηγήσουν σε εφαρμογές σε πολλαπλά πεδία όπως η κατάλυση και η παράδοση φαρμάκων.

Σε αυτή τη διατριβή, πραγματοποιήσαμε υπολογισμούς συναρτησιακού πυκνότητας φορτίου προκειμένου να μελετήσουμε τα νανοσυσσωματώματα Fe-X (X = Cu, Co, Mn) με στόχο την εύρεση των βέλτιστων ρυθμίσεων και μεγεθών συστάδων που εμφανίζουν την υψηλότερη μαγνητική ροπή (MM). Επιλέγουμε υποκατάσταση Cu καθώς είναι ένα κλασικό μη μαγνητικό στοιχείο, ενώ τα γνωστά μαγνητικά στοιχεία Co και Mn εμφανίζουν σύζευξη Ferromagnetic (FM) και Antiferromagnetic (AFM) με Fe αντίστοιχα. Για αυτούς τους λόγους, διερευνούμε διάφορα μεγέθη συστάδων λαμβάνοντας υπόψη διάφορες συνθέσεις και ατομικές διαμορφώσεις που αναλύουν την ηλεκτρονική πυκνότητα καταστάσεων (EDOS), τις κυματοσυναρτήσεις (WF) και τον πληθυσμό των ηλεκτρονίων.

Διαπιστώσαμε ότι τα νανοσυσσωματώματα FeCu εμφανίζουν το υψηλότερο τοπικό MM Fe όταν το Fe βρίσκεται σε περιοχές επιφανείας του συμπλέγματος με τον μικρότερο αριθμό γειτόνων Cu που δεν συμβάλλουν στις μαγνητικές ιδιότητες του συστήματος. Αντίθετα, τα νανοσυσσωματώματα FeCo εμφανίζουν σύζευξη FM με άτομα Co και Fe και αποδίδουν τον υψηλότερο μέσο όρο συστάδων MM, ενώ το τοπικό MM Fe είναι ίσο με τα περιστατικά FeCu. Τα νανοσυσσωματώματα FeMn δείχνουν μια μέση συστάδα MM κοντά στο μηδέν, μιμείται τη συνολική μέση τάση MM του FeCu λόγω της ζεύξης Mn-Mn AFM. Η ηλεκτρονική πυκνότητα καταστάσεων συστάδων 13- και 55 ατόμων εμφανίζει διακριτές και εντοπισμένες καταστάσεις, με αποτέλεσμα μισό μεταλλικό χαρακτήρα. Συγκεκριμένα, οι συστάδες FeCu εμφανίζουν μια πλήρως καταλαμβανόμενη ηλεκτρονική πυκνότητα Spin-up Fe 3d καταστάσεων που αποδίδουν κυματοσυνδέσεις με ομοιογενή κατανομή φορτίου. Αντίθετα, το Spin-down είναι σχεδόν άδειο και εμφανίζει ανασταλτικές καταστάσεις σύνδεσης κοντά στην κατάσταση homo. Οι συστάδες FeCo ή FeMn χαρακτηρίζονται από ηλεκτρονικές καταστάσεις Fe 3d που υβριδοποιούνται έντονα με το Co ή το Mn 3d τόσο για την περιστροφή όσο και για την περιστροφή των EDOS.

Επιπλέον, τα μεγαλύτερα νανοσυσσωματώματα (147 και 309 ατόμων) δείχνουν μια συμπεριφορά που μοιάζει με εκείνη των επιστρώσεων και μεταλλικά χαρακτηριστικά. Σε όλες τις περιπτώσεις, τα νανοσυσσωματώματα εμφανίζουν υψηλότερο MM από τα λεπτά υμένια Fe που συγκλίνουν πάνω από 120 άτομα. Συμπερασματικά, τα νανοσυσσωματώματα FM Fe-Co ή οι

επιστρώσεις Fe στο Co / Cu (111) προτείνονται ως ο καλύτερος υποψήφιος για συστήματα βασισμένα σε Fe με ισοδύναμο συνολικό και τοπικό Fe MM σε σύγκριση με τα αντίστοιχα συστήματα Fe-Cu και Fe-Mn.

Πιστεύουμε ότι αυτά τα αποτελέσματα μπορούν να συμβάλουν στις μελλοντικές εξελίξεις στο σχεδιασμό Fe-X (X = Cu, Co, Mn) περιβαλλοντικά βιώσιμων έξυπνων μαγνητικών συστάδων ή επιχρισμάτων.

ABSTRACT

The interest in the environmentally friendly and sustainable Fe-X (X=Cu, Co, Mn) nanoclusters and coatings is increased nowadays due to their potential superior magnetic properties that can lead to applications in multiple fields like catalysis and drug delivery.

In this thesis, we performed density functional calculations in order to study the Fe-X (X=Cu, Co, Mn) nanoclusters aiming in finding the optimum configurations and cluster sizes exhibiting the highest magnetic moment (MM). We choose Cu substitution since it is a classical non-magnetic element while the well-known Co and Mn magnetic elements exhibit Ferromagnetic (FM) and Antiferromagnetic (AFM) coupling with Fe respectively. For these reasons, we explore various cluster sizes considering several compositions and atomic conformations analyzing the electronic density of states (EDOS), the wave functions (WF) and the electron population.

We found that the FeCu clusters exhibit the highest Fe local MM when Fe is at cluster's surface sites having the smallest number of Cu neighbours that do not contribute in the systems' magnetic properties. On the contrary, FeCo clusters exhibit a FM coupling with Co and Fe atoms and yield the highest average clusters MM, while the Fe local MM is equal to FeCu cases. The FeMn clusters show an average cluster MM close to zero, mimicking the FeCu total average MM trend due to the Mn-Mn AFM coupling. The electronic density of states of 13- and 55-atom clusters exhibit discrete and localized states, resulting in a half metallic character. In particular, the FeCu clusters display a fully occupied Spin-up Fe 3d electronic density of states yielding wavefunctions with homogeneous charge distribution. On the contrary, the Spin-down is almost unoccupied exhibiting dangling bonding states close to the homo state. The FeCo or FeMn clusters' are characterized by Fe 3d electronic states that hybridize strongly with the Co or Mn 3d for both spin up and spin down EDOS's.

In addition, the bigger clusters (147 and 309 atoms) show a band-like behaviour and metallic features. In all cases, the nano-clusters exhibit higher MM than the Fe thin films reaching a plateau above 120 atoms. Concluding, the FM Fe-Co clusters or Fe coating on Co/Cu(111) are suggested as the best candidate for Fe-based systems with equivalent total and local Fe MM compared to the corresponding Fe-Cu and Fe-Mn systems.

We believe that these results can contribute to future developments in the design of Fe-X (X=Cu, Co, Mn) environmentally sustainable smart magnetic clusters or coatings

Committee

Advisor committee

Ch. Lekka (Supervisor)
Associate Professor
Department of Materials Science and Engineering, University of Ioannina
D. Papageorgiou
Associate Professor
Department of Materials Science and Engineering, University of Ioannina
G. Evangelakis
Professor
Department of Materials Science and Engineering, University of Ioannina

Jury committee

E. Lidorikis
Professor
Department of Materials Science and Engineering, University of Ioannina
F. Komniniou
Professor
Physics Department, Aristotle University of Thessaloniki
I. Kioseoglou
Associate Professor
Physics Department, Aristotle University of Thessaloniki
L. Gergidis
Associate Professor
Department of Materials Science and Engineering, University of Ioannina

Acknowledgments

Everybody thinks that this part is the easiest of the thesis, but for me it's the most difficult for two reasons: first it means that I have concluded my thesis, second that I have in my mind the movie of my life, going from the first to the last day I have spent in Ioannina. Four years of my life. I remember every single moment, when I first met the professors and the other colleagues at the University. The first SELECTA meeting, first poster and presentation. For all these moments I have to say thank you to each person that I met.

First, Christina I want to say thank you for having supported me every time that something was not clear and for having introduced me in the research world. Really thanks to Prof. Evangelakis for your precious suggestions. Prof. Papageorgiou, I will never forget your lessons and your advices. Mr. Konstantinos Dimakopoulos, with your patience you helped me every time the computers did not respond to my commands. Really many thanks to Prof. Kioseoglou for the computational time at the National HPC facility, ARIS.

I have to say thank you to Pablo that saved me in more than one administrative problem. Really thank you to the all colleagues in the lab and outside of the lab.

I want to say thank you to all the colleagues and Professors of the SELECTA project, really thanks to introduce me to the experimental counterpart of our work.

Finally, thanks to all my family and Italian friends. In particular thanks to Demetria De Vittor, Matteo Serra and Ricardo Berutti for supporting me all times that I thought 'I cannot make it'.

This work was supported by the SELECTA (No. 642642) H2020- MSCA-ITN-2014 project.

Contents

List of Figures

List of Tables

Abstract

The interest in the environmentally friendly and sustainable Fe-X (X=Cu, Co, Mn) nanoclusters and coatings is increased nowadays due to their potential superior magnetic properties that can lead to applications in multiple fields like catalysis and drug delivery.

In this thesis, we performed density functional calculations in order to study the Fe-X (X=Cu, Co, Mn) nanoclusters aiming in finding the optimum configurations and cluster sizes exhibiting the highest magnetic moment (MM). We choose Cu substitution since it is a classical non-magnetic element while the well-known Co and Mn magnetic elements exhibit Ferromagnetic (FM) and Antiferromagnetic (AFM) coupling with Fe respectively. For these reasons, we explore various cluster sizes considering several compositions and atomic conformations analyzing the electronic density of states (EDOS), the wave functions (WF) and the electron population.

We found that the FeCu clusters exhibit the highest Fe local MM when Fe is at cluster's surface sites having the smallest number of Cu neighbours that do not contribute in the systems' magnetic properties. On the contrary, FeCo clusters exhibit a FM coupling with Co and Fe atoms and yield the highest average clusters MM, while the Fe local MM is equal to FeCu cases. The FeMn clusters show an average cluster MM close to zero, mimicking the FeCu total average MM trend due to the Mn-Mn AFM coupling. The electronic density of states of 13- and 55-atom clusters exhibit discrete and localized states, resulting in a half metallic character. In particular, the FeCu clusters display a fully occupied Spin-up Fe 3d electronic density of states yielding wavefunctions with homogeneous charge distribution. On the contrary, the Spin-down is almost unoccupied exhibiting dangling bonding states close to the homo state. The FeCo or FeMn clusters' are characterized by Fe 3d electronic states that hybridize strongly with the Co or Mn 3d for both spin up and spin down EDOS's.

In addition, the bigger clusters (147 and 309 atoms) show a band-like behaviour and metallic features. In all cases, the nano-clusters exhibit higher MM than the Fe thin films reaching a plateau above 120 atoms. Concluding, the FM Fe-Co clusters or Fe coating on Co/Cu(111) are suggested as the best candidate for Fe-based systems with equivalent total and local Fe MM compared to the corresponding Fe-Cu and Fe-Mn systems.

We believe that these results can contribute to future developments in the design of Fe-X (X=Cu, Co, Mn) environmentally sustainable smart magnetic clusters or coatings.

Chapter 1

Introduction

1.1 State of the art

In the last few decades, an extensive study on magnetic properties of Fe-based nanoparticle (NPs) has been done, due to the increasing interest of their potential applications [10].

In the field of catalysis, for example, magnetic bimetallic NPs, like FeCu, are used into the removal process of heavy metals such as Cr and metalloids, combining interesting reactivity with an easy, economical and environmental friendly method of recovery [11]-[15]. Moreover, in biomedicine, magnetic nano-materials, such as $FeCo$, $FeNi$, $CoFe_2O_4$ and $MnFe_2O_4$ are being investigated for their use in bio-imaging, hyperthermia and drug delivery [16]-[18].

Furthermore, magnetic NPs are attractive in magnetic storage devices. Due to the fact that the magnetic properties are closely related to the dimensions of the system, the increase of the storage density, is related with the magnetic particles that have to become smaller and smaller[19].
Billas et al. [20], showed that Fe, Co, Ni clusters exhibit a larger magnetic moment (MM)/atom compared to the bulk, converging to the bulk value as the cluster's size increases. Theoretical results showed that Fe_{13} cluster displays the largest total MM ($44\mu_B$) among all other unary X_{13} clusters composed of 3d, 4d atoms[21], and Gustev et al [22] found that the Fe cluster's MM can be enhanced by substitution of one Fe with Mn ($Fe_{12}Mn$) or Gd ($Fe_{12}Gd$). Moreover, experiment on Co_nMn_m clusters exhibited an increase in clusters MM depending on Mn concentrations[23], contrary to Co_nV_m which the same phenomena were not observed[24].
Aiming in understanding and improving the magnetic properties of Fe, we shall present in this thesis a systematic study regarding the structural, electronic and magnetic properties of FeX (X=Cu,Co,Mn) coatings and nano-clusters by means of the Density Functional Theory (DFT) calculations.

1.1.1 Fe Magnetic Properties

Because of their great magnetic properties, a lot of experimental and theoretical attention was paid on Fe-based materials but some magnetic mechanisms are not still well identified.
It is known that Fe MM is found to be $4\mu_B$ but when Fe is assembled in the bcc bulk the MM decreases to $2.2\mu_B$ [9]-[26]. At hight temperatures (between 1183 and 1667 K), experiments display an Fe fcc phase[27]. Theoretical calculations revealed the existence of different magnetic Fe fcc phases depending on the volume[28],[29]. For a lattice constant (α) below $3.57\mathring{A}$ were found a paramagnetic (PM) state (α: 3.448 $\mathring{A}$) was found, while a low-spin ferromagnetic (LS-FM) state appeared at small lattice constant(α: 3.463 $\mathring{A}$, MM about $0.62\mu_B$). For α larger than 3.57 $\mathring{A}$, a third magnetic state appeared, known as high-spin ferromagnetic (HS-FM) state, with α $3.632\mathring{A}$ and a MM of $2.54\mu_B$[30]. Starting from this point, Fe thin films were deposited on different fcc substrates in order to stabilise Fe at lower temperature confirming an higher MM compared to the Fe bcc bulk (Fe on Cu(100) $2.8\mu_B$ and Fe on Co(100) $3\mu_B$) [7]-[36].

It is known that, ferromagnetism is caused by the spontaneous mutual alignment of magnetic moments. The spin imbalance is simply defined by the difference in the number of spin-up and spin-down electrons per atom $(n(+) - n(-))$. This effect is well understood in the bulk, but how ferromagnetic properties evolve by increasing the dimensions from atom to the bulk is still an open question [20].

Starting with the smallest case, Fe atom has 8 valence electrons distributed in 3d and 4s levels. Because of the Hund's rule five electrons occupy 3d spin-up levels, two the 4s levels, and the rest in the 3d spin-down states, giving the MM of $4\mu_B$. When Fe atoms are assembled in the bulk, atomic orbitals hybridize and form energy bands. It was shown that 4s orbitals create a wide band which remains partially filled, in contrast with the completely filled 4s orbital in the atom; while the 3d$\downarrow$ and 3d$\uparrow$ orbitals create narrower bands. As a result Fe exhibits a MM of $2.2\mu_B$ where the characteristic non integer MM is due to the partial delocalisation of the 3d electrons [37][38].

Theoretical and experimental results show that the enhanced MM displayed in thin films was caused by the lower coordination number of the atoms at the surface. For a single Fe(100) monolayer (MLs) local MM is theoretically found to be $3.2\mu_B$[39]. In addition, it is demonstrated that small clusters are more magnetic than the bulk structure. Fe local MM was found approximately $3\mu_B$ up to $\sim$ 55 atoms, around $2.5\mu_B$ for few hundred atoms, and converging to the bulk value (2.2 μ_B) for about five hundred atoms[40]-[43]. These properties arise because of the unusual structure. Due to the reduced coordination number of atoms the electrons belong to molecular orbitals and exhibit an energy gap between the highest occupied molecular orbital and the lowest unoccupied molecular orbital defining the HOMO-LUMO gap. The way in which these orbitals are filled and the HOMO-LUMO gap determines not only the stability of the clusters but also their properties[44].

1.1.2 FeCu

In the last paragraphs were shown that it is possible to improve the Fe local MM by depositing Fe film on fcc substrates or, for example, growing Fe-based bimetallic clusters. Fascinating results were found in the FeCu systems. Cu is known to be a no magnetic element, which at room temperature adopt the fcc bulk structure. Magnetic properties of Fe thin films on Cu substrate were known to depend on the number of Fe mono-layers (MLs)[45]-[49]. Interestingly, it is shown that when Fe thin films are deposited by using Pulsed Laser Deposition (PLD) they exhibit different magnetic properties from the films that were grown by the thermal deposition (TD). These results are attributed to the high deposition rate in the PLD technique, demonstrating that magnetic properties of the samples are affected by the deposition technique[50]-[52]. Generally, it is possible to distinguish three different regimes[53]-[57]:

1) Up to four MLs of Fe: the ground-state spin configurations are FM, the film assumes a face-centred-tetragonal (fct) structure. At a coverage of 4 ML Fe forms a complete over layer film which is ferro-magnetic FM with perpendicular magnetic anisotropy;

2) Between $5-10$ MLs: the Fe overlayers adopt an fcc structure, and the topmost two interlayer distances are increased. Moreover, the magnetisation signal is reduced;

3) Above 10 MLs: the Fe film's structure converts gradually to bulk bcc, and the magnetisation switches from perpendicular to in-plane.

Moreover, the local Fe MM decreases going from the topmost to the deeper layers[50][58].
Starting with the simple case, *ab initio* calculations found that for only one Fe ML the local MM was found to be $2.85\mu_B$ on Cu(001)[59][53] and $2.7\mu_B$ on Cu (111)[4][5]. Furthermore, in both surfaces the distance between the Fe layer and the neighbouring Cu layer was larger compared to the bulk. The enhancement in the Fe MM is commonly explained due to the reduction in coordination number and the symmetry of the Fe surface, which causes the d bands to narrow and hence, in general, enhances the paramagnetic state density at the Fermi level [60]. Moreover, due to the presence of the Fe ML, a weak MM was induced on the adjacent Cu site ($0.04\mu_B$/atom). For two Fe ML$_s$, it was found a local MM of $2.83\mu_B$/atom in the first and $2.58\mu_B$/atom in the second layer, resulting in a FM coupling [59][53]. For more than three layers AFM coupling was exhibited and the Fe local MM decreased from the topmost to deepest layers. In addition, it was found that FM coupling favourites the expansion between Fe-Fe layer distances, while a contraction was found between Fe-Fe AFM coupling [61]-[63]. In addition, one Fe ML sandwiched between two Cu thin films exhibited a MM of $2.60\mu_B$/atom, in both Cu(100) and Cu(111) structures[62]-[5]. Moreover, D. Errandonea [64], reported theoretical calculations about Fe and Cu thin films in the $L1_0$ structure. He found that the Fe MM increases, from $2.49\mu_B$ to $2.81\mu_B$, while the Cu MM decreases, from $0.112\mu_B$ to $0.038\mu_B$, when the ratio of the interlayer lattice constant (c) to the intralayer lattice constant (a) c/a increases from 0.8 to 1. B. Lazarovits et al[65] presented a systematic study of magnetic moment of finite monoatomic Fe$_n$ ($1 < n < 9$) chains deposited on top of fcc Cu(001) and Cu(111) surfaces. They found a correlation between the number of Cu nearest-neighbour and the Fe MM. For only one Fe atom on Cu layer, it was found a MM of $3.27\mu_B$ on Cu(111) and $3.19\mu_B$ on Cu(100). They attributed this trend to the number of nearest-neighbour Cu atoms, $N_{Cu} = 3$ in case of Cu(111) and $N_{Cu} = 4$ in case of Cu(001). When the Fe impurity was deposited on the first Cu surface layer, the results were reversed. A larger Fe MM was found on Cu(001)($N_{Cu} = 8$, $3.01\mu_B$) than

on Cu(111) ($N_{Cu} = 9$, 2.91 μ_B). Interestingly, for Fe chains longer than 3 atoms, they found that, Fe MM was systematically higher at the edges of the chains than in the middle. The MM lowering in the middle of the chains was attributed to the larger orbital hybridisation between the orbitals of the Fe atoms. Because of the reduced coordination number of the atoms and higher symmetry an enhanced MM was found also in the clusters. Theoretical results report that clusters exhibit localized electronics band producing an enhancement in magnetisation not only in ferromagnetic elements but also in non-magnetic materials[65]. For example, a weak MM was found in Cu_{13} icosahedral (ICO) cluster ($0.38\mu_B$/atom)[66]. Theoretical and experimental studies have demonstrated that pure Cu clusters display an ICO structure up to 2500 atoms[67]-[69]. Starting with 13 atoms, it was found that in $Cu_{12}Fe$, Fe tends to occupy the central position, showing a MM of $2.72\mu_B$, while Fe-Cu coupling was found to be AFM [70][71]. On the contrary, calculations on $Fe_{12}Cu$ reveal that Cu energetically prefers the surface sites displaying a MM of $0.2\mu_B$, while Fe exhibits a MM of 3.3-3.4μ_B in the shell and $2.1\mu_B$ at the center of the cluster[22]. For larger clusters, like $Cu_{54}Fe$, the energetically favourite structure has always Fe at the centre, with a MM around $2.5\mu_B$[72].

1.1.3 FeCo

For transition metals, the magnetic moments are in most cases absent because of their d-d neighbouring atoms' hybridisations. Exceptions are Cr, Mn, Fe, Co and Ni 3d transition metals that remain magnetic due to the imbalance between spin up and down electronic distributions[73]. Therefore, it is interesting to investigate the magnetic properties of Fe with a magnetic element's substitutions like Co and compare them with the corresponding Fe-Cu cases. Co was chosen as a good candidate known to have MM of $1.7\mu_B$ when in the hcp structure[37][74]. Experimentally, aiming in the studying the Fe fcc thin films' magnetic properties on Co fcc substrate (similarly to the FeCu layers), Co was grown on Cu fcc substrate. It was found that Fe thin films reproduced the same trends with the FeCu system. As it was shown for FeCu, three different region can be distinguished. Up to 5 Fe MLs high-spin state was shown and the fcc structure were preserved. In the second region, between 6 and 10 MLs the ferromagnetic order was restricted to the two topmost layers and the two layers at the interface, while the ferromagnetic order at the interface is induced by the ferromagnetic Co substrate. In the third region, more than 11 MLs, the structure converts from fcc to bcc[75]. In contrast to the growth of the Fe/Cu(100) system, which shows a perpendicular magnetisation in the first two regions, Fe/Co(100) system exhibits in-plane magnetisation throughout to the whole thickness. This result indicates the strong magnetic interaction between the ferromagnetic Co substrate and the Fe overlayers that changes the magnetic direction of the Fe overlayers[76]. Experimentally, Schmitz et all. [7] found an Fe MM of $3.0\mu_B$ up to 4 Fe ML_s on Co(001) and between 5 and 10 Fe ML an average Fe spin moment of $1.1\mu_B$. Turning to Co clusters, two different structures were exhibited theoretically. For less than 50 atoms an HCP structure was found to be the most stable configuration[77], while bigger clusters ($50-500$ atoms) shown ICO configuration [78].

Theoretical calculations on Co_{13} yielded a Co average MM of $1.9\mu_B$/atom in hcp configuration [79] and $2.5\mu_B$/atom in the ICO structure[42]. These have to be compared to the experimental result of $2.30 \pm 0.07\mu_B$/atom[80], $2.00 \pm 0.06\mu_B$[81]. In addition, both theoretically and experimentally, the Co-Co interactions were always found ferromagnetic, reproducing the hcp bulk Co behaviour. Ferromagnetic coupling was preserved also in the bigger Co clusters ($n \geq 55$), and the MM converged to the bulk value as the dimension

of the clusters increased[37][42].
Aguilera-Granja, Vega [82] presented a systematic study of CoFe ICO clusters. Starting with Co_{13} and gradually by substituting one Fe at each time (e.g. $Co_{12}Fe_1$), the Fe_{13} configuration was finally obtained revealing data for all stoichiometries. They found an increase in Co upon Fe decrease. Co MM of 2.36 μ_B and Fe MM $3.63\mu_B$ were found on $Co_{12}Fe$, while, Fe MM $3.44\mu_B$ and Co MM $1.76\mu_B$ were found on $Fe_{12}Co$ [82][22]. Lu et al [66], reported calculations about ICO CuCo clusters. They found that Co, like Fe, preferred the central position in the clusters. The average MM of $Cu_{12}Co$ was found to be $0.2\mu_B$/atom and $1.28\mu_B$ for Co and $0.14\mu_B$ for Cu. In the reverse case, $Co_{12}Cu$, Cu coupling AFM and exhibited a MM of $0.32\mu_B$ while Co MM was found to be $1.83\mu_B$.

1.1.4 FeMn

Mn can be considered as the most complex of all metallic elements, due to its structural and magnetic properties. Mn exhibits four different bulk phases depending on the pressure and temperature[83]:

$\alpha-$phase, under normal conditions of temperature and pressure it adopts an exotic crystalline structure containing 58 atoms in a cubic unit;

$\beta-$phase exists in the temperature interval from 1000 to 1368 K and is simple cubic with twenty atoms per unit;

$\gamma-$phase is found in the high-temperature region between 1368 and 1406 K; it is an fcc structure was exhibit;

$\delta-$phase, at higher temperatures up to the melting point (1517 K) it is a bcc structure.

Theoretically, a free Mn monolayer was known to be AFM with a giant magnetic moment of 4.32 μ_B[84]. Experimental results demonstrated that when only one Mn ML was deposited on fcc Co(100), it exhibits a ferromagnetic order and an enhanced local MM compared to the bulk[85]. In addition, when Mn films are epitaxially grown on (001) bcc Fe, Andrieu et al [86] reported that for uncapped Mn films, a structural and magnetic transition exists between 2 and 3 Mn monolayers. Up to 2 Mn atomic planes Mn displays a bct structure close to the Fe bcc structure and a ferromagnetic behaviour was observed in these films. From 3 to 10 atomic planes, the Mn film structure changes and the ferromagnetic behaviour disappears. They observed in uncapped Mn films that a magnetic transition from a ferromagnetic to an AFM state came up with this structural transition. In their theoretical calculations on Mn ML on Fe(001), Wu et al.[87] found a strong interplay between magnetism and atomic structure. They showed an antiparallel alignment between Mn in the plane with a local magnetic moment of $3.1\mu_B$ and -$3.26\mu_B$. The large MM was found to buckle the reconstruction in the Mn overlayer. Due to hybridisation with the magnetic Fe(001) substrate, the valence bands of the two different Mn atoms differ substantially. Carbone et al. [73] made an experimental and theoretical work comparing $c(2 \times 2)$ CuMn/Cu(100) and $c(2 \times 2)$ MnNi/Ni(100) finding experimentally in both systems an enhancement on Mn local MM and theoretically a MM of $3.75\mu_B$ and $3.5\mu_B$, respectively. Calculations on Fe_xMn_{1-x} alloys showed that for Fe-rich ($x = 75\%$) alloys exhibit a bcc structure with α 2.88$\mathring{A}$ FM state and an average MM of $1.89\mu_B$. For $x = 50\%$ an fcc structure was found with α= 3.65 $\mathring{A}$, AFM behaviour and an average MM of $1.81\mu_B$. For Mn-rich ($x = 75\%$) alloys, the fcc structure was

still mantained with α= 3.66 $\mathring{A}$, along with AFM behaviour and an average MM of 1.96μ_B[88]. Finally, M. Ekholm and I. A. Abrikosov [89], in their calculations found that magnetic properties of $Fe_{0.5}Mn_{0.5}$ are strictly related to the lattice constant revealing for the α experimental value an AFM coupling between atoms.

Turning to the clusters cases, it was found that Mn exhibits an ICO structure as the energetically favoured configuration. In the smallest ICO clusters, Mn_{13} shows a really low average MM 0.23 μ_B due to the spin-segregated state of atomic moments, the atoms in the two pentagonal rings are ferromagnetically aligned, while the two pentagonal rings are antiferromagnetically coupled each other[90]. M. B. Knickelbein in his experiments confirmed the theoretical MM of 0.56μ_B/atom for Mn_{13}[91]. When the central Mn was substituted with an other atom, different magnetic behaviours were displayed. For Ti, V and Cr a ferromagnetic state was found while Mn atoms in the surface shell exhibited a FM coupling. AFM coupling was found between Mn and the substituted central atom but an increase in average MM was observed (Mn_{12}Ti=2.3μ_B/atom, Mn_{12}V=2.2μ_B/atom, Mn_{12}Cr=1.7μ_B/atom). On the contrary, Fe, Co, Ni yielded a non magnetic state and their MM were found to be close to zero. Mn-Mn coupling between the Mn in the shell became AFM giving a cluster average MM close to zero (Mn_{12}Fe=0.6μ_B/atom, Mn_{12}Co=0.5μ_B/atom, Mn_{12}Ni=0.6μ_B/atom)[92].

Furthermore, it was found that the energetically favoured configuration of Fe_{12}Mn clusters was that of a Mn atom in the shell, yielding in an average cluster MM of 3.5μ_B/atom. In this configuration Mn showed a MM of 4.6μ_B and Fe $\sim$ 3.37μ_B. Moreover, when Mn was placed in the centre, it was found an AFM coupling between Fe-Mn and an average MM of 2.7μ_B/atom[93][22]. Study of CoMn clusters showed that for the $Co_{49}Mn_6$ the Mn atoms occupied the surface and their Co first neighbouring atoms showed an approximately $\sim$ 3.9μ_B local MM[94].

Chapter 2

Density Functional Theory

2.1 Many-Body problem

Due to the wave-particle nature of the nuclei and electrons a physical object, such as solid or clusters, needs to be described by the quantum mechanical theory. In quantum mechanics each particle is pictured as a wave-function that it is a solution of the *Schrödinger*'s equation [95]. For a multi-particles system of ions (nucleus plus core electrons) and electrons (valence electrons) the *Schrödinger* equation is written as:

$$H\Psi\{\mathbf{R}_I;\mathbf{r}_i\} = E\Psi\{\mathbf{R}_I;\mathbf{r}_i\} \tag{2.1}$$

where:

- H is the Hamiltonian of the system;
- $\Psi\{\mathbf{R}_I;\mathbf{r}_i\}$ is the many-body wave-function that describes the state of the system;
- E is the energy;

and the Hamiltonian operator is given by [96] [97]:

$$\begin{aligned} H = &-\sum_I \frac{\hbar^2}{2M_I}\nabla^2_{\mathbf{R}_I} - \sum_i \frac{\hbar^2}{2m_e}\nabla^2_{\mathbf{r}_i} \\ &+\frac{1}{2}\sum_{ij(i\neq j)} \frac{e^2}{|\mathbf{r}_i - \mathbf{r}_j|} - \frac{1}{2}\sum_{iI} \frac{Z_I e^2}{|\mathbf{R}_I - \mathbf{r}_i|} + \frac{1}{2}\sum_{IJ(I\neq J)} \frac{Z_I Z_J e^2}{|\mathbf{R}_I - \mathbf{R}_J|} \end{aligned} \tag{2.2}$$

M_I and $\mathbf{R}_I$ are the masses and positions of ions I, and m_e and $\mathbf{r}_i$ are referred to the masses and positions of the electron i. The first two terms are the kinetic energy of the particles (ions and electrons), and the last three terms describe the *electron-electron*, *electron-ion* and *ion-ion* interaction given by the Coulomb interaction. For a system of N particles,$\Psi\{\mathbf{R}_I;\mathbf{r}_i\}$ depends on $3N$ coordinates[98]. Solving a problems with $3N$ variables makes our system impossible to study analytically, thus approximations are necessary [99]. The simplest approximation that can be done is to think ions and electrons independently as it is shown in the next paragraph.

2.1.1 Born-Oppenheimer approximation

Due to the huge difference of mass between ions and electrons (three to five orders of magnitude), the ions can be considered 'frozen' during the motion of the electrons [96]. This is known as the $Born-Oppenheimer$ approximation, and the many-body wave function can be written as a product of the ions and electron wave-function[95]:

$$\Psi\{\mathbf{R}_I;\mathbf{r}_i\} = \Psi_I(\mathbf{R}_I)\Psi_e(\mathbf{R}_I;\mathbf{r}_i) \tag{2.3}$$

where the electrons wave-function depends parametrically on the ions coordinate [100].
Considering ions at rest, we can focus only to the electrons, and the Hamiltonian is reduced to:

$$H = -\sum_i \frac{\hbar^2}{2m_e}\nabla^2_{\mathbf{r}_i} + \frac{e^2}{2}\sum_{ij(i\neq j)}\frac{1}{|\mathbf{r}_i-\mathbf{r}_j|} - \frac{1}{2}\sum_{Ii}\frac{Z_I e^2}{|\mathbf{R}_I-\mathbf{r}_i|} \tag{2.4}$$

Because of the nature of the electrons-electrons interactions, solving for $\Psi(\{\mathbf{r}_i\})$ is an extremely difficult task. A way to solve this problem is to consider electrons as single particles that interact through an effective potential.

2.2 Single particle approximation

A way to simplify the many-body electrons wave function $\Psi(\{\mathbf{r}_i\})$ is to picture electrons as independent quantum mechanical particles. In this approximation, each electron experiences the presence of the other electrons through an effective potential that encapsulates the many-body nature of the true system.

2.2.1 Hartree-approximation

Assuming that electrons are non-interacting particles it is possible to write the many-body wave-function as a product of single orbitals where each orbital is referred to one single electron:

$$\Psi^H(\{\mathbf{r}_i\}) = \phi_1(\mathbf{r}_1)\phi_2(\mathbf{r}_2)\phi_3(\mathbf{r}_3).....\phi_n(\mathbf{r}_n) \tag{2.5}$$

The wave-functions $\phi_i(\mathbf{r}_i)$ are normalized states to unity, in which the individual electrons would be if this was a realistic approximation. This is known as the Hartree approximation (hence the superscript H), and the total energy can be written as:

$$E^H = \langle\Psi^H|\mathcal{H}|\Psi^H\rangle = \sum_i \langle\phi_i|\frac{\hbar^2}{2m_e}\nabla^2_{\mathbf{r}_i} + V_{ion}(\mathbf{r})|\phi_i\rangle + \frac{e^2}{2}\sum_{ij(i\neq j)}\langle\phi_i\phi_j|\frac{1}{\mathbf{r}-\mathbf{r}'}|\phi_i\phi_j\rangle \tag{2.6}$$

Minimizing the energy using the variational principle, the single-particle Hartree equations can be written as:

$$\left[\frac{\hbar^2}{2m_e}\nabla^2_{\mathbf{r}} + V_{ion}\mathbf{r} + e^2\sum_{j\neq i}\langle\phi_j|\frac{1}{\mathbf{r}-\mathbf{r}'}|\phi_j\rangle\right]\phi_i(\mathbf{r}) = \epsilon_i\phi_i(\mathbf{r}) \tag{2.7}$$

where the constants ϵ_i are Lagrange multipliers introduced to take into account the normalization of the single-particle states $\langle\phi_i|\phi_i\rangle = 1$.

In order to take a realistic solution, single-particle states ϕ_i are taken orthogonal, and each electron experiences the ionic potential $V_{ion}(\mathbf{r})$ as well as a potential due to the presence of all other electrons $V_H(\mathbf{r})$, given by:

$$V_i^H(\mathbf{r}) = +e^2 \sum_{j \neq i} \langle \phi_j | \frac{1}{\mathbf{r} - \mathbf{r}'} | \phi_j \rangle \tag{2.8}$$

This is known as Hartree potential and includes only the Coulombic repulsion between electrons [101]. The potential is different for each particle. It is a mean-field approximation of the electron-electron interaction, takes into account the electronic charge only, which is a severe simplification.
Due to the fact that, each orbital $\phi_i(\mathbf{r}_i)$ can be determined by solving the corresponding single-particle *Schrödinger* equation, if all the other orbitals $\phi_j(\mathbf{r}_j)$, $j \neq i$ were known, these equations have to be solved iteratively in the self-consistent way. Starting with a trial ϕ_i^{in}, to determinate the charge density of the system $\rho^{(in)}(\mathbf{r}) = \sum_i |\phi_i^{(in)}(\mathbf{r})|^2$ and then writing the potential to set the Hamiltonian, the new ϕ_i^{out} are taken by solving the *Schrödinger*'s equations. A new charge density can be written as $\rho^{(out)}(\mathbf{r}) = \sum_i |\phi_i^{(out)}(\mathbf{r})|^2$ and the cycle is continued until $\rho^{(out)}(\mathbf{r}) - \rho^{(in)}(\mathbf{r}) < \delta_{tol}$

2.2.2 Hartree-Fock approximation

In the Hartree approximation the Ψ^H was written as a product of the single-electron orbitals making the wave-function symmetric. Due to the Fermionic nature of electrons the multi-particle wave-function has to be antisymmetric, which means that the wave-function must to change sign if two electrons of the same spin interchange the positions: this is known as the *exchange* property, and is a manifestation of the Pauli exclusion principle [96]. Combining Hartree-type wave-functions to form a properly antisymmetrised wave-function for the system, we obtain the Slater determinant:

$$\Psi^{HF}(\{\mathbf{r}_i\}) = \frac{1}{\sqrt{N!}} \begin{vmatrix} \phi_1(\mathbf{r}_1) & \phi_1(\mathbf{r}_2) & . & \phi_1(\mathbf{r}_N) \\ \phi_2(\mathbf{r}_1) & \phi_2(\mathbf{r}_2) & . & \phi_2(\mathbf{r}_N) \\ . & . & . & . \\ . & . & . & . \\ . & . & . & . \\ \phi_n(\mathbf{r}_N) & \phi_n(\mathbf{r}_N) & . & \phi_n(\mathbf{r}_N) \end{vmatrix} \tag{2.9}$$

where N is the total number of electrons. This has the desired property, since interchanging the position of two electrons is equivalent to interchanging the corresponding columns in the determinant, which changes its sign. This is known as the $Hartree - Fock$ (HF) approximation. In the HF approximation, the total energy for the system is written as:

$$E^{HF} = \langle \Psi^{HF} | \mathcal{H} | \Psi^{HF} \rangle = \sum_i \langle \phi_i | \frac{\hbar^2}{2m_e} \nabla_{\mathbf{r}_i}^2 + V_{ion}(\mathbf{r}) | \phi_i \rangle + \frac{e^2}{2} \sum_{ij(i \neq j)} \langle \phi_i \phi_j | \frac{1}{\mathbf{r} - \mathbf{r}'} | \phi_i \phi_j \rangle - \frac{e^2}{2} \sum_{ij(i \neq j)} \langle \phi_i \phi_j | \frac{1}{\mathbf{r} - \mathbf{r}'} | \phi_j \phi_i \rangle \tag{2.10}$$

and the single-particle HF equations, obtained by a variational calculation, are:

$$\left[\frac{\hbar^2}{2m_e} \nabla_{\mathbf{r}}^2 + V_{ion}(\mathbf{r}) + V_i^H(\mathbf{r}) \right] + e^2 \sum_{j \neq i} \langle \phi_j | \frac{1}{\mathbf{r} - \mathbf{r}'} | \phi_i \rangle \phi_j(\mathbf{r}) = \epsilon_i \phi_i(\mathbf{r}) \tag{2.11}$$

Due to the antisymmetric wave-function nature, the equations exhibit one extra term compared with the Hartree equation, the last one, which is called the *exchange* term. The exchange term describes the effects of exchange between electrons. This term cannot be written simply as $V_i^X(\mathbf{r}_i)\phi_i(\mathbf{r}_i)$ (the superscript X denotes *exchange*).
First, the Hartree potential can be written in term of single-particle and the total densities by defining theme as:

$$\rho_i(\mathbf{r}) = |\phi_i(\mathbf{r})|^2 \tag{2.12}$$

$$\rho(\mathbf{r}) = \sum_i \rho_i(\mathbf{r}) \tag{2.13}$$

and the Hartree potential:

$$V_i^H(\mathbf{r}) = e^2 \sum_{j\neq i} \int \frac{\rho_j(\mathbf{r})}{|\mathbf{r}-\mathbf{r}'|} d\mathbf{r}' = e^2 \int \frac{\rho(\mathbf{r}') - \rho_i(\mathbf{r}')}{|\mathbf{r}-\mathbf{r}'|} d\mathbf{r}' \tag{2.14}$$

Moreover, the single-particle exchange density can be written [97]:

$$\rho_i^X(\mathbf{r},\mathbf{r}') = \sum_{j\neq i} \frac{\phi_i(\mathbf{r}')\phi_i^*(\mathbf{r})\phi_j(\mathbf{r})\phi_j^*(\mathbf{r}')}{\phi_i(\mathbf{r})\phi_i^*(\mathbf{r})} \tag{2.15}$$

Then the single-particle HF equations take the form:

$$\left[\frac{\hbar^2}{2m_e}\nabla_{\mathbf{r}}^2 + V_{ion}(\mathbf{r}) + V_i^H(\mathbf{r}) + V_X^H(\mathbf{r}) + \right]\phi_i(\mathbf{r}) = \epsilon_i\phi_i(\mathbf{r}) \tag{2.16}$$

Now, it is possible to rewrite the exchange potential in analogy with the Hartree potential:

$$V_i^X(\mathbf{r}) = -e^2 \int \frac{\rho_i^X(\mathbf{r},\mathbf{r}')}{\mathbf{r}-\mathbf{r}'} d\mathbf{r}' \tag{2.17}$$

Finally, the Hartree and the exchange potential give the HF potential to describe the interaction between electrons:

$$V_i^{HF}(\mathbf{r}) = e^2 \int \frac{\rho(\mathbf{r}')}{|\mathbf{r}-\mathbf{r}'|} d\mathbf{r}' - e^2 \int \frac{\rho_i(\mathbf{r}') + \rho_i^X(\mathbf{r}')}{|\mathbf{r}-\mathbf{r}'|} d\mathbf{r} \tag{2.18}$$

which can be written, with the help of the HF density:

$$\rho_i^{HF}(\mathbf{r},\mathbf{r}') = \sum_j \frac{\phi_i(\mathbf{r}')\phi_i^*(\mathbf{r})\phi_j(\mathbf{r})\phi_j^*(\mathbf{r}')}{\phi_i(\mathbf{r})\phi_i^*(\mathbf{r})} \tag{2.19}$$

as the following expression for the total electron-electron interaction potential:

$$V_i^{HF} = e^2 \int \frac{\rho(\mathbf{r}') - \rho_i^{HF}(\mathbf{r},\mathbf{r}')}{|\mathbf{r}-\mathbf{r}'|} d\mathbf{r}' \tag{2.20}$$

The first term is the total Coulomb repulsion potential of electrons common for all states $\phi_i(\mathbf{r})$, while the second term is the effect of Fermionic exchange, and it is different for each state $\phi_i(\mathbf{r})$.

2.3 Density Functional Theory

In the last two paragraphs we have shown a method to handle the many-body problems picturing electrons like non interacting particles. The interaction between particles is given by the Hartree (2.8) and the HF potential (2.20), and the problem is solved self-consistently due to the fact that the potentials depended on the single state wave-function.
A new way to solve the many-body problem was introduced by Hohenberg, Kohn and Sham. The basic idea was that, instead of dealing with the many-body *Schrödinger* equation (2.1) which involves the many-body wave-function, one deals with a formulation of the problem that involves the total density of electrons $n(\mathbf{r})$, named Density Functional Theory (DFT).

2.3.1 Hoenberg-Kohn theorems

The DFT is based on the Hohenberg-Kohn theorems, that state [102][103]:

- The electron density determines the external potential, and consequently the total energy of the system is a functional of the density $E[n(\mathbf{r})]$;
- The global minimum of $E[n(\mathbf{r})]$, defined by the $E[n_0(\mathbf{r})]$ ground state energy, attains its minimum only for the correct ground state density $n_0(\mathbf{r})$.

First we want to demonstrate that the density $n(\mathbf{r})$ is uniquely defined by an external potential $V(r)$ (this is identified with the ionic potential). To prove this, we will proceed with the unreasonable request that, taking two different potentials, $V(r)$ and $V'(r)$, we will give rise to the same density $n(\mathbf{r})$.
Given $V(r)$ and $V'(r)$ different in a non-trivial way, so that they do not differ merely by a constant:

$$V'(r) - V(r) \neq const$$

and let E and Ψ be the total energy and wave-function for the system with Hamiltonians H and potential V, and E' and Ψ' be the total energy and wave-function for the system with Hamiltonians H' and the potential $V'(r)$, we have:

$$E = \langle \Psi | H | \Psi \rangle \tag{2.21}$$

$$E' = \langle \Psi' | H | \Psi' \rangle \tag{2.22}$$

By using the variational principle:

$$\begin{aligned} E < \langle \Psi' | H | \Psi' \rangle = \\ \langle \Psi' | H + V' - V' | \Psi' \rangle = \langle \Psi | H' + V - V' | \Psi' \rangle \\ = \langle \Psi' | H' | \Psi' \rangle + \langle \Psi' | (V - V') | \Psi' \rangle \\ = E' + \langle \Psi' | (V - V') | \Psi' \rangle \end{aligned} \tag{2.23}$$

the strict inequality is a consequence of the fact that the two potentials are different in a non-trivial way. Similarly it can be proved:

$$E' < E - \langle \Psi | (V - V') | \Psi \rangle \tag{2.24}$$

Adding the equations (2.23) and (2.24), we find that:

$$(E+E') < (E+E') + \langle \Psi' | (V-V') | \Psi' \rangle - \langle \Psi | (V-V') | \Psi \rangle \tag{2.25}$$

The last two terms in the (2.25) give:

$$\begin{gathered} \langle \Psi' | (V-V') | \Psi' \rangle - \langle \Psi | (V-V') | \Psi \rangle = \\ \int n'(\mathbf{r})[V(\mathbf{r}) - V'(\mathbf{r})]d\mathbf{r} - \int n(\mathbf{r})[V(\mathbf{r}) - V'(\mathbf{r})]d\mathbf{r} = 0 \end{gathered} \tag{2.26}$$

we have assumed that $n(\mathbf{r}) = n'(\mathbf{r})$ as a result the two potentials are the same. Obviously it cannot be $E + E' < E + E'$ concluding that the densities cannot be the same [96]. This proves that there is a one-to-one correspondence between an external potential $V(\mathbf{r})$ and the density $n(\mathbf{r})$. Considering that the external potential determines the wave-function, the wave-function must be a unique functional of the density.
Representing the kinetic energy as T and the electron-electron interaction as W, that are the same for all solid, it is possible to define a universal functional that depend only to the electron density:

$$F[n(\mathbf{r})] = \langle \Psi | (T+W) | \Psi \rangle \tag{2.27}$$

Finally, the total energy is a functional of the density given by:

$$E[n(\mathbf{r})] = \langle \Psi | H | \Psi \rangle = F[n(\mathbf{r})] + \int V(\mathbf{r}) n(\mathbf{r}) d\mathbf{r} \tag{2.28}$$

In addition, the functional's minimum is achieved for the correct density $n(\mathbf{r})$ corresponding to $V(\mathbf{r})$. Taking a different charge density $n'(\mathbf{r}) \neq n_0(\mathbf{r})$ we have:

$$E[n'(\mathbf{r})] = \langle \Psi' | H | \Psi' \rangle = F[n'(\mathbf{r})] + \int V(\mathbf{r}) n'(\mathbf{r}) d\mathbf{r} > \langle \Psi | H | \Psi \rangle = E[n_0(\mathbf{r})] \tag{2.29}$$

2.3.2 Thomas-Fermi approximation

The first attempt to use the charge density as a basic variable in the energy functional was made by Thomas-Fermi (TF) [101]. The basic idea was to take a non interacting electron gas where the main contribution in the energy was taken only from the kinetic energy. In addition, they consider a spin-unpolarised system i.e., one with equal numbers of up and down spin electrons, in a spin-independent external potential. In the TF theory, the universal functional $F[n(\mathbf{r})]$ was approximated by the local approximation for non-interacting kinetic energy of a uniform gas, plus the Hartree energy:

$$F^{TF}[n(\mathbf{r}] = A_s \int n^{\frac{5}{3}}(\mathbf{r}) d\mathbf{r} + \frac{1}{2} \int \int \frac{n(\mathbf{r}) n'(\mathbf{r})}{|\mathbf{r} - \mathbf{r}'|} d\mathbf{r} d\mathbf{r}' \tag{2.30}$$

where the coefficient is chosen to agree with that of a uniform gas, given by:

$$A_s = \frac{3}{10} (3\pi^2)^{\frac{2}{3}} \tag{2.31}$$

By adding the external potential, the energy functional was:

$$E_{TF}[n(\mathbf{r})] = A_s \int n^{\frac{5}{3}}(\mathbf{r}) d\mathbf{r} + \frac{1}{2} \int \int \frac{n(\mathbf{r}) n'(\mathbf{r})}{|\mathbf{r} - \mathbf{r}'|} d\mathbf{r} d\mathbf{r}' + V_{ext} \tag{2.32}$$

under the constriction:

$$N = N[n(\mathbf{r})] = \int n(\mathbf{r})d\mathbf{r} \tag{2.33}$$

where N is the total number of electrons. By using the Lagrange multiplier the ground state charge density has to satisfy the variational principle:

$$\delta\left[E_{TF}[n(\mathbf{r})] - \epsilon_{TF}\left(\int n(\mathbf{r})d\mathbf{r} - N\right)\right] = 0 \tag{2.34}$$

that yields the Thomas-Fermi equations:

$$\epsilon_{TF} = \frac{\delta E_{TF}[n(\mathbf{r})]}{\delta n(\mathbf{r})} = \frac{5}{3}A_s n^{\frac{2}{3}}(\mathbf{r}) + \int \frac{n'(\mathbf{r})}{|\mathbf{r}-\mathbf{r}'|}d\mathbf{r}' + V_{ext} \tag{2.35}$$

2.3.3 Kohn-Sham equations

The Hoenberg-Kohn theorems ensure us that it is possible find the ground state of our system if we know the ground state charge density, but they do not give any information about how we can find the charge density. After Thomas-Fermi, another way to calculate $n_0(\mathbf{r})$ and then $E[n_0(\mathbf{r})]$ was proposed by Kohn and Sham in the 1965 [104].

The basic concept is to think the electrons like fictitious Fermionic particles with the only requirement that their density is identical to the real electronic density. These particles can be considered to be non-interacting: this is a very important aspect of the nature of the fictitious particles, which will allow us to simplify the problem considerably. Tacking in account the many-body wave-function in the form of a Slater determinant (2.9), and defining the charge density as:

$$n(\mathbf{r}) = \sum_i |\phi_i(\mathbf{r})|^2 \tag{2.36}$$

then the functional of energy is given by:

$$E[n(\mathbf{r})] = \sum_i \langle\phi_i| - \frac{\hbar^2}{2m_e}\nabla^2_{\mathbf{r}}|\phi_i\rangle + \frac{e^2}{2}\int\int \frac{n(\mathbf{r})n(\mathbf{r}')}{|\mathbf{r}-\mathbf{r}'|}d\mathbf{r}d\mathbf{r}' + \int V(\mathbf{r})n(\mathbf{r})d\mathbf{r} + E^{xc}[n(\mathbf{r})] \tag{2.37}$$

where the first term is the kinetic energy of non-interacting fictitious particle, the second is the coulomb interactions, third the external potential and the last is the $exchange - correlation$ energy, that includes all the effects of the many-body character of the true electron system. We have mentioned previously that the exchange contribution is due to the Pauli exclusion principle, moreover each electron is also affected by the motion of every other electron in the system, this is known as the *correlation* property. E_{xc} is simply the sum of the error made in using a non-interacting kinetic energy and the error made in treating the electron-electron interaction classically.

Writing the variation of the density as:

$$\delta n(\mathbf{r}) = \delta\phi_i^*(\mathbf{r})\phi_i(\mathbf{r}) \tag{2.38}$$

with the restriction that:

$$\int \delta n(\mathbf{r})d\mathbf{r} = \int \delta\phi_i^*(\mathbf{r})\phi_i(\mathbf{r}) = 0 \tag{2.39}$$

so that the total number of particles does not change. By applying the variational principle:

$$\delta\left[E[n(\mathbf{r})] - \epsilon\left(\int n(\mathbf{r})dr - N\right)\right] = 0 \tag{2.40}$$

under the restriction (2.39), the following single-particle equations, through a variational argument can be written:

$$\left[\frac{\hbar^2}{2m_e}\nabla^2_{\mathbf{r}} + V^{eff}(\mathbf{r}, n(\mathbf{r}))\right]\phi_i(\mathbf{r}) = \epsilon_i\phi_i(\mathbf{r}) \tag{2.41}$$

where the effective potential is given by:

$$V^{eff}(\mathbf{r}, n(\mathbf{r})) = V(\mathbf{r}) + e^2\int \frac{n(\mathbf{r}')}{|(\mathbf{r}) - (\mathbf{r}')|}d\mathbf{r}' + \frac{\delta E^{xc}[n(\mathbf{r})]}{\delta n(\mathbf{r})} \tag{2.42}$$

with $V(\mathbf{r})$ the external potential due to the ions; the last term is the unspecified functional $E^{xc}[n(\mathbf{r})]$. The single-particle equations (2.41) are referred to as Kohn-Sham equations and the single-particle orbitals $\phi_i(\mathbf{r})$ are called Kohn-Sham orbitals. The Khon-Sham equations, as the Hartree and HF, have to be solved self-consistently. Interestingly, if the E^{xc} were known exactly, and consequently the potential, the energy obtained by solving the Khon-Sham equations would be exact.

2.3.4 Spin Density Functional Theory

In spin polarized calculation the single particle wave-function is defined as [105]:

$$\begin{aligned}\chi^{\uparrow}(\mathbf{x}) &= \phi^{\uparrow}(\mathbf{r})\alpha(\omega)\\ \chi^{\downarrow}(\mathbf{x}) &= \phi^{\downarrow}(\mathbf{r})\beta(\omega)\end{aligned} \tag{2.43}$$

This formalism is known as *unrestricted* formalism, where the up and down spins are free to have different spatial orbitals $\phi^{\uparrow}(\mathbf{r})$ and $\phi^{\downarrow}(\mathbf{r})$. The total charge density is found as a sum of the density calculated by the Khon-Sham equations (2.41) referred to the spin up and down respectively. In particular, given by the previous paragraphs, the Kohn-Sham Hamiltonians referred to the two (up and down) cases are:

$$\begin{aligned}\hat{h}^{KS\uparrow} &= \frac{\hbar^2}{2m_e}\nabla^2_{\mathbf{r}} + V(\mathbf{r}) + V_H[n(\mathbf{r})] + V_{xc}[n^{\uparrow}(\mathbf{r})]\\ \hat{h}^{KS\downarrow} &= \frac{\hbar^2}{2m_e}\nabla^2_{\mathbf{r}} + V(\mathbf{r}) + V_H[n(\mathbf{r})] + V_{xc}[n^{\downarrow}(\mathbf{r})]\end{aligned} \tag{2.44}$$

Splitting the problem in spin up and down parts, it was found that:

- Spatial orbitals are free to have different energy
- The Hamiltonians also depend on the total density (up plus down spins) through the Hartree operator so they are coupled and have to be solved simultaneously.

In collinear magnetic system, we can define the total density as:

$$n(\mathbf{r}) = n_{\uparrow}(\mathbf{r}) + n_{\downarrow}(\mathbf{r}) = \sum_{i=1}^{N_{el\uparrow}} |\phi_i^{\uparrow}(\mathbf{r})|^2 + \sum_{i}^{N_{el\downarrow}} |\phi_i^{\downarrow}(\mathbf{r})|^2 \tag{2.45}$$

and the spin density:

$$n^{spin}(\mathbf{r}) = n_{\uparrow}(\mathbf{r}) - n_{\downarrow}(\mathbf{r}) = \sum_{i}^{N_{el\uparrow}} |\phi_i^{\uparrow}(\mathbf{r})|^2 - \sum_{i}^{N_{el\downarrow}} |\phi_i^{\downarrow}(\mathbf{r})|^2 \tag{2.46}$$

The difference in the density of spin up and down states define the magnetic moment of the system.

2.3.5 LDA and LSDA approximations

For the special case of a uniform electronic system, the E^{xc} can be written as [106]:

$$E^{xc}[n(\mathbf{r})] = \int n(\mathbf{r})\epsilon_{xc}[n(\mathbf{r})]d\mathbf{r} \tag{2.47}$$

where $\epsilon_{xc}[n(\mathbf{r})]$ is the correlation-exchange energy of each particle of a homogeneous electron gas having a density $n(\mathbf{r})$. It can be separated into exchange and correlation contributions:

$$\epsilon_{xc}(n(\mathbf{r})) = \epsilon_x[n(\mathbf{r})] + \epsilon_c[n(\mathbf{r})] \tag{2.48}$$

the exchange energy $\epsilon_x[n(\mathbf{r})]$ has been proven by Bloch and Dirac to be equal to:

$$\epsilon_x^{unif}[n(\mathbf{r})] = -\frac{3}{4}\left(\frac{3n(\mathbf{r})}{\pi}\right)^{\frac{1}{3}} \tag{2.49}$$

Correlation is far more sophisticated, as it depends explicitly on the physical ground-state wave-function of the uniform gas. A useful measure of the density is the Wigner-Seitz radius defined by:

$$r_s(\mathbf{r}) = \left(\frac{3}{4\pi(\mathbf{r})}\right)^{\frac{1}{3}} \tag{2.50}$$

which is the radius of a sphere around electron such that the volume of all spheres matches the total density of electrons. Having defined the Wigner-Seitz radius, it is possible to write the correlation energy as:

$$\begin{aligned} E_c(r_s) = \frac{A}{2}\Bigg[ln\frac{r_s}{r_s + b\sqrt{r_s} + c} + \frac{2b}{\sqrt{4c-b^2}}tan^{-1}\frac{\sqrt{4c-b^2}}{2\sqrt{r_s}+b} \\ -\frac{bx_0}{x_0^2 + bx_0 + c}\Bigg[ln\Bigg[\frac{(\sqrt{r_s}-x_0)^2}{r_s + b\sqrt{r_s} + c}\Bigg] \\ +\frac{2(b+2x_0)}{\sqrt{4c-b^2}}tan^{-1}\frac{\sqrt{4c-b^2}}{2\sqrt{r_s}+b}\Bigg]\Bigg] \end{aligned} \tag{2.51}$$

where A, x_0, b and c being suitable fitting constants. The LDA has be proven to be a remarkably fruitful approximation. For example, properties such as structure, vibrational frequencies, elastic moduli are described reliably for many systems. Because the LDA approximation is derived from the hypothesis that we have an homogeneous electron gas, one would expect that it is not a very accurate approach for all real systems. It is known that there are very significant errors in the exchange and correlation energies but, due to the fact that, as the exchange energy is generally underestimated and the correlation energy overestimated, these errors tend to cancel. The success of the LDA appears to be in part due to this cancellation of errors. In the spin density functional theory the up and down spin densities are treated separately. In this case the E^{xc} was written as:

$$E^{xc}[n(\mathbf{r})] = \int n(\mathbf{r})\epsilon_{xc}[n^{\uparrow}(\mathbf{r}), n^{\downarrow}(\mathbf{r})]d\mathbf{r} \tag{2.52}$$

where $\epsilon_{xc}[n^{\uparrow}(\mathbf{r}), n^{\downarrow}(\mathbf{r})]$ is the known exchange-correlation energy per particle for an electron gas of uniform spin densities $n^{\uparrow}(\mathbf{r}), n^{\downarrow}(\mathbf{r})$. This approximation is known as the Local Spin Density Approximation (LSDA) [107].

2.3.6 GGA approximations

The LSDA exchange-correlation energies are insufficiently negative (by about 10%) for almost all atoms, molecules, and solids [108]. In some cases this approximation is a reliable, moderate-accuracy approximation, in the meaning of the errors are regular and chemical trends are reproduced. For many solid-state purposes, the LSDA level of accuracy is sufficient. For example, LSDA is not accurate enough for most chemical applications, that require the determination of energy differences with a considerable precision. An improvement in the LSDA is made by introducing the dependency of the density gradient in the exchange correlation energy. This approximation is named *Generalised Gradient* Approximation (GGA). The typical form for a GGA functional is [107]:

$$E^{xc}[n(\mathbf{r})] = \int n(\mathbf{r})\epsilon_{xc}[n(\mathbf{r}), \nabla(\mathbf{r})]d\mathbf{r} \tag{2.53}$$

Several GGA functionals have been developed.

2.4 Pseudopotential

It is known that only valence electrons are mainly responsible in the interactions between atoms. In order to simplify our calculations it is possible to separate the core and valence electrons description by using the pseudopotetial method. This approach was presented for the first time by Phillips and Kleinman[109]. The pseudopotential method provides the possibility of neglecting the core electrons and write a smoother potential for the valence electrons. Separating valence(v) and core(c) electrons and defining $|\psi^{(n)}\rangle$ the single-particle states as the solutions of the single-particle equations, we can write:

$$H^{sp}|\psi^{(v)}\rangle = \epsilon^{(v)}|\psi^{(v)}\rangle \tag{2.54}$$

$$H^{sp}|\psi^{(c)}\rangle = \epsilon^{(c)}|\psi^{(c)}\rangle \tag{2.55}$$

H^{sp} is the single-particle Hamiltonian for each atom. Now we consider a new set of single-particle valence states $|\tilde{\phi}^{(v)}\rangle$ defined by:

$$|\psi^{(v)}\rangle = |\tilde{\phi}^{(v)}\rangle - \sum_c \langle\psi^{(c)}|\tilde{\phi}^{(v)}|\psi^{(c)}\rangle \tag{2.56}$$

Applying the single-particle Hamiltonian to this equation, we obtain:

$$\Big[H^{sp} + \sum_c \Big(\epsilon(v) - \epsilon(c)\Big)|\psi^{(c)}\rangle\langle\psi^{(c)}|\Big]|\tilde{\phi}^{(v)}\rangle = \epsilon^{(v)}|\tilde{\phi}^{(v)}\rangle \tag{2.57}$$

The modified potential for these states is called the *pseudopotential* V^{ps} and the corresponding $|\tilde{\phi}^{(v)}\rangle$ *pseudo-wavefunction*. V^{ps} is written as:

$$V^{ps} = V^{sp} + \sum_c \Big(\epsilon(v) - \epsilon(c)\Big)|\psi^{(c)}\rangle\langle\psi^{(c)}| \tag{2.58}$$

now we have obtained a *pseudo-wavefunctions* that experiences a weaker potential near the atomic nucleus, and the proper ionic potential away from the core region. The huge advantage of the pseudopotentials is that in the solid we have to deal with the valence electrons only, while we can consider the core electrons essentially frozen in their atomic wave-functions. Moreover, the pseudopotentials are smooth so that standard numerical methods can be applied to solve the single-particle equations[96].
According to Kleinman-Bylander[110], the pseudopotentials can take the form of:

$$V^{KB} = V^{sp} + \sum_c \frac{|\delta V^{ps}\psi^c\rangle\langle\psi^c\delta V^{ps}|}{\langle\psi^c|\delta V^{ps}|\psi^c\rangle} \tag{2.59}$$

where V^{KB} is the Kleinman-Bylander pseudopotentials and V^{sp} is the potential of one particle.

2.5 Projector augmented-wave method

In the previous paragraph we have shown that it is possible to separate the core and valence problem aiming in simplifying the computational effort. Another way to achieve this purpose was suggested by Bloch[111] first, and Kresse and Joubert[112] after, introducing the Projector Augmented-Wave method (PAW). In PAW the all-electron wave function ψ is written as[113]:

$$|\psi\rangle = |\tilde{\psi}\rangle + \sum_i (|\phi_i\rangle - |\tilde{\phi}_i\rangle)\langle\tilde{p_i}|\tilde{\psi}_i\rangle \tag{2.60}$$

where:

1. $|\tilde{\psi}\rangle$ is a pseudo wave function expanded in plane waves;
2. ϕ_i, $\tilde{\phi}_i$ and $\tilde{p_i}$ are the atom centred localised functions.

The all electron partial waves ϕ_i are obtained for a reference atom, the $\tilde{\phi}_i$ partial nodeless pseudo waves are equivalent to the ϕ_i outside a core radius r_c and match continuously onto $\tilde{\phi}_i$ inside the core radius.

2.6 Basis set

In order to solve Kohn-Sham equations, we need to define a basis set to write the unknown wave-function in terms of a set of known functions. For example, an unknown molecular orbital (MO) can be thought as a function of infinite coordinates system spanned by a complete basis set. When a finite basis set is used, only the components of the MO along those coordinate axes can be represented. There are two guidelines for choosing the basis functions[100]:

1. They should have a behaviour that agrees with the physics of the problem, to guarantee reasonably rapid convergence;
2. the chosen functions should make it easy to calculate all required integrals.

The basis set can be composed of atomic orbitals or plane waves.

2.6.1 LCAO

Defining χ as a basis set of molecular orbital ϕ we can write:

$$\phi_i = \sum_{\alpha=1}^{n} C_{\alpha i}\chi_\alpha = C_{1i}\chi_1 + C_{2i}\chi_2 ..... + C_{ni}\chi_n \tag{2.61}$$

where ϕ_i is a molecular orbital represented as the sum of n atomic orbitals χ_α. This method was introduced by Roothaan in 1951[114], called Linear Combination of Atomic Orbitals (LCAO)[100]. If the basis set χ is complete, where complete means that was been used an infinite number of functions $\alpha \to \infty$, any function ϕ_i could be fully described by equation 2.61. If α was infinite, our problem is impossible to be solved. The reason why the LCAO is a very powerful method is because it simplifies the optimisation problem from a nonlinear problem to a linear one with unique variable $C_{\alpha i}$. Several types of atomic orbitals can be used: Gaussian-type orbitals (GTO), Slater-type orbitals (STO), or numerical atomic orbitals (NAO).

2.6.2 NAO

NAO basis set is numerical solution of the Kohn-Sham Hamiltonian for the isolated pseudo-atom with the same approximations (xc, pseudos) as for the condensed system. Depending on the required accuracy and available computational power we can choose single ζ basis set or multiple ζ basis set. If it is used only one single radial function per angular momentum channel we referred to it as single ζ basis set. Radial flexibilisation is obtained by adding a second function per channel, in this case we referred to it with double ζ. In literature several scheme are proposed to generate this second function. The scheme applied in SIESTA code consists of supplementing each basis orbital with a new basis function. This new basis function reproduces exactly the tail of the original orbital from a given matching radius r_m outwards. The inner part goes smoothly towards the origin as $r^l(a - br^2)$, where a and b are chosen to ensure continuity of the function and its derivative at r_m[115].

2.6.3 Plane Waves

For infinite systems, molecular orbitals assemble energy bands, since the energy spacing between distinct levels vanishes, behaving like free electrons. The solutions of the Schrödinger's equation for a free electron is known to be a plain wave function, for this reason the electrons in a band can be described by orbitals expanded in a basis set of plane waves, written as:

$$\chi_k(\mathbf{r}) = e^{i\mathbf{k}\cdot\mathbf{r}} \tag{2.62}$$

The wave vector $\mathbf{k}$ is related to the energy of the system through the expression:

$$E = \frac{1}{2}\mathbf{k}^2 \tag{2.63}$$

The allowable $\mathbf{k}$ values are given by the unit cell translational vector $\mathbf{t}$, i.e. $\mathbf{k}\cdot\mathbf{t} = 2\pi m$, with m being a positive integer. This leads to a typical spacing between k vectors of ~ 0.01eV, and the size of the basis set

is thus uniquely characterized by the highest energy **k** vector included. For example, a typical energy cutoff of 200 eV thus corresponds to a basis set with ∼20000 functions[100].
Due to the free character of electrons, plane waves are perfect to describe valence electrons in metals. On the contrary, a description of core electrons, because of their strongly localization around the nuclei, required a lot of rapidly oscillating functions making $\mathbf{k}_{max}$ very large. In addition, plane wave basis cannot describe the singularity of the nucleus-electron potential, for this reason this type of basis set is used in connection with pseudo-potentials. Finally, while plane wave basis sets have primarily been used for periodic systems, they can also be used for molecular species by employing a supercell approach, where the molecule is placed in a sufficiently large unit cell such that it does not interact with its own image in the neighbouring cells.

2.7 Hellman-Feynman Theorem

The *Schrödinger* equation allow us to know the spatial distribution of the electron, but not the all forces acting on the our system. In order to calculate all forces that act on our system, we use the Hellmann-Feynman theorem. The Hellmann-Feynman theorem states that: the exact electronic energies and wave functions of an atom or molecule obey the relation[116][117]:

$$\frac{\partial E}{\partial \lambda} = \left\langle \Psi \left| \frac{\partial E}{\partial \lambda} \right| \Psi \right\rangle \tag{2.64}$$

λ being any parameter that affects the Hamiltonian of the system. Classically, the force acting on a given particle is equal to the negative of the derivative of the total energy with respect to the position. The force on a nucleus in an atomic system is shown to be just the classical electrostatic force that would be exerted on this nucleus by other nuclei and by the electrons' charge distribution[118]. Employing the Hellmann-Feynman theorem we can write the forces acting on the nuclei equal to:

$$F_X = -\frac{\partial E}{\partial X} = -\left\langle \Psi \left| \frac{\partial E}{\partial X} \right| \Psi \right\rangle \tag{2.65}$$

Once the spatial distribution of the electrons has been determined by solving the *Schrödinger* equation, all forces in the system can be calculated using classical electrostatics.

Chapter 3

Computational Details

In this thesis we performed DFT computational calculations by using SIESTA and VASP packages. We focused in the structural and electronic properties of FeCu, FeCo, FeMn icosahedral clusters and thin film structures aiming in understanding their magnetic behaviour. The first step was to obtain the systems' energetically favoured configurations and then we evaluated the electronic properties by plotting the electronic density of states (EDOS) and the corresponding wave functions.

3.1 SIESTA

Siesta (Spanish Initiative for Electronic Simulations with Thousands of Atoms) is both a way to perform electronic structure calculations and *ab initio* molecular dynamics simulations of molecules and solids[119]. Methods and approximations used in SIESTA are:

1. Kohn-Sham density functional method was used to solve the equations in self-consistent way;
2. LDA or GGA approximations;
3. Linear combination of numerical atomic orbitals (NAO) was used as bases set[120]-[122];
4. Norm-conserving pseudopotentials in their fully nonlocal (Kleinman-Bylander) form[109].

In figure 3.1 we present the self-consistent cycle in the SIESTA package. The self-consistent cycle starts with a trial charge density $n(\mathbf{r})$ that it is used to set the Hamiltonian. The $n(\mathbf{r})$ depends on the number and the type of atoms as well as on the bases set and the pseudo-potential chosen. From the solution of the Kohn-Sham equations we calculate a new charge density $n'(\mathbf{r})$, which is compared to the original value. If the difference of the original charge density with the new is greater than the predetermined value then $n(\mathbf{r})$ is replaced by $n'(\mathbf{r})$ and the same cycle is repeated. If the difference between the original charge density $n(\mathbf{r})$ and the new $n'(\mathbf{r})$ is less than a predetermined value then the forces between the atoms in the system are calculated. If these forces are less than a preset value then geometric optimization is assumed to be achieved

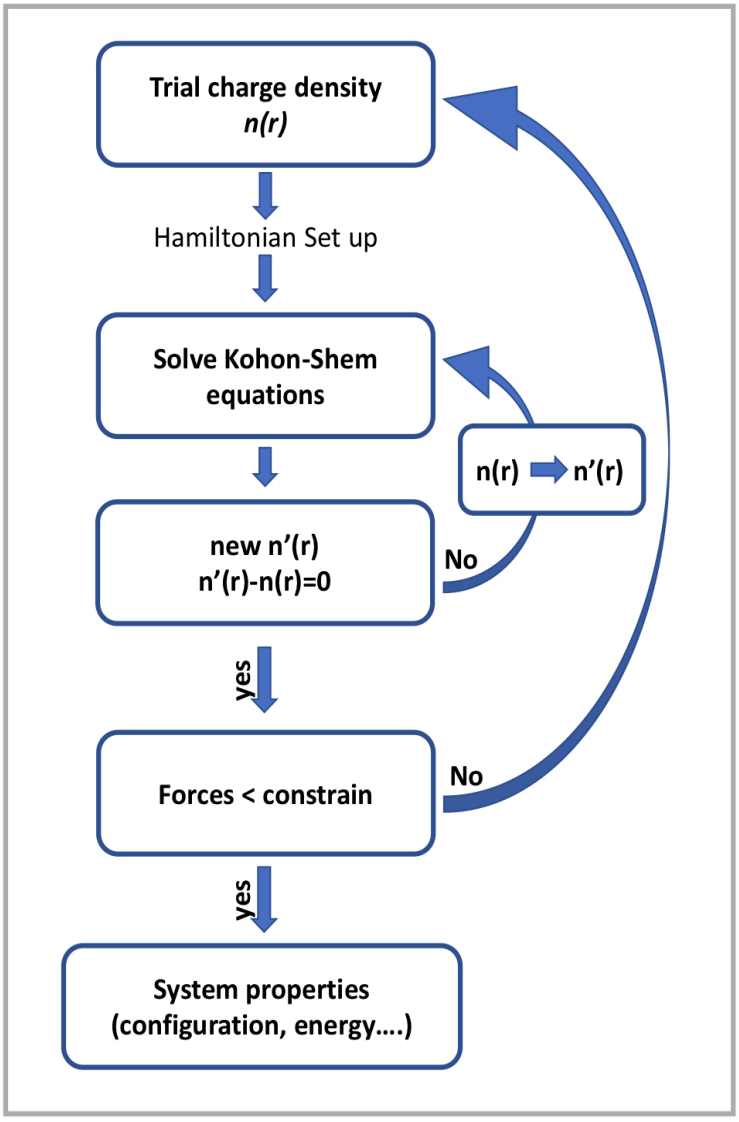

Figure 3.1: SIESTA code: self-consistent cycle

and all properties are calculated. Unless these forces are greater than the default value, ions are moved from their positions and a new configuration of the system is selected.

3.2 VASP

VASP (Vienna Ab-initio Simulation Package) is a complex package for performing *ab-initio* quantum-mechanical molecular dynamics (MD) simulations using pseudopotentials or the projector-augmented wave method and a plane wave basis set. The approach implemented in VASP is based on the (finite-temperature) local-density approximation with the free energy as variational quantity and an exact evaluation of the instantaneous

electronic ground state at each MD time step. VASP uses efficient matrix diagonalization schemes based on the conjugate gradient scheme, block Davidson scheme, or a residual minimization scheme-direct inversion in the iterative subspace, and an efficient Pulay/Broyden charge density mixing. Some highlights of the VASP[123]:

1. VASP uses the PAW method or ultra-soft pseudopotentials;
2. VASP uses plane wave basis set;
3. VASP uses a rather 'traditional' and 'old-fashioned' self-consistency cycle to calculate the electronic ground-state.

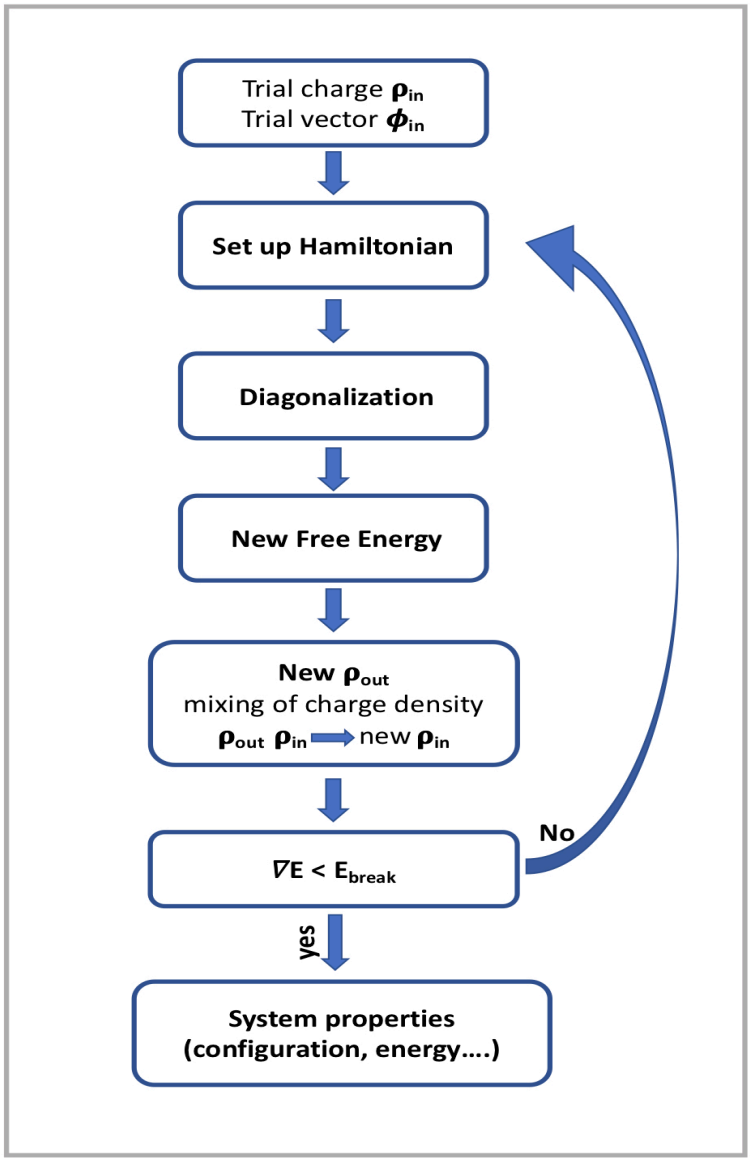

Figure 3.2: VASP code: self-consistent cycle

In figure 3.2 we present the self-consistent cycle in the VASP package. Starting with a trial charge density and trial wavefunctions in each selfconsistency loop the charge density is used to set up the Hamiltonian. Then the wavefunctions are optimized iteratively so that they get closer to the exact wavefunctions of this Hamiltonian. From the optimized wavefunctions a new charge density is calculated, which is then mixed with the old input-charge density. Within each selfconsistency loop the charge density is used to set up the Hamiltonian, then the wavefunctions are optimized iteratively so that they get closer to the exact wavefunctions of this Hamiltonian. From the optimized wavefunctions a new charge density is calculated, which is then mixed with the old input-charge density. The cycle stops when the difference in energy between two consecutive cycles is less than a predetermined value set in the input file named E_{break}.

3.3 SIESTA vs VASP

The next table 3.1 the mainly differences between SIESTA and VASP codes used in our input file are reported:

Table 3.1: SIESTA vs VASP code

	SIESTA	VASP
Basis set	NAO	PW
Pseudop.	Norm Conserving in Kleinman-Bylander form	PAW
E_{xc}	GGA (PBE)	
Ionic relaxation	Coniugate Gradient	

In our calculations we used GGA as the exchange correlation approximation but both packages can perform calculations by using also LDA. Furthermore, VASP allows different ionic relaxations methods depending on the system understudy.

3.4 Electronic Density of State

After solving single-particle equations for electrons, the resulting energy eigenvalues (band structure) and corresponding eigenfunctions provide information about how electrons are arranged in the solid. It is known that magnetic properties depend on the different electronic distribution in the two channels spin up and down then the electronic density of state give us the possibility to describe the magnetic properties of the materials under study. The Density Of States (DOS) of a system can be defined as the number of states per interval of energy at each energy level that are available to be occupied by electrons. For a 3D structure the number of available states between $\epsilon + d\epsilon$ energy is given by:

$$g(\epsilon)d\epsilon = \frac{1}{2\pi^2}\left(\frac{2m}{\hbar^2}\right)^{\frac{3}{2}}\epsilon^{\frac{1}{2}}d\epsilon \tag{3.1}$$

In a metal, the energy of the highest occupied single particle state defines the Fermi energy (E_F). In VASP[123] the density of states (DOS) $\bar{n}$, is actually determined as the difference of the integrated DOS between two pins:

$$\bar{n}(\epsilon_i) = \frac{N(\epsilon_i) - N(\epsilon_i - 1)}{\Delta\epsilon} \tag{3.2}$$

where $\Delta\epsilon$ is the distance between two pins (energy difference between two grid points in the DOSCAR file), and $N(\epsilon_i)$ is the integrated DOS:

$$N(\epsilon_i) = \int_{-\infty}^{\epsilon_i} n(\epsilon) d\epsilon \tag{3.3}$$

conserving the total number of electron exactly. In SIESTA[119] the DOS $\bar{n}$ is given by δ-functions centered in ϵ_i eigenvalue. In order to make easier the plot the functions they were expanded to Gaussian functions. For each energy state ϵ_i the $\bar{n}$ is given by the relation:

$$\bar{n}(\epsilon_i) = \sum_{i}^{N} e^{-\frac{(\epsilon-\epsilon_i)^2}{2\sigma}} \tag{3.4}$$

where N is the number of occupied states and σ is the Gaussian smearing. For a system a high DOS at a specific energy level means that there are many states available for occupation and zero DOS means that no state can be occupied at that energy level. In a metal, states below (E_F) correspond to the occupied states of the system, while those in energies higher than (E_F) are unoccupied states. The gap between the highest occupied and the lowest not occupied states defines the difference among conductor, semi-conductor and insulating. In conductor materials no gap is shown in the DOS, while depending of the size of the gap it is possible to recognize semi-conductor or insulating.

3.5 Surface

Most of the metals in the bulk assume: (a) Body Centered Cubic (BCC), (e.g Fe); (b) Face Center Cubic (FCC), (e.g. Cu); (c) Hexagonal Close Packed structure (HCP), (e.g.Co), as presented in figure 3.3.
Considering that magnetic properties are strictly connected to the structure of the system, the main features of the BCC, FCC, and HCP are reported in the next paragraphs.

3.5.1 Body Centered Cubic Structure

In the BCC structure, the atoms exist at each cube corner and one atom is at the center of the cube. The main characteristics of a BCC lattices are shown in the table 3.2.

The vectors that connect the particle placed in the origin of the cube to the particle at the body center define

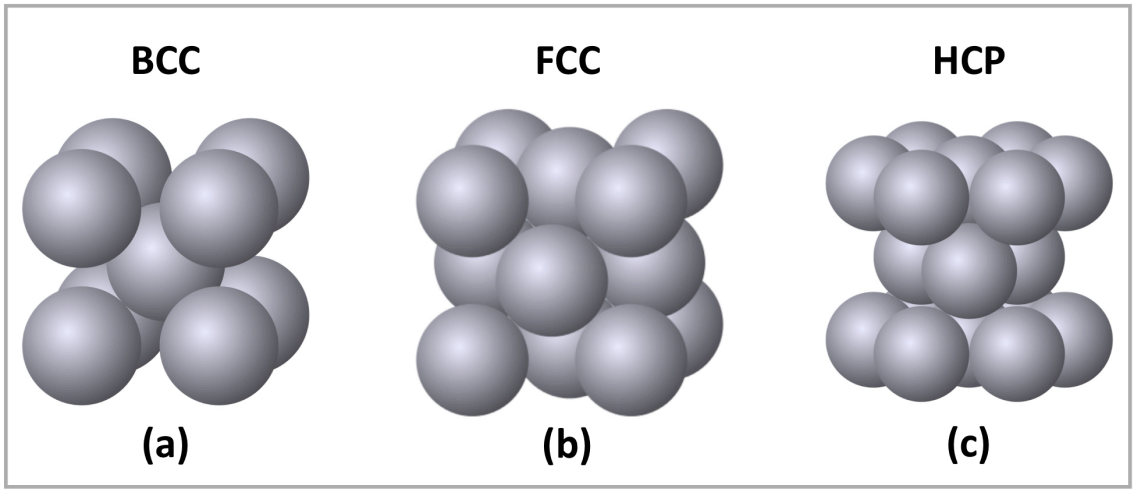

Figure 3.3: Structures: (a) BCC, (b) FCC and (c) HCP

Table 3.2: BCC lattice properties [1]. α is the lattice constant of the system.

Lattice point per cell	2
Primitive cell volume	$\alpha^3/2$
Lattice points per unit volume	$2/\alpha^3$
Number of nearest neighbours	8
Nearest-neighbour distance	$\alpha\sqrt{3}/2 = 0.866\alpha$

the primitive translation vectors. In terms of α, the primitive lattice vectors are:

$$\begin{aligned} \mathbf{a}_1 &= \frac{1}{2}\alpha(\hat{x} + \hat{y} - \hat{z}) \\ \mathbf{a}_2 &= \frac{1}{2}\alpha(-\hat{x} + \hat{y} + \hat{z}) \\ \mathbf{a}_3 &= \frac{1}{2}\alpha(\hat{x} - \hat{y} + \hat{z}) \end{aligned} \tag{3.5}$$

Since the position of a particle in a cell in terms of the atomic coordinate is specified by:

$$\mathbf{r}_j = x_j\mathbf{a}_1 + y_j\mathbf{a}_2 + z_j\mathbf{a}_3 \tag{3.6}$$

each coordinate is a fraction of the axial length $\mathbf{a}_1$, $\mathbf{a}_2$, $\mathbf{a}_3$ in the direction of the coordinate axis, with the origin taken at one corner of the cell. Thus the coordinate of the body center of a cell are $\left(\frac{1}{2}, \frac{1}{2}, \frac{1}{2}\right)$.

3.5.2 Face Center Cubic Structure

The FCC Structure consists of an atom at each cube corner and an atom in the center of each cube face. The main properties of a FCC lattices are shown in the table 3.3.

Table 3.3: FCC lattice properties [1]. α is the lattice constant of the system.

Lattice point per cell	4
Primitive cell volume	$\alpha^3/4$
Lattice points per unit volume	$4/\alpha^3$
Number of nearest neighbours	12
Nearest-neighbour distance	$\alpha/\sqrt{2} = 0.707\alpha$

In the FCC structure the primitive translation vectors $\mathbf{a}_1$, $\mathbf{a}_2$, $\mathbf{a}_3$ connect the lattice point at the origin with the particles at the faces centers. They are defined by:

$$\begin{aligned} \mathbf{a}_1 &= \frac{1}{2}\alpha(\hat{x} + \hat{y}) \\ \mathbf{a}_2 &= \frac{1}{2}\alpha(\hat{y} + \hat{z}) \\ \mathbf{a}_3 &= \frac{1}{2}\alpha(\hat{z} + \hat{x}) \end{aligned} \tag{3.7}$$

and the angle between the axes are $\pi/3$. When the origin is taken at one corner of the cell, the coordinate of the particle at the face centers are $\left(\frac{1}{2}\frac{1}{2}, 0\right)$, $\left(0\frac{1}{2}\frac{1}{2}\right)$, $\left(\frac{1}{2}0\frac{1}{2}\right)$.

3.5.3 Hexagonal Closed Packed structure

The primitive cell of the HCP structure is presented in figure 3.4. It shows $\mathbf{a}_1 = \mathbf{a}_2$ with an included angle of 120°, and the $\mathbf{a}_3$ axis is normal to the plane formed by $\mathbf{a}_1$ and $\mathbf{a}_2$.
The ideal HCP structure has $c = 1.633\alpha$.

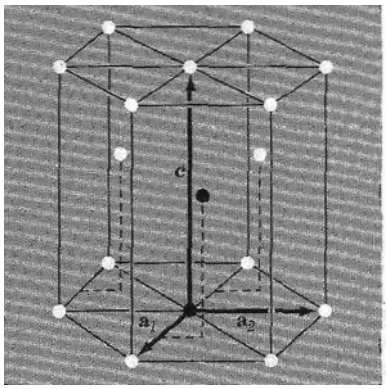

Figure 3.4: HCP structure[1]: primitive translation vectors

When one atom of the basis occupies the origin, the other atom is at $\left(\frac{2}{3}\frac{1}{3}\frac{1}{2}\right)$ which means at the position:

$$\mathbf{r} = \frac{2}{3}\mathbf{a}_1 + \frac{1}{3}\mathbf{a}_2 + \frac{1}{2}\mathbf{a}_3 \tag{3.8}$$

3.5.4 Miller Indices for a crystal

The orientation of a crystal plane is determined by three points in the plane. If each point lay on a different crystal axis, the plane could be specified by giving the coordinate of the points in terms of the $\mathbf{a}_1$, $\mathbf{a}_2$, $\mathbf{a}_3$. In order to determinate the indices of the plane we have to find:

1) the intercepts of the axes in terms of $\mathbf{a}_1$, $\mathbf{a}_2$, $\mathbf{a}_3$;

2) Take the reciprocal of this numbers and then reduce theme at the smallest integer by multiplying them for their common denominator.

3) The result (hlm) are index of Miller

For an intercepts at infinity, the corresponding index is zero. For example, the cube faces of a cube crystal are (100), (010), (001).

3.5.5 Close packed layer

Close-packed layer are layer where each sphere in the plane of the crystal is in contact with six other in the plane. This configuration is the basal plane of the HCP structure or (111) FCC plane. We take this plane and we name it (A). We build a similar layer (B) by placing spheres in contact with three spheres in the bottom plane (A). A third layer (C) may be added in two different ways:

- FCC is the obtained structure if the spheres of the third layer are added over the holes in the first layer that are not occupied by (B). As a result we have ABCABC;
- HCP structure is obtained when the spheres in the third layer are placed directly over the centers of the spheres in first layer (A). As a result we have ABAB.

Finally, BCC structures have no close packed planes.

3.6 Icosahedral clusters

As reported in the introduction, clusters have gained a lot of attention because of their particular properties. For instance, gold particles with macroscopic size are not active for catalytic applications, while, gold particles with about 1.5 nm ($\sim$ 55 atoms) exhibit unexpected catalytic behaviour for several reactions[124]. Moreover, experiments probe that transition-metal elements that are nonmagnetic on their bulk phase can exhibit surprising great MM for particles with few atoms, (e.g Rh_n n=12-32)[125], whereas magnetic bulk materials exhibit an increase of their MM at nanoscale[126]. Interestingly, clusters with 13 atoms have a high rate of occurrence for Fe, Ti, Zr, Nb, Ta, and Al [127] which have been supported by theoretical calculations[128]. In addition, structural model analysis based on close-packed icosahedral ICO configurations revealed the preference for clusters with 13, 55, and 147 atoms. In icosahedral shell packing (i.s.c.), the atoms can occupy three different positions in the shell:

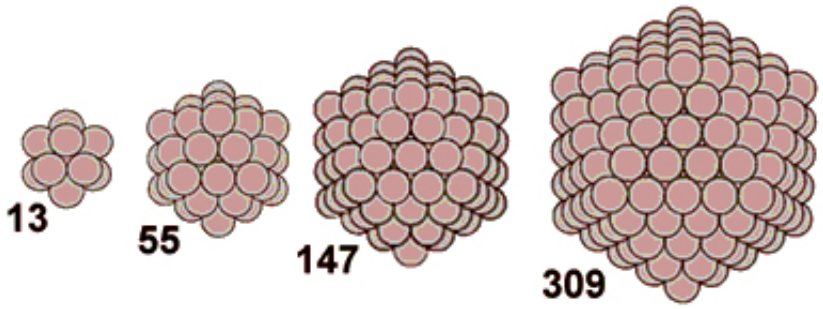

Figure 3.5: Icosahedral Shell Packing

1. (a) on vertices
2. (b) on edges
3. (c) in the faces

In the n_{th} shell there are 12 spheres of the first kind (a), $30(n-1)$ of the second kind (b) and $10(n^2-3n+2)$ of the third (c).
An ICO cluster of n shells contains $(\frac{10}{3n^3}+5n^2+\frac{11}{3n}+1)$ atoms. Moreover, It was found that the i.s.c. density was higher (0.68818) compared to the body-centred cubic packing (0.68017) and lower than cubic close-packed (0.74048) or body-centered tetragonal packing (0.69813)[129]. Finally, the triangular faces on the shell are the (111) planes of the face centered cubic (FCC) closely packed sequence ABCA[130].

Chapter 4

Surface

The aim of this chapter is to investigate the structural, electronic and magnetic properties of Fe-X (Cu,Co,Mn) atomic layer's coating on Cu and Fe surfaces.

For all calculations we use VASP package while SIESTA results are reported for comparison. In particular, we utilise GGA approximations as proposed by Perdew et al [131], also the Brillouin zone integration is performed using an $(9 \times 9 \times 1)$ Monkhorst-Pack grid (12 k-points in the irreducible wedge) and the smearing methods based on a Methfessel-Paxton [123].

The whole system of Fe-X (Cu,Co) atomic layer's coating on Cu surfaces consist of six layers. Three Cu layers are fixed in order to stabilise the surface, while the others Cu, Fe and Co coatings are free to move in the z direction. Moreover, in the FeMn atomic layer's coating on Fe surfaces we fix the first three Fe layers in order to stabilise the surface, whereas the other Fe and Mn coatings are able to move only in the z direction.

4.1 Cu and Fe bulk

4.1.1 Cu bulk: structural, electronic and magnetic properties

It is well known that the Cu bulk does not show any magnetic property and it exhibits a FCC geometry.

The electronic structure of Cu is given by $[Ar]3d^{10}4s^1$, therefore Cu-3d orbitals are fully occupied leaving $4s^1$ electron empty. When Cu atoms aggregate in a structure, the hybridisations among orbitals appear. Consequently, we find that Cu PEDOS shows a symmetric behaviour between spin up and spin down distribution, giving a bulk average MM of zero.

Table 4.1 displays the lattice constant α ($\AA$) and the bulk modulus B (GPa) of the FCC Cu. Moreover, in the last two columns we report the available theoretical and experimental results for comparison reasons.

Table 4.1: Cu bulk: lattice constant α ($\AA$), bulk modulus B (GPa) of the FCC Cu. In the last two columns theoretical and experimental references are reported for comparison.

	VASP	SIESTA	Theo. ref	Exp. ref
α	3.63	3.56	3.64	3.61
B	142	195	136	137

We observe that our VASP calculations show a good agreement with literature, while SIESTA underestimates the lattice constant and overestimates the bulk modulus.

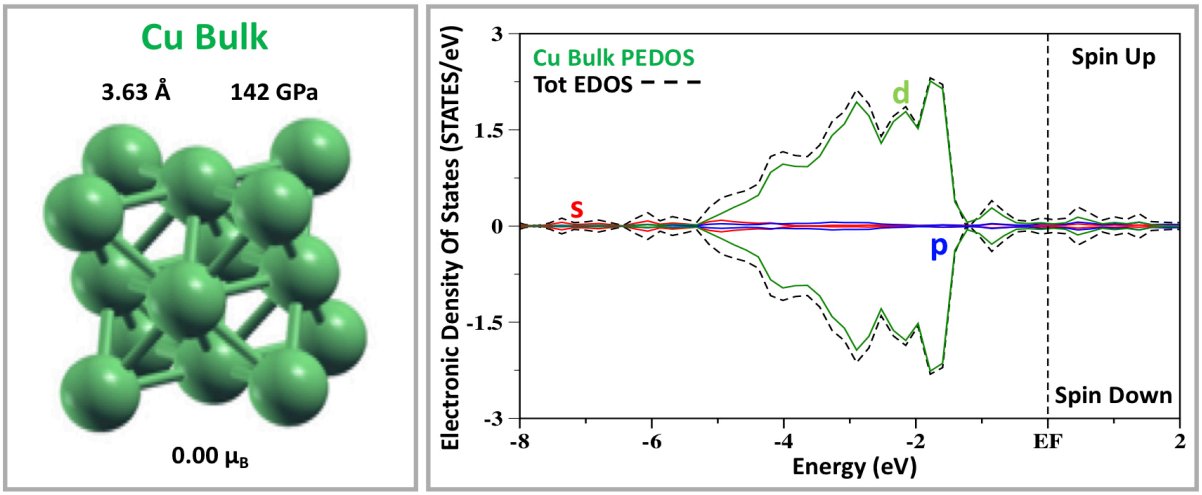

Figure 4.1: Cu Bulk: (a) structural and magnetic properties. (b) Total cluster EDOS (dashed black line); PEDOS (the s, p and d PEDOS is presented with red, blue and green lines, respectively)

In figure 4.1.(a) we present the Cu bulk structural and magnetic properties, while in figure 4.1.(b) we report the Cu bulk the total and partial EDOS. In agreement with literature, we observe the symmetric behaviour between majority and minority population, resulting in a no magnetic structure. In particular, we observe broad s- and p-band, while the 3d electrons are located between -5eV and -1eV.

4.1.2 Fe bulk: structural, electronic and magnetic properties

It is well known that the Fe bulk is a magnetic structure and it exhibits a BCC geometry. Fe atom exhibits an electronic structure given by $[Ar]3d^6 4s^2$. Specifically, Fe-3d-up orbitals are fully occupied while Fe-3d-down display four unoccupied energy levels giving a MM of $4\mu_B$. In the Fe bulk, s orbitals hybridize, overlapping each others and giving rise to energy bands. Levels corresponding to the 4s-electrons are strongly delocalized, resulting in a very broad s-band. On the contrary, the d-electrons remain rather localized on the atomic sites and the band is relatively narrow[40].

In the table 4.2 we provide the lattice constant $\alpha(\AA)$, bulk modulus B (GPa) and magnetic moment MM (μ_B)

of the Fe bulk. Furthermore, in the last two columns we display the available theoretical and experimental results for comparison. We note that our VASP results show a good agreement with literature especially

Table 4.2: Fe bulk: lattice constant α ($\AA$), bulk modulus B (GPa) and magnetic moment MM (μ_B), of the BCC Fe. In the last two columns theoretical and experimental references are reported for comparison.

	VASP	SIESTA	Theo. ref	Exp. ref
α	2.84	2.90	2.88	2.87
B	172	163	190	168
MM	2.21	2.39	2.35	2.22

those concerning the lattice constant as expected. Furthermore, SIESTA overestimates the Fe bulk MM and the lattice constant, it while underestimates the bulk modulus.

In figure 4.2.(b) we display the Fe bulk PEDOS.

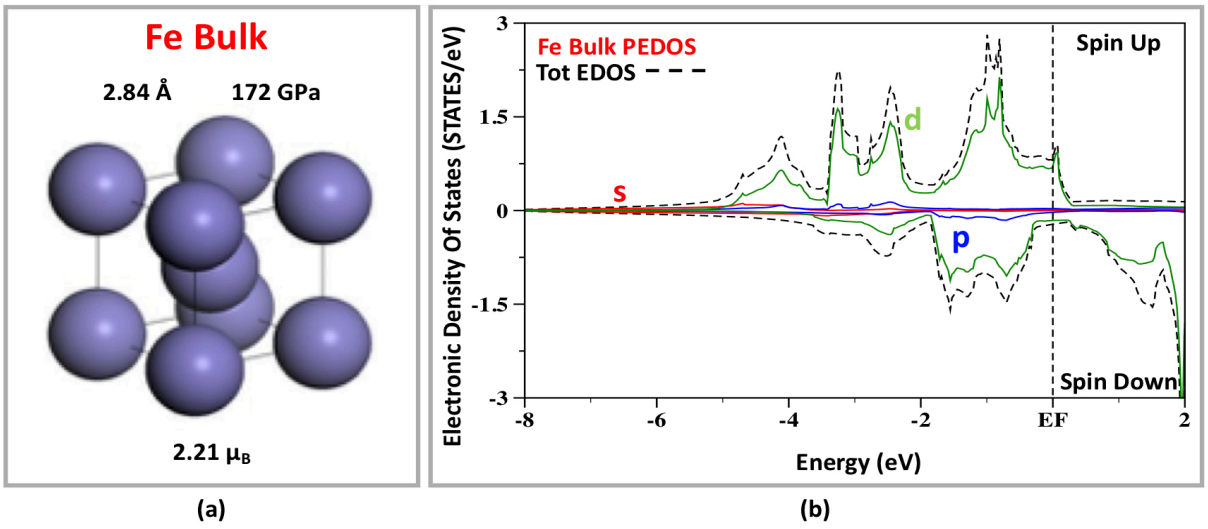

Figure 4.2: Fe Bulk: (a) structural and magnetic properties. (b) Total cluster EDOS (dashed black line); PEDOS (the s, p and d PEDOS is presented with red, blue and green lines, respectively)

The Fe-3d electrons are more localized than Fe-4s orbitals, in agreement with literature. Moreover, 3d-down electrons are shifted far from the Fermi energy leaving the minority channel partially unoccupied, originating the Fe bulk magnetic moment.

4.2 Fe on Cu substrate

4.2.1 Fe on Cu(100): structural, electronic and magnetic properties

We begin the surfaces' study investigating the structural and magnetic properties of Fe monolayers (ML_s) on Cu(100). For simplicity reasons, we display Fe atoms in red and Cu in green.

Concerning the structural properties, we calculate the contraction and expansion between layers using the formula:

$$d_{ij}\% = \frac{(d_i - d_j) - d_{Cu}}{d_{Cu}} \times 100 \tag{4.1}$$

where d_{Cu} is the theoretical Cu-Cu interlayer distance $d_{Cu} = 1.82\mathring{A}$.

In figure 4.3 we present structural and magnetic properties of (a) one, (b) two and (c) three Fe monolayers (ML_s) on Cu(100). In particular, in the figures we present only the first four layers of the whole system. Moreover, we exhibit VASP results are in green, SIESTA in black, while blue [2] and violet [3] values are reported as references for comparison.

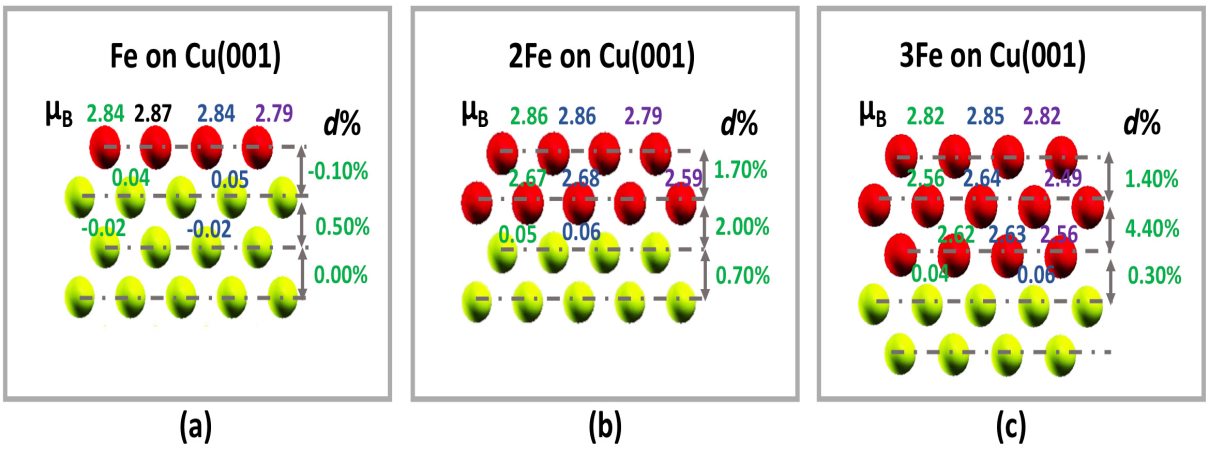

Figure 4.3: Fe on Cu(100): (a) one, (b) two and (c) three Fe monolayers (ML_s) on Cu(100). MM (μ_B) (VASP, SIESTA, ref [2] and [3] are reported in green, black, blu and violet, respectively). $d\%$ layer relaxation.

We observe that configuration (a) exhibits a small contraction between Fe-Cu ML_s in agreement with Spišak and Hafner [55]. Furthermore, configurations (b) and (c) report Fe-Fe and Fe-Cu expansion, in line with LEED experimental results and other theoretical calculations [52][50][63][54]. Concerning the magnetic properties, we note that, due to the reduced coordination number, the outermost Fe layer exhibits the highest MM, while the Fe surface MM decreases in the inner layer.

In the table 4.3 we present the local Fe magnetic contribution for (a), (b) and (c) cases. Moreover, we refer to the Fe(I), Fe(II), Fe(III) as the first (the outermost), second and third (the inner) layers.

In the Fe(I) layer, s and d orbitals exhibit a larger occupation in the majority population than in the minority ones, showing the highest Fe local MM. Moreover, p orbitals displays zero or a really small amount

Table 4.3: Fe on Cu(100): Fe atoms' local magnetic contribution of (a), (b) and (c) structures. Fe(I), Fe(II), Fe(III) are referred to the first (the outermost), second and third (the inner) layers.

	Fe(I)				Fe(II)				Fe(III)			
	s	p	d	tot	s	p	d	tot	s	p	d	tot
(a)	0.02	-0.01	2.83	2.84								
(b)	0.01	-0.01	2.87	2.87	-0.01	-0.02	2.69	2.66				
(c)	0.00	-0.01	2.83	2.82	-0.02	-0.05	2.63	2.56	-0.01	-0.02	2.65	2.62

of the minority charge. Looking at Fe(II) and Fe(III) layers, the charge distribution shows that s and p minority orbitals are more filled than the majority ones, lowering the local Fe MM. In addition, we find that configuration (a) shows the highest Fe local MM.

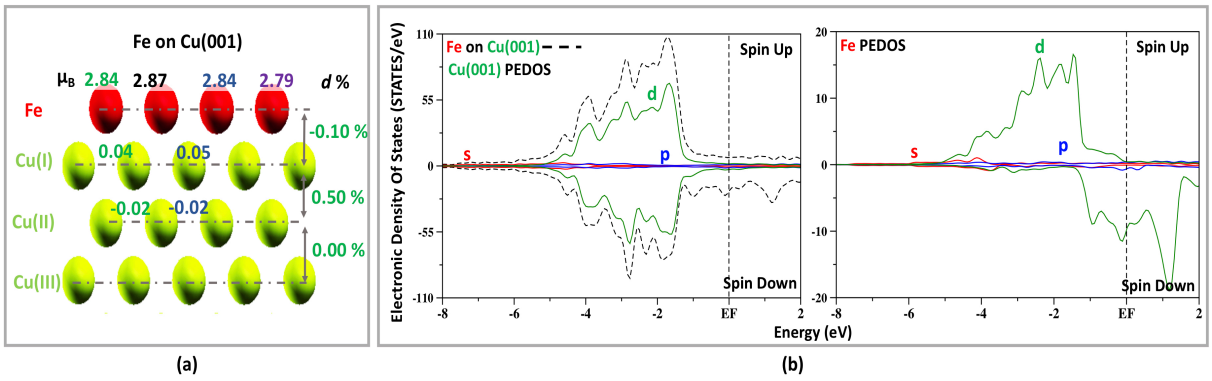

Figure 4.4: Fe on Cu(100): (a) magnetic and structural properties (VASP, SIESTA, ref [2] and [3] are reported in green, black, blu and violet, respectively). (b) Left panel: Total EDOS (dashed black line); Cu substrate PEDOS (the s, p and d PEDOS is presented with red, blue and green lines, respectively). Right panel: Fe monolayer PEDOS.

In figure 4.4.(a) we present the structural and magnetic properties of the (a) one Fe ML on Cu(001) system. We observe an Fe surface layer MM of $2.84\mu_B$. Moreover, the Cu layer (I) displays a weak Cu local MM of $0.04\mu_B$. Additionally, we note a contraction between Fe-Cu ML_s of 0.1%, while the next two Cu ML_s result relaxed of 0.5%.

In figure 4.4.(b), panel left displays the total Fe on Cu(001) EDOS and the Cu substrate PEDOS. The Cu substrate PEDOS exhibits a symmetric distribution between spin up and down populations, reflecting the no-magnetic tendency of the Cu element. Furthermore, Fe PEDOS in 4.4.(b) panel right shows a considerable difference between up and down charge distribution. Fe-3d up are enclosed by -5eV and -1eV, resulting almost fully occupied (4.49(↑)). Fe-3d down orbitals are shifted towards the hight energies around -1eV and EF, leaving the down states less filled (1.65(↓)) than the majority ones.

4.2.2 Fe on Cu(111): structural, electronic and magnetic properties

In this paragraph we present Fe ML_s on Cu(111) substrate. Figure 4.4 exhibits structural and magnetic properties of (a) one and (b) two Fe monolayers (ML_s) on Cu(111). Moreover, for simplicity reasons in the picture we exhibit only the first four layers of the whole system. Furthermore, we display VASP results in green, SIESTA in black, while in blu [4] and violet [5] are reported as references for comparison.

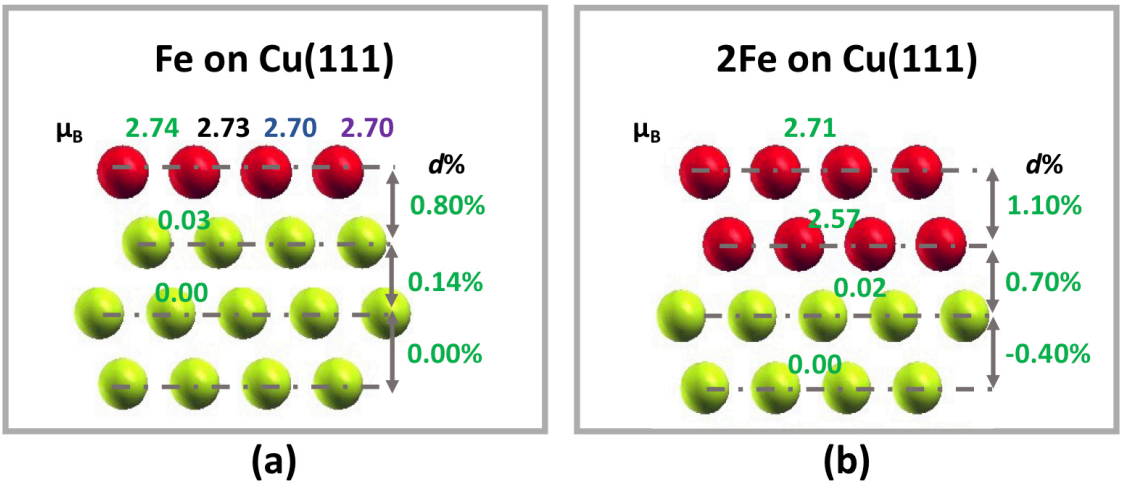

Figure 4.5: Fe on Cu(111): (a) one and (b) two Fe monolayers (ML_s) on Cu(111). MM (μ_B) (VASP, SIESTA, ref [4] and [5] are reported in green, black, blu and violet, respectively). d% layer relaxation.

First we observe that both (a) and (b) structures display an expansion between Fe-Cu and Fe-Fe layers. Concerning the magnetic properties, Fe layers exhibit a lower MM compared to the Fe layers MM on Cu(001). This trend could be attributed to the larger coordination number of Fe atoms on Cu(111) than on Cu(001). In addition, experimental results reported an Fe MM of $2.98\mu_B$ when Fe is deposited using vapor deposition [132], while an Fe local MM of $2.50\mu_B$ is reported by using spattering and annealing techniques [133]. The discrepancy between the theoretical prediction and experimentally measures seems to be caused by the variation of the Fe coverage and island formations on the Cu(111) surface [5].

Table 4.4 displays the local Fe magnetic contribution for (a) and (b) cases. Moreover, we refer to Fe(I) and Fe(II) as the first (the outermost) and the second (the inner) layers. We observe that Fe ML_s exhibit a larger

Table 4.4: Fe on Cu(111): Fe atoms' local magnetic contribution of (a) and (b) structures. Fe(I) and Fe(II) are referred to the first (the outermost) and the second (the inner) layers.

	Fe(I)				Fe(II)			
	s	p	d	tot	s	p	d	tot
(a)	0.00	-0.02	2.76	2.74				
(b)	-0.01	-0.02	2.74	2.71	-0.01	-0.04	2.62	2.57

occupation in the minority population respect to the Fe on Cu(100) counterpart, resulting in a lower Fe local

MM. Moreover, the Fe local MM is larger in the (a) configuration than in the configuration (b). Also in this case, the Fe local MM decreases from the outermost layer to the inner ones.

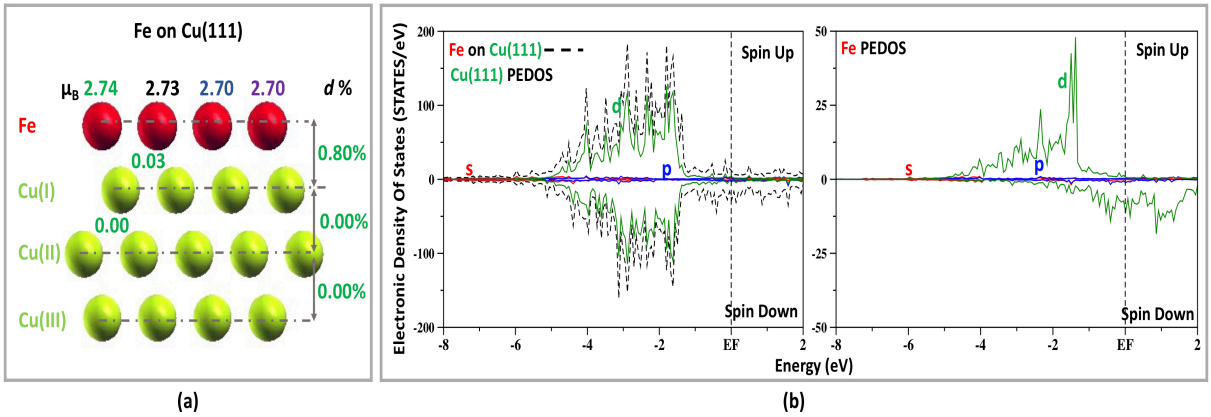

Figure 4.6: Fe on Cu(111): (a) magnetic and structural properties (ref. [4] and [5] are reported in blu and violet, respectively). (b) Left panel: Total EDOS (dashed black line); Cu substrate PEDOS (the s, p and d PEDOS is presented with red, blue and green lines, respectively). Right panel: Fe monolayer PEDOS.

Figure 4.6.(a) presents the structural and magnetic properties of the (a) one Fe ML on Cu(111) structure. We observe an expansion of 0.80% between the Fe and Cu layers, that is larger than the Fe-Cu expansion on Cu(001). Concerning to the Fe local MM, we find a value of $2.74\mu_B$ that is lower compared with the previous Fe on Cu(001) case. In addition, the Cu layer MM is $0.03\mu_B$ that is smaller than the Fe on Cu(001) counterpart.

Figure 4.6.(b) panel left displays the total Fe on Cu(111) EDOS and the Cu substrate PEDOS. Cu PEDOS present a symmetric distribution between majority and minority orbitals, resulting in a no-magnetic character. Furthermore, the Fe PEDOS in figure 4.6.(b) panel right exhibits a substantially different Fe-3d occupation between spin up and down. Fe-3d spin up occupy the energy between -5eV and -1eV, resulting almost fully occupied (4.44(↑)). Additionally, Fe-3d spin down orbitals are shifted towards higher energies enclosed by -1eV and the EF, leaving the minority states less filled than the majority ones (1.69(↓)).

4.2.3 FeCu mix on Cu(001) and Cu(111): structural, electronic and magnetic properties

In this paragraph we present a new structure of FeCu coatings on Cu surfaces. We substituted 50% of Cu atoms with Fe atoms in the first two layers of our system. The Fe atoms are placed in order to repeat the FeCu sequence, aiming in having an FeCu with mixed atoms.

Figure 4.7 reports the Fe and the Cu local MM and the Fe-Cu rippling effect of the (a) FeCu on Cu(001) and (b) FeCu on Cu(111). For simplicity reasons, we display only the first four layers of the whole system. Concerning to the configuration (a), figure 4.7.(a) shows an Fe(I) local MM of $2.89\mu_B$ and $2.41\mu_B$ in Fe(2). Moreover, in figure 4.7.(b) the configuration (b) exhibits an Fe(I) local MM of $2.76\mu_B$ and $2.54\mu_B$ in Fe(2).

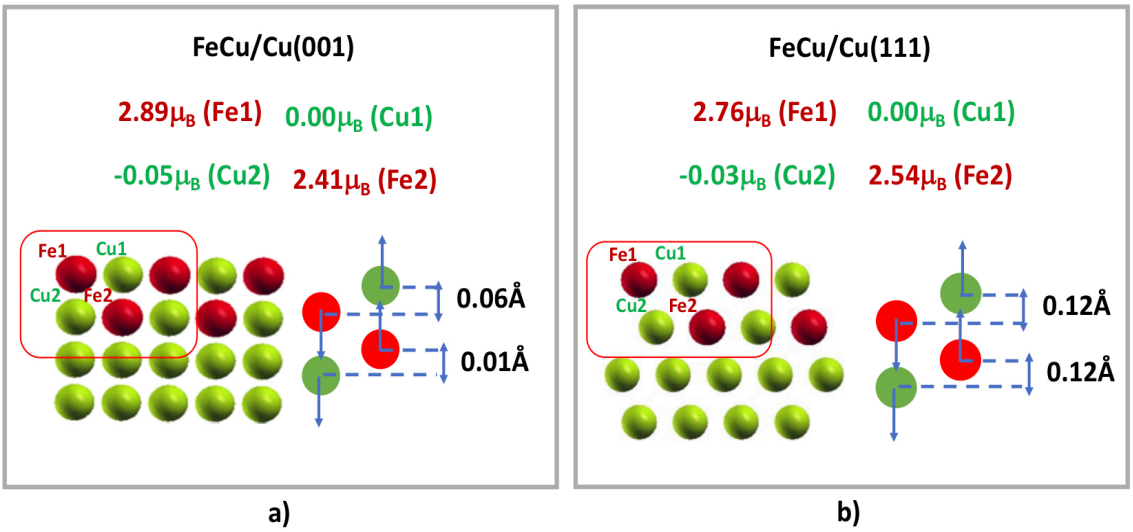

Figure 4.7: Fe local MM and the Fe and Cu rippling effect of: a) FeCu on Cu(001) and b) FeCu on Cu(111)

Lazarovits et al found that a single Fe impurity deposited on a Cu(001) surface shows larger magnetic moment ($3.19\mu_B$) than the corresponding Fe MM surface value ($2.73\mu_B$). In addition, one Fe atom embedded on a Cu(111) substrate displayed a lower local MM compared to the corresponding Fe on Cu(100). They attributed this behaviour to the larger coordination number of Cu(111) substrate compared to Cu(001)[65]. Furthermore, we observe a larger rippling effect in configuration (b) than the configuration (a).

Table 4.5 displays majority(↑) and minority(↓) occupation and the local MM (↑-↓) (μ_B) of the Fe atoms in the outermost layer in both (a) and (b) systems.

Table 4.5: Majority(↑) and minority(↓) occupation and the local MM (μ_B) of the Fe atoms in the outermost layer in both (a) and (b) systems

	Majority(↑)	Minority (↓)	(↑)-(↓)
(a)	5.357	2.492	2.86
(b)	5.278	2.528	2.76

Our results show that the Cu(001) substrate favours an increaset in the Fe local MM. In particular, we observed that the majority/minority imbalance is larger in (a) than in (b), resulting in a higher Fe local MM.

4.3 CoFe and FeCo on Cu(111) substrate

In this section we analyse the structural, electronic and magnetic properties of CoFe and FeCo coatings on Cu(111) substrate.

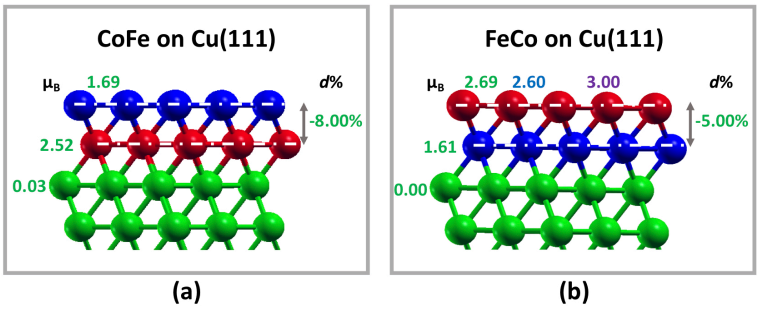

Figure 4.8: (a) CoFe and (b) FeCo on Cu(111): surface atom MM (μ_B) of Co,Fe and Cu layers (VASP results, references [6] and [7] are reported in green, blu and violet, respectively). Layer relaxation ($d\%$)

In figure 4.8 we report on magnetic and structural properties of: (a) CoFe on Cu(111) and (b) FeCo on Cu(111) structures. For clearness, we report only the first four layers of the whole system. We observe that (a) and (b) configurations show a contraction between the Co-Fe and Fe-Co layers, respectively. Concerning the magnetic properties, we note that configuration (b) exhibits the highest Fe surface's atom MM, while it decreases in configuration (a). On the contrary, configuration (a) shows the highest Co surface layer MM and configuration (b) the lowest, as expected. Looking at the Cu substrate, we find that configuration (a) exhibits a weak Cu local MM, while no magnetic moment is displayed in configuration (b).

4.3.1 CoFe on Cu(111): structural, electronic and magnetic properties

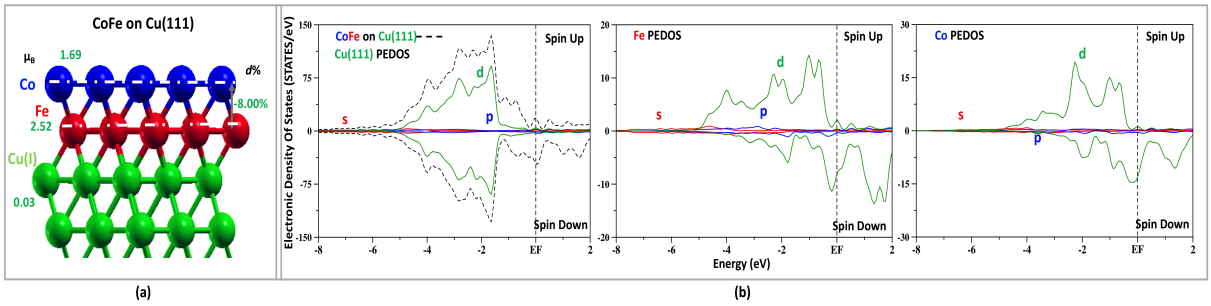

Figure 4.9: CoFe on Cu(111): (a) magnetic and structural properties. (b) Left panel: Total EDOS (dashed black line); Cu substrate PEDOS (the s, p and d PEDOS is presented with red, blue and green lines, respectively). Central panel: Fe monolayer PEDOS. Right panel: Co monolayer PEDOS.

Figure 4.9.(a) presents magnetic and structural properties of the CoFe coatings on Cu(111). We observe a Co surface's atom MM of $1.69\mu_B$, while the Fe surface's atom MM is $2.52\mu_B$ that is higher than the Co surface. Moreover, the Cu(I) layer displays a weak surface's atom MM of $0.03\mu_B$. Finally, we find a Co-Fe contraction of 8%.

In the figure 4.9.(b) left panel we present the total CoFe coatings on Cu(111) EDOS and the Cu substrate PEDOS. The Cu substrate shows a symmetric behaviour between spin up and down electron occupation, confirming the no-magnetic character of the Cu substrate. Figure 4.9.(b) central panel reports the Fe surface

layer PEDOS. We observe 3d up orbitals between -5eV and -0.2eV, resulting in an almost fully occupied. On the contrary, 3d down electrons are shifted between -3eV and over the EF, leaving the 3d minority charge less filled than the majority ones. Figure 4.9.(b) right panel displays the Co surface layer PEDOS. We can see that 3d up states are among -5eV and -0.2eV, while the 3d down are moved towards higher energy from the -3eV and above the EF.

Table 4.6 displays majority(↑) and minority(↓) occupation and the surface's atom MM (↑-↓) (μ_B) of the Co, Fe and Cu coatings.

Table 4.6: Spin up (↑), Spin Down (↓) electron population and surface's atom MM (μ_B) of Co, Fe and Cu layers in CoFe on Cu(111).

		s	p	d	total
Co	Spin Up (↑)	0.23	0.17	4.49	4.89
	Spin Down (↓)	0.24	0.20	2.76	3.20
	μ_B (↑)-(↓)	-0.01	-0.03	1.73	1.69
Fe	Spin Up (↑)	0.23	0.23	4.38	4.84
	Spin Down (↓)	0.24	0.26	1.83	2.33
	μ_B (↑)-(↓)	-0.01	-0.03	2.55	2.51
Cu	Spin Up (↑)	0.22	0.18	4.61	5.02
	Spin Down (↓)	0.23	0.20	4.55	4.99
	μ_B (↑)-(↓)	-0.01	-0.02	0.06	0.03

Concerning the Co and the Fe surface's atom electronic distribution, we observe s and p minority orbitals more filled than the majority ones. In line with the Co and Fe PEDOS, we find that the Co and Fe 3d majority states are almost fully occupied. Moreover, the Co 3d up-down imbalance is smaller compared to the Fe surface's atom electron distribution, resulting in a lower Co surface's atom MM. The Cu surface's atom electron distribution exhibit a small imbalance between 3d up and down occupation, giving a weak Cu surface's atom MM.

4.3.2 FeCo on Cu(111): structural, electronic and magnetic properties

In figure 4.10.(a) we present the structural and magnetic properties of the FeCo on Cu(111). We found an Fe-Co contraction of 5% that is smaller than the Co-Fe contraction in the CoFe on Cu(111). Concerning the magnetic properties, we found an Fe surface's atom MM of $2.69\mu_B$, that is higher than the corresponding value in CoFe on Cu(111) structure. On the contrary, the Co surface's atom MM is $1.61\mu_B$ lower than the Co surface's atom MM in the CoFe on Cu(111) system. Differently from the previous case, the Cu substrate shows a surface's atom MM of zero.

Figure 4.10.(b), the left panel exhibits the total FeCo coatings on Cu(111) EDOS and the Cu substrate PEDOS. We found a symmetric spin up-down Cu substrate PEDOS, in line with the trend shown in CoFe on Cu(111). In figure 4.10.(b), the central panel shows the Co surface layer PEDOS. We observe 3d up electrons

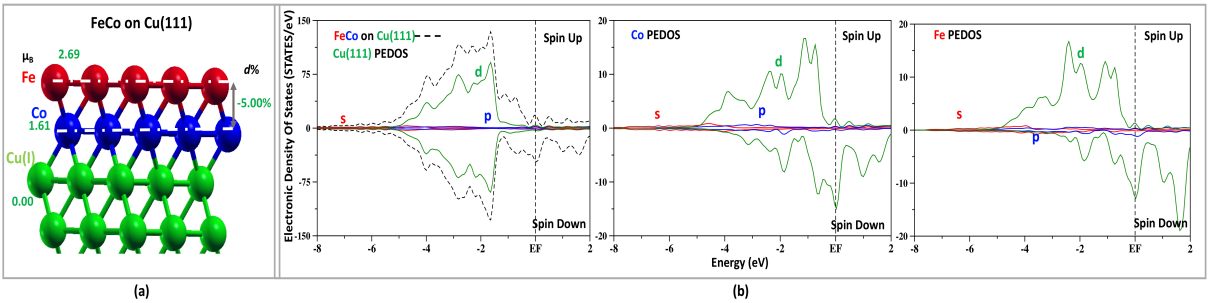

Figure 4.10: FeCo on Cu(111): (a) magnetic and structural properties. (b) Left panel: Total EDOS (dashed black line); Cu substrate PEDOS (the s, p and d PEDOS is presented with red, blue and green lines, respectively). Central panel: Co monolayer PEDOS. Right panel: Fe monolayer PEDOS.

between -5eV and -0.2eV, that are almost fully occupied. The 3d down states are moved over the EF, the 3d down electrons are between -3.5eV and the EF, leaving less filled the minority occupation than the majority ones. Figure 4.10.(b), in the right panel, displays the Fe surface layer PEDOS. We can note that 3d up orbitals are between -5eV and -0.2eV, while the 3d down are shifted above the EF. In particular, we found that the 3d down electrons are located between -2eV and the EF, leaving the spin down states less occupied than the spin up ones.

Table 4.7 displays majority(↑) and minority(↓) occupation and the surface's atom MM (↑-↓) (μ_B) of the Fe, Co and Cu coatings on the Cu(111).

Table 4.7: Spin up (↑), Spin Down (↓) electron population and surface's atom MM (μ_B) of Fe, Co and Cu layers in FeCo on Cu(111).

		s	p	d	total
Fe	Spin Up (↑)	0.23	0.19	4.44	4.86
	Spin Down (↓)	0.23	0.21	1.73	2.17
	μ_B (↑)-(↓)	0.00	-0.02	2.71	2.69
Co	Spin Up (↑)	0.22	0.21	4.45	4.88
	Spin Down (↓)	0.24	0.24	2.79	3.27
	μ_B (↑)-(↓)	-0.02	-0.03	1.69	1.61
Cu	Spin Up (↑)	0.22	0.19	4.58	4.99
	Spin Down (↓)	0.22	0.19	4.58	4.99
	μ_B (↑)-(↓)	0.00	0.00	0.00	0.00

Focusing on the Co and Fe surface layer, we observe s and p minority orbitals more filled than the majority ones. This behaviour is in line with the reverse CoFe coatings on Cu(111) case. In agreement with the Co and Fe surface layer PEDOS, we found the 3d spin up states more occupied than the spin down. Furthermore, the Cu substrate does not show any imbalance between majority and minority occupation, resulting in a no-magnetic substrate.

4.4 Mn and FeMn coatings on Fe(110) substrate

In this paragraph we present the structural and magnetic properties of: Fe(110), Mn and FeMn coatings on Fe(110) substrate.

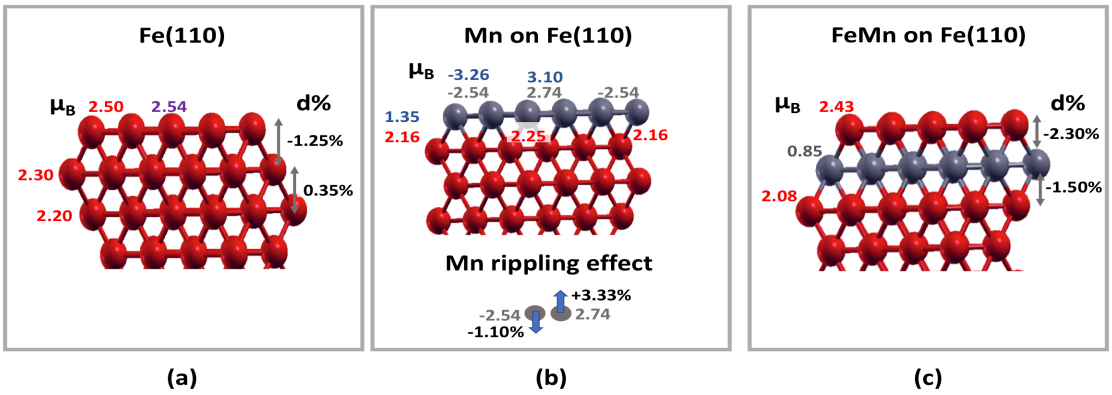

Figure 4.11: Surface atom MM (μ_B) of: (a) Fe(110), (b) Mn on Fe(110) and (c) FeMn on Fe(110). In green is reported the VASP results while in violet and blue are reported [8] and [9] as references.

Figure 4.9.(a) presents the structural and magnetic properties of the Fe(110) structure. For clarity, we exhibit only the first four layers. We find a contraction between the first two Fe layers, while we observe a relaxation among the second ones. Concerning the magnetic properties, we can see that the surface's atom MM decreases from the outermost layer to the inner ones. Finally, we spot a good agreement with Qian and H*ü*bner results reported in violet [8].

In figure 4.9.(b) we display the structural and magnetic properties of the Mn mono layer on Fe(110). First of all, we found that the Mn surface's atom MM depends on the position of the Mn surface's atom in the layer. We observe an antiferromagnetic coupling among the Mn atoms in the same layer and between Mn atoms in first layer and Fe surface's atom in the second ones. Moreover, we note the rippling effect caused by the spin orientation of the Mn surface's atoms. In particular, Mn atoms oriented spin up relaxes outward the surface, while Mn atoms oriented spin down relaxes inward the bulk. As a consequence, a different Fe surface's atom MM appears in the second Fe surface layer. This behaviour is in line with Yu et all. results presented in the blue for comparison [9].

Figure 4.9.(c) exhibits the structural and magnetic properties of the FeMn coatings on Fe(110). This structure exhibits a contraction among the Fe-Mn layers and between the Mn-Fe layers. Contrary to the previous structure, the Mn layer shows a surface's atom MM close to zero. Furthermore, the Fe atoms display a lower surface's atom MM compared with the Fe(110), while it is larger than the corresponding value in the Mn mono layer on Fe(110).

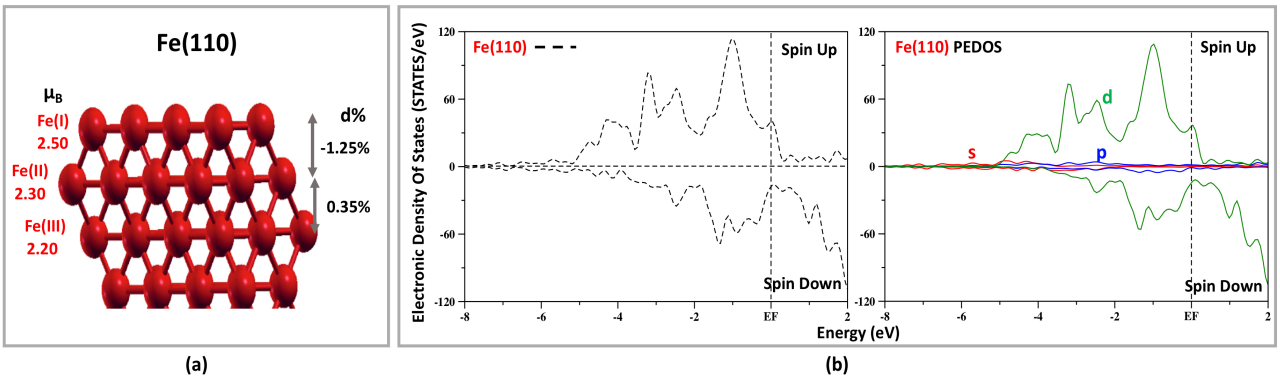

Figure 4.12: Fe(110): (a) magnetic and structural properties. (b) Left panel: Fe110 Total EDOS (dashed black line). Right panel Fe110 PEDOS (the s, p and d PEDOS is presented with red, blue and green lines, respectively).

4.4.1 Fe(110): structural, electronic and magnetic properties

In figure 4.12.(a) we exhibit the structural and magnetic properties of the Fe(110). For simplicity reasons, we name Fe(I), Fe(II) and Fe(III) the first the second and the third Fe surface layers. Concerning the structural properties, we observe a contraction of 1.25% between Fe(I)-Fe(II), while Fe(II)-Fe(III) are relaxed of 0.35%, in agreement with Yu et al. [9]. Focusing on the magnetic properties, we can see that the Fe surface's atom magnetic moment decreases from the Fe(I) to the Fe(III). In particular we find an Fe(I) surface's atom MM of 2.56 μ_B, the Fe(II) surface's atom MM is 2.30 while Fe(III) shows a surface's atom MM of 2.19μ_B.

Figure 4.12.(b) left panel displays the Fe(110) total EDOS. We can see that the majority orbitals are between -5eV and the EF, while the minority states are shifted over the EF, remaining less filled than the majority ones. In figure 4.12.(b) right panel, we present the Fe(110) PEDOS. We discovered that the Fe surface's layer MM is mainly due to the different distribution of the Fe 3d spin up and down electrons. Moreover, we observed that s and p orbitals are delocalized, resulting in the broader bands.

The table 4.8 displays majority(↑) and minority(↓) occupation and the surface's atom MM (↑-↓) (μ_B) of the Fe(I), Fe(II) and Fe(III) layers.

In line with the total and partial EDOS, we can see that the 3d majority orbitals are almost fully occupied, while the minority states are less filled. On the contrary, s and p minority orbitals result more loaded than the majority ones. Interestingly, the spin up-down imbalance increases from the inner layer Fe(III), to the outermost Fe(I), resulting in the highest surface's atom MM.

4.4.2 Mn on Fe(110): structural, electronic and magnetic properties

Figure 4.13.(a) exhibits the structural and magnetic properties of the Mn monolayer on Fe(110). Interestingly, we have found that Mn surface's atoms are coupled antiferromagnetically. We name Mn(u) the Mn atom

Table 4.8: Spin up (↑), Spin Down (↓) electron population and surface's atom MM (μ_B) of Fe(I), Fe(II) and Fe(III) layers in the Fe(110).

		s	p	d	total
Fe(I)	Spin Up (↑)	0.24	0.19	4.40	4.83
	Spin Down (↓)	0.24	0.20	1.83	2.27
	μ_B (↑)-(↓)	0.00	-0.01	2.57	2.56
Fe(II)	Spin Up (↑)	0.24	0.24	4.31	4.79
	Spin Down (↓)	0.25	0.30	1.94	2.49
	μ_B (↑)-(↓)	-0.01	-0.06	2.37	2.30
Fe(III)	Spin Up (↑)	0.24	0.24	4.25	4.73
	Spin Down (↓)	0.25	0.30	1.99	2.54
	μ_B (↑)-(↓)	-0.01	-0.06	2.26	2.19

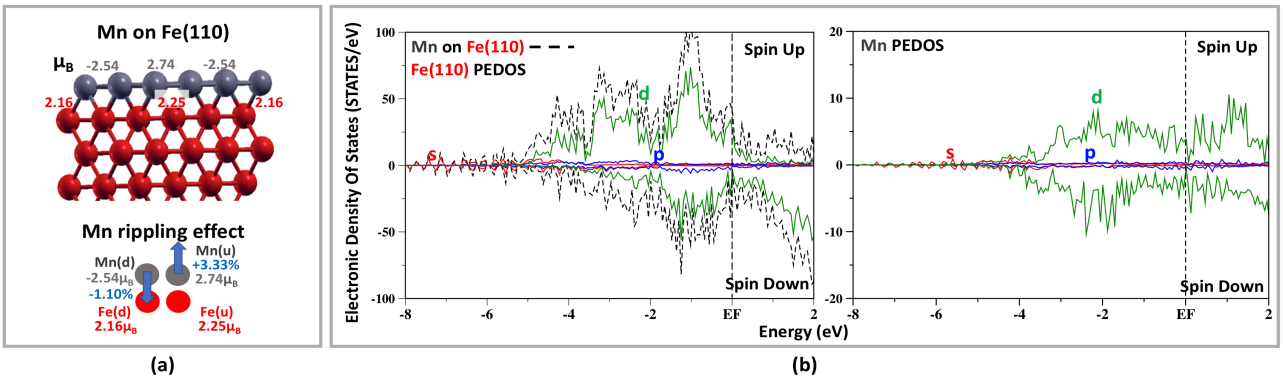

Figure 4.13: Mn on Fe(110): (a) magnetic and structural properties. (b) Left panel: Mn on Fe110 Total EDOS (dashed black line) and Fe substrate PEDOS (the s, p and d PEDOS is presented with red, blue and green lines, respectively). Right panel: Mn monolayer PEDOS.

oriented spin up, Mn(d) the Mn atom oriented spin down, while Fe(u) and Fe(d) the Fe surface's atom close to the Mn(u) and Mn(d), respectively. Concerning the magnetic properties, we observe that the Mn(u)s show a surface's atom MM of 2.74μ_B, whereas the Mn(d)s exhibit a surface's atom MM of -2.55μ_B. As a consequence, we find a rippling effect in agreement with Wu and Freeman [93]. Mn(u)s relaxes outwards the surface by 3.3%, while Mn(d)s relaxes inwards the bulk by 1.1%. Focusing on the Fe layer, we can see that the Fe surface's atoms display a different MM depending on the Mn first neighbouring atoms. When the Fe atom is close to the Mn(u) exhibits an Fe surface's atom MM of 2.25μ_B, while when it is next to the Mn(d) it assumes an Fe surface's atom MM of 2.16μ_B.

In figure 4.13.(b) left panel, we present the Mn on Fe(110) total EDOS and the PEDOS of the Fe(110) substrate. About the Fe(110) substrate, we found that the 3d majority electrons are between -5eV and the EF, while the 3d minority orbitals are shifted over the EF. Concerning to the Mn PEDOS, figure 4.13.(b) right panel shows a symmetric distribution among spin up and spin down. This behaviour is due to the spin up and down electron contributions of the Mn spin atom in the surface.

Table 4.9 displays majority(↑) and minority(↓) occupation and the surface's atom MM (↑-↓) (μ_B) of the Mn and Fe monolayer. We discover that Mn(u) shows majority orbitals more occupied than the minority ones.

Table 4.9: Spin up (↑), Spin Down (↓) electron population and surface's atom MM (μ_B) of Mn and Fe layers in MnFe on Fe(110). Mn(u) is the Mn atom oriented spin up, Mn(d) is the Mn atom oriented spin down, while Fe(u) and Fe(d) the Fe atoms close to the Mn(u) and Mn(d), respectively

		s	p	d	total
Mn(u)	Spin Up (↑)	0.20	0.16	3.88	4.25
	Spin Down (↓)	0.19	0.15	1.16	1.51
	μ_B (↑)-(↓)	-0.01	0.01	2.72	2.74
Mn(d)	Spin Up (↑)	0.18	0.16	1.28	1.62
	Spin Down (↓)	0.20	0.18	3.78	4.17
	μ_B (↑)-(↓)	-0.02	-0.02	-2.50	-2.55
Fe(u)	Spin Up (↑)	0.24	0.25	4.29	4.76
	Spin Down (↓)	0.25	0.29	1.98	2.51
	μ_B (↑)-(↓)	-0.01	-0.04	2.31	2.25
Fe(d)	Spin Up (↑)	0.25	0.26	4.21	4.73
	Spin Down (↓)	0.25	0.28	2.03	2.57
	μ_B (↑)-(↓)	0.00	-0.02	2.18	2.16

On the contrary, Mn(d) exhibits the spin down states more filled than the spin up. As a consequence, in line with the Mn PEDOS, we found almost the same spin up and down electron contributions, resulting in a symmetric majority and minority occupation. Moreover Fe surface's atoms show a larger spin up-down imbalance when the Fe is close to the Mn(u), while a smaller spin up-down imbalance is exhibited when the Fe is by the Mn(d).

4.4.3 FeMn on Fe(110): structural, electronic and magnetic properties

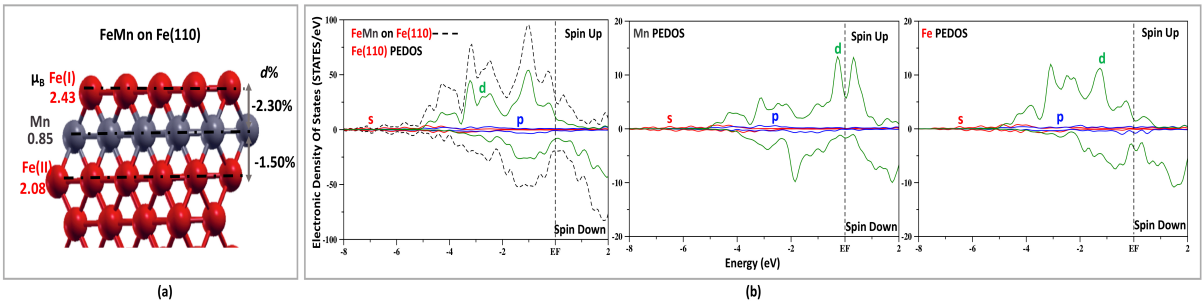

Figure 4.14: FeCo on Cu(111): (a) magnetic and structural properties. (b) Left panel: Total EDOS (dashed black line); Fe110 substrate PEDOS (the s, p and d PEDOS is presented with red, blue and green lines, respectively). Central panel: Mn monolayer PEDOS. Right panel: Fe monolayer PEDOS.

In figure 4.14.(a) we display the structural and magnetic properties of the FeMn coatings on Fe(110) substrate. We observe a contraction of 2.3% between Fe(I) and Mn while a contraction of 1.5% is exhibited among Mn and Fe(II) layers. Concerning the magnetic properties, the Mn layer's atoms exhibit a MM of $0.85\mu_B$, that it is lower than the corresponding value in the Mn on Fe(110) system. Moreover, the Fe(I) surface's atom MM is $2.43\mu_B$, whereas the Fe(II) show a lower surface's atom MM of $2.08\mu_B$.

Figure 4.14.(b) left panel presents the FeMn on Fe(110) total EDOS and the Fe(110) substrate PEDOS. We observe 3d spin up electrons between -5eV and the EF, while the minority orbitals are shifted over the EF, in line with the previous results. The Mn PEDOS, in figure 4.14.(b) central panel, displays 3d up orbitals move over the EF, while the 3d down are between -4eV and the EF. Figure 4.14.(b), right panel, displays the FePEDOS. We observe that the 3d majority orbitals are enclosed by -5eV and the EF. On the contrary, 3d minority states are shifted above the EF, leaving the 3d spin down orbitals less filled.

Table 4.10 displays majority(↑) and minority(↓) occupation and the surface's atom MM (↑-↓) (μ_B) of the Fe and Mn coatings.

Table 4.10: Spin up (↑), Spin Down (↓) electron population and surface's atom MM (μ_B) of Fe and Mn layers in FeMn on Fe(110).

		s	p	d	total
Fe(I)	Spin Up (↑)	0.24	0.21	4.33	4.78
	Spin Down (↓)	0.24	0.22	1.89	2.35
	μ_B (↑)-(↓)	0.00	-0.01	2.44	2.43
Mn	Spin Up (↑)	0.19	0.20	3.00	3.39
	Spin Down (↓)	0.20	0.23	2.10	2.54
	μ_B (↑)-(↓)	-0.01	-0.03	0.90	0.85
Fe(II)	Spin Up (↑)	0.24	0.26	4.20	4.69
	Spin Down (↓)	0.25	0.30	2.06	2.61
	μ_B (↑)-(↓)	-0.01	-0.04	2.14	2.08

We can notice that the Mn surface position affects substantially the surface's atom MM. In particular, we observe a value close to zero when it is located at the second layer, while when it is at the outermost surface we have found a Mn surface's atom MM of $2.74\mu_B$ and $-2.55\mu_B$. Additionally, we can see that the Mn surface's atom MM is the same in the whole surface, and the Mn atoms couple ferromagnetically. Concerning the Fe surface, it shows a larger surface's atom MM than the Mn layer and than the corresponding value in the MnFe coatings on Fe(110).

4.5 Conclusion

In this section we investigated the Fe-X (X=Cu, Co) on Cu surfaces and FeMn on Fe layers. Regarding the Fe mono layer on Cu surfaces, we presented two configurations: (a) Fe layer on Cu(001) and (b) Fe

layer on Cu(111). We found that the configuration (a) exhibits an higher Fe surface's atom MM ($2.84\mu_B$) compared to the corresponding value in (b) ($2.73\mu_B$). Moreover, for more than one Fe layer, we can see that the Fe surface's atom MM decreases from the outermost layer to the inner ones. This trend is attributed to the larger coordination number of the Fe surface's atoms in the second and third layer than in the first ones. In particular, it is well known in the literature that for a large coordination number, the electrons are forced to occupy more the minority orbitals than the majority ones, reducing the imbalance between the majority and minority occupation [40]. Interestingly, an increase in the Fe surface's atom MM is observed in a new structure that we name FeCu mixed. Also in this case, we have studied two systems: (a) FeCu mix on Cu(001) and (b) FeCu mix on Cu(111). Structure (a) shows an Fe local atom MM of $2.89\mu_B$ while a smaller value is exhibited in (b) ($2.76\mu_B$). We can conclude that the (001) structure favours the majority-minority orbital imbalance, making the Fe surface's atom MM higher in the (001) geometry than in the (111) structure. In addition, the Fe surface's atom MM is enhanced when the Fe atoms have Cu atoms like first neighbours.

Concerning the FeCo coatings on Cu(111) we studied two structures: (a) CoFe on Cu(111) and (b) FeCo on Cu(111). We found a higher Fe surface's atom MM ($2.69\mu_B$) in configuration (b), while a smaller value is shown in the (a) ($2.52\mu_B$). In particular, we noticed that the Fe electronic charge distribution changes depending on the Fe coating position. In configuration (b), we found that the minority orbitals are less occupied than the corresponding minority orbitals in (a), where the Fe coating is sandwiched between Co and Cu surfaces. In addition, we found a Co surface's atom MM of $1.69\mu_B$ in configuration (a), whereas the structure (b) exhibits a value of $1.61\mu_B$, revealing the importance of the position of the layer.

Focusing on MnFe on Fe(110) surfaces, we analyzed two configurations: (a) MnFe on Fe(110) and (b) FeMn on Fe(110). First of all, we note that the Fe layer displays the lowest Fe surface's atom MM compared to the previous systems. In configuration (a), Mn surface layer shows an in plain AFM coupling between Mn atoms, making the average surface magnetic moment close to zero. A similar behaviour is found in another theoretical study referring to the Mn bulk [83]. Interestingly, the Fe surface's atoms acquire a different surface's atom MM depending on the Mn surface's atom first neighbour. In configuration (b), we found that the Mn layer's atoms exhibit a FM coupling among their surface's atoms neighbour and between the Fe surface's atoms in the first and in the third layers. As a consequence, the Fe layer's atoms assume all the same surface's atom MM.

In conclusion, we found that the highest Fe surface's atom MM is shown when the Fe layers are deposited on the Cu surfaces. In addition, the Fe local atom MM can be increased when the Fe atoms have Cu atoms like first neighbours.

Chapter 5

Pure metal clusters

It is well known that the magnetic properties are affected by the systems' dimensions. Nevertheless, the evolution of the magnetic moment as the system's dimensions increases (from atom to bulk) is still an open issue. Although, a lot of work is performed for pure small clusters, (e.g. 13 and 55 atoms), studies concerning bigger clusters (e.g. with 147 and 309 atoms) are rather limited due to their great computational effort that is required. The magnetic moment evolution for different cluster's sizes, for pure Fe, Co, Cu, Mn and Fe-mixed clusters will be presented in the next two chapters. All calculations are done by using SIESTA[122] and VASP[134][135] computational packages.

SIESTA, employs linear combination of pseudo-atomic orbitals as basic sets. The atomic core is replaced by a nonlocal norm-conserving Troullier-Martins pseudo-potential [136] that is factorised in the Kleinman-Bilander form[110]. In addition, it may include nonlinear core correction terms to account for the significant overlap of the core charges with the valence d orbitals. The code allows performing, together with the electronic calculation, structural optimization using a variety of algorithms. In the present study, we used the GGA exchange and correlation potential as parametrized by Perdew et al [131]. In SIESTA, the ionic pseudopotentials is generated using the following atomic configurations: $3d^n$, $4s^1$, and $4p^0$ with n=7 for Fe, n=8 for Co and n=10 for Cu. The s, p, and d cutoff radii were 2.00, 2.00, and 2.00 a.u. for Fe and Co. The valence states are described using double-zeta polarised DZP basis sets.

In VASP, the standard projector augmented wave PAW pseudopotentials is employed [111][112]. The electronic configuration considered is $3d^7\ 4s^1$ for Fe, $3d^8\ 4s^1$ for Co, $3d^8\ 4s^1$ for Mn and $3d^10\ 4s^1$ for Cu. For the analysis of local magnetic structure of the clusters, the default values of Wigner-Seitz radii of atoms are used as provided in VASP. Consequently, the sum of local atomic magnetic moments computed around each atom is not exactly equal to the overall total magnetic moment of a cluster but this does not affect the energy of the cluster and its electronic and magnetic properties. Moreover, a cubic simulation box is used for the relaxation of isolated freestanding clusters. The simulation boxes have lattice parameters of 15 $\AA$ for 13-atom, 25 $\AA$ for 55-atom, and 40 $\AA$ for 147-atom clusters. These simulation boxes neglect the interactions between a cluster

and its images. All cluster calculations are made using the Γ point only. The ionic relaxations are made by using the conjugate gradient optimization method. The structural optimization is stopped when each force component at each atom in the cluster is smaller than 0.005eV/$\mathring{A}$ for small clusters (13 and 55 atoms) and 0.05 eV/$\mathring{A}$ for the larger.

In addition, for all under study structures, the binding energy E_B is calculated with the formula:

$$E_B = \frac{E_{A_l B_m} - ((l \cdot E_A) + (m \cdot E_B))}{l + m} \tag{5.1}$$

where A and B are the atoms in the system, $E_{A_l B_m}$ is the total energy of the system, l and m the number of atoms for each element, and E_A and E_B refer to the energy of only one A or B atom. The local charge attributed to each atom is calculated by the sum of the density of spin up and down populations: $n(\mathbf{r}) = n_\uparrow(\mathbf{r}) + n_\downarrow(\mathbf{r})$ while the local magnetic moment is given by: $n^{spin}(\mathbf{r}) = n_\uparrow(\mathbf{r}) - n_\downarrow(\mathbf{r})$.

Additionally, since the distinction between spin up and spin down populations is purely conventional it will be assumed that spin up is represented by the majority of electronic population, that is, the total magnetic moment is always positive. This convention, applied universally, does not affect the generality of analysis[137]. Moreover, in order to analyze the charge distribution the total and partial density of states (EDOS and PEDOS) are presented.

Finally, the structure's stability is described in terms of the energy gap between the highest molecular orbital occupied (HOMO) and the lowest unoccupied molecular orbital (LUMO). The HOMO-LUMO energy gap (H-L gap) is usually considered as an important quantity that reflects chemical activity of cluster. A big energy gap (>1eV) corresponds to a high chemical stability[138][139][140].

5.1 Iron

5.1.1 Fe_{13}

Fe_{13}: Ground-state structure

The first step towards the theoretical modelling of clusters is to determine their ground-state structure. The transition-metal clusters prefer compact geometries in order to maximise the interaction between the rather localized d orbitals [141]. There are three most compact and highly coordinated structures for 13 atom clusters: icosahedron, cuboctahedron, and hexagonal closed packed geometries [142][124], that are exhibited in figure 5.1.

Table 5.1 displays the binding energy (E_B) and the average magnetic moment (MM) of the Fe_{13} clusters calculated by both SIESTA and VASP packages. Moreover, in the last two columns we report theoretical

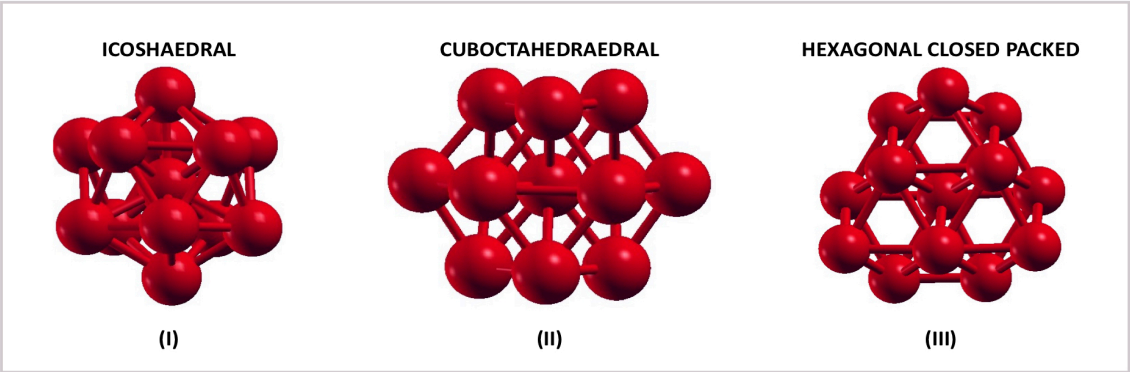

Figure 5.1: Fe_{13} cluster: (I) Icosahedral (ICO), (II) Cuboctahedral (CUBO), (III) Hexagonal Closed Packed (HCP)

Table 5.1: Binding energy E_B (eV), average cluster's MM (μ_B) of the Fe_{13} structures. In the last two columns theoretical and experimental references are reported for comparison.

	SIESTA		VASP		Ref	
Structure	E_B	MM	E_B	MM	MM Theo.	MM Exp
ICO	-3.07	3.38	-3.36	3.39	3.38[43][82][42][124]	3.00 [40]
CUBO	-3.01	3.23			3.08[42][124]	
HCP	-2.96	3.08			3.08[43][124]	

and experimental references for comparison. In agreement with the literature, we found the ICO structure as the most stable configuration. In particular, we observe a E_B of -3.07eV with SIESTA, while we obtain -3.36eV by VASP. Conversely, CUBO shows a E_B of -3.01eV, whereas HCP exhibits a value of -2.96eV. In addition, the Fe_{13} ICO clusters displays the largest average cluster's MM.

Fe_{13}: Structural, electronic and magnetic properties

In figure 5.2.(a) we present the structural and magnetic properties of Fe_{13} Icosahedral cluster. First of all, we observe that the Fe atom's MM depends on the position of the Fe in the cluster. For simplicity, we refer with Fe(C) to the Fe atom in the cluster's center. Interestingly, we discovered that the Fe atoms in the shell assume a various local MMs depending on the distance from the center. We name Fe(N), the nearest Fe atom from the Fe(C) and Fe(D) the farther. We found a Fe(N)-Fe(C) interatomic distance of 2.32$\AA$ with VASP, while a distance of 2.48$\AA$ was found with SIESTA. The MM of Fe(N) atom is 3.06 by VASP and 3.41 with SIESTA. Moreover, the Fe(D)-Fe(C) distance is 2.42$\AA$ by VASP and 2.57$\AA$ with SIESTA that it is larger than Fe(N)-Fe(C). Focusing on Fe(D), we observe an Fe(D) atom MM of 3.09μ_B with VASP and 3.44μ_B by SIESTA that it is bigger than Fe(N). In addition, Fe(C) shows a local MM of 2.63μ_B with VASP and 3.00μ_B smaller than both Fe(N) and Fe(D), in line with the shell models displays by the Billas et all [37][40].

Figure 5.2.(b) exhibits the spin up and down Wave Function (WF) at the homo state. Focusing on the spin

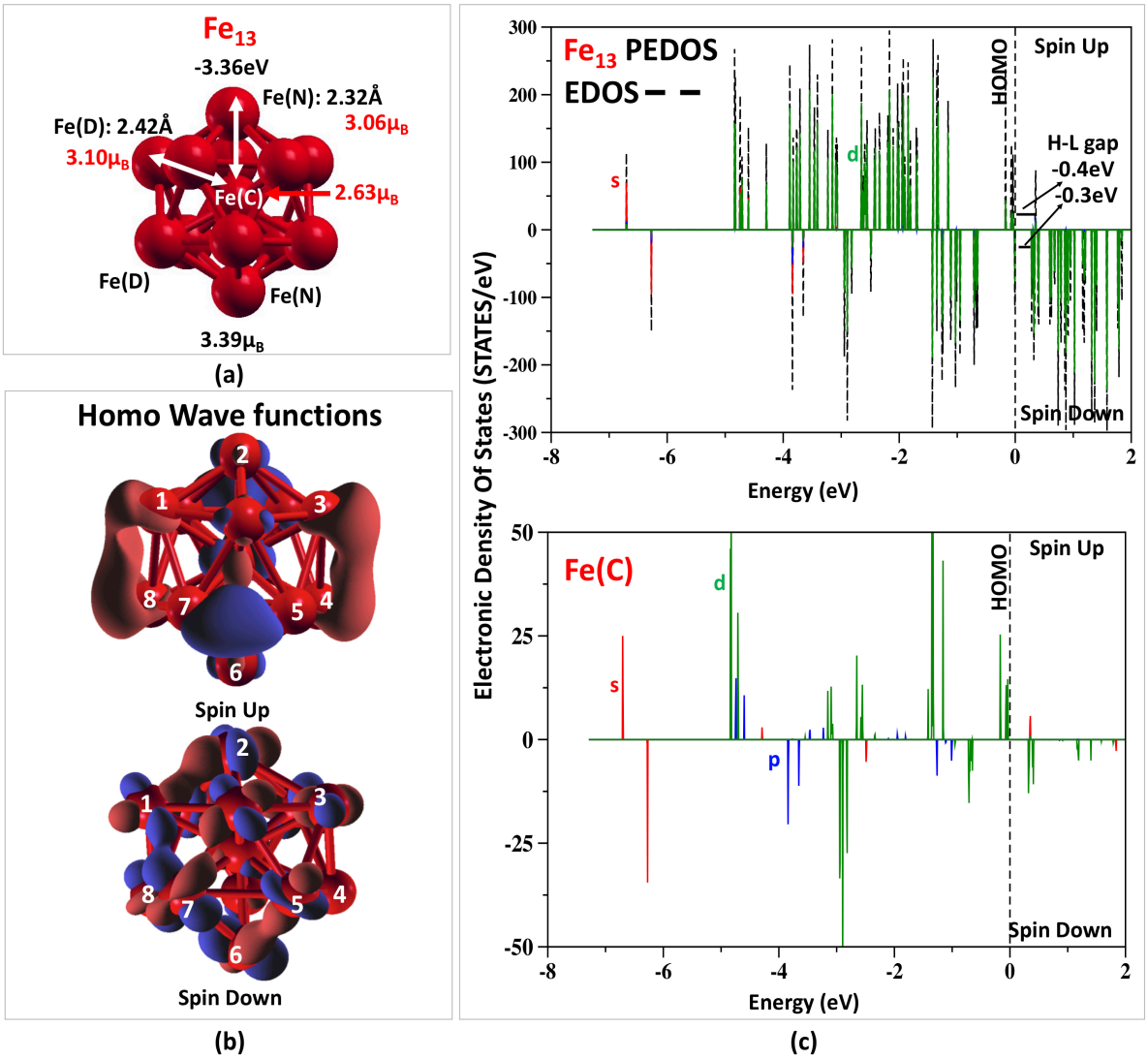

Figure 5.2: Fe_{13}: (a) magnetic and structural properties. (b) Spin up and Spin down Wave Functions (WF) at the homo level. Red and blue area stand for the negative and positive charge of the WF.(c) Panel up: Total cluster EDOS (dashed black line); Fe_{13} PEDOS (the s, p and d PEDOS is presented with red, blue and green lines, respectively). Panel down: Fe(C) PEDOS

up WF, we find the charge localized on both Fe(C) and Fe(N), Fe(D) atoms in the shell. For simplicity reason, we name the Fe atoms with numbers (from 1 to 8). Concerning to the Fe in the shell, we observe 3d orbital bonding hybridizations between Fe(1)-Fe(8), Fe(3)-Fe(4) and between Fe(5)-Fe(7) atoms. Concerning to the Fe(C), we found 3d electrons located on the Fe, while no bonding hybridizations are shown among the Fe(C) and the others Fe atoms in the shell. Moving to the spin down WF, we observe Fe-3d hybridization orbitals between Fe(1)-Fe(2) and Fe(1)-Fe(8), and betwixt Fe(5)-Fe(6). In addition, we found only a small amount of charge located on the Fe(C), no orbital hybridisation between the Fe(C) and the others Fe atoms in the shell are shown.

In figure 5.2.(c) panel up we display the total EDOS and Fe PEDOS. Referring to the Fe PEDOS, we observe Fe-3d up orbitals between -5eV and the homo state, while 4s-up states are a lower energy around -7eV. Furthermore, Fe-3d down orbitals are in an higher energy interval than the Fe-3d up, between -3eV and the homo state. In addition, we found 4s down electrons around -6eV and -4eV. Moving on Fe(C), figure5.2.(c) panel down, we observe the Fe-3d up orbitals enclosed by the -5eV and the homo state, while the Fe-3d down are between -3eV and -1.5eV. Moreover, 4s-up and -down electrons are at low energy between -7eV and -6eV. Finally, we find 4p-up electrons close to -5eV, while the 4p-down states are close to -4eV and -1.5eV. Concluding, the total majority EDOS shows a H-L gap of -0.4eV whereas the minority counterpart exhibits a H-L gap of -0.3eV, in line with Refs.[143][144].

In the table 5.2, we present the majority (↑) and the minority (↓) Fe electron populations and local atom MM (μ_B) of Fe atoms. Furthermore, the positive/negative sign of μ_B denotes its resulting up/down direction, respectively.

Table 5.2: Spin up (↑), Spin Down (↓) electron population and local atom MM (μ_B) of Fe atoms in Fe_{13}.

atom		VASP				SIESTA	REF
		s	p	d	total	total	
Fe(C)	Spin Up (↑)	0.25	0.28	4.61	5.14		
	Spin Down (↓)	0.29	0.39	1.82	2.51		
	μ_B (↑)-(↓)	-0.04	-0.10	2.79	2.63	3.00	2.20[22]
Fe(N)	Spin Up (↑)	0.25	0.16	4.58	5.00		
	Spin Down (↓)	0.23	0.13	1.59	1.94		
	μ_B (↑)-(↓)	0.02	0.03	2.99	3.06	3.41	3.40[22]
Fe(D)	Spin Up (↑)	0.27	0.17	4.58	5.02		
	Spin Down (↓)	0.22	0.14	1.57	1.93		
	μ_B (↑)-(↓)	0.05	0.03	3.01	3.09	3.44	3.50[22]

Starting with Fe(C), it is worth noticing that the Fe(C) assumes the lowest Fe atom MM. We observe that Fe(C) bonds with all other Fe atoms in the cluster, assuming the highest coordination number in the structure. For this reason, the 4s and 4p minority orbitals are more filled than the majority, lowering the Fe(C) local MM. Referring to the Fe in the shell, we find that Fe(D) presents 4s and 3d majority orbitals more occupied than Fe(N) majority orbitals counterpart, resulting in a higher Fe atom MM. On the contrary, we found the same spin up and down imbalance in the 4p states. In addition, we observed a parallel coupling between the spin of the Fe atoms in the shell and the spin of Fe(C), resulting in a larger average cluster's MM compared to the Fe bulk.

5.1.2 Fe_{55}

In this paragraph we continue our study presenting the Fe icosahedral cluster with 55 atoms. It is worth to be noticed that 55 atoms icosahedral clusters show two shells. For simplicity, we refer to the Fe atom in the center with Fe(C), when Fe atoms occupy the first shell we use Fe(I), while for the Fe atoms in the second

shell we write Fe(II).

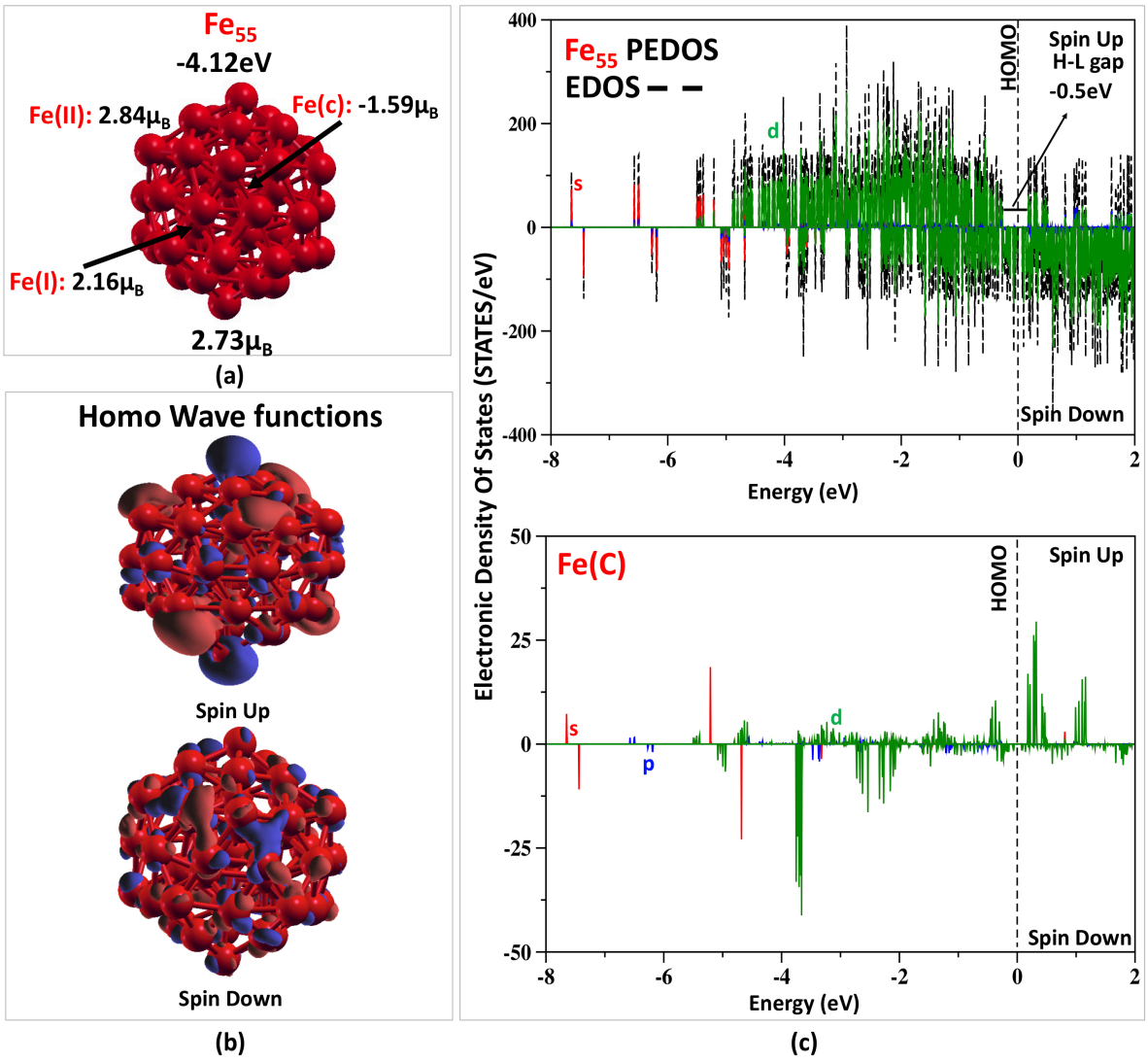

Figure 5.3: Fe_{55}: (a) magnetic and structural properties. (b) Spin up and Spin down Wave Functions (WF) at the homo level. Red and blue area stand for the negative and positive charge of the WF. (c) Panel up: Total cluster EDOS (dashed black line); Fe_{55} PEDOS (the s, p and d PEDOS is presented with red, blue and green lines, respectively). Panel down: Fe(C) PEDOS

In figure 5.3.(a) we report on the structural and magnetic properties of Fe_{55}. First, we focus on two possible magnetic configurations. We refer to FerroMagnetic (FM) to the cluster's configuration where all spins of the atoms are aligned parallel, while we name AntiFerroMagnetic (AFM) the configuration where the spins of the atoms are aligned anti-parallel. In line with literature [42][68], we found a binding energy of -4.09eV for the Fe_{55} (FM), while we observe a binding energy of -4.12eV for (AFM), resulting in the most stable configuration. Furthermore, we found an average cluster's MM of $2.73\mu_B$. On the contrary, SIESTA shows a FM structure with a binding energy of -3.63eV and an average cluster's MM of $2.19\mu_B$. Concerning the

interatomic distances, we found an Fe(C)-Fe(I) distance of 2.43$\AA$ and Fe(I)-Fe(II) 2.36$\AA$ with VASP, while we found 2.51$\AA$ between Fe(C) and Fe(I) and 2.48$\AA$ beteen Fe(I) and Fe(II) with SIESTA. Focusing on the VASP calculation, we observe an Fe(C) atom MM of -1.59μ_B, that is anti-parallel aligned to the Fe(I) 2.16μ_B. In addition, the Fe(II) atoms exhibit a local MM of 2.84μ_B. In contrast to VASP, SIESTA calculates a Fe(C) MM of 2.66μ_B that is parallel to the Fe(I) atoms showing a local MM of 2.62μ_B. Furthermore, we found a local MM of 3.12μ_B when Fe atoms occupy the second shell.

Figure 5.3.(b) exhibits the spin up and down Wave Function (WF) at the homo state. Focusing on the spin up WF, we observe Fe-3d hybridization bonding between the Fe(II) atoms, while a small amount of 3d charge is located on the Fe atoms in the inner shell. Concerning to the spin down WF, we found Fe-3d hybridization bonding between the Fe(II) atoms, whereas no charge is visible in the inner shells.

In figure 5.3.(c) panel up we present the total EDOS and Fe PEDOS. We can see that the Fe-3d up orbitals are between -5eV and -0.5eV, while Fe-4s up states are a lower energy between -8eV and -5eV. Furthermore, Fe-3d down are enclosed by -3.5eV and the homo state, whereas the Fe-4s down are -7.5eV and -5.5eV. Figure 5.3.(c) panel down exhibits the Fe(C) partial EDOS. We observe that the 3d electrons are around -4eV and -0.5eV in the spin up orbitals, while the 3d down electrons are around -3.5eV and the homo state. Moreover, 4s states are at low energies between -8eV and -4.5eV. Finally, we observe a H-L gap of -0.4eV in the majority EDOS, while no gap is shown in the minority counterpart, resulting in a half-metallic cluster.

In the table 5.3, we present the majority (↑) and the minority (↓) Fe electron population and local atom MMs (μ_B) of Fe atoms. Furthermore, the positive/negative sign of μ_B denotes its resulting up/down directions, respectively. Focusing on Fe(C), the VASP calculations yielded an AFM coupling between Fe(C) and Fe(I),

Table 5.3: Spin up (↑), Spin Down (↓) electron population and local atom MM (μ_B) of Fe atoms in Fe_{55}.

atom		VASP				SIESTA	REF
		s	p	d	total	total	
Fe(C)	Spin Up (↑)	0.26	0.61	2.41	2.98		
	Spin Down (↓)	0.31	0.69	3.87	4.57		
	μ_B (↑)-(↓)	-0.05	-0.08	-1.46	-1.59	2.66	
Fe(I)	Spin Up (↑)	0.24	0.26	4.28	4.79		
	Spin Down (↓)	0.26	0.32	2.04	2.62		
	μ_B (↑)-(↓)	-0.02	-0.06	2.24	2.17	2.62	
Fe(II)	Spin Up (↑)	0.24	0.15	4.49	4.93		
	Spin Down (↓)	0.24	0.15	1.66	2.10		
	μ_B (↑)-(↓)	0.00	0.00	2.83	2.83	3.12	2.80[42]

caused by the more filled minority orbitals in the Fe(C). This result reflected the partial Fe(C) EDOS reported in figure 5.3.(c) panel down. On the contrary, SIESTA results exhibit a FM coupling between Fe(C) and Fe(I), and Fe(C) assumes a larger local MM than Fe(I). It is worth to be noticed that, in both VASP and SIESTA, the Fe local MMs decrease going from the outermost shell to the inner. In particular, we find that Fe(I) atoms display s and p minority orbitals more occupied than the majority, lowering the Fe atom MMs. Concerning to the Fe(II) atoms, they exhibit the highest local MM, in agreement with available experimental

and theoretical results[42][37].

5.1.3 Fe_{147}

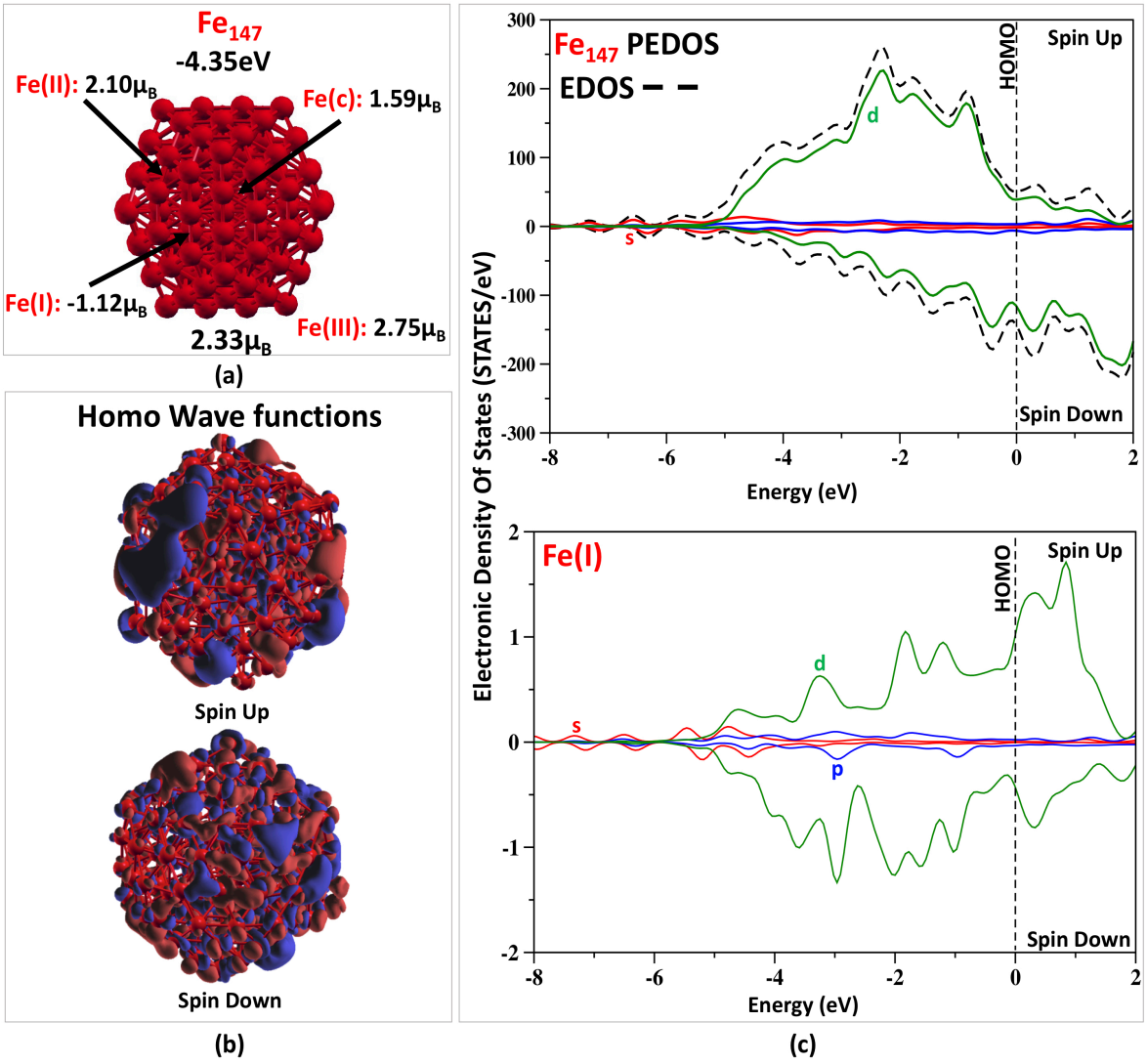

Figure 5.4: Fe_{147}: (a) magnetic and structural properties. (b) Spin up and Spin down Wave Functions (WF) at the homo level. Red and blue area stand for the negative and positive charge of the WF. (c) Panel up: Total cluster EDOS (dashed black line); Fe_{147} PEDOS (the s, p and d PEDOS is presented with red, blue and green lines, respectively). Panel down: Fe(C) PEDOS

In figure 5.4 we present the structural, electronic and magnetic properties of the Fe_{147} icosahedral cluster. In line with the last paragraph, we refer to the Fe atom in the center with Fe(C), and with Fe(I), Fe(II), Fe(III) to the Fe atoms in the first, second and third shell respectively. Starting with 5.4.(a), we found a binding energy of -4.35eV and an average cluster's MM of $2.33\mu_B$ with VASP. Furthermore, we found an Fe(C)-Fe(I)

interatomic distance of 2.39$\mathring{A}$, 2.43$\mathring{A}$ Fe(I)-Fe(II) and 2.44$\mathring{A}$ Fe(II)-Fe(III). Focusing on the local Fe MM, we found a value of 1.59μ_B for Fe(C), -1.12μ_B for Fe(I), 2.10μ_B for the Fe(II) and finally 2.75μ_B Fe(III). Concerning to the SIESTA results, we calculated a binding energy of -3.86eV and an average cluster's MM of 2.41μ_B, while the interatomic distances are 2.43$\mathring{A}$ between Fe(C) and Fe(I), 2.60$\mathring{A}$ between Fe(I)-Fe(II) and 2.45$\mathring{A}$ between Fe(II)-Fe(III), respectively. Interestingly, we observed that, both VASP and SIESTA calculations showed the AFM coupling between Fe(C) and Fe(I) atoms, and Fe(I) and Fe(II) atoms. In particular, the spins of the Fe atoms in the first shells are coupled anti-parallel with Fe(C) and the Fe atoms in the second shell.

Figure 5.4.(b) shows the spin up and down Wave Function (WF) at the homo state. In both spin up and down WF, we observed Fe-3d hybridization bonding between the Fe(III) atoms, while a small amount of 3d charge is located on the Fe atoms in the inner shell.

In figure 5.4.(c) panel up we display the total EDOS and the total Fe PEDOS. Focusing on Fe total PEDOS, we found Fe-3d spin up electrons between -5eV and the homo state, while the Fe-4s electrons are in the low energy levels around -8eV and -6eV. The Fe-3d spin down are shifted to the higher energy compared to the spin up counterpart and they are enclosed by -3eV and the homo state. In the panel down, we present the Fe(I) PEDOS. We observe that spin down orbitals are more occupied than the spin up counterpart, resulting in aligned anti-parallel with the spins of the Fe(C) and Fe(II) atoms. In addition, the total EDOS exhibits a band like behaviour, while we cannot see any H-L gap, thus yielding a metallic character of the Fe_{147} icosahedral cluster.

Table 5.4 presents the majority (↑) and the minority (↓) Fe electron population and local atom MM (μ_B) of Fe atoms. Furthermore, the positive/negative sign of μ_B denotes its resulting up/down direction, respectively.

Table 5.4: Spin up (↑), Spin Down (↓) electron population and local atom MM (μ_B) of Fe atoms in Fe_{147}.

atom		VASP				SIESTA
		s	p	d	total	total
Fe(C)	Spin Up (↑)	0.32	0.39	3.97	4.67	
	Spin Down (↓)	0.30	0.36	2.42	3.08	
	μ_B (↑)-(↓)	0.02	0.03	1.55	1.59	1.20
Fe(I)	Spin Up (↑)	0.26	0.29	2.61	3.16	
	Spin Down (↓)	0.28	0.32	3.59	4.28	
	μ_B (↑)-(↓)	-0.02	-0.03	-1.08	-1.12	-2.03
Fe(II)	Spin Up (↑)	0.24	0.25	4.21	4.69	
	Spin Down (↓)	0.25	0.29	2.05	2.59	
	μ_B (↑)-(↓)	-0.01	-0.04	2.16	2.10	2.46
Fe(III)	Spin Up (↑)	0.26	0.16	4.48	4.91	
	Spin Down (↓)	0.25	0.13	1.78	2.16	
	μ_B (↑)-(↓)	0.01	0.03	2.70	2.75	3.12

Focusing on Fe(I), we observe that minority orbitals are more occupied than the majority, reflecting the behaviour showsn in the Fe(I) PEDOS presented in fig.5.4.(c) panel down. The AFM behaviour is in agreement with the shell model described by the Billas et all. in their experimental works[20][37]. Referring to the Fe(II), we found that only s and p orbitals exhibit minority orbitals more occupied than the majority, resulting coupled FM with the Fe(III). Moreover, Fe(C) display all s, p and d majority states more occupied than the minority. Despite the AFM coupling, the Fe atom MM decreases from the outermost shell to the inner shell in agreement with other theoretical and experimental works [40][42].

5.1.4 Fe_{309}

In this section we focus on the structural, electronic and magnetic properties of the Icosahedral Fe_{309} cluster.

In figure 5.5.(a) we present structural and magnetic properties of the Fe_{309}. We found a binding energy of -3.98eV and an average cluster MM of $2.79\mu_B$. Contrary to the Fe_{147}, we observed a FM coupling among Fe atoms in various shells. For simplicity, we name the Fe atoms with Fe(C) when the Fe is at the cluster center, while we refer to the Fe atoms with Fe(I), Fe(II), Fe(III) and Fe(IV) for the Fe in the first second, third and forth shell, respectively. We found that the Fe atom MM decreases from the outermost to the inner shell. Interestingly, in agreement with the shell model [20][37], we found that Fe(II) and Fe(III) exhibit a local MM smaller than the Fe(C) and Fe(I), while the Fe(IV) shows the highest Fe local MM. In addition, focusing on the interatomic distance, we found $2.61\mathring{A}$ between Fe(C) and Fe(I), while Fe(I)-Fe(II) atoms display $2.53\mathring{A}$. Moreover, we found a distance between Fe(II)-Fe(III) of $2.45\mathring{A}$ and Fe(III)-Fe(IV) exhibits $2.36\mathring{A}$.

Figure 5.5.(b) presents the spin up and down Wave Function (WF) at the homo state. Concerning to the spin up WF, we found Fe-3d hybridization bonding between the Fe atom first neighbours in the outermost shell. Moreover, a small amount of charge is visible located on the Fe atoms in the inner shell. Moving to the spin down WF, figure 5.5.(b) reports that the charge is more localized on the own Fe atoms compared to the majority counterpart. Moreover, no hybridisation bonding or weak hybridization bonds are shown in the minority homo state.

In figure 5.5.(c) panel up we display the total EDOS. First of all we observed a band-like behaviour, and no H-L gap is found in the majority and minority Fe_{309} EDOS, resulting in a metallic cluster. Figure 5.5.(c) panel down presents the Fe_{309} PEDOS. We found that Fe-3d up electrons occupy the energies between -5eV and -1eV. In addition, Fe 3d down orbitals are shifted towards higher energies enclosed by -3eV and the homo state, leaving the minority orbitals less occupied than the majority.

In the table 5.5 we display the majority ($\uparrow$) and the minority ($\downarrow$) Fe electron population and local atom MM (μ_B) of Fe atoms. Moreover, the positive/negative sign of μ_B denotes its resulting up/down direction, respectively. Focusing on the electron population, we found that majority orbitals are more occupied than the minority counterpart, resulting in large Fe atom MM. This behaviour reflects the trend reported in figure 5.5.(c) and it is the origine of the FM coupling among all Fe atoms in the cluster. Interestingly, Fe(II) and Fe(III) atoms exhibit smaller spin up-down imbalance compared to the Fe(I) atoms, causing a lower Fe(II)-Fe(III) atom MM than Fe(I).

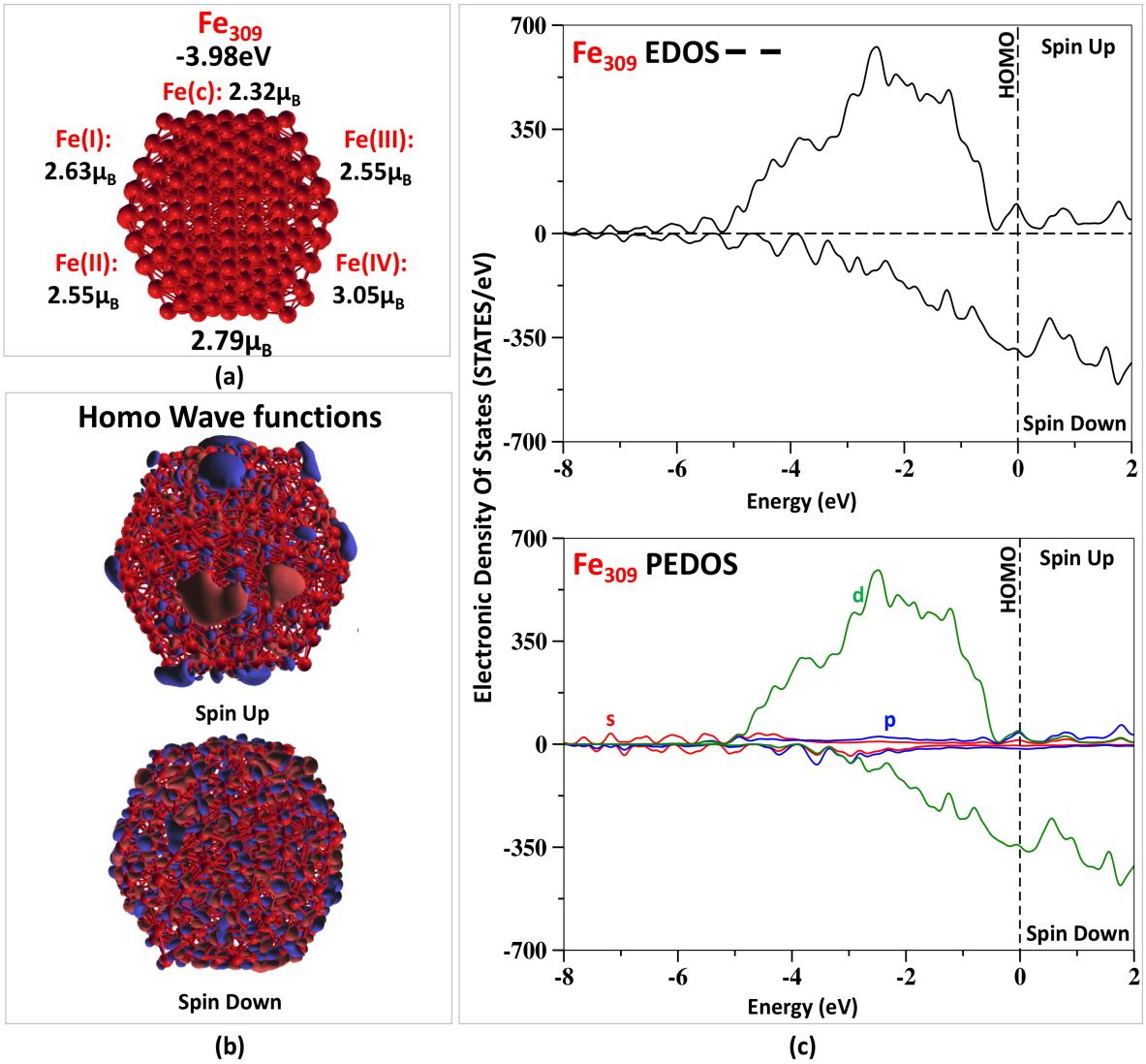

Figure 5.5: Fe_{309}: (a) magnetic and structural properties. (b) Spin up and Spin down Wave Functions (WF) at the homo level. Red and blue area stand for the negative and positive charge of the WF. (c) Panel up: Total cluster EDOS (dashed black line). Panel down: Fe_{309} PEDOS (the s, p and d PEDOS is presented with red, blue and green lines, respectively).

5.2 Copper

5.2.1 Cu_{13}

Cu_{13}: Ground-state structure

In line with the Fe_{13} cluster, we wanted to find the favoured Cu_{13} configuration. We studied three different Cu_{13} cluster structures: Buckled-Biplanar (BBP), Icosahedral (ICO), Cuboctahedral (CUBO), that are

Table 5.5: Spin up (↑), Spin Down (↓) Fe electron population and local atom MM (μ_B) of Fe_{309} icosahedral cluster.

	SIESTA		
atom	Spin Up (↑)	Spin Down (↓)	μ_B(↑)-(↓)
Fe(C)	7.87	5.55	2.32
Fe(I)	8.19	5.56	2.63
Fe(II)	7.94	5.38	2.55
Fe(III)	8.15	5.60	2.55
Fe(IV)	8.59	5.54	3.05

reported in figure 5.6.

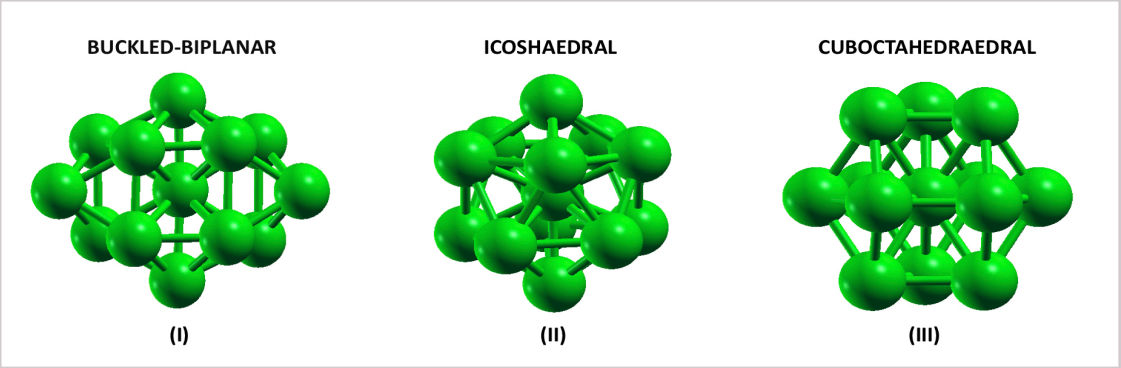

Figure 5.6: Fe_{13} cluster: (I) Buckled-Biplanar (BBP), (II) Icosahedral (ICO), (III) Cuboctahedral (CUBO)

In the table 5.6, we display the binding energy and the average MM of the Cu_{13} clusters calculated with both SIESTA and VASP packages. Moreover, in the last column we report other theoretical results for comparison. In agreement with other theoretical calculations [124][145], we observe that the BBP structure as the most

Table 5.6: Binding energy E_B (eV), average cluster's MM (μ_B) of the Cu_{13} structures. In the last column theoretical references are reported for comparison.

	SIESTA		VASP		Ref
Structure	E_B	MM	E_B	MM	MM Theo.
BBP	-2.86	0.01			
ICO	-2.82	0.39	-2.24	0.39	0.385[66]
CUBO	-2.74	0.23			

stable geometry. Interestingly, experimental and theoretical works exhibit the ICO arrangement as the most stable configuration for larger Cu clusters (e.g. 55, 147 and 309 atoms)[68][69]. For this reason in the next paragraph we proceed our analysis focusing on the Cu_{13} ICO structure.

Cu_{13}: Structural, electronic and magnetic properties

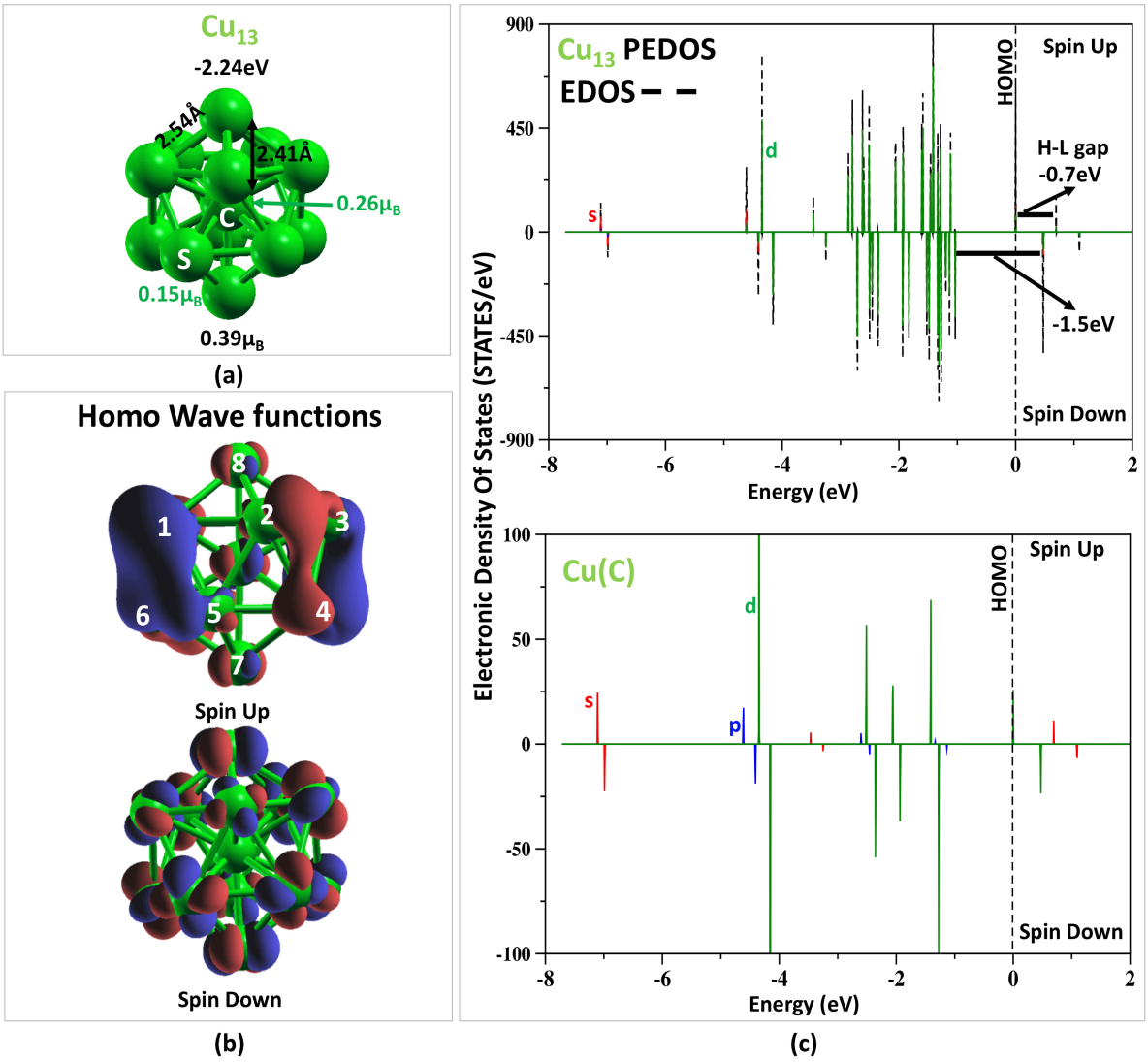

Figure 5.7: Cu_{13}: (a) magnetic and structural properties. (b) Spin up and Spin down Wave Functions (WF) at the homo level. Red and blue area stand for the negative and positive charge of the WF. (c) Panel up: Total cluster EDOS (dashed black line); Cu_{13} PEDOS (the s, p and d PEDOS is presented with red, blue and green lines, respectively). Panel down: Cu(C) PEDOS

In figure 5.7.(a) we present the structural and magnetic properties of Cu_{13} icosahedral cluster. We refer to the Cu atom in the cluster's center as Cu(C), while with Cu(S) we name the Cu atoms in the shell. We found a binding energy of -2.82eV with VASP and -2.24eV with SIESTA. Although Cu bulk system is known to be non magnetic, we observe a small average cluster's MM. In agreement with literature [66][72], we found a value of $0.39\mu_B$ fby both VASP and SIESTA calculations. Focusing on the Cu atom MM, we can see that Cu(C) shows a local MM of $0.27\mu_B$ by VASP and $0.25\mu_B$ with SIESTA. Moreover, Cu atoms in the shell display a local MM of $0.15\mu_B$ with VASP and $0.39\mu_B$ with SIESTA. Concerning to the interatomic distances,

we find a Cu(C)-Cu(S) distance of 2.41$\AA$ by VASP and 2.43$\AA$ with SIESTA, while we find a Cu(S)-Cu(S) distance of 2.54$\AA$ with VASP and 2.58$\AA$ by SIESTA.

Figure 5.7.(b) exhibits the spin up and down Wave Function (WF) at the homo state. Focusing on spin up WF, we name the Cu atoms with numbers (from 1 to 8) for simplicity reasons. We discovered Cu-3d bonding hybridisation among Cu(1)-Cu(5)-Cu(6), Cu(2)-Cu(4) and Cu(2)-Cu(3). On the contrary, we observed 3d electrons located on Cu(7), Cu(8) and Cu(C). Concerning to the spin down WF, we observe that the 3d electrons are localized on the Cu atoms in the shell, while the Cu in the center were found completely clean.

In figure 5.7.(c) panel up we report the total EDOS and Cu PEDOS. We observe Cu-3d up orbitals between -4.5eV and the homo state, while the Cu 3d spin down are between -4eV and -1eV. In addition, 4s orbitals are at low energies enclosed in the region -8eV and -4.5eV. Moving to Cu(C) in figure 5.7.(c) panel down, we found Cu-3d up electrons between -5eV and the homo state, whereas the 3d-down are between -4eV and -1eV. The 4s and 4p electrons are at low energies between -7.5eV and -4.5eV. Finally, we observe a H-L gap of -0.7eV in the majority total EDOS, while a H-L gap of -1.5eV was found in the minority counterpart, giving an half-metallic character to the Cu_{13} ICO cluster.

Table 5.7 presents the majority (↑) and the minority (↓) Cu electron population and local atom MM (μ_B) of Cu atoms. Furthermore, the positive/negative sign of μ_B denotes its resulting up/down direction, respectively. Focusing on VASP calculations we can see that Cu(C) exhibits a higher local MM than the Cu(S). In

Table 5.7: Spin up (↑), Spin Down (↓) electron population and local atom MM (μ_B) of Cu atoms.

atom		VASP				SIESTA	REF
		s	p	d	total	total	
Cu(C)	Spin Up (↑)	0.23	0.24	4.74	5.22		
	Spin Down (↓)	0.23	0.25	4.46	4.95		
	μ_B (↑)-(↓)	0.00	-0.01	0.28	0.27	0.25	0.21[66]
Cu(S)	Spin Up (↑)	0.26	0.13	4.64	5.02		
	Spin Down (↓)	0.18	0.08	4.61	4.87		
	μ_B (↑)-(↓)	0.08	0.05	0.03	0.16	0.39	0.40[66]

particular, 3d Cu(C) orbitals display a larger spin up-down imbalance compared to the 3d Cu(S) orbitals. On the contrary, SIESTA yielded a Cu(S) local MM higher than Cu(C), in agreement with the literature.

5.2.2 Cu_{55}

In this section we present results referring to the Cu_{55} icosahedral cluster. In figure 5.8.(a) we provide structural and magnetic properties of Cu_{55}. We name Cu(C) the copper atom in the center of the cluster, and with Cu(I) and Cu(II) the copper atoms in the first and second shells, respectively. We found a binding energy of -2.85eV with VASP and -3.63eV with SIESTA, while we observe an average cluster MM of $0\mu_B$ with both SIESTA and VASP calculations. Concerning to the interatomic distance, VASP and SIESTA tielded a

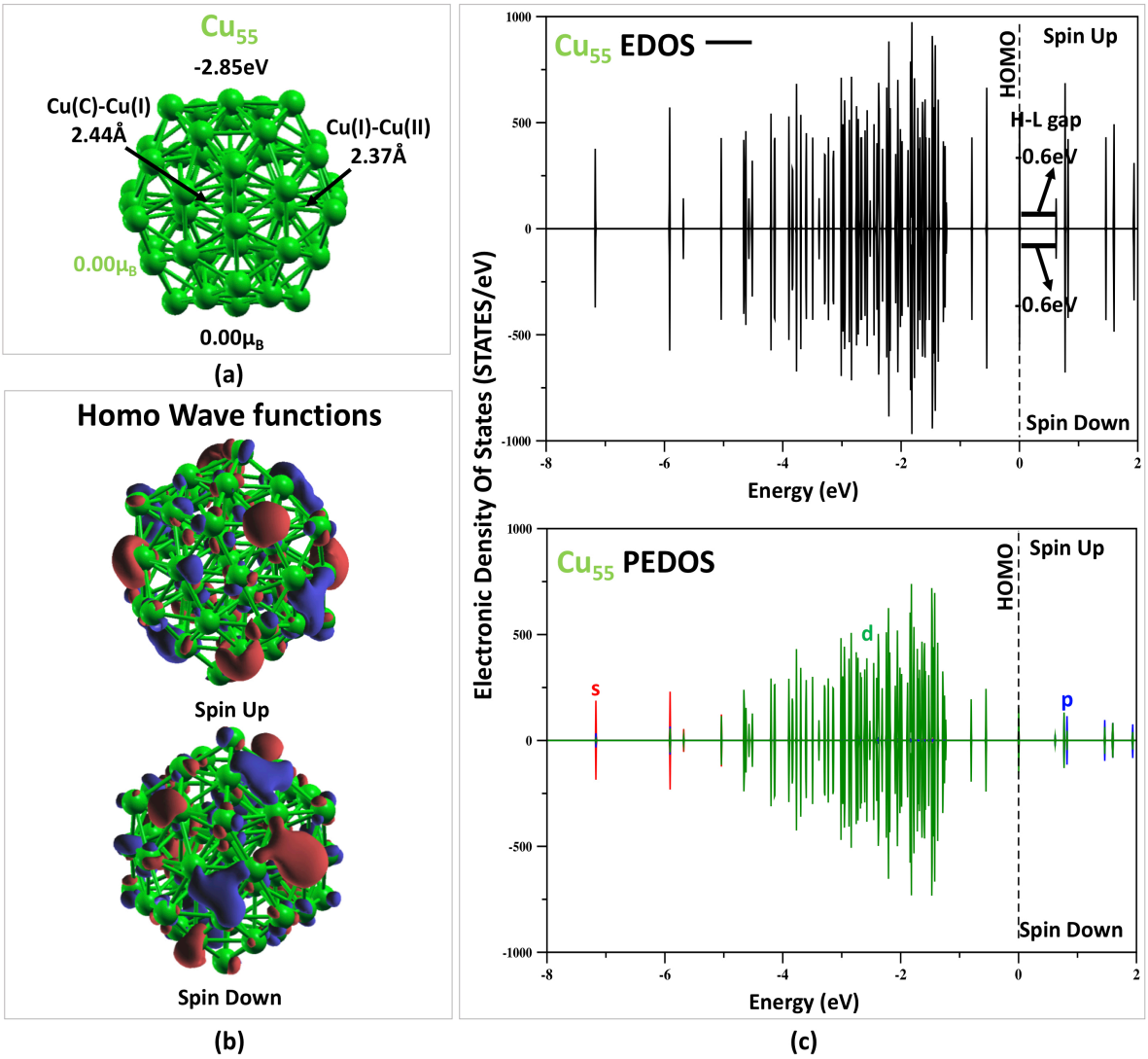

Figure 5.8: Cu_{55}: (a) magnetic and structural properties. (b) Spin up and Spin down Wave Functions (WF) at the homo level. Red and blue area stand for the negative and positive charge of the WF. (c) Panel up: Total cluster EDOS (dashed black line). Panel down: Cu_{55} Cu PEDOS (the s, p and d PEDOS is presented with red, blue and green lines, respectively).

Cu(C)-Cu(I) distance of 2.44$\mathring{A}$, while we found a Cu(I)-Cu(II) distance of 2.37$\mathring{A}$ with VASP and 2.42$\mathring{A}$ with SIESTA. Focusing on the Cu atom MM, we discovered that the Cu local MM drops to zero when the cluster size increases. In fact, we observed a weak Cu atom MM in the Cu_{13}, whereas the Cu atom MM in Cu_{55} was found to be zero.

Figure 5.8.(b) displays the spin up and down Wave Function (WF) at the homo state. It is interesting to note that the distribution of charge in both spin up and down WF appears similar. In particular, both spin up and down WF show Cu-3d hybridization bonding among Cu atoms in the outermost shell. Moreover,

we note a small amount of charge located on the Cu atoms in the inner shell. In figure 5.8.(c) panel up, we present the total Cu_{55} EDOS. First of all, the EDOS exhibit a symmetric behaviour in the spin up and down energy states, giving a non magnetic character to the Cu_{55} cluster. Moreover, due to the size of the system, we found that the states are localized and discrete. In addition, we found a H-L gap of -0.6eV in both majority and minority total EDOS. Focusing on the Cu_{55} PEDOS in figure 5.8.(c) panel down, we observed Cu-3d electrons between -5eV and -1eV, while 4s states are at low energies around -7eV and -6eV.

In the table 5.8, we present the majority (↑) and the minority (↓) Cu electron population and local atom MM (μ_B) of Cu atoms. Additionally, the positive/negative sign of μ_B denotes its resulting up/down directions, respectively. Concerning the electron population, we did not observe any majority-minority orbitals

Table 5.8: Spin up (↑), Spin Down (↓) electron population and local atom MM (μ_B) of Cu atoms.

atom		VASP				SIESTA
		s	p	d	total	total
Cu(C)	Spin Up (↑)	0.24	0.26	4.59	5.09	
	Spin Down (↓)	0.24	0.26	4.59	5.09	
	μ_B (↑)-(↓)	0.00	0.00	0.00	0.00	0.00
Cu(I)	Spin Up (↑)	0.24	0.21	4.60	5.03	
	Spin Down (↓)	0.24	0.21	4.60	5.03	
	μ_B (↑)-(↓)	0.00	0.00	0.00	0.00	0.00
Cu(II)	Spin Up (↑)	0.24	0.21	4.60	5.03	
	Spin Down (↓)	0.24	0.21	4.60	5.03	
	μ_B (↑)-(↓)	0.00	0.00	0.00	0.00	0.00

imbalance. In other words, spin up and down states are occupied with the same amount of charge, avoiding an abundance of the majority or minority electron population. These results reflect the behaviour exhibited in the WF and the total EDOS displayed in figures 5.8.(b), 5.8.(c).

5.2.3 Cu_{147}

Figure 5.9.(a) reports on the structural and magnetic properties of Cu_{147} cluster. We found a binding energy of -3.03eV with VASP, while SIESTA yielded a binding energy of -3.88eV. In line with Cu_{55}, we observe a Cu atom MM of $0\mu_B$ and consequently an average cluster MM of $0\mu_B$. Concerning the interatomic distances, we found a Cu(C)-Cu(I) distance of $2.39\mathring{A}$, while Cu(I)-Cu(II) is $2.43\mathring{A}$ and finally we found a distance of $2.44\mathring{A}$ between Cu(II) and Cu(III) atoms, with VASP. Moreover, SIESTA resulted in a Cu(C)-Cu(I) interatomic distance of $2.43\mathring{A}$, Cu(I)-Cu(II) is $2.45\mathring{A}$ and Cu(II)-Cu(III) is $2.42\mathring{A}$.

In figure 5.9.(b) we present the spin up and down Wave Function (WF) at the homo state. In agreement with the Cu_{55} results, we observed the same charge distribution in the spin up and down WF. In particular, focusing on the third shell, we found Cu-3d electrons localized on some Cu atoms, whereas we observed some weak Cu-3d orbitals hybridization among the other ones. Referring to the second shell, we observed 3d hybridization bonding among the Cu(II) atoms.

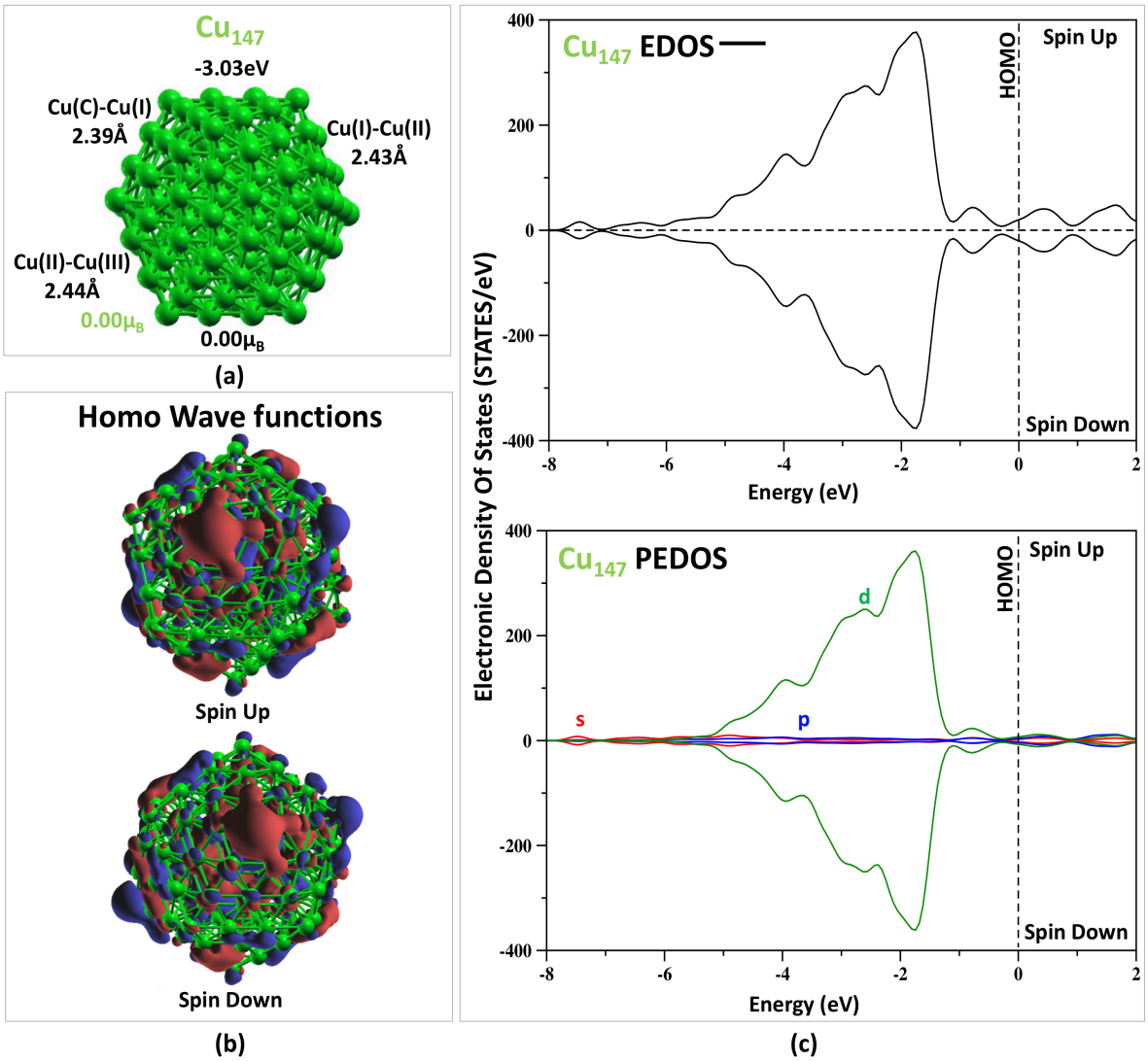

Figure 5.9: Cu_{147}: (a) magnetic and structural properties. (b) Spin up and Spin down Wave Functions (WF) at the homo level. Red and blue area stand for the negative and positive charge of the WF. (c) Panel up: Total cluster EDOS (dashed black line). Panel down: Cu_{147} Cu PEDOS (the s, p and d PEDOS is presented with red, blue and green lines, respectively).

Figure 5.9.(c) panel up shows the Cu_{147} total EDOS. Conform to the Cu_{55} total EDOS, we observed a symmetric distribution between spin up and spin down population, resulting in a non-magnetic cluster. In addition, due to the dimension of the cluster, the Cu_{147} total EDOS shows a band-like behaviour. Finally, no H-L gap is displayed in both majority and minority charge distributions, resulting in a metallic cluster.

Table 5.9 exhibits the majority (↑) and the minority (↓) Cu electron population and local atom MM (μ_B) of Cu atoms. Furthermore, the positive/negative sign of μ_B underlines its resulting up/down direction, respectively. Similarly to the Cu_{55} cluster, we note that all Cu atoms exhibit the same majority and minority

Table 5.9: Spin up (↑), Spin Down (↓) electron population and local atom MM (μ_B) of Cu atoms.

atom		VASP				SIESTA
		s	p	d	total	total
Cu(C)	Spin Up (↑)	0.25	0.25	4.60	5.11	
	Spin Down (↓)	0.25	0.25	4.60	5.11	
	μ_B (↑)-(↓)	0.00	0.00	0.00	0.00	0.00
Cu(I)	Spin Up (↑)	0.23	0.22	4.59	5.04	
	Spin Down (↓)	0.23	0.22	4.59	5.04	
	μ_B (↑)-(↓)	0.00	0.00	0.00	0.00	0.00
Cu(II)	Spin Up (↑)	0.23	0.20	4.60	5.03	
	Spin Down (↓)	0.23	0.20	4.60	5.03	
	μ_B (↑)-(↓)	0.00	0.00	0.00	0.00	0.00
Cu(III)	Spin Up (↑)	0.24	0.09	4.62	4.95	
	Spin Down (↓)	0.24	0.09	4.62	4.95	
	μ_B (↑)-(↓)	0.00	0.00	0.00	0.00	0.00

orbitals occupation. We did not find any spin up-down imbalance, confirming the behaviour displayed in the total EDOS (fig.5.9.(c) panel up) and the no-magnetic character of the Cu_{147} ICO cluster.

5.2.4 Cu_{309}

In this paragraph we focus on the Cu_{309} icosahedral cluster. In figure 5.10.(a) we present the structural and magnetic properties of the Cu_{309} system. We calculate a binding energy of -4.01 eV, while we found an average cluster's MM of zero, in line with the smaller Cu structures. We refer as Cu(C), Cu(I), Cu(II), Cu(III) and Cu(IV) for the Cu atom in the cluster's center and in the first, second, third and forth shell, respectively. The interatomic distances are 2.43$\mathring{A}$ between Cu(C) and Cu(I), while Cu(I)-Cu(II) is 2.47$\mathring{A}$, Cu(II)-Cu(III) is 2.46$\mathring{A}$ and Cu(III)-Cu(IV) is 2.41$\mathring{A}$.

Figure 5.10.(b) displays the spin up and down Wave Function (WF) at the homo state. In agreement with the Cu_{147}, we found similar spin up and down WF. In particular, we observed Cu-3d weak orbital hybridizations among the Cu(IV) atoms. In addition, some amount of 3d charge is localized on the Cu atoms in the inner shell.

In figure 5.10.(c) panel up we display the Cu_{309} total EDOS. We observed a band-like behaviour and a symmetric distribution between spin up and down states, in agreement with the smaller Cu systems. No H-L gap is shown in the majority/minority total EDOS, exhibiting the metallic character of the cluster. Figure 5.10.(c) panel down shows the Cu_{309} total PEDOS. We can see that both Cu-3d up and down orbitals are enclosed by -5eV and -1eV.

In table 5.10 we report on the majority (↑) and the minority (↓) Cu electron population and local atom MM (μ_B) of Cu atoms. Additionally, the positive/negative sign of μ_B denotes its resulting up/down direction,

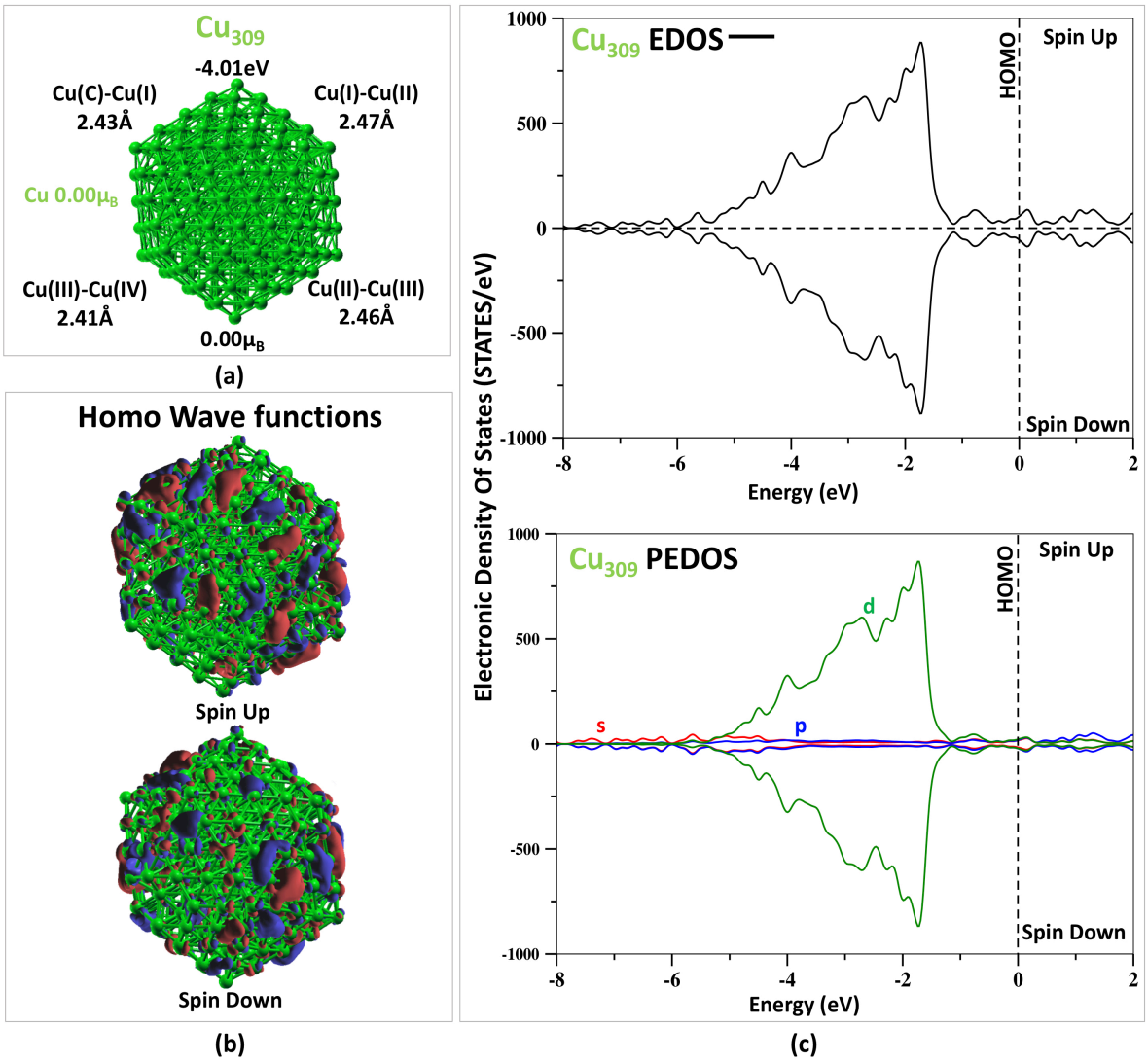

Figure 5.10: Cu_{309}: (a) magnetic and structural properties. (b) Spin up and Spin down Wave Functions (WF) at the homo level. Red and blue area stand for the negative and positive charge of the WF. (c) Panel up: Total cluster EDOS (dashed black line). Panel down: Cu_{309} Cu PEDOS (the s, p and d PEDOS is presented with red, blue and green lines, respectively).

respectively. We observed that all Cu atoms exhibit the same spin up and down electron population, reflecting the total EDOS behaviour and the no magnetic character of the Cu_{309} cluster.

Table 5.10: Spin up (↑), Spin Down (↓) Fe electron population and local atom MM (μ_B) of Cu_{309} icosahedral cluster.

	SIESTA		
atom	Spin Up (↑)	Spin Down (↓)	μ_B(↑)-(↓)
Cu(C)	5.51	5.51	0.00
Cu(I)	5.50	5.50	0.00
Cu(II)	5.51	5.51	0.00
Cu(III)	5.51	5.51	0.00
Cu(IV)	5.50	5.50	0.00

5.3 Cobalt

5.3.1 Co_{13}

Co_{13}: Ground-state structure

In this section we present structural, electronic and magnetic properties of Co clusters. We studied three diverse geometries in order to discover the Co_{13} favoured structure. Specifically, in figure 5.11 we present (I) Hexagonal Closed Packed (HCP), (II) Icosahedral (ICO), (III) Cuboctahedral (CUBO) of the Co_{13} clusters' geometries.

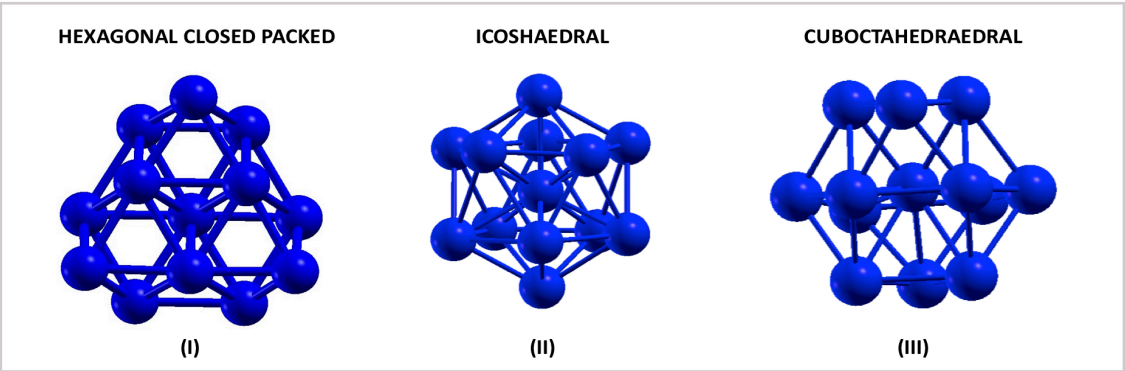

Figure 5.11: Co_{13} cluster: (I) Hexagonal Closed Packed (HCP), (II) Icosahedral (ICO), (III) Cuboctahedral (CUBO)

In table 5.11 we report the binding energy (E_B) and the average magnetic moment (MM) of the Co_{13} clusters calculated by both SIESTA and VASP packages. Additionally, in the last two columns we report theoretical and experimental references for comparison reasons.
In line with available data [124][145][77], we found that the HCP as the most stable Co cluster configuration, mimicking the Co bulk structure. In addition, the Co atom MM ($2.01\mu_B$) is higher than the corresponding

Table 5.11: Binding energy E_B (eV), average cluster's MM (μ_B) of the Co_{13} structures. In the last two columns theoretical and experimental references are reported for comparison.

	SIESTA		VASP		Ref	
Structure	E_B	MM	E_B	MM	MM Theo.	MM Exp
HCP	-3.18	2.01			2.08[82][124]	
ICO	-3.13	2.21	-3.33	2.33	2.39[43][82][42][124]	2.30[40]
CUBO	-3.12	2.05			2.08[42][124]	

value in the Co bulk ($1.7\mu_B$). However, experimental and theoretical works exhibit the ICO structure as the most stable configuration for larger Co clusters (e.g. 55, 147 and 309 atoms)[42][78]. For this reason in the next paragraph we will focus on Co_{13} ICO structure.

Co_{13}: Structural, electronic and magnetic properties

In figure 5.12.(a) we present structural and magnetic properties of the Co_{13} ICO cluster. For simplicity reason, we refer to Co atoms in the center with Co(C), whereas we name Co(S) the Co atoms in the shell. Concerning to the structural properties, we found a binding energy of -3.33eV with VASP and -3.13eV with SIESTA. The Co(C)-Co(S) interatomic distance is $2.33\mathring{A}$ with VASP, while $2.47\mathring{A}$ with SIESTA. Furthermore, Co(S)-Co(S) distance is $2.45\mathring{A}$ with VASP and around $2.67\mathring{A}$ by SIESTA. Referring to the magnetic properties, the average cluster MM is $2.33\mu_B$ by VASP, whereas $2.21\mu_B$ was found by SIESTA. Additionally, Co(C) shows a lower local MM than Co(S). We found a Co(C) local MM of $1.94\mu_B$ with VASP and it is $1.89\mu_B$ with SIESTA. Moreover, Co(S) exhibits a local value of $2.16\mu_B$ using VASP and $2.25\mu_B$ with SIESTA.

Figure 5.12.(b) shows the spin up and down Wave Function (WF) at the homo state. Focusing on the spin up WF, we can note the Co-3d hybridization bonding among Co atoms in the shell. Moreover, we observed 3d orbitals localized on the Co(C), while no bonds are shown between Co(C) and the other Co(S) atoms. Concerning the spin down WF, we observe Co-3d orbitals located on Co(S) atoms, while no charge is localized on Co(C).

In figure 5.12.(c) panel up we present the total EDOS and Co PEDOS. Focusing on the spin up electrons, we found Co-3d orbitals between -5.5eV and close to the homo states, while 4s states are at low energy around -7.5eV. Moreover, Co-3d spin down electrons are shifted toward higher energy compared to the 3d spin up orbitals. Specifically, they are between -4eV and the homo state. In addition, we found 4s down states at -7eV. Moving to the figure 5.12.(c) panel down, Co(C) EDOS shows Co-3d majority orbitals between -5.5eV and close to the homo state. Furthermore, we observed Co-3d minority charge between -4eV and -0.5eV. Additionally, 4s up and down states are mainly at low energies between -8eV and -7eV. Finally, total majority EDOS shows a H-L gap of -0.5eV, while no H-L gap is exhibited in the minority counterpart, making the Co_{13} ICO a half-metallic cluster.

In the table 5.12 we depict the majority ($\uparrow$) and the minority ($\downarrow$) Co electron population and local atom MM (μ_B) of Co atoms. In addition, the positive/negative sign of μ_B denotes its resulting up/down direction,

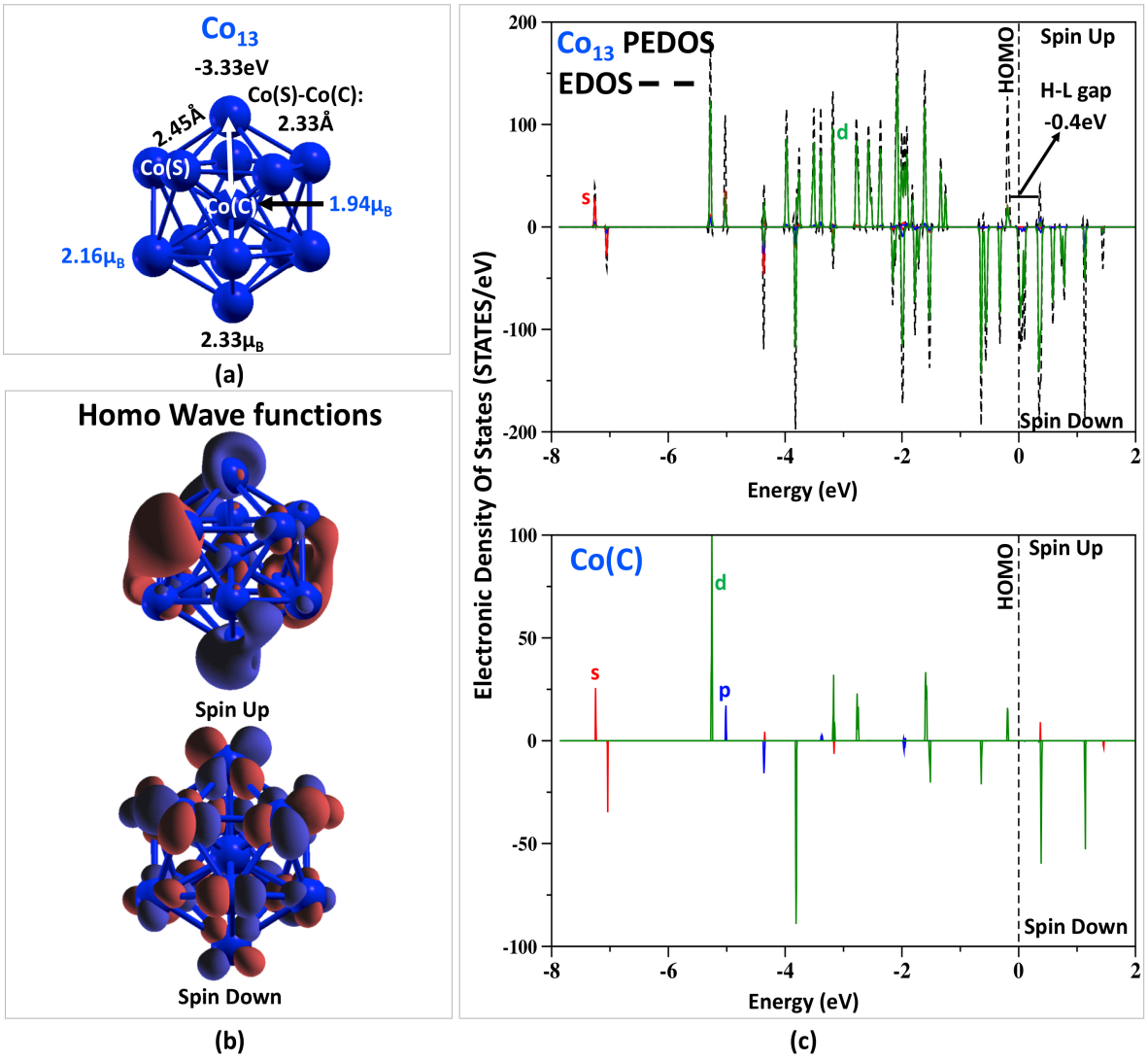

Figure 5.12: Co_{13}: (a) magnetic and structural properties. (b) Spin up and Spin down Wave Functions (WF) at the homo level. Red and blue area stand for the negative and positive charge of the WF.(c) Panel up: Total cluster EDOS (dashed black line); Co_{13} PEDOS (the s, p and d PEDOS is presented with red, blue and green lines, respectively). Panel down: Co(C) PEDOS

respectively. Focusing on the Co(S) atoms, we found the largest local atom MM. We observed that all s, p and d majority orbitals are more occupied than the minority, enhancing the Co atom MM. On the contrary, due to the higher coordination number, the Co(C) orbitals display s and p minority states, which are more occupied than the majority, lowering therefore the Co(C) atom MM.

Table 5.12: Spin up (↑), Spin Down (↓) electron population and local atom MM (μ_B) of Co atoms.

atom		VASP				SIESTA	REF
		s	p	d	total	total	
Co(C)	Spin Up (↑)	0.26	0.31	4.72	5.29		
	Spin Down (↓)	0.29	0.38	2.67	3.35		
	μ_B (↑)-(↓)	-0.03	-0.07	2.05	1.94	1.89	1.88[66]
Co(S)	Spin Up (↑)	0.28	0.17	4.61	5.06		
	Spin Down (↓)	0.22	0.12	2.56	2.90		
	μ_B (↑)-(↓)	0.06	0.05	2.05	2.16	2.25	2.43[66]

5.3.2 Co_{55}

In this paragraph we present the Co_{55} ICO structure. For simplicity, we refer to the Co atom in the cluster's center with Co(C), while we name Co(I) and Co(II) the Co atoms in the first and second shells, respectively.

Figure 5.13.(a) exhibits the structural and magnetic properties of the Co_{55} ICO cluster. We calculated a binding energy of -4.29eV with VASP and -3.85eV with SIESTA. Referring to the VASP results, the Co(C)-Co(I) interatomic distance is 2.37$\mathring{A}$, while Co(I)-Co(II) is 2.33$\mathring{A}$. Moreover, with SIESTA we obtained a Co(C)-Co(I) distance of 2.51$\mathring{A}$ and Co(I)-Co(II) is 2.48$\mathring{A}$. The average cluster MM is 1.87μ_B with VASP and 1.91μ_B with SIESTA. Focusing on the Co atom MM, we note that it decreases from the outermost to the inner shell, in line with theoretical and experimental works [42][37]. Interestingly, we discovered that the Co(II) atom MM is smaller than the corresponding Co atom MM in the Co_{13} ICO cluster.

In figure 5.13.(b), we display the spin up and down Wave Function (WF) at the homo state. Examining the spin up WF, we observe Co-3d bonding hybridization between Co atoms in the second shell. Moreover, we can see a small amount of 3d charge localized in the Co atoms in the inner shells. Moving to the spin down WF, we found that Co-3d electrons are located on the Co atoms, while we did not observe any hybridizations.

Figure 5.13.(c) panel up exhibits the Co_{55} total EDOS. Referring to the total EDOS we observed that the energy states are localized and discrete, this behaviour is principally due to the dimensions of the cluster. Moreover, we observed a H-L gap of -0.6eV in the majority EDOS, while we did not find any H-L gap in the minority counterpart, giving an half-metallic character to this cluster. Moving to the Co_{55} PEDOS in figure 5.13.(c) panel down, we observed 4s states at low energy between -7.5eV and -6.5eV. Furthermore, 3d spin up orbitals are between -5.5eV and -1eV, whereas 3d spin down are between -4eV and the homo state, leaving the minority population less occupied than the majority counterpart.

In the table 5.13 we display the majority (↑) and the minority (↓) Co electron population and local atom MM (μ_B) of Co atoms. In addition, the positive/negative sign of μ_B denotes its resulting up/down direction, respectively. In agreement with the shell model, we observed that the Co local MM increases from the inner to the outermost shells. Co(C) and Co(I) electronic populations show s and p minority orbitals which are more occupied than the majority ones, lowering the Co local atom MM. Moreover, Co(II) atoms display the

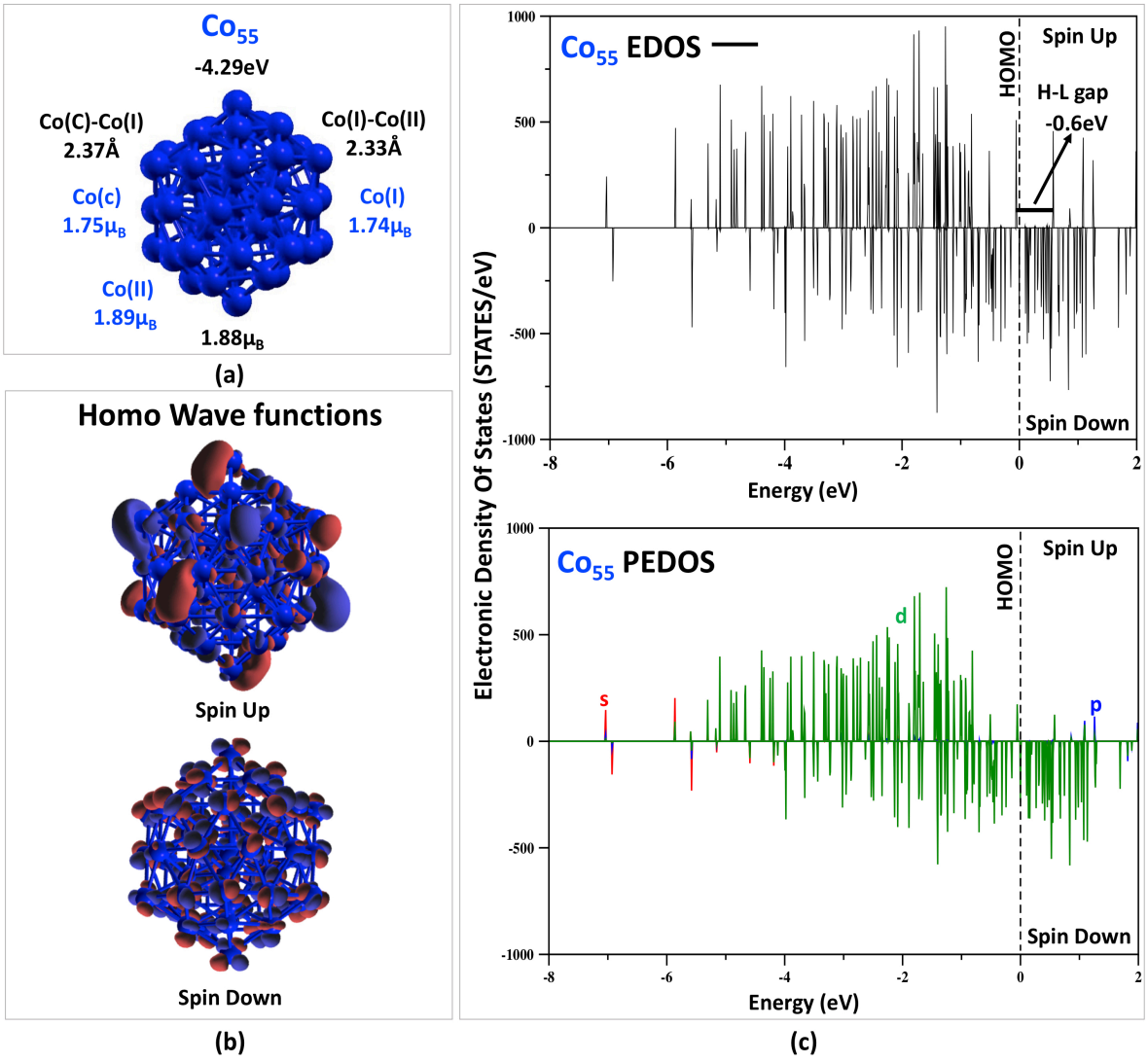

Figure 5.13: Co_{55}: (a) magnetic and structural properties. (b) Spin up and Spin down Wave Functions (WF) at the homo level. Red and blue area stand for the negative and positive charge of the WF. (c) Panel up: Total cluster EDOS (dashed black line). Panel down: Co_{55} Co PEDOS (the s, p and d PEDOS is presented with red, blue and green lines, respectively).

3d majority orbitals more filled than the minority ones, giving the largest imbalance between majority and minority occupation and resulting in the highest Co local MM. Contrary to the Fe_{55}, we found a FM coupling between Co(C), Co(I) and Co(II) atoms.

Table 5.13: Spin up (↑), Spin Down (↓) electron population and local atom MM (μ_B) of Co atoms.

atom		VASP				SIESTA
		s	p	d	total	total
Co(C)	Spin Up (↑)	0.25	0.58	4.56	5.10	
	Spin Down (↓)	0.28	0.61	2.76	3.35	
	μ_B (↑)-(↓)	-0.03	-0.03	1.80	1.75	1.80
Co(I)	Spin Up (↑)	0.26	0.28	4.56	5.10	
	Spin Down (↓)	0.27	0.33	2.76	3.36	
	μ_B (↑)-(↓)	-0.01	-0.05	1.80	1.74	1.81
Co(II)	Spin Up (↑)	0.24	0.18	4.58	5.00	
	Spin Down (↓)	0.24	0.21	2.67	3.11	
	μ_B (↑)-(↓)	0.00	-0.03	1.91	1.89	2.10

5.3.3 Co_{147}

In line with the previous paragraph, we name Co in the cluster's center Co(C), while we refer with Co(I), Co(II) and Co(III) to the Co atoms in the first, second and third shell respectively.

In figure 5.14.(a) we present the structural and magnetic properties of the Co_{147}. Focusing on the VASP results, we calculated a binding energy of -4.40eV and an average cluster's MM of 2.18μ_B that is smaller compared to the corresponding Co_{55} cluster value. The interatomic distances are 2.40$\mathring{A}$ Co(C)-Co(I), 2.43$\mathring{A}$ Co(I)-Co(II) and Co(II)-Co(III) 2.44$\mathring{A}$. Moreover, in agreement with the last section and with other theoretical calculations and experimental results, we observed that the Co local MM increases from the center to the outermost shell. Moving to the SIESTA results, we found a binding energy of -4.10eV, while we observed an average cluster MM of 1.78μ_B lower than the VASP value. The interatomic distances are: Co(C)-Co(I) 2.45$\mathring{A}$, Co(I)-Co(II) 2.56$\mathring{A}$ and Co(II)-Co(III) 2.48$\mathring{A}$. In addition, the Co atom MM rises from the center to the outermost shell, in line with VASP results.

Figure 5.14.(b) exhibits the spin up and down Wave Function (WF) at the homo state. The spin up WF displays Co-3d hybridization bonding between Co(III) atoms. Moreover, we observed a small amount of charge localized on the Co atoms in the inner shell. Focusing on the spin down WF, we found that Co 3d electrons are located on the Co atoms, while no hybridizations bonding are shown among Co atoms.

Finally, in figure 5.14.(c) panel up we present the Co_{147} total EDOS. First of all, we note that the EDOS shows a band-like behaviour, mainly due to the dimensions of the cluster. Furthermore, both majority and minority EDOS did not exhibit any H-L gap, confirming the metallic character of the cluster. Concerning to the Co_{147} PEDOS reported in figure 5.14.(c) panel down, we observe that the Co 3d up orbitals are enclosed by -5eV and -1eV. However, the Co 3d spin down are shifted toward higher energy, leaving less filled the minority population. Specifically, we found the Co 3d down between -4eV and the homo state.

Table 5.14 shows the majority (↑) and the minority (↓) Co electron population and local atom MM (μ_B) of Co atoms. Furthermore, the positive/negative sign of μ_B denotes its resulting up/down direction, respectively.

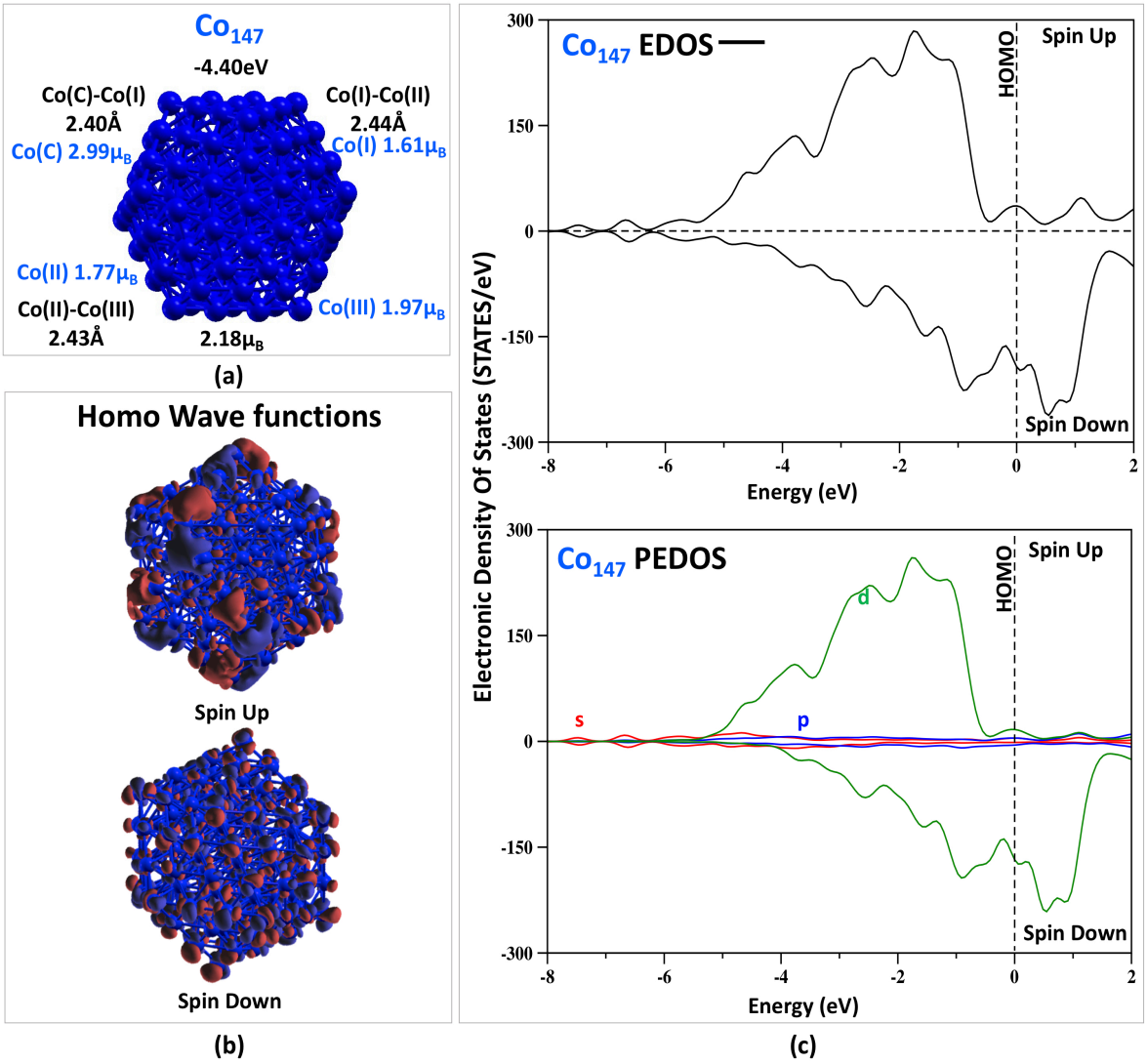

Figure 5.14: Co_{147}: (a) magnetic and structural properties. (b) Spin up and Spin down Wave Functions (WF) at the homo level. Red and blue area stand for the negative and positive charge of the WF. (c) Panel up: Total cluster EDOS (dashed black line). Panel down: Co_{147} Co PEDOS (the s, p and d PEDOS is presented with red, blue and green lines, respectively).

We observed that the Co atoms in the inner shells have the s and p minority orbitals more occupied than the majority ones, resulting in a low Co local MM. On the contrary, Co(III) atoms exhibited all spin up orbitals more filled than the spin down. As a result, Co(III) display a large 3d up and down imbalance, giving an enhanced Co local MM. Moreover, we note that the Co local MM in Co_{147} cluster is smaller than the corresponding value Co in the Co_{55}, lowering the Co_{147} average cluster's MM. Finally, the Co_{147} show the FM coupling among all Co atoms in the cluster.

Table 5.14: Spin up (↑), Spin Down (↓) electron population and local atom MM (μ_B) of Co atoms.

atom		VASP				SIESTA	Ref
		s	p	d	total	total	
Co(C)	Spin Up (↑)	0.27	0.60	3.89	4.33		
	Spin Down (↓)	0.28	0.65	2.49	2.99		
	μ_B (↑)-(↓)	-0.01	-0.05	1.40	1.34	1.45	1.70 [37]
Co(I)	Spin Up (↑)	0.24	0.24	4.49	4.98		
	Spin Down (↓)	0.25	0.29	2.82	3.37		
	μ_B (↑)-(↓)	-0.01	-0.05	1.67	1.61	1.66	2.10 [37]
Co(II)	Spin Up (↑)	0.23	0.22	4.54	4.98		
	Spin Down (↓)	0.24	0.27	2.71	3.21		
	μ_B (↑)-(↓)	-0.01	-0.05	1.83	1.77	1.72	0.70 [37]
Co(III)	Spin Up (↑)	0.24	0.11	4.57	4.93		
	Spin Down (↓)	0.23	0.11	2.62	2.96		
	μ_B (↑)-(↓)	0.01	0.00	1.95	1.97	2.02	2.50 [37]

5.3.4 Co_{309}

In this paragraph we present the structural, electronic and magnetic properties of the Co_{309} ICO cluster. In agreement with the last two paragraph we refer as Co(C), Co(I), Co(II), Co(III) and Co(IV) the cobalt atoms in the cluster's center, in the first, second, third and fourth shell, respectively.

In figure 5.15.(a), we report the Co_{309} structural and magnetic properties. We calculate a binding energy of -4.25eV and an average cluster's MM of $1.72\mu_B$ that it is lower compared to the cluster's average MM of Co_{147}. The interatomic distance are: $2.45\mathring{A}$ between Co(C) and Co(I), $2.52\mathring{A}$ between Co(I) and Co(II), while Co(II)Co(III) distance is $2.57\mathring{A}$ and finally Co(III)-Co(IV) $2.50\mathring{A}$. Additionally, we found that the Co atom MM increases from the center to the outermost shell, in line with the previous sections.

Figure 5.15.(b) displays the spin up and down Wave Function (WF) at the homo state. We observed a small amount of 3d charge localized on Co atoms in both spin up and down WF, whereas weak 3d orbitals hybridization are shown among some Co atoms in the fourth shell.

In figure 5.15.(c) panel up we present the Co_{309} total EDOS. Also in this case, we observed a band-like behaviour and a metallic character of the Co_{309} cluster. Concerning to the Co_{309} PEDOS in figure 5.15.(c) panel down, we found that 3d down orbitals are shifted toward higher energy compared to the 3d up counterpart. Specifically, the Co 3d up are between -5eV and -1eV, whereas Co 3d down are enclosed by -3eV and the homo state, leaving the minority orbitals less filled that the majority.

In the table 5.15 we report the majority (↑) and the minority (↓) Co electron population and local atom MM (μ_B) of Co atoms. Additionally, the positive/negative sign of μ_B denotes its resulting up/down direction, respectively.

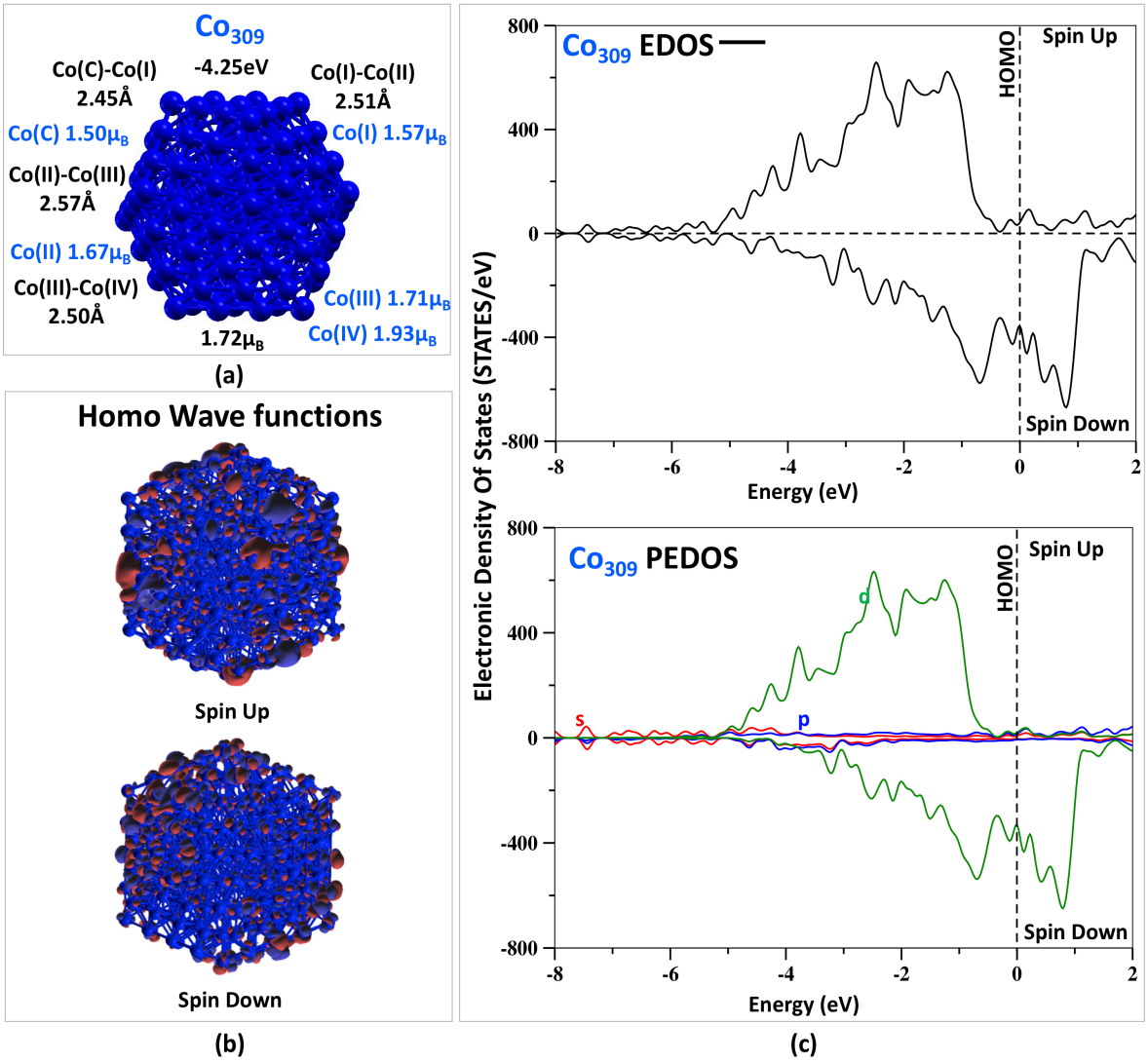

Figure 5.15: Co_{309}: (a) magnetic and structural properties. (b) Spin up and Spin down Wave Functions (WF) at the homo level. Red and blue area stand for the negative and positive charge of the WF. (c) Panel up: Total cluster EDOS (dashed black line). Panel down: Co_{309} Co PEDOS (the s, p and d PEDOS is presented with red, blue and green lines, respectively).

Interestingly, we observed that the Co local MM decreases with the dimension of the cluster. In particular, we found a Co atom MM lower than the corresponding Co atom MM in the Co_{147}. In addition, we observed a FM coupling between all Co atoms in the cluster as reported in the smaller Co ICO systems.

Table 5.15: Spin up (↑), Spin Down (↓) Fe electron population and local atom MM (μ_B) of Co_{309} icosahedral cluster. In the last column the reference is reported for comparison.

	SIESTA			
atom	Spin Up (↑)	Spin Down (↓)	μ_B(↑)-(↓)	Ref.
Co(C)	7.85	6.35	1.50	1.7[37]
Co(I)	8.09	6.52	1.57	2.1[37]
Co(II)	8.02	6.35	1.67	2.5[37]
Co(III)	8.31	6.60	1.71	0.7 [37]
Co(IV)	8.48	6.55	1.93	2.5 [37]

5.4 Manganese

5.4.1 Mn_{13}

Mn_{13} clusters: Magnetic configuration and ground-state structure

It is known that manganese atom exhibits the highest MM ($5\mu_B$) while the Mn bulk system displays an exotic crystal structure that it is found to be non magnetic. Theoretical calculations show that the non magnetic feature of Mn bulk is mainly due to the AFM coupling among Mn atoms. In order to discover the favoured Mn_{13} cluster geometry, we have to investigated diverse structural and magnetic configurations.

First, we relaxed our system with spin *collinear* calculation, assuming only parallel spin direction (up and down). In figure 5.16.(a) we present the binding energy (E_B) and the average cluster's MM of the Mn_{13} icosahedral (ICO) clusters, considering in the INPUT file: (I) FM and (II) AFM spin coupling. Additionally, figure 5.16.(b) displays the binding energy (E_B) and the average cluster's MM of the Mn_{13} cuboctahedral (CUBO) clusters, taking in the INPUT file: (I) FM and (II) AFM spin alignment.

It is worth to be noted that, although in the cluster 5.16.(a).(I) we started our calculation with a FM configuration, the relaxed structure shows AFM coupling between the Mn atom at the cluster's center and the others Mn atoms in the shell. On the contrary, the 5.16.(a).(II) did not change the magnetic arrangement. We observed the same behaviour in the cuboctahedral systems. Furthermore, we found the ICO structure as the most stable configuration, while the CUBO geometry shows a larger average cluster's MM.

We continue our investigation by relaxing the Mn_{13} ICO clusters using the spin *non collinear* calculation. We assume that the spin of di electrons are free to orient in every direction during the relaxation. In figure 5.17 we present three different spin arrangements in the INPUT: (a) all spins are oriented parallel (0°); (b) the spin are 45° oriented; (c) the spin are 90° oriented.

Interestingly, although in the (b) and (c) structures we set non parallel spin orientation in the input, we found that the relaxed structures exhibit almost a spin collinear arrangement, in agreement with other theoretical

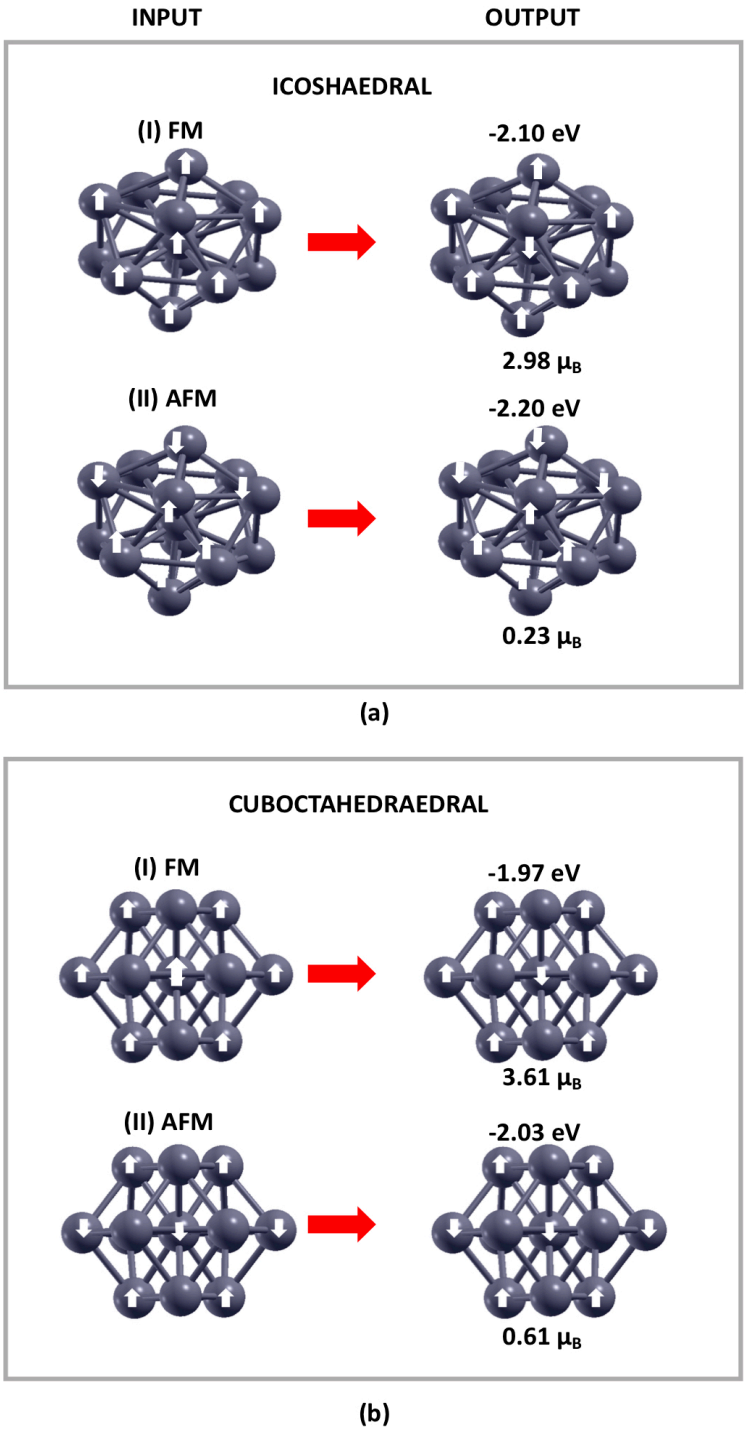

Figure 5.16: Mn_{13} clusters: (a) ICO, input: (I) FM spin coupling, (II) AFM spin coupling. (b) CUBO, input: (I) FM spin coupling, (II) AFM spin coupling.

works[90][146].

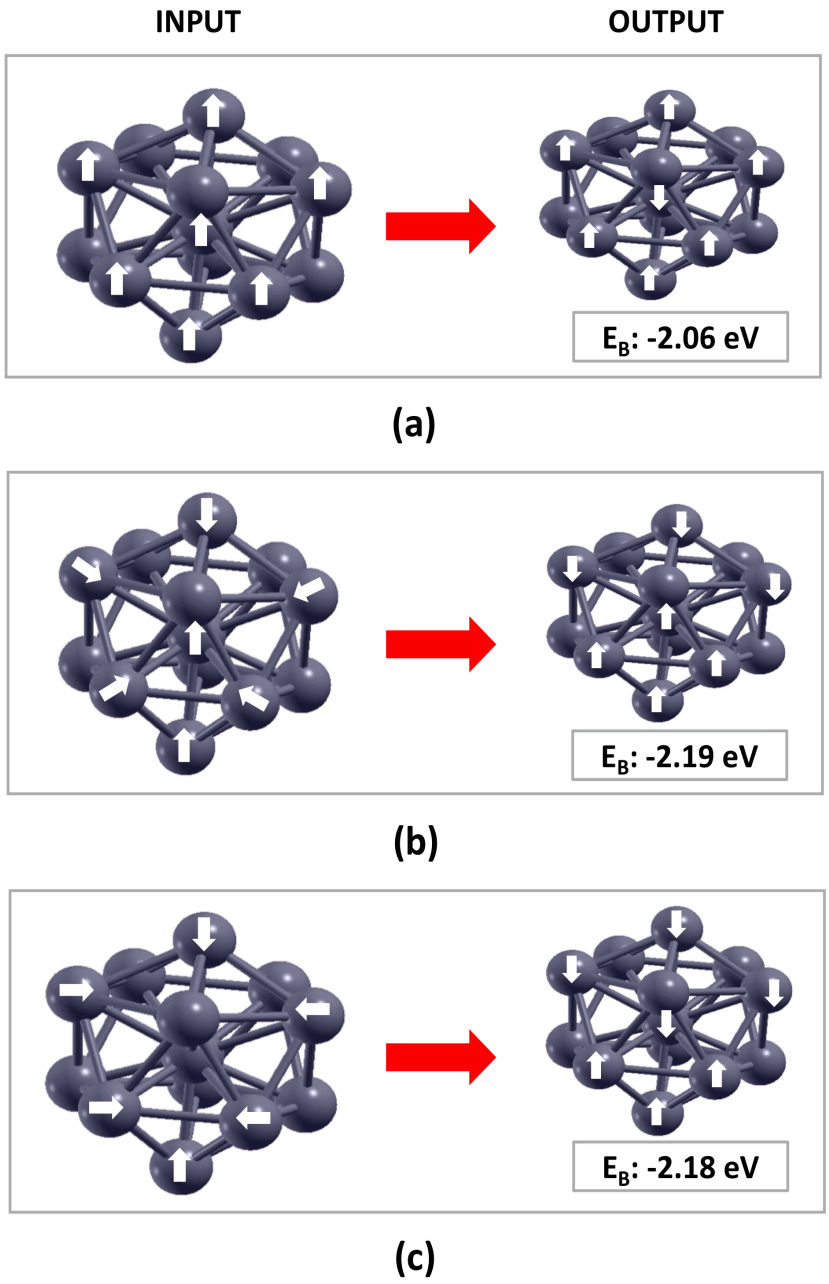

Figure 5.17: Mn_{13} clusters: (a) spin oriented parallel, 0°. (b) spin oriented 45°. (c) spin oriented 90°.

Additionally, the (b) and (c) output structures, exhibited in figure 5.17, showed the energetically favoured magnetic configurations. We found that in these schemes, atoms might be considered to belong at two different rings. Atoms in the same ring are FM coupled, while the two rings are AFM aligned with each other, mimicking the 5.16.(a).(II) magnetic structure. For this reason in the next section we will focus on the Mn_{13} ICO cluster using collinear calculation.

Mn_{13} clusters: Structural, electronic and magnetic properties

In the last paragraph we found two possible ICO magnetic configuration that are reported in 5.16.(a).

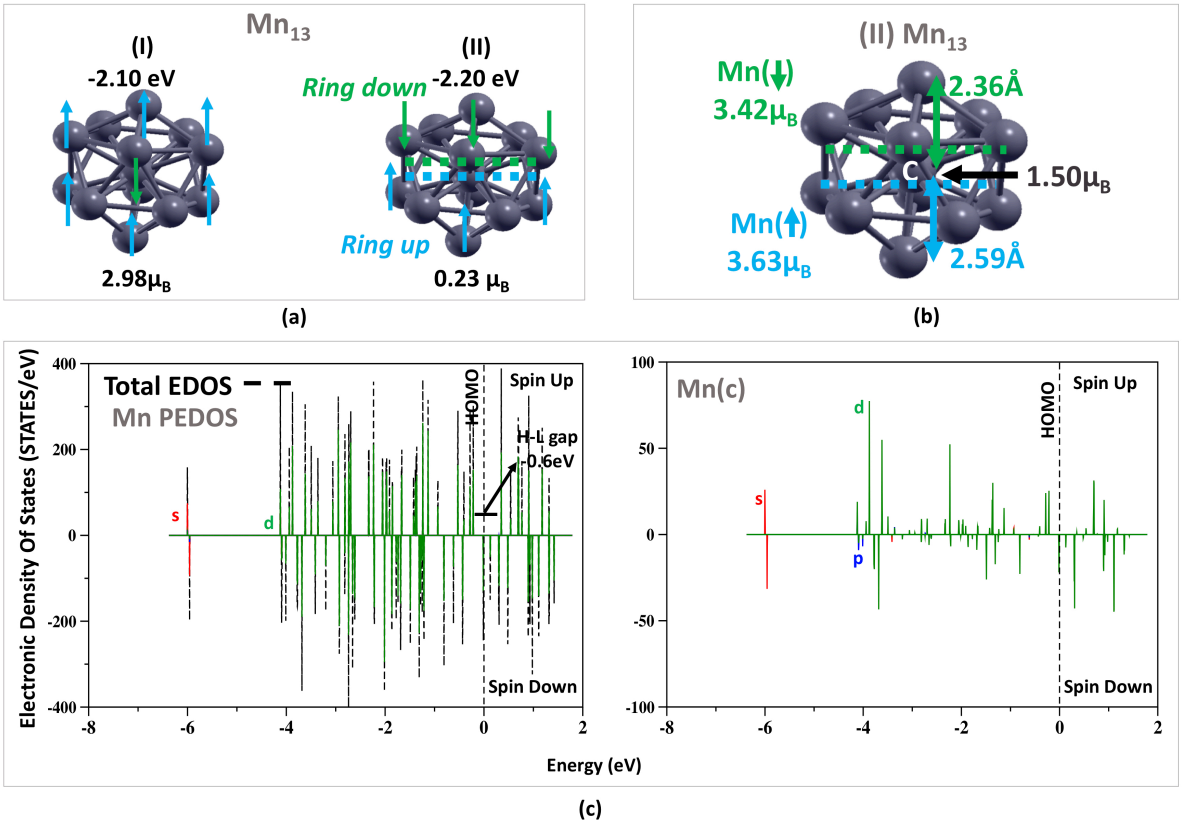

Figure 5.18: Mn_{13}: (a) (I) and (II) AFM arrangement, binding energy and average cluster's MM. (b) Structural and magnetic properties of (II) Mn_{13} ICO cluster. (c) Panel left: Total cluster EDOS (dashed black line); Mn PEDOS (the s, p and d PEDOS is presented with red, blue and green lines, respectively). Panel right: Mn(C) PEDOS.

In figure 5.18.(a) we present the binding energy and the cluster's average MM of the (I) Mn_{13} and (II) Mn_{13} ICO cluster. The spin up in blue (↑) and the spin down in green (↓) are shown for simplicity reason. The (I) Mn_{13} ICO structure shows an AFM coupling among the Mn atoms in the shell (↑) and the Mn in the center (↓). This configuration displays a binding energy of -2.10eV and an average cluster MM of $2.98\mu_B$. Moreover, the (II) Mn_{13} ICO cluster also exhibits an AFM behaviour. We observed the cluster's ring green in the up part of the system that couples AFM with the cluster's ring blue in the down. For this configuration we found a binding energy of -2.20eV that is lower than the corresponding value of (I) Mn_{13}, resulting in the most stable configuration. Additionally, we observed an average cluster's MM of $0.23\mu_B$ that it is smaller than the average cluster's MM exhibited in the (I) Mn_{13}.

In figure 5.18.(b) we report the structural and magnetic properties of the (II) Mn_{13} system. We refer to the Mn at the cluster center with Mn(C), while with Mn(↑) and Mn(↓) to the Mn atoms aligned spin up (↑) and

spin down (↓), respectively. The interatomic distances are ≈ 2.36$\mathring{A}$ between Mn(C)-Mn(↓), whereas ≈ 2.59$\mathring{A}$ Mn(C)-Mn(↑). Furthermore, we found a Mn(C) atom MM of 1.50μ_B, the Mn(↑) atom MM is 3.63$\mathring{A}$, while the Mn(↓) atom MM is -3.42$\mathring{A}$.

Figure 5.18.(c) panel left displays the (II) Mn_{13} ICO total and partial EDOS. We observed discrete and localized energy states and a symmetric distribution in the majority and minority populations. Contrary to the Cu, we found that each Mn atom contributes with its own positive or negative local MM. Due to the different spin alignments, (↑) or (↓), the 3d electrons of each atom occupies either only the spin up or only the spin down orbitals, resulting in a symmetric majority and minority occupation. Moreover, we found that Mn-3d up electrons are between -4.0eV and -0.5μ_B, whereas the Mn-3d down orbitals are enclosed by -4.0eV and the homo state. Mn-4p are at low energies around -6eV. Furthermore, majority total EDOS exhibits a H-L gap of -0.6eV while no gap is shown in the minority counterpart, giving an half metallic character to the (II) Mn_{13} ICO cluster. In figure 5.18.(c) panel right, we present the Mn(C) PEDOS. We observe, 3d up orbitals are enclosed by -4eV and -0.5eV, while the 3d-down are between -4eV and the homo states. The 4s orbitals are at low energies around -6eV.

In table 5.16 we report the majority (↑) and the minority (↓) Mn electron population and local atom MM (μ_B) of Mn atoms. We found that the Mn atom MM contribution is mainly due to the 3d orbital occupation.

Table 5.16: Spin up (↑), Spin Down (↓) electron population and local atom MM (μ_B) of Mn atoms.

atom		s	p	d	total	Ref.
Mn(C)	Spin Up (↑)	0.23	0.23	3.30	3.79	
	Spin Down (↓)	0.21	0.23	1.82	2.29	
	μ_B (↑)-(↓)	0.02	0.00	1.48	1.50	≈ 0 [92] [90]
Mn(↑)	Spin Up (↑)	0.21	0.10	4.28	4.59	
	Spin Down (↓)	0.16	0.09	0.71	0.96	
	μ_B (↑)-(↓)	0.06	0.01	3.57	3.63	3.8-4.0[92] [90]
(Mn↓)	Spin Up (↑)	0.17	0.10	0.82	1.10	
	Spin Down (↓)	0.19	0.08	4.24	4.52	
	μ_B (↑)-(↓)	-0.02	0.02	-3.42	-3.42	3.8-4.0 [92] [90]

For all atoms, we observed that the s- and p-up and -down imbalance is almost zero, resulting in the same amount of charge in the spin up and spin down states. On the contrary, a really large imbalance is exhibited between majority and minority orbitals in the 3d states. Specifically, only the majority or minority orbitals are filled in the Mn(↑) or Mn(↓). As a result the spins of Mn atoms are aligned spin up (↑) or spin down (↓), reflecting the behaviour shown in the total EDOS (fig.5.18.(c)).

5.4.2 Mn_{55}

In this passage we focus on Mn_{55} icosahedral cluster. In figure 5.19.(a) we report the structural and magnetic properties of the Mn_{55}. We calculate a binding energy of -2.75eV and an average cluster's MM of 0.00 μ_B.

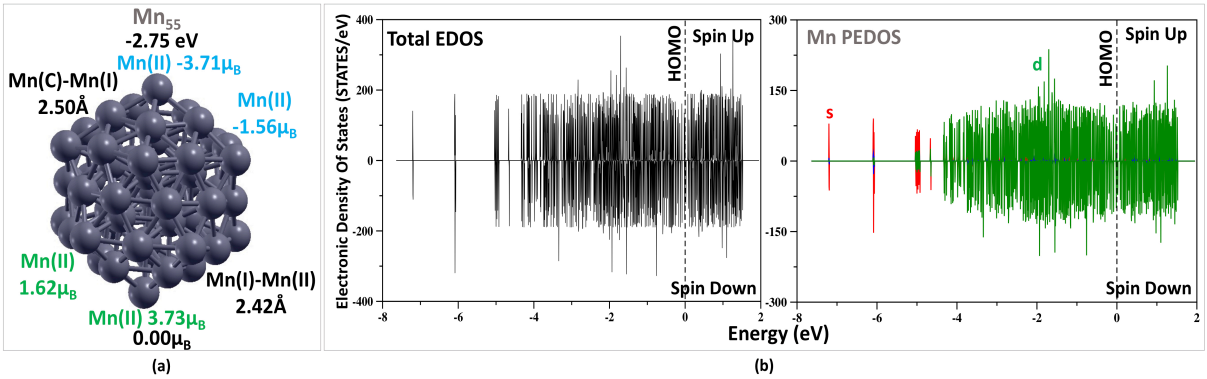

Figure 5.19: Mn_{55}:

We refer as Mn(C) to the Mn atom in cluster center, while Mn(I) and Mn(II) the Mn atoms in the first and second shell, respectively. Interestingly, we discover that the Mn(C) atom MM is $0.05\mu_B$, while the Mn atoms in the first and the second shell coupled AFM, making the average cluster's MM zero. In particular, we observe that a part of the atoms in first shell are aligned spin up, while the remaining atoms are aligned spin down, as reported in the Mn_{13} cluster. Additionally, the second shell mimics the first ones. For this reason, we write Mn for the Mn atom aligned spin up and Mn for the Mn atom aligned spin down. We observed that the spin of the Mn(II) atoms, which have Mn(I) as the first neighbour, are aligned spin down, coupling AFM each other. Mn(I) atoms show an atomic MM between 0.50-1.90μ_B and Mn(I) atoms exhibit an atomic MM between 0.46-1.66μ_B. Moreover, the Mn(II) atoms display a local MM enclosed by 1.62-3.72μ_B, whereas the Mn(II) are betwixt 1.56-3.71μ_B. Furthermore, the interatomic distances are 2.50$\mathring{A}$ between Mn(C) and Mn(I), while Mn(I)-Mn(II) are around 2.42$\mathring{A}$.

Figure 5.19.(b) panel left displays the Mn_{55} total EDOS. In line with Mn_{13} cluster, we observed a symmetric spin up and down distribution. Additionally, we did not find any H-L gap in the majority/minority total EDOS, giving a metallic character to the cluster. Figure 5.19.(b) panel right exhibit the Mn_{55} PEDOS. We can see both spin up and down orbitals are enclosed by -4eV and the homo state, while the 4s states are at low energies between -8eV and 4.5eV.

In table 5.17 we report the majority (↑) and the minority (↓) Mn electron population and the local atom MM (μ_B) of Mn atoms.

We observed that the s, p and d Mn(C) occupations are symmetric resulting in a almost zero local atom MM of the Mn(C). Interestingly, we found that Mn(I) and Mn(I) contribute in the average cluster's MM with almost the same local MM but aligned anti-parallel. In addition, Mn(II) and Mn(II) mimic the Mn(I)/Mn(I) atoms' behaviour, reflecting the Mn_{55} total EDOS.

5.5 Conclusion

In this chapter we investigated the structural, electronic and magnetic properties of Fe, Cu, Co and Mn pure clusters.

Table 5.17: Spin up (↑), Spin Down (↓) electron population and local atom MM (μ_B) of Mn atoms.

atom		s	p	d	total
Mn(C)	Spin Up (↑)	0.23	0.27	2.61	3.11
	Spin Down (↓)	0.23	0.27	2.56	3.06
	μ_B (↑)-(↓)	0.00	0.00	0.05	0.05
Mn(I)	Spin Up (↑)	0.23	0.26	3.45	3.94
	Spin Down (↓)	0.19	0.20	1.64	2.04
	μ_B (↑)-(↓)	0.04	0.06	1.81	1.90
Mn(I)	Spin Up (↑)	0.19	0.20	1.76	2.15
	Spin Down (↓)	0.23	0.25	3.33	3.81
	μ_B (↑)-(↓)	-0.04	-0.05	-1.57	-1.66
Mn(II)	Spin Up (↑)	0.21	0.11	4.33	4.65
	Spin Down (↓)	0.18	0.07	0.68	0.92
	μ_B (↑)-(↓)	0.03	0.04	3.65	3.73
Mn(II)	Spin Up (↑)	0.18	0.07	0.68	0.93
	Spin Down (↓)	0.21	0.11	4.33	4.64
	μ_B (↑)-(↓)	-0.03	-0.04	-3.65	-3.71

Focusing on the Fe systems, we found the ICO geometry as the most stable configuration for all cluster's dimensions. About the magnetic properties, we observed an Fe atoms FM coupling only in the smallest structure. For more than 13 atoms, we note an AFM coupling among the Fe atoms. In particular, in the 55 atoms ICO cluster the spin of the central cluster's atom is aligned no-parallel with the Fe atoms in the first shell. Moreover, the 147 atoms ICO structure exhibits a AFM coupling among the Fe atoms in the first and in the second shell. In agreement with the shell model, reported by Billas et al. [20][40], the charge distribution of the atoms in the inner shells exhibits a larger occupation in the minority orbitals than in the majority ones. Furthermore, we note that the Fe local MM decreases with the dimension of the clusters, and from the outermost to the inner shells.

Focusing on the Cu clusters, it is well known that the Cu bulk is non magnetic. Our results, in agreement with literature, display that Cu_{13} shows a weak average cluster's and Cu local MM. Furthermore, for a number of Cu atoms greater than 13 the average cluster's MM drops to zero. The non magnetic character of the Cu structures is revealed in total and partial EDOS. The total EDOS exhibits a symmetric distribution of the majority-minority states, resulting in a zero average cluster's MM.

Moving to the Co clusters, we found that the 13 atoms ICO cluster adopts the HCP geometry as the most stable configuration, mimicking the Co bulk structure. In line with the literature, by increasing the number of atoms, we found that the ICO cluster is the most stable geometry. Contrary to the Fe systems, we observed a FM coupling among the Co atoms for all 13, 55, 147 and 309 Co clusters. In agreement with other theoretical calculations [37], we discovered that the clusters' inner shells exhibit a larger s and p minority

orbitals occupation than the majority states. On the contrary, Co-3d majority orbitals are always more filled than the minority ones, resulting in a FM coupling among all Co atoms.

Regarding the Mn clusters, we found the ICO structure as the most stable configuration for both 13 and 55 ICO Mn systems. Interestingly, these clusters show an AFM coupling among the Mn atoms in the same shell. In particular, our calculations show that Mn atoms assume a magnetic arrangement that minimise the average cluster MM. First, observing the smallest case 13 atoms, we found that atoms might be considered as belonging at two different rings with AFM coupling. Second, considering the 55 atoms cluster, we can separate the shells in two parts: a part where the spin of the Mn atoms are oriented up, and the another one where the spin of the Mn atoms are oriented down. As a result, the atoms in the first shell couple AFM with the Mn atoms in the second ones, making the average cluster's MM zero.

In conclusion, we found an enhanced Co and Fe average cluster's MM compared to their bulk counterpart. Interestingly, we found that the average cluster's MM increases from the largest to the smallest cluster dimension. This behaviour can be attributed to the fact that, when the number of atoms is low enough the orbitals are more localized, as a consequence the majority-minority imbalance increases resulting in a larger local atom MM. On the contrary, Cu and Mn clusters display a non-magnetic character in line with their bulk structure. Both elements in their total EDOS exhibit a symmetric spin up and down distribution, resulting in a average cluster's MM close to zero. In all cases, small clusters display a half-metallic character, while they become metallic by increasing the size of the system. Finally, the local atom magnetic moment decreases, converging toward the bulk value when the size of the system increases.

Chapter 6

Fe-X clusters

In chapter 5 we presented the structural, electronic and magnetic properties of the pure Fe, Co, Cu and Mn clusters. In this chapter, we will investigate the corresponding properties of the mixed of Fe-X (X = Cu, Co and Mn) icosahedral clusters. It is well known that the icosahedral cluster's geometry exhibits high symmetry and interesting element arrangement in the surface shell. It is important to mention that the icosahedral clusters' faces are triangular following the fcc (111) surface structure. The nomenclature used in

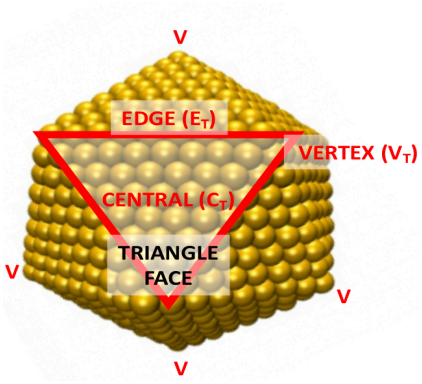

Figure 6.1: Icosahedral cluster

the whole chapter, to describe the different types of atoms in the cluster's shell is reported in the figure 6.1. In particular, we refer the cluster's vertex atoms with V. We name the atoms of the triangular face as:

1. E_T atoms in the edge of the triangular face;
2. V_T atoms in the face's vertex;
3. C_T atoms inside the triangular face

For the Fe-X clusters, we will study several atomic rearrangements in order to reveal the energetically favoured configuration. Moreover, (I)S, (II)S and (III)S denote the atoms in the first, second and third shell,

respectively. For characteristic cases, we will present a detailed spin up and down electronic density of state analysis aiming in finding the origin of the magnetic moment.

6.1 FeCu

Initially, we will analyze the FeCu clusters. It is worth mentioning that Fe is a magnetic element while Cu is known not to be magnetic in the bulk structure. The purpose of this first part is to investigate the evolution of Fe cluster's magnetic properties upon Cu substitutions.

6.1.1 Fe_xCu_{13-x} (X=0-13)

In this paragraph we present the electronic structure of the smallest 13 atoms icosahedral cluster.
In figure 6.2 we report the binding energy, average cluster's MM and the local MM of the $Cu_{13-x}Fe_x$ (X = 0-13) clusters.

Cu_{13} shows the smallest average and atomic MM of $0.4\mu_B$ in agreement with other theoretical studies [66][72]. In figure 6.2.(b), we present the two configurations of $FeCu_{12}$ which we obtain when we substitute one Cu atom by an Fe atom in the Cu_{13} cluster: (I) Fe atom occupy the center, (II) Fe is a shell atom. We found that configuration (I) is more stable than the (II) one. In addition, both configurations show approximately the same average MM, while Fe local MM is larger in configuration (II) than in (I) conformation.

In Fe_2Cu_{11}, our calculations display that the system is more stable when one Fe atom occupies the shell and the second Fe is in the cluster's center, fig.6.2.(c), than the case of two Fe shell atoms. In particular, we calculated a binding energy of -2.61eV for the case reported in fig.6.2.(c), while we found a binding energy of -2.36eV when both Fe atoms are in the shell. For this reason, we continued our clusters analysis with configurations where Fe atom occupies the cluster's center. Increasing the amount of Fe, from Fe_3Cu_{10} (d) to $Fe_{11}Cu_2$ (n) in fig.6.2, we observed a decrease in the binding energy, suggesting that the structure becomes more stable upon substitution by Fe atoms in the system. In addition, the average MM increases due to the Fe local MM contributions, as we expect since we enhance the number of Fe atoms.

In figure 6.2.(o) we display the two possibilities of $Fe_{12}Cu_1$: (I) Cu atom occupy the central site, (II) Cu is a shell atom. The most stable configuration is when Fe is the central atom. Specifically, for both structures we found approximately the same average MM and the same Fe local MM.

Finally, in Figure 6.2 we observe that the Fe local atomic MM is highest for the $FeCu_{12}$(II) cluster. Therefore, we will further investigate the FeCu(I) and FeCu(II) clusters aiming in understanding the reason for this local Fe MM difference.

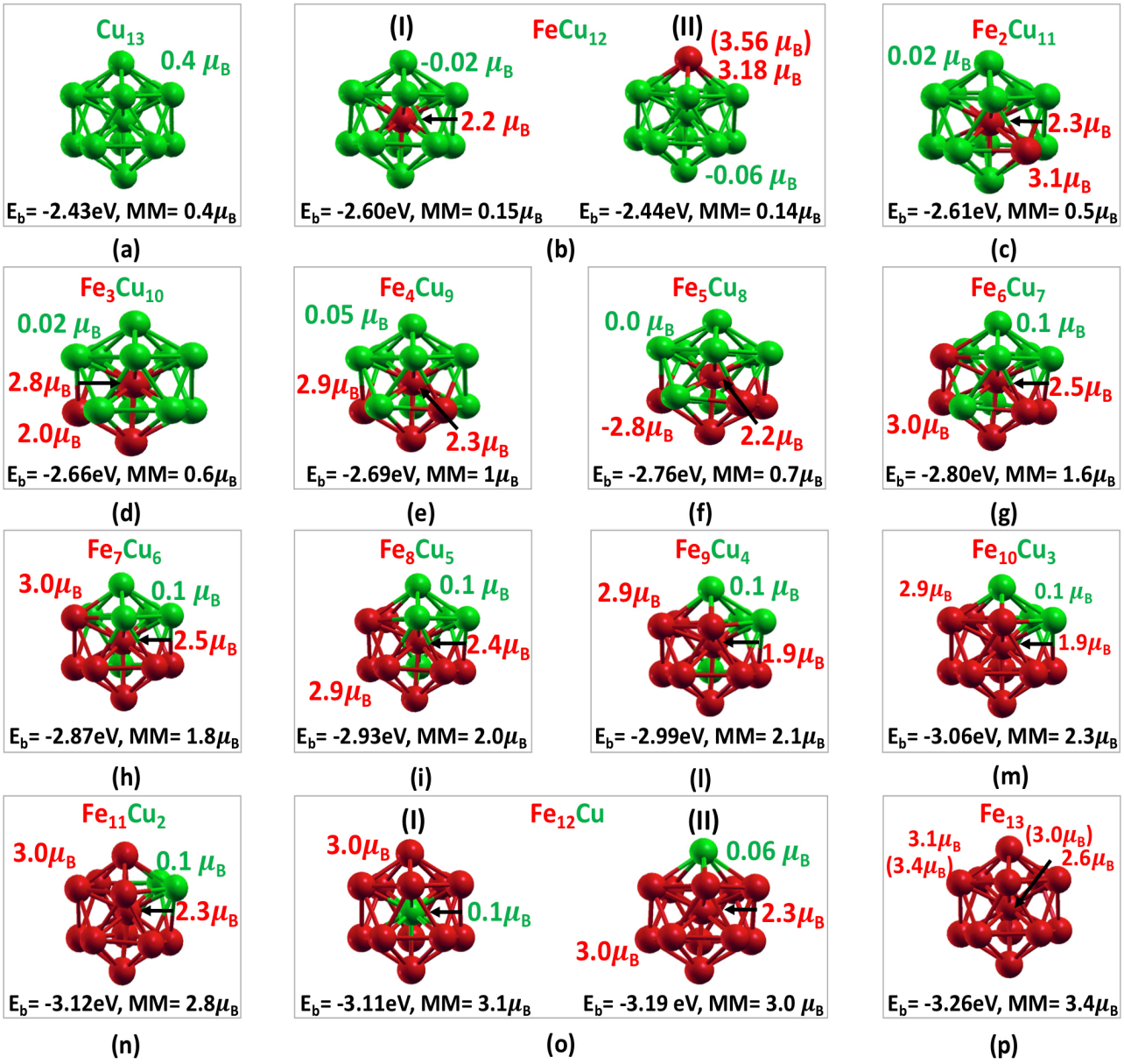

Figure 6.2: Binding energy E_b (eV), clusters' average MM(μ_B) and Fe and Cu local atomic MM (μ_B) of Fe_xCu_{13-x} (X = 0-13)

(I) $FeCu_{12}$: Fe atom at the cluster's center

In figure 6.4.(a) we report the structural and the magnetic properties of $FeCu_{12}$(I) when Fe atom occupies the central site. We found a binding energy of -2.60eV while the average Fe-Cu interatomic distances are 2.41$\AA$ with VASP and approximately 2.45$\AA$ with SIESTA. Interestingly, we can see that in Cu_{13} the interatomic distance between Cu in the central site and Cu in the shell is 2.40$\AA$, revealing that substitution of Cu with Fe do not significant enlarge the cluster's radius compared to Cu_{13} cluster. In addition, the average Cu-Cu

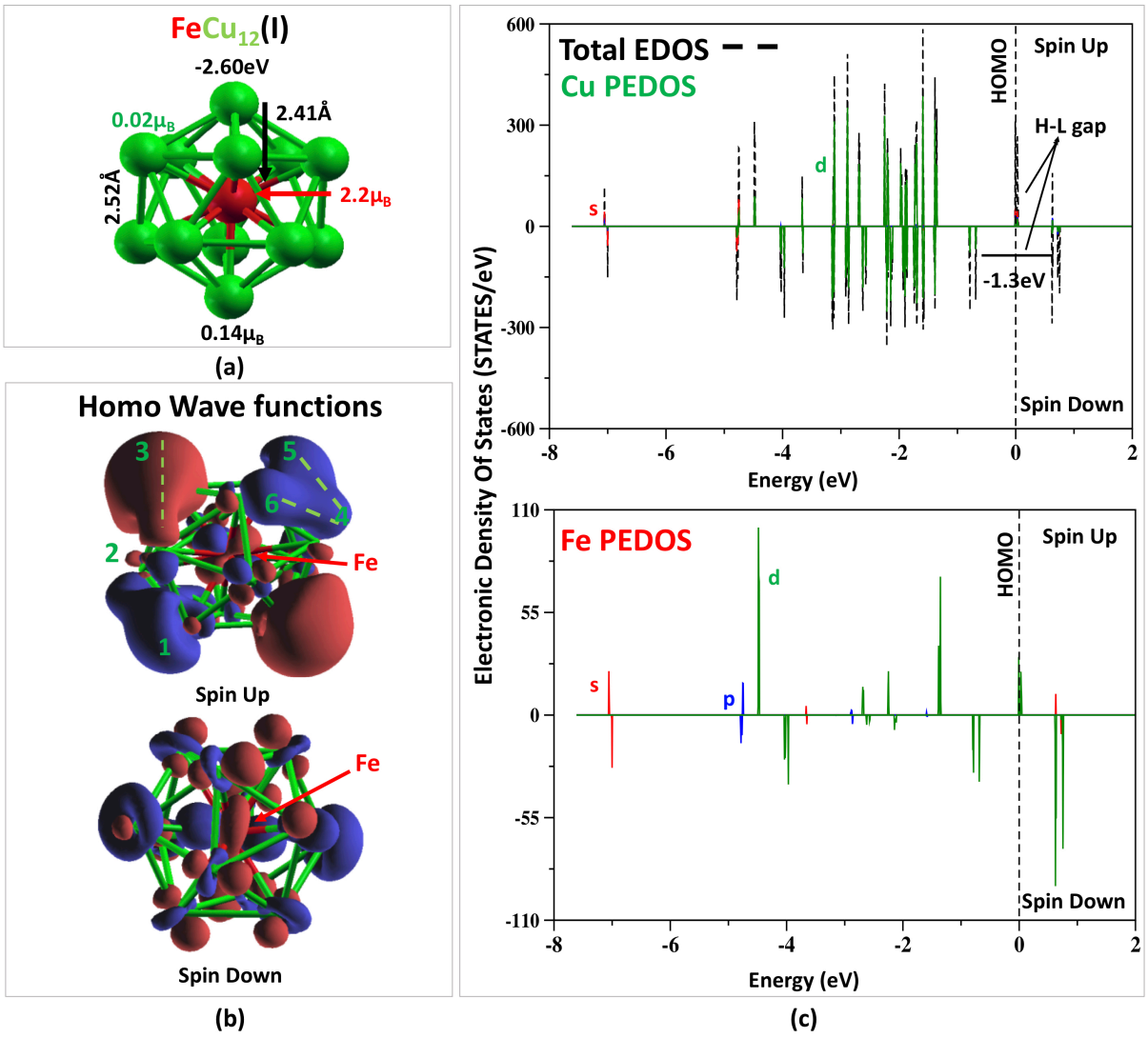

Figure 6.3: $FeCu_{12}$(I) cluster: (a) magnetic and structural properties. (b) Spin up and Spin down Wave Functions (WF) at the homo level. Red and blue area stand for the negative and positive charge of the WF.(c) Panel up: Total cluster EDOS (dashed black line); Cu PEDOS (the s, p and d PEDOS is presented with red, blue and green lines, respectively). Panel down: Fe PEDOS.

distances are 2.52$\AA$ with VASP and 2.67$\AA$ with SIESTA. Moreover, Fe exhibits a local MM of 2.2μ_B, and an average cluster MM of 0.15μ_B by both SIESTA and VASP calculations.

In figure 6.4.(b) we present the spin up and down Wave Function (WF) at the homo state. Focusing on the spin up WF, we name the Cu atoms with numbers (from 1 to 6) for simplicity reason. We observe orbital bonding hybridizations between Cu(2)-3d and Cu(3)-4s electrons and Cu-3d and Cu-3d orbital bonding hybridizations among Cu(6)-Cu(4), and Cu(5)-Cu(4). Furthermore, in the spin down WF we found that the

charge is localized on Cu atoms. Interestingly, Fe-3d$_{t2g}$ and Fe-3d$_{eg}$ orbitals are occupied in the spin up and spin down homo WF, resulting in antibonding or weak hybridizations with the Cu shell atoms.

In figure 6.4.(c) panel up we display the total EDOS and Cu PEDOS. Focusing on Cu PEDOS, we observe a symmetric distribution in the spin up and spin down occupations, resulting in an almost non magnetic behaviour for the Cu atoms. Cu 3d-up electrons occupy an interval of energies between -4eV and -2.5eV, while Cu 3d-down are between -5eV and -0.5eV. Moreover, the Cu-4s are well localized near -7eV. Turning on Fe PEDOS, fig.6.4.(b) panel down, we also observe the Fe-4s electrons around -7eV and Fe-4p close to -5eV in both majority and minority occupations. Interestingly, Fe-3d orbitals exhibit a difference between spin up and down populations. In particular, Fe-3d up are -4.8eV and -1.8eV while Fe-3d down states are around -4eV and -1eV, revealing the origin of Fe's local MM. In addition, we calculated a Homo-Lumo gap (H-L gap) close to zero, -0.04eV, in the majority total EDOS while we found a gap of -1.3eV in the minority. The presence of H-L gap in the spin down and the absence in the spin up suggests an half-metallic character for this cluster.

In the table 6.1, we present the majority (↑) and the minority (↓) Fe and Cu electron population and local atom MM (μ_B) of Fe and Cu atoms. Furthermore, the positive/negative sign of μ_B denotes its resulting up/down direction, respectively. We observe that the Fe orbitals are more occupied in the majority orbitals

Table 6.1: Spin up (↑), Spin Down (↓) electron population and local atom MM (μ_B) of Fe and Cu in FeCu$_{12}$(I) with Fe in the center.

atom		VASP				SIESTA	REF
		s	p	d	total	total	
Fe	Spin Up (↑)	0.23	0.28	4.25	4.76		
	Spin Down (↓)	0.22	0.27	2.06	2.55		
	μ_B (↑)-(↓)	0.01	0.01	2.19	2.21	2.20	2.72[70] 2.28[72]
Cu	Spin Up (↑)	0.21	0.15	4.6	4.95		
	Spin Down (↓)	0.23	0.15	4.6	4.97		
	μ_B (↑)-(↓)	-0.02	0.00	0.00	-0.02	-0.02	0.025 [72]

than in the minority, on the contrary Cu atoms display an equivalent percentage especially for the p and d orbitals resulting the lowest -0.02μ_B. Although the Cu μ_B is really small, its negative value compare to the positive Fe μ_B could indicate an AFM coupling between these atoms.

(II) FeCu$_{12}$: Fe atom in the cluster's shell

In figure 6.4.(a) we report the structural and magnetic properties of FeCu$_{12}$(II) configurations having an Fe shell atom. We found a binding energy of -2.44eV. The interatomic distances between Fe and Cu in the center are 2.50$\AA$ with VASP and 2.57$\AA$ with SIESTA, revealing that the presence of Cu in the central site enlarge the cluster's radius compared to FeCu$_{12}$(I) cluster. In addition, the average Cu-Cu distances, for both Cu in the shell, are 2.51$\AA$ with VASP and SIESTA and the average Fe-Cu distance are 2.51$\AA$ with VASP and

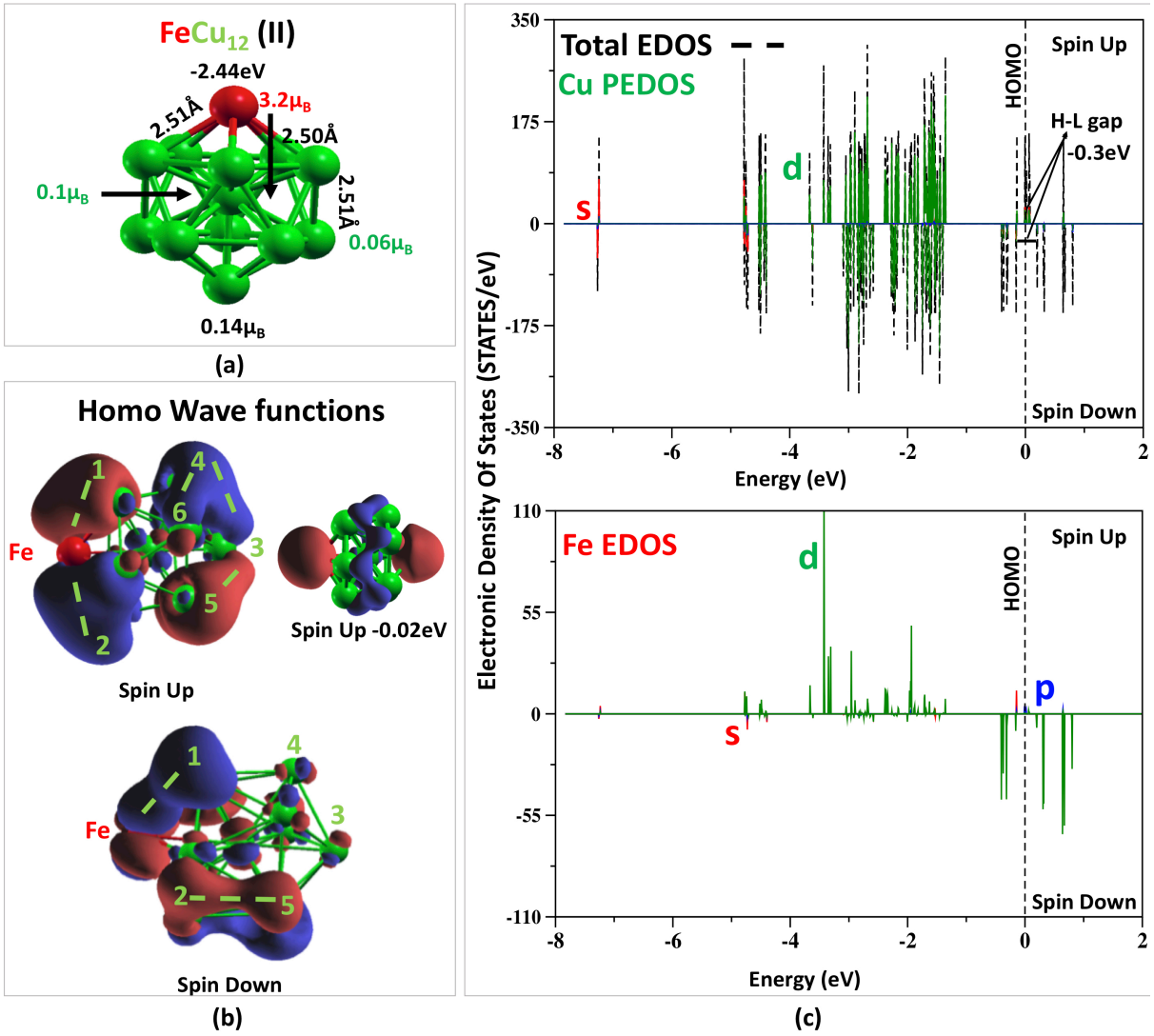

Figure 6.4: $FeCu_{12}$(II) cluster: (a) magnetic and structural properties. (b) Spin up and Spin down Wave Functions (WF) at the homo level. Red and blue area stand for the negative and positive charge of the WF.(c) Panel up: Total cluster EDOS (dashed black line); Cu PEDOS (the s, p and d PEDOS is presented with red, blue and green lines, respectively). Panel down: Fe PEDOS.

2.58$\AA$ with SIESTA for the Fe and Cu shell atoms. Furthermore, Fe displays a local MM of 3.18μ_B with VASP, and 3.56μ_B with SIESTA, reporting an average MM of 0.14μ_B.

Next, in figure 6.4.(b) we present the spin up and spin down WF at the homo level. Looking at the spin up WF, we observe orbital bonding hybridisations between Fe-4p and Cu(1)-3d and Fe-4p and Cu(2)-3d orbitals. In the specular counterpart, we can see orbital bonding hybridisations betwixt Cu(4)-4s and Cu(6)-3d, between Cu(4)-4s and Cu(3)-3d, and Cu(3)-3d and Cu(5)-3d. Moreover, spin down WF show orbital bonding hybridisations between Fe-3d and Cu(1)-4s-3d orbitals, whereas Cu-4p and Cu-4p bonding hybridisation is

displayed between Cu(2) and Cu(5).

In figure 6.4.(c) panel up we display the total EDOS and Cu PEDOS. Focusing on Cu PEDOS, spin up and spin down distributions show Cu-3d symmetric occupation between -5eV and -1eV. Cu-4s occupy low energy approximately at -7eV. Turning to Fe 6.4.(c) panel down, Fe-4p and Fe-4s are close to -7eV and -5eV, evidencing their high localisation. Furthermore, Fe-3d spin up occupy the interval between -4eV and -1eV, whereas Fe-3d spin down are between -0.5eV and the homo state. As a result, majority and minority PEDOS imbalance causes a large local magnetic moment on the Fe atom.
Finally, we find a H-L gap close to zero in the majority population, while a H-L gap of -0.3eV is obtained in the minority distribution, which although small could give a half metallic character to this cluster.

In the table 6.2, we present the majority (↑) and the minority (↓) Fe and Cu electron population and local atom MM (μ_B) of Fe and Cu atoms. Moreover, the positive/negative sign of μ_B denotes its resulting up/down direction, respectively. We observe that Cu minority d orbitals are more occupied than the majority while the

Table 6.2: Spin up (↑), Spin Down (↓) electron population and local atom MM (μ_B) of Fe and Cu in $FeCu_{12}$(II) with Fe in the shell.

atom		VASP				SIESTA
		s	p	d	total	total
Fe	Spin Up (↑)	0.28	0.14	4.57	4.98	
	Spin Down (↓)	0.16	0.12	1.50	1.79	
	μ_B (↑)-(↓)	0.12	0.02	3.07	3.18	3.56
Cu	Spin Up (↑)	0.23	0.24	4.56	5	
	Spin Down (↓)	0.24	0.25	4.65	5.1	
	μ_B (↑)-(↓)	-0.01	0.00	-0.09	-0.10	-0.12

Cu s and p orbital show almost equivalent spin up and down percentage. On the contrary, Fe atom exhibits s, p and d majority electrons higher occupied than the minority, resulting in an AFM coupling between Cu and Fe atoms. In addition, comparing Fe-3d spin-up and down occupations we can observe that Fe-3d majority orbitals are almost fully occupied compared to the Fe-3d minority. This behaviour is reflected in the Fe PEDOS, fig. 6.4.(c) panel down, where the shift of Fe-3d down population toward high energy levels leaves Fe-3d minority orbitals less occupied than the Fe-3d majority. Our results are in agreement with the shell model displayed by the Billas et al. [20][37][40] in their experimental works. Furthermore, other theoretical results [147][148] reported that it is energetically favoured for majority-spin electrons to move toward the outside of the cluster, and that minority-spin electrons prefer the interior of the cluster where they might become the local majority.

To summarise, we investigated two diverse cases: $FeCu_{12}$(I) and $FeCu_{12}$(II). We discovered that configuration $FeCu_{12}$(I) is the most stable configuration while configuration $FeCu_{12}$(II) displays the highest Fe local MM, in good agreement with literature [72][70]. Focusing on the charge distributions, we found that s, p and d orbitals' occupation depends on the position of the Fe atom. In particular, when Fe occupies the shell, the difference between majority and minority charge is maximum, resulting in a large Fe MM. We concluded

that small coordination numbers favours large discrepancies in occupation between spin up and down populations, enhancing the local Fe MM. This behaviour is in agreement with theoretical and experimental results [40][147].

6.1.2 Fe_xCu_{55-x} (X= 0, 1, 6, 12, 42, 55), icosahedral clusters

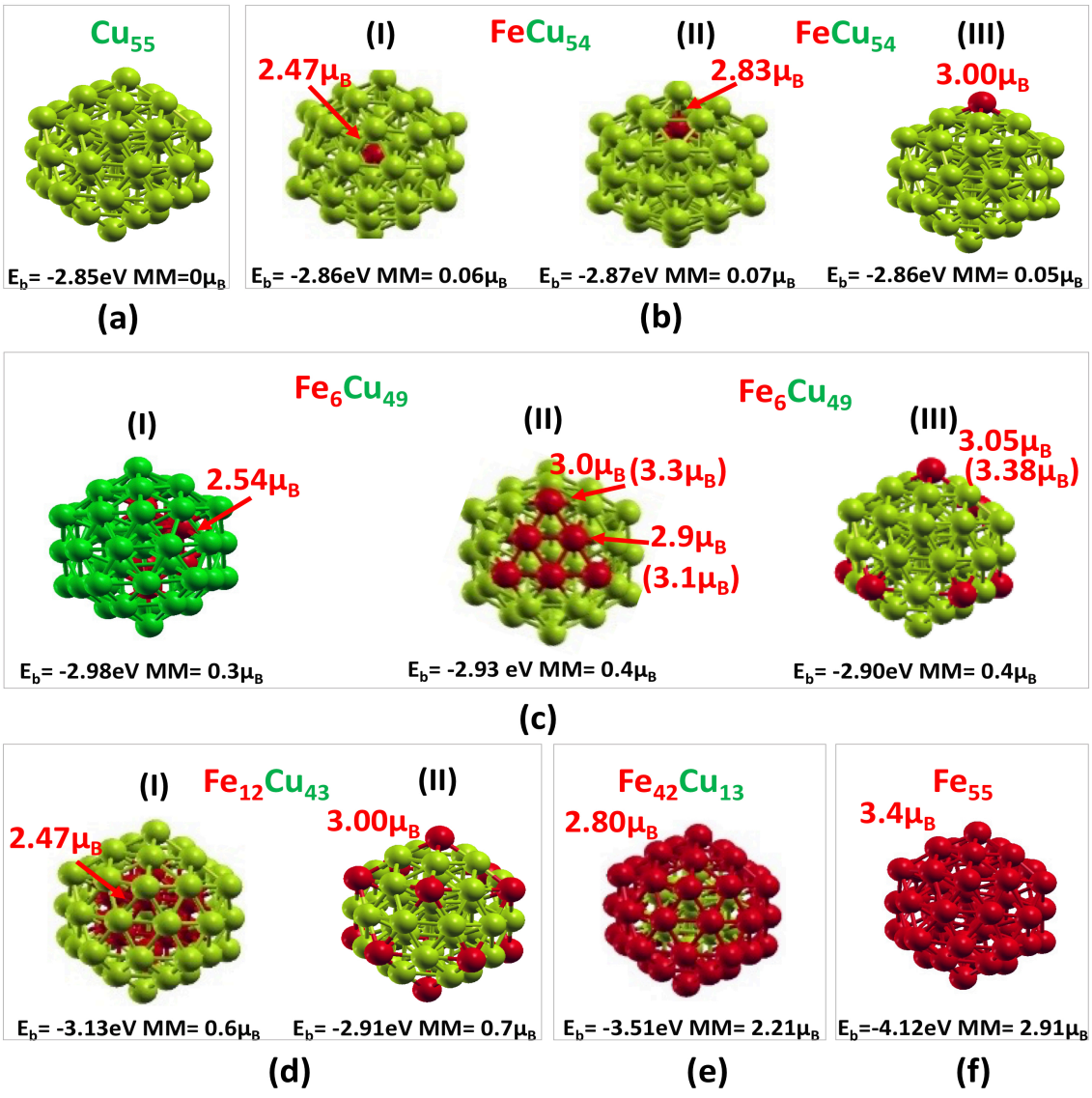

Figure 6.5: $Cu_{55-x}Fe_x$ (X= 0, 1, 6, 12, 42, 55): Binding energy, Fe and Cu local and average cluster's MM

In this section we continue our study, presenting the CuFe clusters with 55 atoms. Figure 6.5 reports the binding energy E_B, average cluster's MM and the local MM of the Fe_xCu_{55-x} (x = 0, 1, 6, 12, 42, 55) clusters. In figure 6.5.(a) Cu_{55} shows the absence ($0\mu_B$) of the average cluster's MM thus mimicking the bulk structure. We start our investigation with the simplest case of one Fe atom substituting a Cu atom in

Cu_{55}. In Fig.6.5.(b) we present: (I) the Fe atom in the cluster's center, (II) the Fe atom in the first shell and (III) the Fe in the second shell. We discover that $FeCu_{54}$ (III) is the most stable configuration, while the Fe local atom's MM increases from the center to the outermost shell ((I) 2.46μ_B, (II) 2.78μ_B, (III) 2.86 μ_B). Moreover, we observe the highest cluster average MM in $FeCu_{54}$ (II), when Fe is placed in the first shell.

Aiming in aving the same amount of Fe atoms in the triangle face and in the outermost shell, we substitute six Fe atoms. In figure 6.5.(c), we report three particular Fe_6Cu_{49} configurations: (I) Fe atoms in the first shell, (II) Fe atoms in the clusters' triangle face, (III) Fe atoms in the clusters' vertex. Our calculations yielded that the configuration with six Fe atoms aggregated together in the first shell, fig.6.5.(c).(I), is more stable than the Fe atoms in the first shell in random positions. Furthermore, we find energetically favoured the configuration having Fe atoms in the vertex sites, fig.6.5.(c).(II), than in the edge of the triangle face when six Fe atoms occupy the second shell. We found Fe_6Cu_{49} (II) arrangement as the most stable system. Interestingly, clusters with Fe in the outermost shell, Fe_6Cu_{49} (II) and Fe_6Cu_{49} (III) fig.6.5.(c), exhibit the highest Fe local MM.

Moreover, we considered the case where the first shell is fully occupied by Fe atoms resulting in a composition of $Fe_{12}Cu_{43}$, fig.6.5.(d).(I). This configuration is energetically favoured against the one when Fe atoms occupy the cluster's vertex in the outermost shell, fig.6.5.(d).(II). Additionally, we looked upon configuration fig.6.5.(e), where we replace all Cu atoms in the second shell with Fe. We found that the system becomes more stable than the others, in line with the 13 atom clusters reported in fig.6.2.

Finally, in fig.6.5, we observe that Fe_6Cu_{49} (III) shows the highest Fe local atom MM, while Fe_6Cu_{49} (II) is the most stable configuration with the same amount of Fe atoms. Aiming in findin the origin of this large Fe local atomic MM, in the next two paragraphs we will focus on these two configurations.

(II) Fe_6Cu_{49}: cluster having Fe triangle cluster's face

In figure 6.6.(a) we present the magnetic properties of Fe_6Cu_{49} with Fe atoms fully occupying the triangle cluster's face. We found a binding energy of -2.93eV and an average MM of 0.4μ_B. We observed that Fe atoms relax in two particular positions: the edge of the triangle face Fe(E_F) or the vertex Fe(V_F). The local atom MM of 2.98μ_B with VASP and 3.29μ_B by SIESTA for Fe(V_F) is higher than the corresponding local atom MM of 2.93μ_B with VASP and 3.12μ_B with SIESTA of Fe(E_F). Similarly to Fe_xCu_{13-x} (X=0-13) clusters, Cu atoms exhibit a MM close to zero.

In fig.6.6.(b) we present the spin up and spin down WF at the homo level. Focusing on the homo up WF, we found that the Fe atoms at the edge of the triangle face exhibit bonding hybridizations mostly between Fe-3d orbitals. Moreover, a small amount of charge is localized around the Cu surface atoms. We see that the Cu atoms in the outermost shell display orbital bonding hybridizations between Cu-3d and Cu-3d. In addition, the homo down WF exhibits enhanced charge localisation on Fe atoms, showing orbital bonding

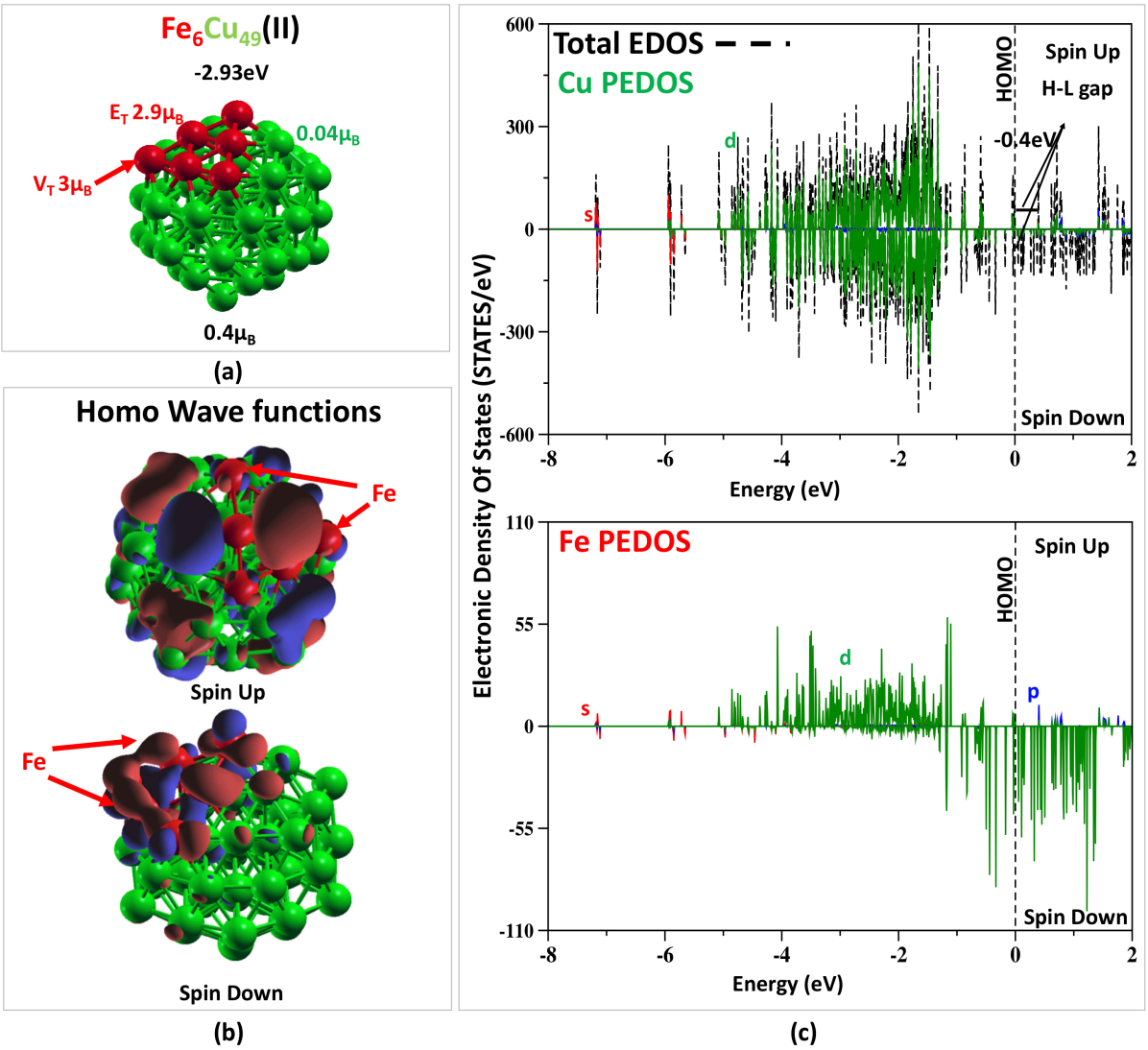

Figure 6.6: Fe_6Cu_{49}(II) cluster: (a) magnetic and structural properties. (b) Spin up and Spin down Wave Functions (WF) at the homo level. Red and blue area stand for the negative and positive charge of the WF.(c) Panel up: Total cluster EDOS (dashed black line); Cu PEDOS. Panel down: Fe PEDOS (the s, p and d PEDOS is presented with red, blue and green lines, respectively).

hybridizations mainly between Fe-3d orbitals.

In figure 6.6.(c) panel up, we present the total EDOS and Cu PEDOS. Focusing on the Cu PEDOS, Cu atoms always display a symmetric occupation in the spin up and down orbitals, giving zero contribution to the magnetic moment. In particular, we found Cu-3d electrons between -5eV and -1eV, while 4s electrons are close to -7eV. Fe atoms, in fig.6.6.(b) panel down, show Fe-3d spin up electrons between -5eV and -1eV. On the other hand, Fe-3d down are in the energy between -1.5eV and the homo state. In addition, Fe-4s are close to -7eV and between -6eV and -4eV in both spin up and down distributions. Finally, the H-L gap

is -0.4eV in the majority population, while it is close to zero in the spin down EDOS, giving half metallic features to this cluster.

In table 6.3, we present the majority (↑) and the minority (↓) Fe and Cu electron population and the local atom MM (μ_B) of Fe and Cu atoms. Additionally, the positive/negative sign of μ_B denotes its resulting up/down direction, respectively. Moreover, we name Cu(II) the Cu atoms in the second shell, Cu(I) the Cu atoms in the first shell, and Cu(C) the Cu atom at the center. First of all, we found that the position of the

Table 6.3: Spin up (↑), Spin Down (↓) Fe and Cu electron population and local atom MM (μ_B) of Fe_6Cu_{49} when Fe atoms are in the triangle cluster's face.

atom		VASP				SIESTA
		s	p	d	total	total
Fe(V_T)	Spin Up (↑)	0.26	0.14	4.54	4.94	
	Spin Down (↓)	0.22	0.12	1.62	1.96	
	(μ_B) (↑)-(↓)	0.04	0.02	2.92	2.98	3.29
Fe(E_T)	Spin Up (↑)	0.25	0.17	4.52	4.94	
	Spin Down (↓)	0.21	0.19	1.61	2.01	
	μ_B (↑)-(↓)	0.04	-0.02	2.91	2.93	3.12
Cu(II)S	Spin Up (↑)	0.23	0.26	4.62	4.98	
	Spin Down (↓)	0.23	0.26	4.58	4.94	
	μ_B (↑)-(↓)	0.00	0.00	0.04	0.04	0.05
Cu(I)S	Spin Up (↑)	0.45	0.21	4.62	4.98	
	Spin Down (↓)	0.45	0.21	4.58	4.94	
	μ_B (↑)-(↓)	0.00	0.00	0.04	0.04	0.05
Cu(C)	Spin Up (↑)	0.24	0.26	4.57	5.09	
	Spin Down (↓)	0.25	0.27	4.58	5.11	
	μ_B (↑)-(↓)	-0.01	-0.01	-0.01	-0.03	-0.02

Fe atom affects the orbital occupation. Specifically, Fe(V_T) atoms in the vertex of the triangle face show a local atom MM ($2.98\mu_B$) that is larger than Fe(E_T) atoms in the edge of the triangle ($2.93\mu_B$). It is worth to be noted that Fe(V_T) has a lower coordination number and smaller number of Fe first neighbours atoms than the Fe(E_T). Looking at the Fe(E_T) electron population, we observed that the minority 4p orbitals are more occupied than the majority, giving a lower Fe local atom MM. On the contrary, Fe(V_T) majority orbitals are more filled than the minority ones, resulting in a larger local atom MM than Fe(E_T). Concerning to Cu atoms, we observe a local atom MM close to zero. In particular, the Cu atoms in the first and second shell show local MM of $0.04\mu_B$, while Cu(C) shows a MM of $-0.02\mu_B$. Interestingly, Cu(C) exhibit s, p and d minority orbitals more occupied than the majority ones, resulting in AFM coupling with Cu atoms in the first shell. This behaviour is in line with $FeCu_{12}$(II) configurations and in agreement with the shell model display by Billas et al. in their experimental results [20][37][40] and other theoretical calculations [147][148].

(III) Fe_6Cu_{49}: Fe in cluster with the cluster's vertex

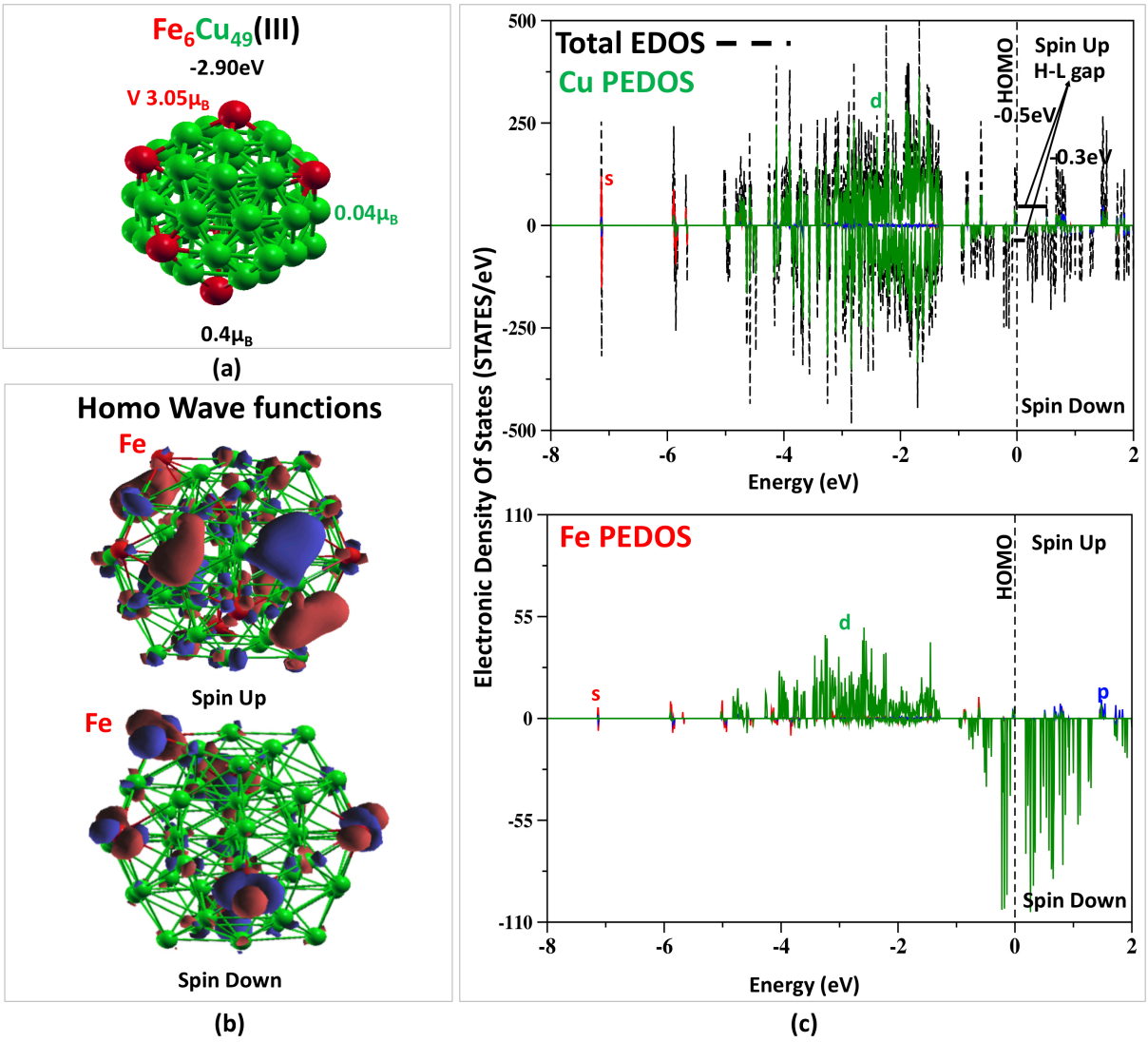

Figure 6.7: Fe_6Cu_{49}(III) cluster: (a) magnetic and structural properties. (b) Spin up and Spin down Wave Functions (WF) at the homo level. Red and blue area stand for the negative and positive charge of the WF.(c) Panel up: Total cluster EDOS (dashed black line); Cu PEDOS. Panel down: Fe PEDOS (the s, p and d PEDOS is presented with red, blue and green lines, respectively).

In figure 6.7.(a) we present the magnetic properties of Fe_6Cu_{49} when Fe atoms are in cluster's vertex. We found a binding energy of -2.90eV that it is higher than Fe_6Cu_{49}(I) and Fe_6Cu_{49}(II) in fig.6.5.(c). Additionally, Fe_6Cu_{49}(III) shows an average MM of $0.4\mu_B$ equal to Fe_6Cu_{49}(II) and higher than Fe_6Cu_{49}(I). Moreover, we observe an Fe local atom MM of $3.06\mu_B$ with VASP and $3.38\mu_B$ by SIESTA that is lower compared to the $FeCu_{12}$ ($3.19\mu_B$)

In figure 6.7.(b) we present the spin up and spin down WF at the homo level. Focusing on spin up WF, we observe a small amount of charge localised on Cu and Fe atoms. Additionally, only some Cu atoms in the outermost shell exhibit hybridisations bonding between Cu-3d and Cu-3d. On the contrary, similar to the Fe_6Cu_{49}(II), in the spin down WF the charge is localized only on the Fe atoms. In particular, we found $3d_{eg}$ electrons on Fe atoms, while Cu atoms remain almost totally unoccupied.

Focusing on Fe PEDOS 6.7.(c) panel down, we observe Fe-3d electrons between -5eV and -1.5eV in the majority populations. Moreover, minority orbitals are mainly between -1eV and the homo state. Concluding, we found a H-L gap of -0.5eV in the majority population and a H-L gap close to zero in the minority occupation, giving the half metallic character to the system.

In the table 6.3, we present the majority (↑) and the minority (↓) Fe and Cu electron population and local atom MM (μ_B) of Fe and Cu atoms. Additionally, the positive/negative sign of μ_B denotes its resulting up/down direction, respectively. Furthermore, we name Cu(II) Cu atoms in the second shell, Cu(I) Cu atoms in the first shell, and Cu(C) the Cu atom at the center.

Table 6.4: Spin up (↑), Spin Down (↓) Fe and Cu electron population and local atom MM (μ_B) of Fe_6Cu_{49} when Fe atoms are in the cluster's vertex.

atom		VASP				SIESTA
		s	p	d	total	total
Fe(V)	Spin Up (↑)	0.25	0.13	4.56	4.94	
	Spin Down (↓)	0.21	0.11	1.56	1.88	
	μ_B(↑)-(↓)	0.04	0.02	3.00	3.06	3.38
Cu(II)S	Spin Up (↑)	0.23	0.13	4.61	4.97	
	Spin Down (↓)	0.21	0.13	4.61	4.94	
	μ_B (↑)-(↓)	0.02	0.00	0.00	0.03	0.05
Cu(I)S	Spin Up (↑)	0.22	0.20	4.63	5.05	
	Spin Down (↓)	0.24	0.22	4.57	5.03	
	μ_B (↑)-(↓)	-0.02	-0.02	0.06	0.02	0.02
Cu(C)	Spin Up (↑)	0.24	0.26	4.59	5.09	
	Spin Down (↓)	0.25	0.27	4.59	5.11	
	μ_B (↑)-(↓)	-0.01	-0.01	0.00	-0.02	-0.02

Looking at the Fe-3d charge, we found a large imbalance between majority and minority population. As we have seen in the Fe PEDOS 6.7.(c) panel down, Fe-3d majority orbitals result in almost fully occupied (4.56↑), while Fe-3d minority charge appears less filled (1.56↓) due to the shift of the spin down orbitals towards higher energy levels. Additionally, we observe that in this configuration the Fe local atom MM ($3.06\mu_B$) is larger compared to the corresponding Fe local atom MM showed in the triangle face configuration ($2.97\mu_B$). On the other hand, we found a smaller Fe local atom MM compared with the Fe local atom MM in the $FeCu_{12}$ when Fe is in the shell ($3.19\mu_B$). Concerning the Cu atoms, Cu(II) shows a local atom MM of $0.05\mu_B$, while

for Cu(I) we found $0.02\mu_B$. Interestingly, we observe that in line with other theoretical results [147][148], the Cu(II) s and p majority orbitals are more occupied than the minority, while Cu(I) atoms reveal s and p minority orbitals that are more occupied than the majority ones. In addition, Cu(C) displays s, p and d spin down orbitals more occupied than the spin up, resulting in AFM coupling between Cu(C) and Cu(I) atoms as we found in the triangle face cluster.

To summarise, in this paragraph we have analysed two configurations: the Fe_6Cu_{49}(II) with Fe on the clusters' triangle face(II) and the Fe_6Cu_{49}(III) with Fe in the clusters' vertex. We found Fe_6Cu_{49} (II) as the most stable configuration, while Fe_6Cu_{49} (III) shows the highest Fe local atomic MM. Focusing on Fe electrons distribution, we observed two conditions that improve the Fe local MM. The first one is the larger imbalance between majority and minority bands. This condition is enhanced when Fe atoms occupy the clusters' vertex position while when Fe atoms are placed at the clusters' triangle face the spin up and down imbalance result decreased. The second one is related to the observation that the proximity of Cu atoms facilitate the occupation of the Fe majority orbitals, leaving the Fe minority population less filled. Concluding, in order to improve the Fe local MM we found two relevant conditions: a) the small coordination number and b) the presence of Cu atoms as first neighbours.

6.1.3 Fe_xCu_{147-x}

Aiming to find the conditions that can improve the Fe local atom MM, in the next two paragraphs we present: $Fe_{10}Cu_{137}$ where Fe atoms are in the cluster's face and $Fe_{12}Cu_{135}$ with Fe atoms in the cluster's vertex, in line with the previous sections.

(a) $Fe_{10}Cu_{137}$ cluster: Fe in the cluster's face

In figure 6.8.(a) we display the geometry of $Fe_{10}Cu_{137}$ when Fe atoms are in the cluster's triangle face. We calculated a binding energy of -3.09eV and we found an average MM of $0.19\mu_B$ that is smaller than Fe_6Cu_{49} (II) ($0.4\mu_B$). $Fe_{10}Cu_{137}$ presents three shells. We refer to the Cu atoms in the first with Cu(I)(S), to the Cu atoms in the second with Cu(II) and in the third with Cu(III), while we name the Cu at the center Cu(C). Additionally, this 147 atom cluster shows a bigger triangular face compared to the 55 atom icosahedral cluster. Therefore, Fe atoms display different local atom MM depending on their position in the triangle face. We name the Fe atoms in the vertex of the triangle with Fe(V_T), the Fe atoms in the triangle's edge with Fe(E_T) and finally with Fe(C_T) the Fe atoms in the triangle face's center. Focusing on the Fe local atom MM we found a value of $2.8\mu_B$ for Fe(V_T) with VASP and $3.1\mu_B$ with SIESTA, while Fe(C_T) exhibits $2.7\mu_B$ by VASP and $2.8\mu_B$ with SIESTA. It is worth to note that the Fe local atom MM is smaller than the corresponding Fe local atom MM in the 55 cluster. This behaviour highlights that when the number of atoms increases the local atom MM decreases converging towards the bulk value.

In figure 6.8.(b) we present the spin up and spin down WF at the homo level. Concerning to the spin up WF, we observe that the charge is homogeneously distributed on the cluster. On the contrary, the spin down

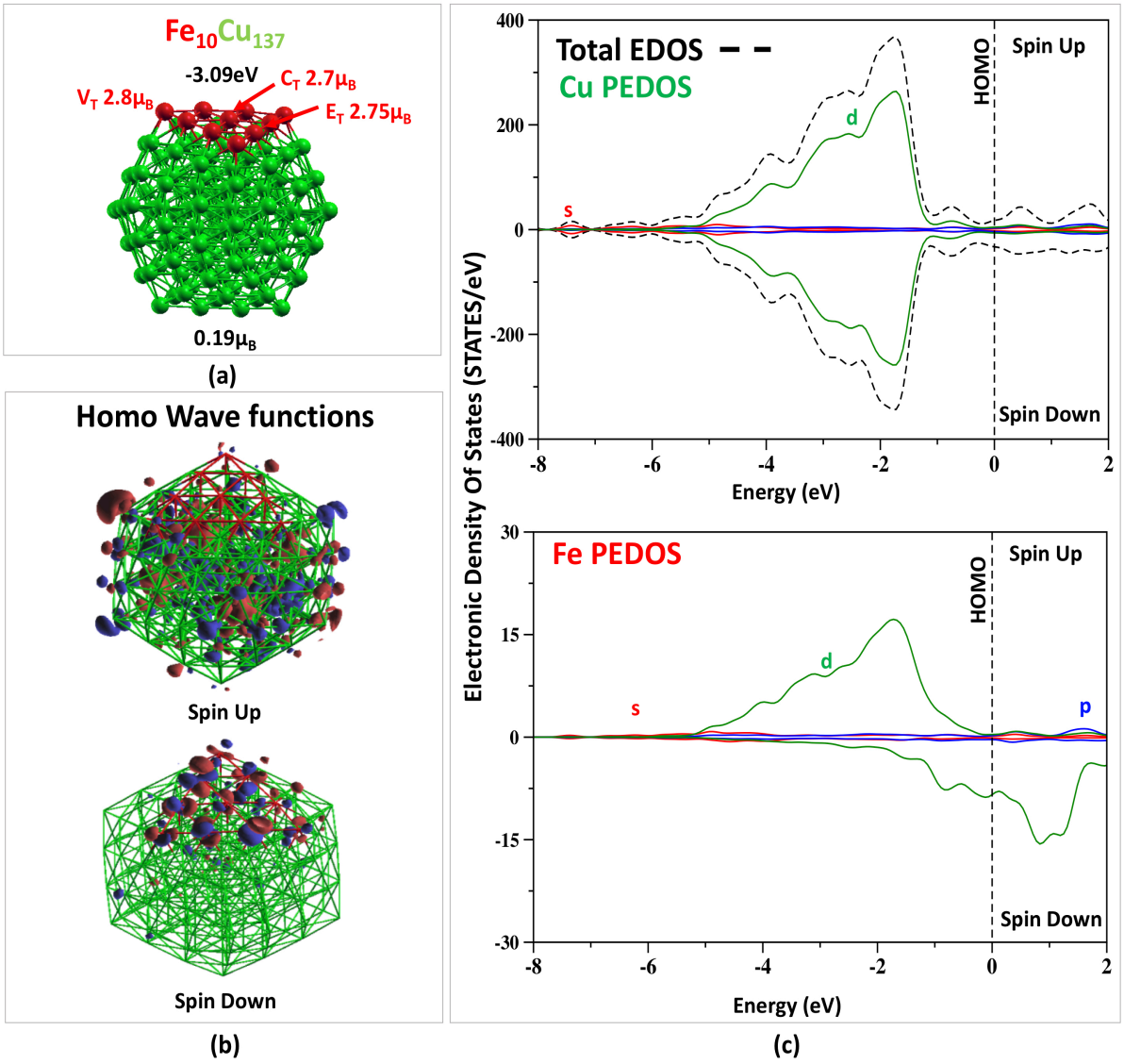

Figure 6.8: $Fe_{10}Cu_{137}$: (a) magnetic and structural properties. (b) Spin up and Spin down Wave Functions (WF) at the homo level. Red and blue area stand for the negative and positive charge of the WF.(c) Panel up: Total cluster EDOS (dashed black line); Cu PEDOS (the s, p and d PEDOS is presented with red, blue and green lines, respectively). Panel down: Fe PEDOS.

displays a charge distribution localised on Fe atoms, reflecting the same distribution in the corresponding Fe_6Cu_{49} triangle face.

In figure 6.8.(c) panel up we present the total EDOS and Cu PEDOS. Looking at the total EDOS, it worth's mentioning that for a large number of atoms in the clusters, the energy levels are broader than the small configurations, resulting in a band-like behaviour distribution. Concerning to the Fe atoms, fig.6.8.(c) panel

down, we found the presence of Fe-3d orbitals between -5eV and -1eV, while Fe-3d down are between -2eV and the homo state. Interestingly, we observe the same behaviour in the corresponding Fe_6Cu_{49} (II) reported in figure 6.6.(b) panel down. Finally, we did not observe any H-L gap and as a consequence this cluster has metallic character.

In the table 6.5, we present the majority (↑) and the minority (↓) Fe and Cu electron population and local atom MM (μ_B) of Fe and Cu atoms. In line with the 55 triangle face cluster, we observe that the Fe position

Table 6.5: Spin up (↑), Spin Down (↓) Fe and Cu electron population and local atom MM (μ_B) of $Fe_{10}Cu_{137}$ when Fe atoms are in the triangle cluster's face.

atom		VASP				SIESTA
		s	p	d	total	total
Fe(V_T)	Spin Up (↑)	0.26	0.14	4.49	4.89	
	Spin Down (↓)	0.23	0.13	1.73	2.09	
	μ_B(↑)-(↓)	0.03	0.01	2.76	2.80	3.09
Fe(E_T)	Spin Up (↑)	0.24	0.17	4.46	4.87	
	Spin Down (↓)	0.22	0.17	1.72	2.12	
	μ_B(↑)-(↓)	0.02	0.00	2.74	2.75	2.93
Fe(C_T)	Spin Up (↑)	0.23	0.17	4.44	4.84	
	Spin Down (↓)	0.23	0.22	1.69	2.14	
	μ_B(↑)-(↓)	0.00	-0.05	2.75	2.70	2.79
Cu(III)S	Spin Up (↑)	0.24	0.10	4.6	4.95	
	Spin Down (↓)	0.24	0.10	4.6	4.95	
	μ_B (↑)-(↓)	0.00	0.00	0.00	0.00	0.00
Cu(II)S	Spin Up (↑)	0.23	0.20	4.60	5.00	
	Spin Down (↓)	0.23	0.20	4.60	5.00	
	μ_B (↑)-(↓)	0.00	0.00	0.00	0.00	0.00
Cu(I)S	Spin Up (↑)	0.23	0.22	4.60	5.00	
	Spin Down (↓)	0.23	0.22	4.60	5.00	
	μ_B (↑)-(↓)	0.00	0.00	0.00	0.00	0.00
Cu(C)	Spin Up (↑)	0.26	0.26	4.60	5.11	
	Spin Down (↓)	0.26	0.26	4.60	5.11	
	μ_B (↑)-(↓)	0.00	0.00	0.00	0.00	0.00

in the triangle affects the electron population and consequently the local atom MM. Specifically, Fe(C_T) shows higher 4p minority occupation than the majority, while Fe(V_T) always displays spin up population more occupied than the spin down. For these reasons, we found a larger local MM on Fe(V_T) than Fe(C_T) corresponding cases. Additionally, Fe(E_T) exhibits an atomic MM of $2.75\mu_B$ with VASP and $2.93\mu_B$ with SIESTA. We observe that it is in the middle of the atomic MM of Fe(V_T) and Fe(C_T), due to the different spin up and down occupations shown in the table. Therefore, we observe that for both Fe(C_T) and Fe(V_T)

the local atom MM is lower than the corresponding Fe local atom MM in the Fe_6Cu_{49} cluster structure, in line with the decrement exhibited in the average cluster MM due to the dimension of the cluster. Concerning to the Cu atoms, for all Cu positions we found a symmetric occupation between majority and minority orbitals, in line with the reflecting the Cu PEDOS behaviour reported in figure 6.8.(c) panel up.

(b) $Fe_{12}Cu_{135}$: Fe in the cluster's vertex

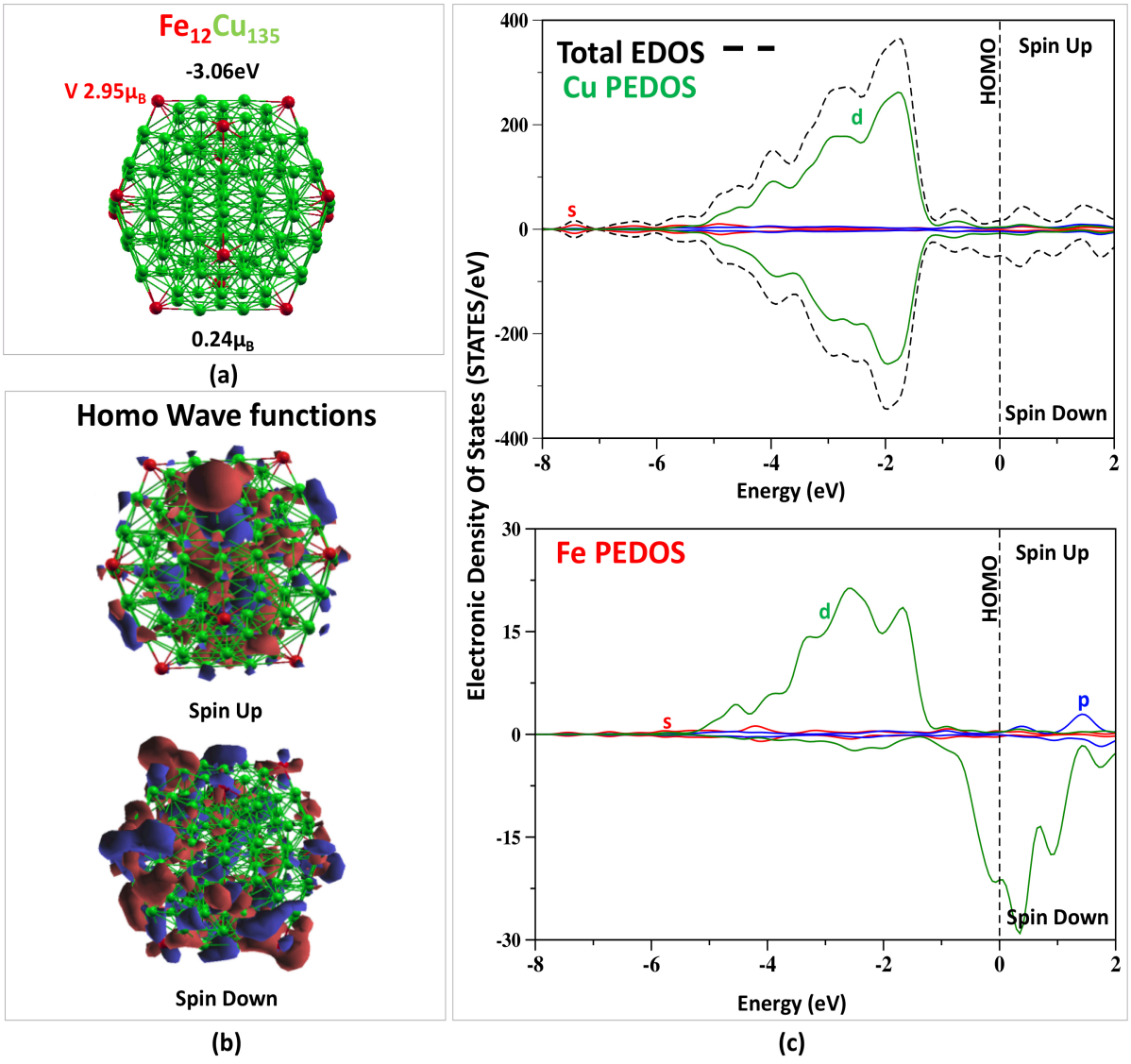

Figure 6.9: $Fe_{12}Cu_{135}$: (a) magnetic and structural properties. (b) Spin up and Spin down Wave Functions (WF) at the homo level. Red and blue area stand for the negative and positive charge of the WF.(c) Panel up: Total cluster EDOS (dashed black line); Cu PEDOS (the s, p and d PEDOS is presented with red, blue and green lines, respectively). Panel down: Fe PEDOS.

In figure 6.9.(a) we display the atomic structure of $Fe_{12}Cu_{135}$ when Fe atoms are in the cluster's vertex. We calculated a binding energy of -3.06eV and the average MM is approximately $0.24\mu_B$ that is lower than the average cluster MM exhibiting in Fe_6Cu_{49}(II) ($0.4\mu_B$). Furthermore, we found an Fe local atom MM of $2.95\mu_B$ with VASP and $3.26\mu_B$ with SIESTA smaller than $3.07\mu_B$ in the 55 atoms cluster and $3.19\mu_B$ in the smallest 13 atoms structure. It is worth to be noted that the Fe local atom MM decreases with the dimension of the cluster, converging towards the Fe bulk value $2.2\mu_B$, revealing that when we decrease the number of atoms the local atom MM increases.

In figure 6.9.(b) we present the spin up and down WF at the homo state. Referring to the homo spin up, we observe that the charge occupation is mainly located inside the cluster. On the other hand, the homo spin down WF shows the charge principally localized on the cluster's surface.

Fe PEDOS, in figure 6.9.(c) panel down, displays Fe-3d up electrons between -5eV and -1eV. Moreover, the Fe-3d spin down orbitals are between -0.8eV and the homo state. Additionally, Fe PEDOS in the triangle face in figure 6.8.(c) shows that the Fe-3d spin down orbitals are less localized (around -2eV and homo state) than the present arrangement. Moreover, we found that the Fe-3d spin up electrons are in the same interval (between -5eV and -1eV in fig.6.9.(c) panel down). We can attribute to this behaviour as the origin of the low Fe local atom MM exhibited in the triangle face structure.

In table 6.6, we present the majority ($\uparrow$) and the minority ($\downarrow$) Fe and Cu electron population and local atom MM (μ_B) of Fe and Cu atoms. Additionally, the positive/negative sign of μ_B denotes its up/down direction, respectively. Focusing on Fe-3d electron population, we observe that the spin up population is almost fully occupied ($4.9\uparrow$). In addition, Fe-3d spin down is only partially filled ($1.95\downarrow$), due to the shift of the minority orbitals towards hight energy levels, as reported in the Fe PEDOS in figure 6.9(c) panel down. In the corresponding triangle face cluster we found a distribution of Fe-3d electrons ($4.49\uparrow$) and ($1.73\downarrow$). We conclude that the distribution of the Fe atoms in the cluster's surface strongly affect the distribution of the charge between majority and minority orbitals. When Fe atoms occupy the vertex of the cluster and they have Cu atoms as first neighbours, the occupation of the majority orbitals is favoured. This increases the imbalance between the spin up and down occupation, enlarging therefore the Fe local atom's MM. Finally, we observe the symmetric distribution between majority and minority Cu orbitals as reported in the Cu PEDOS in figure 6.9(c) panel up and in line with the previous cluster structures.

In conclusion, in this paragraph we reported a comparison between two configurations: a) Fe atoms in the clusters' triangle face $Fe_{10}Cu_{137}$ and b) Fe atoms in the clusters' vertex $Fe_{12}Cu_{135}$. We found that $Fe_{10}Cu_{137}$ is the most stable structure while $Fe_{12}Cu_{135}$ is the system that shows the highest Fe local atom MM. Interestingly, in $Fe_{12}Cu_{135}$ the Fe local atom MM show a larger imbalance between majority and minority Fe orbitals occupation compared to the $Fe_{10}Cu_{137}$. In addition, 13 and 55 atoms PEDOS displayed localized and discrete energy states, while both $Fe_{10}Cu_{137}$ and $Fe_{12}Cu_{135}$ exhibit a band-like behaviour. Moreover, the overlap between valence and conduction bands provides metallic character to these clusters contrary to 13-atoms and 55-atoms FeCu clusters which reveal semi-metallic character, in line with previous

Table 6.6: Spin up (↑), Spin Down (↓) Cu and Fe electron population and local atom MM (μ_B) of $Fe_{12}Cu_{135}$ when Fe are in the cluster's vertex.

atom		VASP				SIESTA
		s	p	d	total	total
Fe(V)	Spin Up (↑)	0.25	0.12	4.53	4.90	
	Spin Down (↓)	0.21	0.11	1.63	1.95	
	μ_B(↑)-(↓)	0.04	0.01	2.90	2.95	3.26
Cu(III)S	Spin Up (↑)	0.22	0.08	4.6	4.94	
	Spin Down (↓)	0.22	0.09	4.6	4.95	
	μ_B (↑)-(↓)	0.00	-0.01	0.00	-0.01	0.00
Cu(II)S	Spin Up (↑)	0.23	0.20	4.60	5.05	
	Spin Down (↓)	0.24	0.22	4.57	5.03	
	μ_B (↑)-(↓)	-0.01	-0.02	0.00	0.02	0.00
Cu(I)S	Spin Up (↑)	0.23	0.22	4.60	5.05	
	Spin Down (↓)	0.23	0.22	4.60	5.05	
	μ_B (↑)-(↓)	0.00	0.00	0.00	0.00	0.00
Cu(C)	Spin Up (↑)	0.26	0.26	4.61	5.13	
	Spin Down (↓)	0.27	0.25	4.59	5.11	
	μ_B (↑)-(↓)	-0.01	0.01	0.02	0.02	0.00

studies [42][149]. Finally, we found that the Fe local atom MM increases when the number of first neighbour atoms is small and the element is Cu.

6.1.4 Fe_xCu_{309-x}

In this section we focus on 309 cluster atoms. We present: a) $Fe_{15}Cu_{294}$ where Fe atoms are in the cluster's face, and b) $Fe_{12}Cu_{297}$ with Fe atoms in the cluster's vertex, in line with the previous sections.

(a) $Fe_{15}Cu_{294}$ cluster: Fe in the triangle cluster's face

In figure 6.10.(a) we display the structural properties, the average cluster's MM and the Fe and Cu atomic MM. We observe a binding energy of -4.02eV and an average cluster's MM of $0.13\mu_B$ that is smaller than $Fe_{10}Cu_{137}(0.19\mu_B)$. In line with the previous sections the Fe atomic MM depends on the position of the Fe atoms in the triangle face. Also in this case, we refer with Fe(V_T) to the Fe atoms in the triangle's face in the outermost shell, with Fe(E_T) to the Fe atoms in the edge of the triangle and finally with Fe(C_T) the Fe atoms in the triangle's center. We found the highest Fe atomic MM when the Fe occupy the triangle's vertex Fe(V_T), whereas the lowest is displayed when the Fe atoms occupy the center of the triangle face, Fe(C_T). In addition, we found a similar Fe local MM value compared to the corresponding Fe local MM value with

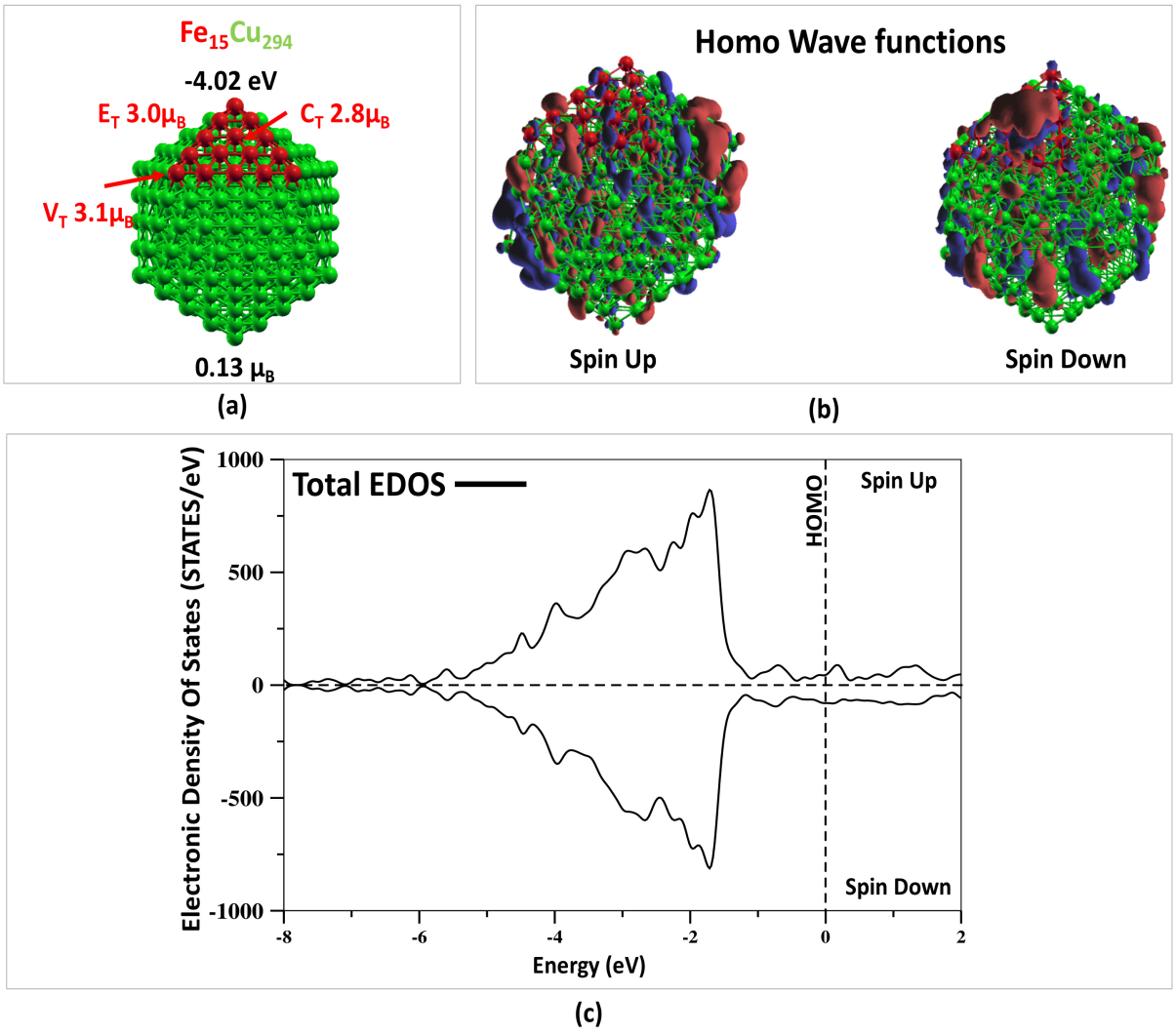

Figure 6.10: $Fe_{15}Cu_{294}$: (a) magnetic and structural properties. (b) Spin up and Spin down Wave Functions (WF) at the homo level. Red and blue area stand for the negative and positive charge of the WF. (c) Total cluster EDOS (dashed black line).

SIESTA in the $Fe_{10}Cu_{137}$ structure. Referring to the Cu atoms we observe that the Cu atomic MM is zero or close to zero in all inner shells.

Figure 6.10.(b) exhibits the spin up and down WF at the homo state. Focusing on the spin up, we found only a small amount of charge localized on Fe atoms. On the contrary, we observe hybridizations between Cu-3d orbitals in the outermost shell. Referring to the spin down WF, the charge distribution exhibits hybridizations between Fe-3d orbitals in the triangle face, whereas we observe only a slight amount of charge on Cu atoms.

In figure 6.10.(c) we present the total $Fe_{15}Cu_{294}$ EDOS. In line with the previous sections the total EDOS shows a band-like behaviour and a symmetric spin up and down distribution. In particular, we observe that

both majority and minority electrons are between -5eV and -1.5eV, revealing the no magnetic character of this cluster. Also in this case the cluster assumes a metallic character, while no gap is found in the majority and minority total EDOS.

In table 6.7, we present the majority (↑) and the minority (↓) Fe and Cu electron population and local atom MM (μ_B) of Fe and Cu atoms. Comparing the spin up and down populations in Fe(V_T), Fe(E_F) and Fe(C_T)

Table 6.7: Spin up (↑), Spin Down (↓) Fe and Cu electron population and local atom MM (μ_B) of $Fe_{15}Cu_{294}$ when Fe atoms are in the triangle cluster's face.

SIESTA			
atom	Spin Up (↑)	Spin Down (↓)	μ_B(↑)-(↓)
Fe(V_T)	8.75	5.62	3.13
Fe(E_T)	8.62	5.64	2.98
Fe(C_T)	8.48	5.69	2.79
Cu(III)S	5.42	5.45	-0.03
Cu(II)S	5.50	5.52	-0.02
Cu(I)S	5.50	5.50	0.00
Cu(C)	5.50	5.50	0.00

we found that Fe(V_T) shows the highest occupation in the spin up orbitals. Conversely, the Fe(V_T) spin down states are less filled compared to the Fe(E_T) and Fe(C_T), resulting in the highest Fe atomic MM. Referring to the Cu atoms, they display almost the same occupation in the spin up and spin down orbitals, giving no imbalance between the majority and minority occupation. This behaviour reflects the trend shown in the total EDOS in figure 6.10.(c), confirming the no magnetic character of Cu atoms.

(b) $Fe_{12}Cu_{297}$: Fe at the cluster's vertex

In figure 6.11.(a) we report the binding energy, the average cluster's MM and the Fe and Cu atomic MM. We observe a binding energy of -4.03eV, resulting in a little smaller value compared with the $Fe_{15}Cu_{294}$ configuration(-4.02eV). In addition, we found an average cluster's MM of $0.09\mu_B$ that it is lower compared with $Fe_{15}Cu_{294}$ ($0.13\mu_B$). Referring to the Fe atomic MM, in this configuration the Fe atoms exhibit a larger value compared to the corresponding Fe atomic MM shown in the $Fe_{15}Cu_{294}$ cluster.

In figure 6.11.(b) we present the spin up and down WF at the homo state. Concerning to the spin up WF, we observe that the charge is located only to the Cu atoms in the outermost shell. We can see Cu-3d and Cu-3d bonding hybridization between Cu first neighbour atoms. Moving on the spin down WF, the charge is mainly localized on Fe showing 3d orbitals. In addition, Cu-3d and Fe-3d bonding hybridization are shown between Fe and Cu atoms at the outest shell.

Finally, figure 6.11.(c) displays the $Fe_{12}Cu_{297}$ total EDOS. Also in this case, in agreement with the $Fe_{15}Cu_{294}$ configuration, we observe a symmetric behaviour in the spin up and down EDOS. Specifically, we found the

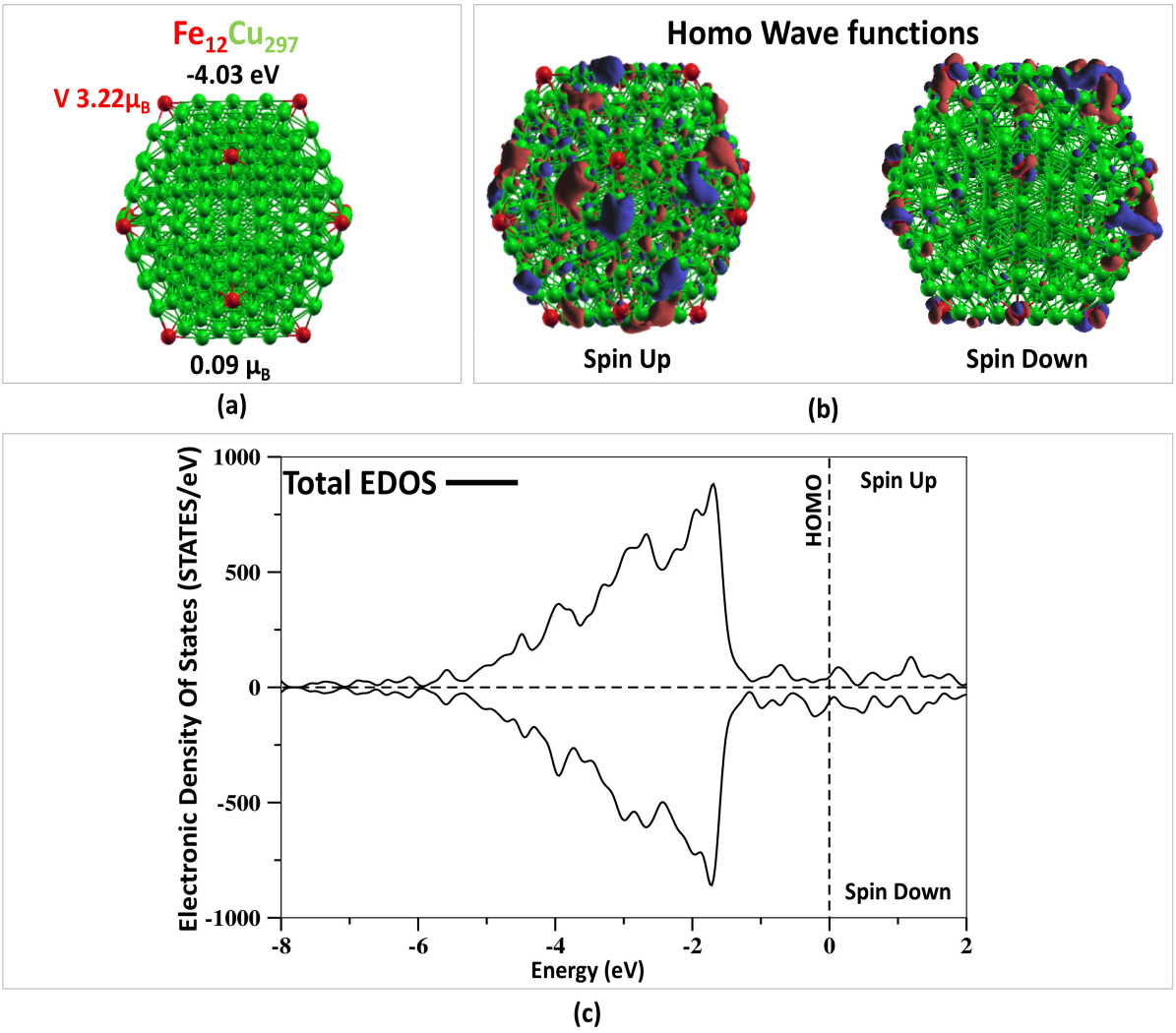

Figure 6.11: $Fe_{12}Cu_{297}$: (a) magnetic and structural properties. (b) Spin up and Spin down Wave Functions (WF) at the homo level. Red and blue area stand for the negative and positive charge of the WF. (c) Total cluster EDOS (dashed black line).

spin up and down electrons enclosed by -5eV and -1.5eV, revealing the non magnetic character of Cu atoms. In addition, we can note that the position of the Fe atoms does not affect the character of the FeCu clusters with 309 atoms.

In table 6.8, we present the majority (↑) and the minority (↓) Fe and Cu electron population and local atom MM (μ_B) of Fe and Cu atoms.
Focusing on Fe(V), we observe an occupation of 8.99(↑) in the majority occupation that it is higher than the spin up occupation (8.75(↑)) of Fe(V_F) in $Fe_{15}Cu_{294}$. In addition, we found an occupation of 5.77(↓) in the minority orbitals while the corresponding Fe(V_F) value in $Fe_{15}Cu_{294}$ is 5.62(↓). As a result, we observe that in this case the imbalance between spin up and down population is bigger than in the previous $Fe_{15}Cu_{294}$

Table 6.8: Spin up (↑), Spin Down (↓) Fe and Cu electron population and local atom MM (μ_B) of $Fe_{12}Cu_{297}$ when Fe atoms are in the vertex of the cluster.

SIESTA			
atom	Spin Up (↑)	Spin Down (↓)	μ_B(↑)-(↓)
Fe(V)	8.99	5.77	3.22
Cu(III)S	5.48	5.54	-0.06
Cu(II)S	5.49	5.51	-0.02
Cu(I)S	5.49	5.51	-0.02
Cu(C)	5.51	5.51	0.00

structure, resulting in a larger Fe atomic MM. Interestingly, Cu atoms show minority orbitals more occupied than the majority in the inner cluster's shell, giving an AFM coupling with the Fe atoms in the outermost. Additionally, Cu atoms in the third shell display an atomic MM higher than in the $Fe_{15}Cu_{294}$ triangle case, while in both case the Cu atom at the cluster's center does not exhibit any atomic MM.

In conclusion, in line with the previous sections we have analyzed two FeCu clusters with 309 atoms. We present: a) $Fe_{15}Cu_{294}$, Fe atoms are in the triangle's face in the outermost shell, b) $Fe_{12}Cu_{297}$, Fe atoms occupy the cluster's vertex. We found that configuration a) is more stable than b). In addition, configuration a) exhibits an average clusters MM larger than b), while the highest Fe local MM is displayed in configuration b). By comparing the Cu atom MM, we can see that in configuration b), the Cu atoms in the inner shell assume a local atom MM higher than in configuration a). For this reason configuration a) shows an average cluster's MM larger than b). Finally, both a) and b) configurations exhibit a metallic character and a band-like behaviour distribution in the total EDOS.

6.2 FeCo

In line with the purpose of this thesis investigate Fe-based systems with no magnetic and magnetic elements, in the next section we will analyze FeCo icosahedral clusters. Co is known to be magnetic in its hcp bulk system, showing a magnetic moment of 1.7μ_B

6.2.1 Fe_xCo_{13-x} (X=0-13)

We begin this paragraph by presenting the electronic structure of the smallest 13 atoms icosahedral cluster. In figure 6.12 we present the binding energy, average cluster's MM and the local MM of the $Co_{13-x}Fe_x$ (X = 0-13) structures.

Co_{13} displays an average and atomic MM close to 2.30μ_B that is higher compared to the Co bulk MM, in agreement with other theoretical works [79][42]. We proceed by substituting one Fe atom in the Co_{13}

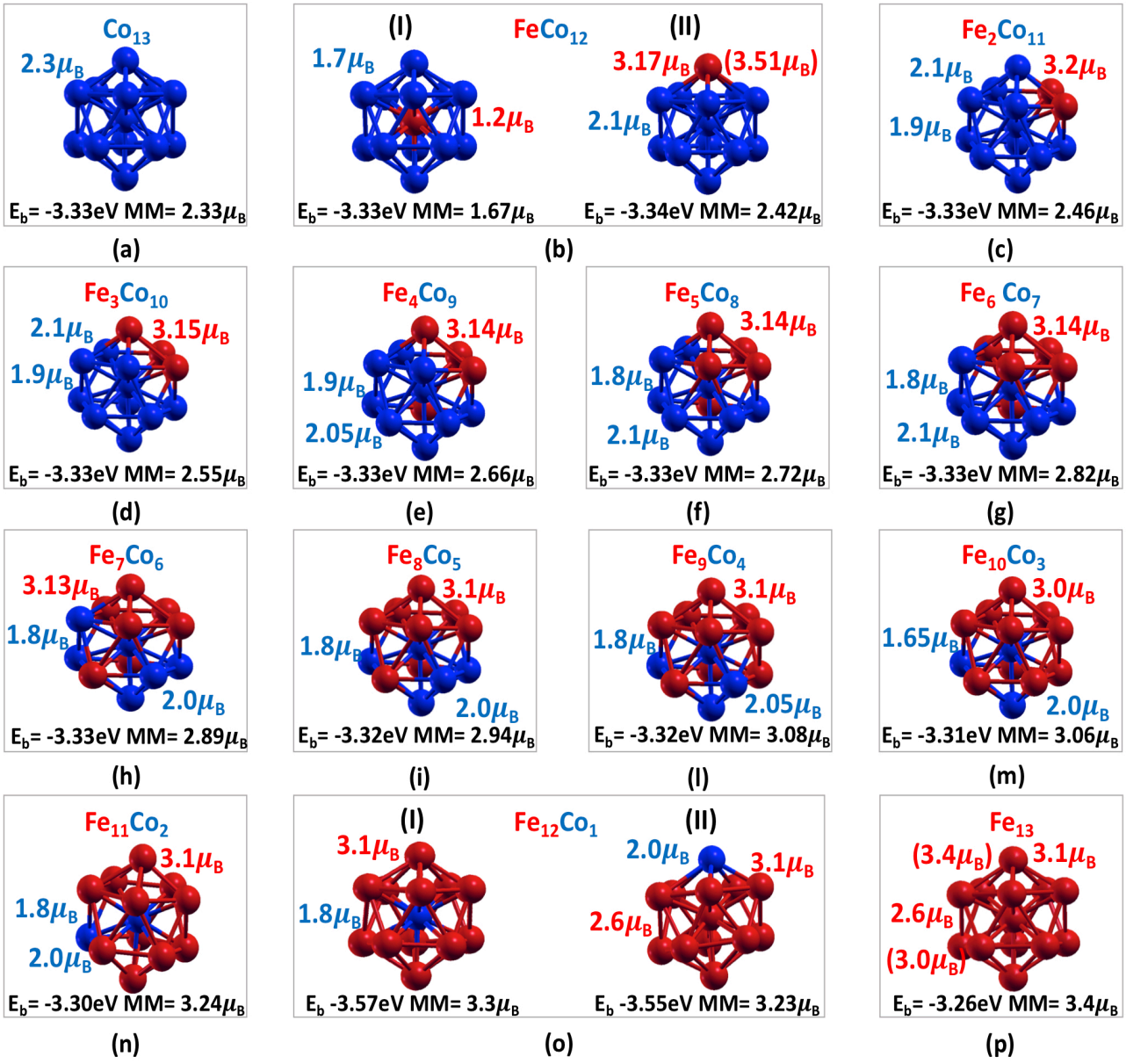

Figure 6.12: Binding energy E_b (eV), clusters' average MM(μ_B) and Fe and Cu local atomic MM (μ_B) of Fe_xCo_{13-x} (X = 0-13)

clusters, as reported in the previous section about FeCu systems. In figure 6.12.(b), we present the two $FeCo_{12}$ configurations: (I) Fe atom occupy the center, (II) Fe is a shell atom. We observe approximately the same binding energy in both configurations (I) and (II), on the contrary the average cluster MM change substantially depending on the Fe atom position. In fact, we found that configuration (I) shows an Fe atomic MM of $1.2\mu_B$ and a Co atomic MM of $1.7\mu_B$. On the contrary, configuration (II) exhibits an Fe atomic MM of $3.17\mu_B$ and a Co atomic MM of $2.1\mu_B$, resulting in an higher average cluster MM and an Fe and Co local MM than the configuration (I).

In Fe_2Co_{11}, fig.6.12.(c), we found that the system with both Fe atoms in the shell shows a binding energy smaller than the configuration where one Fe atom occupies the center and the other one is placed in the shell. Specifically, we calculated a binding energy of -3.33eV for the case reported in fig.6.12.(c), while we found a binding energy of -3.32eV in the second one. For this reason, we continue our analysis on clusters with all Fe atoms in the shell.
Adding the Fe atoms' amount, from Fe_3Co_{10} (d) to $Fe_{11}Co_2$ (n) in fig.6.12, the binding energy remain almost the same for all cases under study. Furthermore, due to the enlargement of the Fe local MM contributions the average MM increases, as we expect since we enhance the number of Fe atoms.

In figure 6.12.(o) we display the two possibilities of $Fe_{12}Co_1$: (I) Co atom occupy the central site, (II) Co is a shell atom. The most stable configuration and the highest average cluster MM is shown when Co is the central atom.

In line with FeCu systems, in figure 6.12 we observe that the Fe local atomic MM is the highest for the $FeCo_{12}$(II) cluster. Accordingly with the previous section, we will further investigate the FeCo(I) and FeCo(II) clusters aiming in understanding the reason for this local Fe MM difference.

(I) $FeCo_{12}$: Fe atom in the cluster's center

In figure 6.13.(a) we present the structural and the magnetic properties of $FeCo_{12}$(I) when Fe atom occupies the central site. We found a binding energy of -3.33eV while the average cluster's MM is $1.7\mu_B$ for both VASP and SIESTA. Fe-Co interatomic distances are $2.34\mathring{A}$ with VASP and approximately $2.48\mathring{A}$ with SIESTA. Interestingly, the Fe-Co interatomic distances in $FeCo_{12}$(I) cluster and the corresponding Co-Co interatomic distances in Co_{13} show almost the same value close to $2.33\mathring{A}$. On the contrary, in $FeCu_{12}$(I) cluster the Fe-Cu interatomic distance is $2.41\mathring{A}$, revealing the importance of the host cluster element in the enlargement of the cluster's radius. Moreover, the average Co-Co distances are $2.42\mathring{A}$ with VASP and $2.60\mathring{A}$ with SIESTA. Additionally, Fe displays an atomic MM of $1.21\mu_B$ with VASP and $2.77\mu_B$ with SIESTA, while Co exhibits an atomic MM of $1.75\mu_B$ with VASP and $2.22\mu_B$ with SIESTA.

Proceeding with figure 6.13.(b), we show the spin up and down Wave Function (WF) at the homo state. We observe Co-3d electrons remain or close to Co atoms or hybridize with the Co-3d electrons of the first Co neighbour. In addition, Fe-3d electrons are localized on Fe, resulting in antibonding between Fe the other Co atoms. In the spin down WF the charge is localized on Co atoms, whereas no charge is shown on Fe atom at the homo state.

Figure 6.13.(c) panel up displays the total EDOS and Co PEDOS. Focusing on Co PEDOS, we observe Co 3d-up electrons enclose to -5eV and -1eV while 4s-up are at the lower energy around -7eV and -5eV. Additionally, Co 3d-down charge is between -5eV and the homo state. Turning on Fe PEDOS, fig.6.13.(b) panel down, Fe 4s-up and down electrons are close to -7eV, whereas Fe 4p electrons are between -5eV and -4eV. Moreover, Fe 3d-up are betwixt -5eV and -1eV, while Fe 3d-down are almost by to the -4eV, -1.5eV

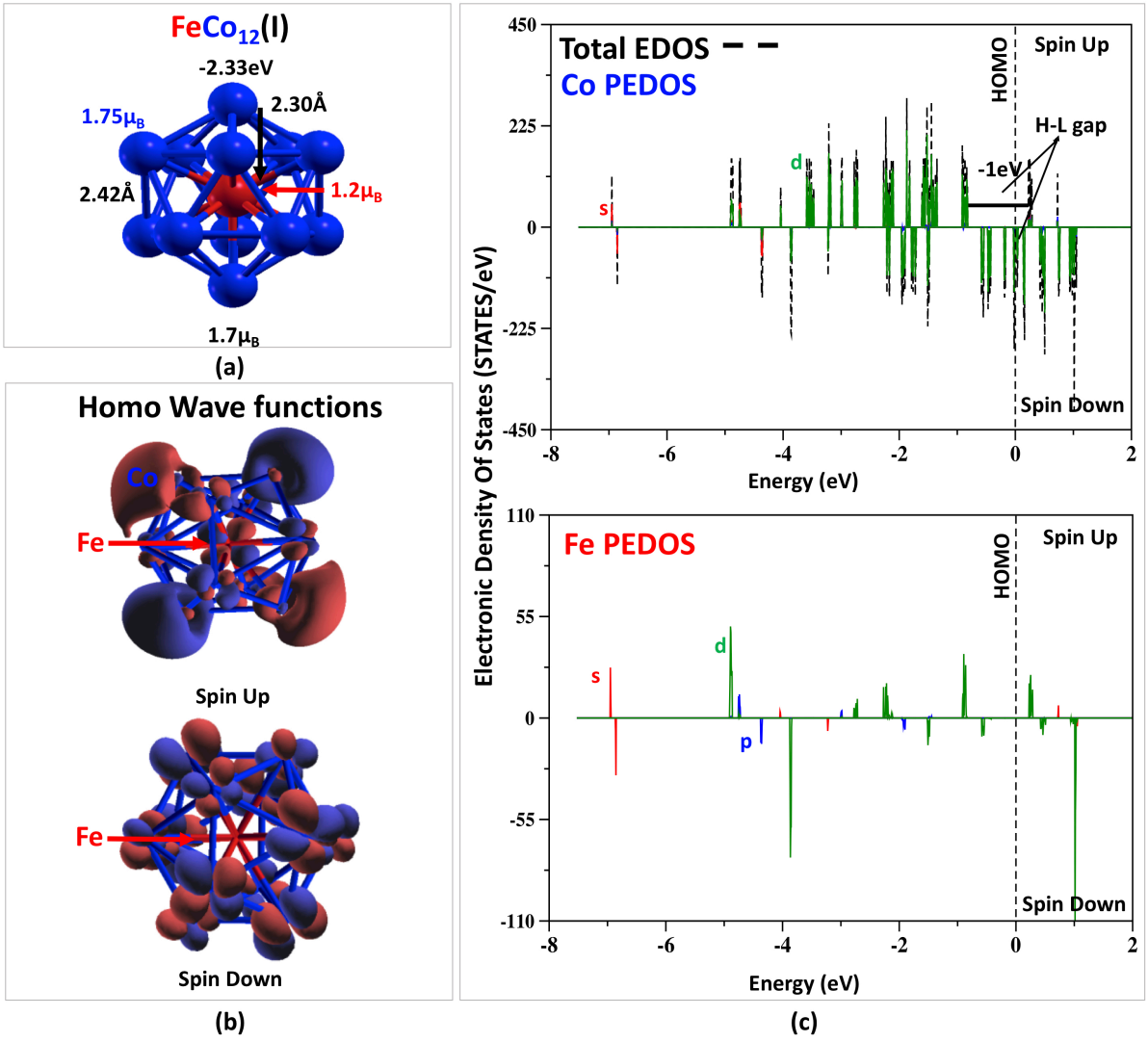

Figure 6.13: $FeCo_{12}$(I) cluster: (a) magnetic and structural properties. (b) Spin up and Spin down Wave Functions (WF) at the homo level. Red and blue area stand for the negative and positive charge of the WF.(c) Panel up: Total cluster EDOS (dashed black line); Cu PEDOS (the s, p and d PEDOS is presented with red, blue and green lines, respectively). Panel down: Fe PEDOS.

and -0.5eV. Finally, we calculated a large H-L gap approximately of -1eV, in the majority total EDOS while no gap is shown in the minority. The presence of H-L gap in the spin up and the absence in the spin down suggests a half-metallic character for this cluster.

In the table 6.9, we present the majority (↑) and the minority (↓) Fe and Co electron population and local atom MM (μ_B) of Fe and Co atoms. Furthermore, the positive/negative sign of μ_B denotes its resulting up/down direction, respectively. Focusing on Fe and Co s and p charge, we found that the minority charge

Table 6.9: Spin up (↑), Spin Down (↓) electron population and local atom MM (μ_B) of Fe and Co in $FeCo_{12}$(I) with Fe in the center.

atom		VASP				SIESTA
		s	p	d	total	total
Fe	Spin Up (↑)	0.28	0.35	3.88	4.51	
	Spin Down (↓)	0.30	0.41	2.59	3.30	
	μ_B (↑)-(↓)	-0.02	-0.06	1.29	1.21	2.77
Co	Spin Up (↑)	0.22	0.14	4.93	4.93	
	Spin Down (↓)	0.24	0.15	3.18	3.19	
	μ_B (↑)-(↓)	-0.02	-0.01	1.75	1.72	2.22

are more occupied than the majority. On the contrary, both Fe and Co 3d spin up orbitals are more filled than the spin down. In particular as reported in 6.13.(c) panel up, we observed that the Co-3d spin down electrons are shifted toward higher energy level compared to the Co-3d spin up. For this reason, Co 3d minority orbitals results less occupied than the majority, resulting in a Co atomic MM of 1.75μ_B. The same behaviour is reported for the Fe atom in fig. 6.13.(c) panel down, originating an atomic MM of 1.21μ_B

(II) $FeCo_{12}$: Fe atom in the cluster's shell

In figure 6.14.(a) we present the structural and the magnetic properties of $FeCo_{12}$(II) when Fe atom occupies the shell site. For simplicity we name Co(C) the Co atom that occupies the cluster's center and Co(S) the Co atom at the shell. We calculate a binding energy of -3.34eV and an average cluster MM of 2.42μ_B that is higher than the average cluster MM previously found for the $FeCo_{12}$(I). Additionally, we observe an Fe atomic MM of 3.17μ_B with VASP and 3.51μ_B with SIESTA. Furthermore, Co(S) shows an atomic MM of 2.10μ_B with VASP and 2.25μ_B with SIESTA, while Co(C) exhibit an atomic MM of 1.92μ_B with VASP and 1.89μ_B with SIESTA. Fe-Co(C) interatomic distance are 2.29$\AA$ with VASP and 2.41$\AA$ with SIESTA, whereas we calculate 2.49$\AA$ by VASP and 2.63$\AA$ with SIESTA between Fe and Co(S).

Figure 6.14.(b) displays the spin up and down Wave Function (WF) at the homo state. In both cases Co and Fe WF show $3d_{t2g}$ and $3d_{eg}$ orbitals localized on the own atom, resulting in antibonding between Co-Co atoms, and Co-Fe atoms respectively.

Proceeding with 6.14.(c) panel up, we report the total EDOS and Co PEDOS. We observe Co-4s up and down electrons close to -7eV, while Co-3d up are enclosed between-5eV and -1eV. In addition, Co-3d down are between -4eV and the homo state. Fe atom in fig.6.14.(c) panel down, shows 3d-up electrons in the interval between -5eV and -1eV, while Fe 4s-up are at the lower energy, around -5eV. Furthermore, Fe spin down electrons are moved toward high energy compared to the majority population. Specifically, we found Fe 3d-down between -2eV and the homo state, whereas Fe 4s-down around -4eV. Finally, we calculated a H-L gap of -0.5eV in the majority population and a gap close to zero in the minority charge, revealing the half-metallic character of the this cluster.

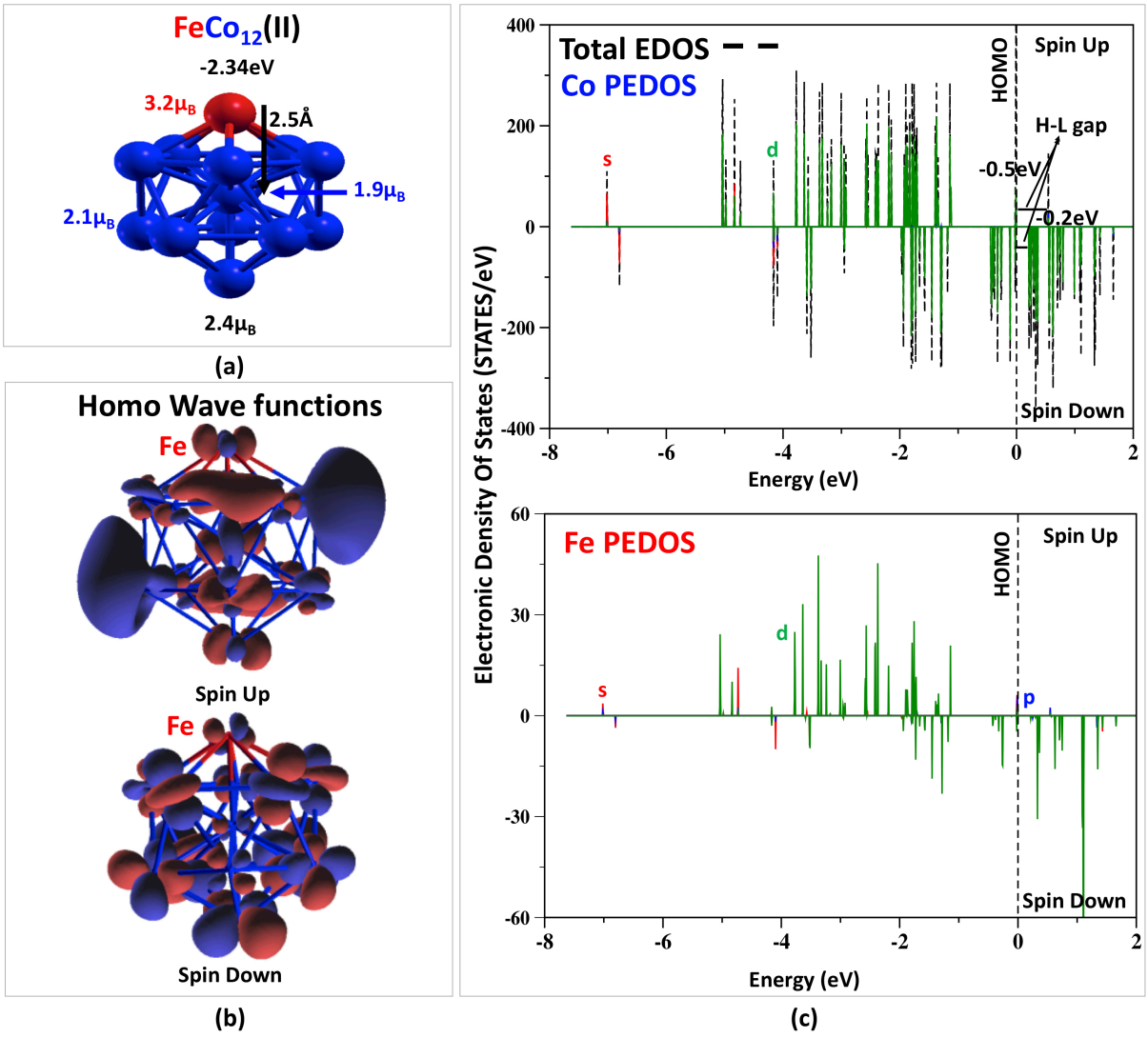

Figure 6.14: $FeCo_{12}$(II) cluster: (a) magnetic and structural properties. (b) Spin up and Spin down Wave Functions (WF) at the homo level. Red and blue area stand for the negative and positive charge of the WF.(c) Panel up: Total cluster EDOS (dashed black line); Cu PEDOS (the s, p and d PEDOS is presented with red, blue and green lines, respectively). Panel down: Fe PEDOS

In the table 6.10, we present the majority (↑) and the minority (↓) Fe and Co electron population and local atom MM (μ_B) of Fe and Co atoms. Furthermore, the positive/negative sign of μ_B denotes its resulting up/down direction, respectively.

Looking at the Fe we observe that, differently from the $FeCo_{12}$(I) configuration table6.9, in this case s, p and d majority orbitals are more occupied than the minority. We can attribute this behaviour to the reduce Fe coordination number when Fe is in the shell, giving a larger Fe atomic MM compared to the Fe atomic

Table 6.10: Spin up (↑), Spin Down (↓) electron population and local atom MM (μ_B) of Fe and Co in $FeCo_{12}$(II) with Fe in the shell.

atom		VASP				SIESTA	REF
		s	p	d	total	total	
Fe	Spin Up (↑)	0.28	0.18	4.59	5.06		
	Spin Down (↓)	0.21	0.13	1.54	1.87		
	μ_B (↑)-(↓)	0.07	0.05	3.05	3.19	3.51	3.63[82] 3.34[21]
Co(C)	Spin Up (↑)	0.26	0.31	4.71	5.28		
	Spin Down (↓)	0.29	0.38	2.68	3.36		
	μ_B (↑)-(↓)	-0.03	-0.07	2.03	1.92	1.89	
Co(S)	Spin Up (↑)	0.27	0.17	4.61	5.05		
	Spin Down (↓)	0.22	0.12	2.63	2.97		
	μ_B (↑)-(↓)	0.05	0.05	1.98	2.08	2.25	2.36[82] 2.8[21]

MM when Fe is in the center ($1.21\mu_B$). Moving on Co(S), we see that s, p and d spin up states are more occupied than the down, resulting in a higher Co atomic MM than the corresponding Co atomic MM showing in the $FeCo_{12}$(I) cluster. Contrary to Co(S), Co(C)-s and p majority orbitals are less filled than the minority, lowering the Co(C) atomic MM.

In conclusion, we investigated two diverse $FeCo_{12}$ arrangements: $FeCo_{12}$(I) and $FeCo_{12}$(II) clusters. We found that $FeCo_{12}$(II) configuration is the energetically favoured. Interestingly, we observed that the Fe atom position in the cluster affects both the average cluster MM and the Fe and Co atomic MM. As reported in the table 6.9, when the Fe atom occupies the center we found that s and p minority orbitals are more filled than the majority for both Fe and Co atoms. In addition, we observed a small imbalance between 3d spin up and down electrons, resulting in a low atomic MM. On the contrary, in the configuration $FeCo_{12}$(II) table 6.10, Co(S) and Fe exhibit s and p majority populations more occupied than the minority. Moreover, the spin up-down imbalance is more pronounced in this configuration than in the configuration (I), increasing the Co and Fe atomic MM. These results are in good agreement with literature [82].

6.2.2 Fe_xCo_{55-x} (X= 0, 1, 6, 12, 42, 55) icosahedral clusters

In this paragraph we continue our study presenting FeCo clusters with 55 atoms. In figure 6.15 we show the binding energy, average cluster's MM and the local MM of Fe_xCo_{55-x} (X= 0, 1, 6, 12, 42, 55). In figure 6.15.(a) Co_{55} exhibits an average cluster's MM close to $1.9\mu_B$ that is higher compared to the Co bulk value. Mimicking the FeCu analysis, we begun the FeCo clusters investigation by substituting only one Fe atom in the Co_{55}. Fig6.15.(b) displays: (I) Fe atom in the cluster's center, (II) Fe atom in the first shell and (III) Fe atom in the second shell. We observe that all configurations show the same binding energy and the same average cluster's MM. Concerning to the Fe atomic MM, we find that the higher value is exhibited in the configuration (III), ((I) $2.34\mu_B$, (II) $2.53\mu_B$, (III) $2.99\mu_B$), when the Fe atom is the outermost shell in line with the FeCu case.

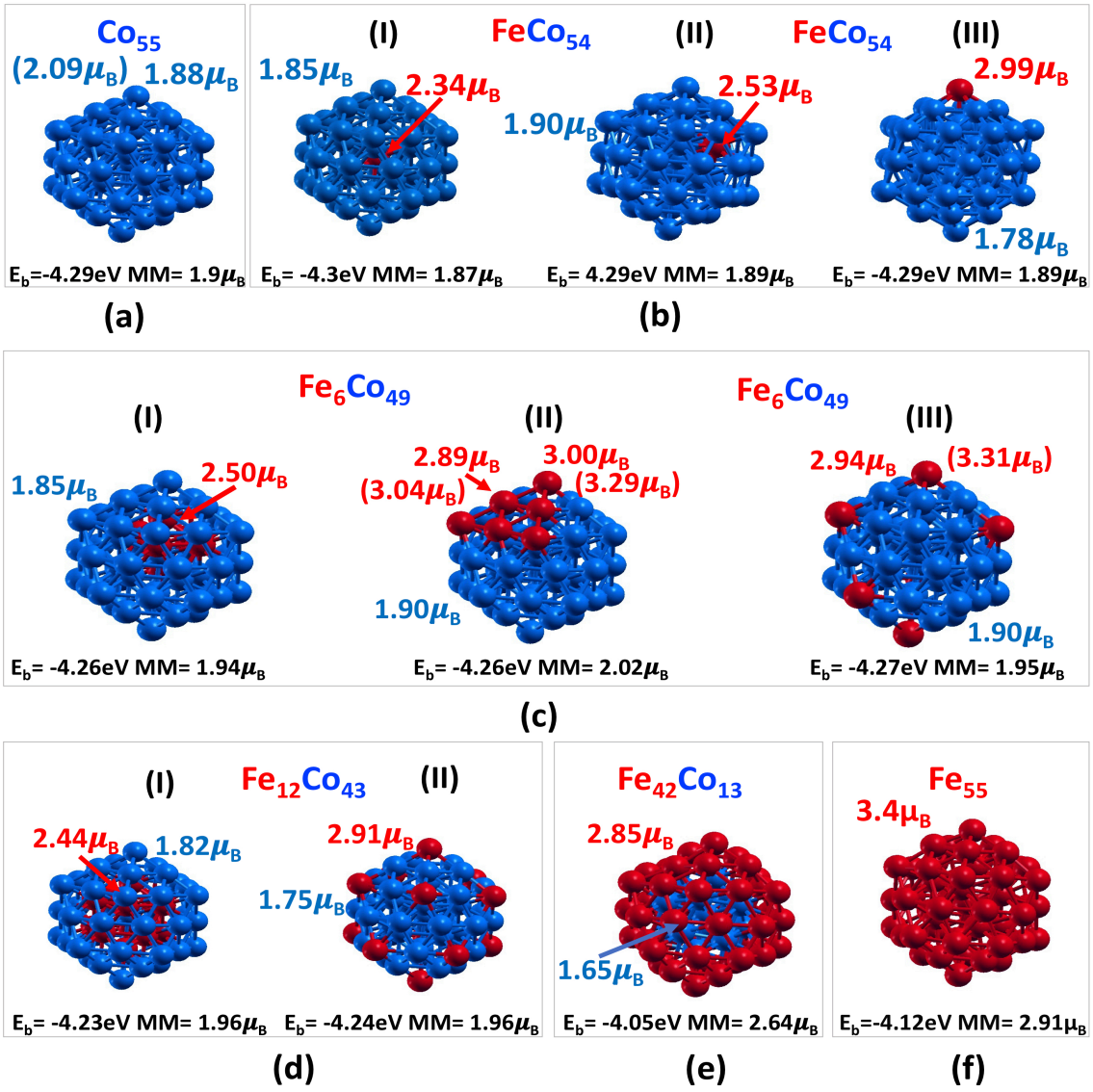

Figure 6.15: $Co_{55-x}Fe_x$ (X= 0, 1, 6, 12, 42, 55): Binding energy, Fe and Co local and average cluster's MM

As reported in FeCu structures, we proceed our work by substituting six Fe atoms. In figure 6.15.(c) we display three different Fe_6Co_{49} configurations: (I) Fe atoms in the first shell, (II) Fe atoms in the triangle face, (III) Fe atoms in the clusters' vertex. We found the same binding energy for all three cases, observing that the position of the Fe atoms do not affect the stability of the clusters. On the contrary we notice that configuration (II) shows the highest average cluster MM, ((I) $1.94\mu_B$, (II) $2.02\mu_B$, (III) $1.95\mu_B$).

Furthermore, we continue by replacing 12 Fe atoms in the Co_{55} as presented in figure 6.15.(d). We report two different $Fe_{12}Co_{43}$ configurations: (I) all Fe in the first shell, (II) all Fe in the cluster's vertex. We see that the Fe atom positions do not affect the binding energy and the average clusters' MM of the system. Interestingly, configuration $Fe_{12}Co_{43}$(I) exhibits an Fe atomic MM smaller than $Fe_{12}Co_{43}$(II), whereas we observe the

reverse behaviour for the Co atoms. Additionally, covering all second shell with Fe atoms, fig6.15.(e), we find a smaller binding energy compared with others FeCo clusters, underlying the low stability of this cluster. On the contrary, we observe an increase average cluster MM due to the larger amount of the Fe atoms.

Finally, we observe that Fe_6Co_{49}(II) and Fe_6Co_{49}(III) display the highest Fe atomic MM. In order to compare the Fe magnetic properties in FeCo and FeCu structures and aiming in finding the origin of this large Fe local atomic MM, in the next two sections we will focus on these two configurations.

(II) Fe_6Co_{49} : Fe in the cluster's triangle face

In figure 6.16.(a) we display the magnetic properties of Fe_6Co_{49} with Fe atoms fully occupying the triangle cluster's face. We found a binding energy of -4.26eV and an average MM of $2.02\mu_B$. We observe that Fe and Co local MM strictly depends on the the occupied positions. For simplicity we name Fe(V_T) the Fe atoms in the triangle's vertex face and Fe(E_T) the Fe atoms in the edge triangle's face. In the same way, we indicate with Co(V_T) and Co(E_T) the corresponding Co atoms in the vertex and in the edge in the Co triangle face in the outest cluster's shell. In line with Fe_6Cu_{49}(II), we found that Fe(V_T) shows a local MM larger than Fe(E_T). Specifically, we calculate a local MM of $3.00\mu_B$ for Fe(V_T) and a local MM of $2.89\mu_B$ for Fe(E_T). Referring to the Co atoms, we observe a local MM of $1.97\mu_B$ for Co(V_T) and $1.87\mu_B$ for Co(E_T). Interestingly, we found a Co local MM of 1.75 μ_B in the first shell, and a Co local MM of $1.73\mu_B$ in the cluster's center.

Fig.6.16.(b) reports the spin up and spin down WF at the homo level. Focusing on the homo up WF, we observe that Fe atoms in the edge of the triangle face show bonding hybridisation between Fe-3d and Co-3d orbitals. In addition, Co-3d and Co-3d hybridizations are displayed between Co atoms in the outermost shell. Spin down WF exhibits Fe-3d orbital hybridizations among Fe atoms in the center of the triangle face. Moreover, Co-3d and Co-3d bonds are displayed between all Co atoms in the second shell.

In fig.6.16.(c) panel up, we present the total EDOS and Co PEDOS. Referring to the Co PEDOS, we observe Co-3d up charge in the energy interval between -6eV and close to the Homo state, while 4s up orbitals are at lower energy close to -7eV and -6eV. Co-3d down electrons are at the higher energy levels compared to the corresponding Co-3d up, they are between -4.5eV and the homo state, whereas 4s down are around -7eV and -5eV. Moving to the Fe fig.6.16.(c) panel down, we can see that Fe 3d up orbitals are enclosed between -5eV and the homo state, while Fe 3d down electrons are at the higher energy between -3eV and the homo state. In addition, a small contribution of Fe 4s electrons is given at lower energy compared to the Fe 3d orbitals, around -7eV and -5eV. Finally, we calculated a H-L gap in the majority EDOS of -0.6eV, while no gap is shown in the minority revealing the half metallic character of this cluster.

In table 6.11, we present the majority (↑) and the minority (↓) Fe and Co electron population and the local atom MM (μ_B) of Fe and Co atoms. Additionally, the positive/negative sign of μ_B denotes its resulting up/down direction, respectively. Moreover, we name with Co(I) the Co atom in the first shell and Co(C) the Co atom in the cluster's center. Focusing on Fe atoms, we observe that the edge triangle's position favours the minority orbitals occupation, in line with Fe_6Cu_{49}(II) structures. Specifically, we can note that when an Fe atom occupy the edge of the triangle face the imbalance between spin up and down orbitals is

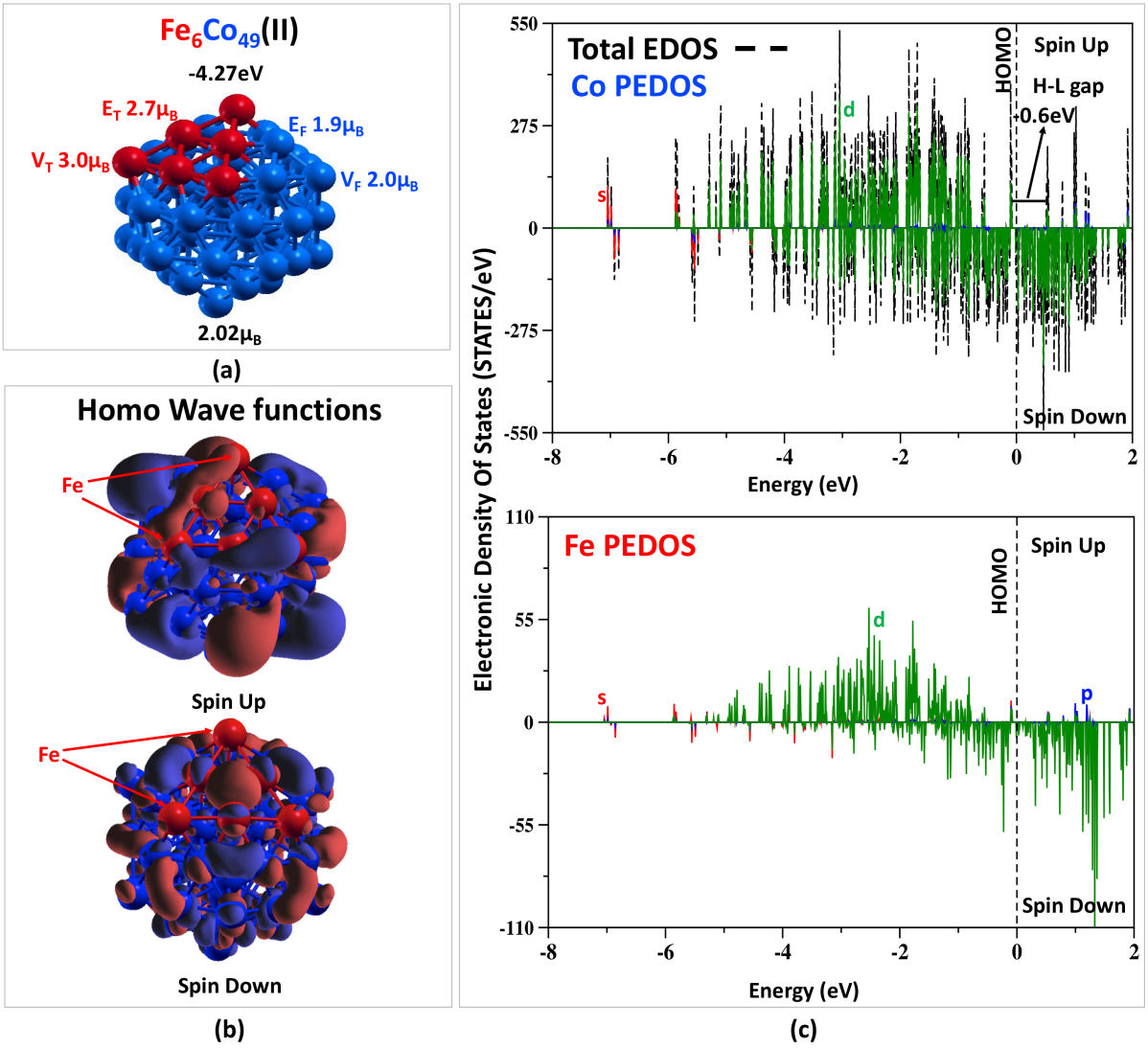

Figure 6.16: Fe_6Co_{49}(II) cluster: (a) magnetic and structural properties. (b) Spin up and Spin down Wave Functions (WF) at the homo level. Red and blue area stand for the negative and positive charge of the WF.(c) Panel up: Total cluster EDOS (dashed black line); Co PEDOS. Panel down: Fe PEDOS (the s, p and d PEDOS is presented with red, blue and green lines, respectively).

smaller than when the Fe atom is placed in the vertex. Fe(V_T) shows an occupation of 4.97(↑) and 1.97(↓) while Fe(E_T) exhibits 4.95(↑) and 2.06(↓) resulting in a lower Fe atomic MM for the first one. Similarly, we observe the same behaviour for the Co atoms. In particular, we report an occupation of 5.00(↑) and 3.03(↓) for Co(V_T) whereas Co(E_T) displays an occupation of 5.00(↑) and 3.12(↓) In addition, in line with the shell model presented by Billas et al. [20][37][40], we notice that Co(I)S and Co(C) present s and p minority orbitals more occupied than the majority, further lowering the Co local atomic MM compared to the value in the outermost shell.

Table 6.11: Spin up (↑), Spin Down (↓) Fe and Cu electron population and local atom MM (μ_B) of Fe_6Cu_{49} when Fe atoms are in the triangle cluster's face.

atom		VASP				SIESTA
		s	p	d	total	total
Fe(V_T)	Spin Up (↑)	0.27	0.14	4.56	4.97	
	Spin Down (↓)	0.23	0.13	1.61	1.97	
	(μ_B) (↑)-(↓)	0.04	0.01	2.95	3.00	3.29
Fe(E_T)	Spin Up (↑)	0.24	0.18	4.53	4.95	
	Spin Down (↓)	0.23	0.20	1.63	2.06	
	μ_B (↑)-(↓)	0.01	-0.02	2.90	2.89	3.04
Co(V_T)	Spin Up (↑)	0.27	0.14	4.59	5.00	
	Spin Down (↓)	0.24	0.01	2.67	3.03	
	μ_B (↑)-(↓)	0.03	0.02	1.92	1.97	2.09
Co(E_T)	Spin Up (↑)	0.22	0.18	4.60	5.00	
	Spin Down (↓)	0.22	0.21	2.70	3.12	
	μ_B (↑)-(↓)	0.00	-0.03	1.90	1.87	1.87
Co(I)S	Spin Up (↑)	0.26	0.28	4.56	5.10	
	Spin Down (↓)	0.28	0.33	2.75	3.35	
	μ_B (↑)-(↓)	-0.02	-0.05	1.81	1.75	1.80
Co(C)	Spin Up (↑)	0.27	0.32	4.56	5.15	
	Spin Down (↓)	0.29	0.36	2.77	3.44	
	μ_B (↑)-(↓)	-0.02	-0.04	1.79	1.73	1.80

(III) Fe_6Co_{49}: Fe in the cluster's vertex

In figure 6.17.(a) we present the magnetic properties of Fe_6Co_{49} when Fe atoms are in cluster's vertex. We calculate a binding energy of -4.27eV slightly smaller than the binding energy of Fe_6Co_{49}(II) (-4.26eV), while we observe a cluster average MM of 1.95μ_B lower compared to the corresponding Fe_6Co_{49}(II)'s cluster average MM. Referring to Fe the local atomic MM we found a value of 2.94μ_B with VASP and 3.31μ_B with SIESTA. Moreover, the Co atoms in the second shell report a local atomic MM of 1.90μ_B with VASP and 2.07μ_B whit SIESTA when they are at the vertex of the triangle face, whereas they show a local atomic MM of 1.80μ_B with VASP and 1.87μ_B with SIESTA when they are at the edge of the triangle. Furthermore, in line with the Fe_6Co_{49}(II) results we notice a decremease in the Co atomic MM for the Co in the first shell and at the cluster's center. Specifically, we find a Co atomic MM of 1.72μ_B with VASP and 1.78μ_B with SIESTA for the Co atoms in the cluster's first shell, while a value of 1.56μ_B with VASP and 1.79μ_B with SIESTA is exhibited for the Co at the center of the cluster.

Figure 6.17.(b) displays the spin up and spin down WF at the homo level. Differently from Fe_6Co_{49}(II), spin up WF exhibits a small amount of charge localized on both Co and Fe atoms in the outermost shell. Moreover, the spin down shows hybridizations bonding between Co-3d and Co-3d, whereas no charge is

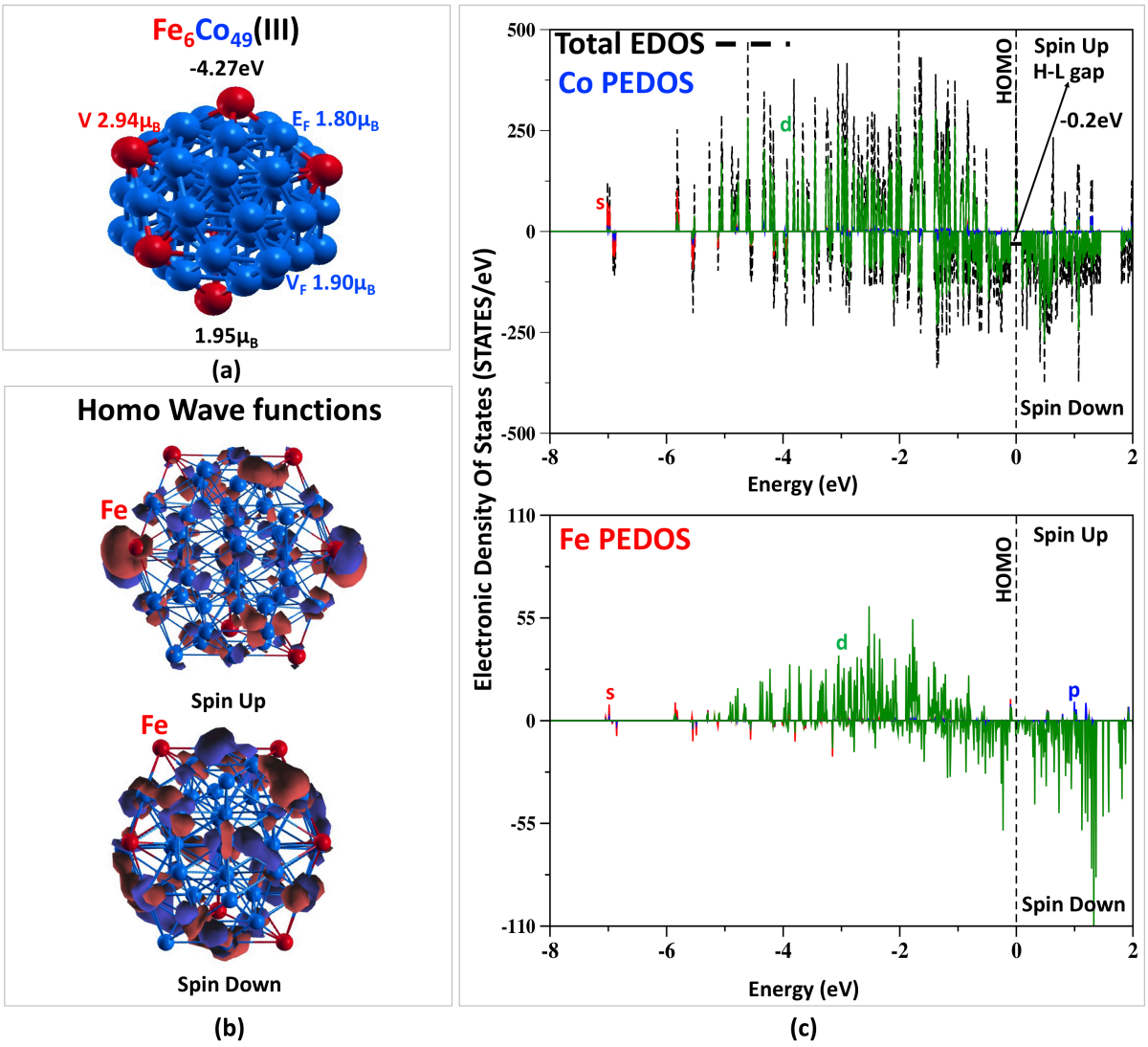

Figure 6.17: Fe_6Co_{49}(III) cluster: (a) magnetic and structural properties. (b) Spin up and Spin down Wave Functions (WF) at the homo level. Red and blue area stand for the negative and positive charge of the WF.(c) Panel up: Total cluster EDOS (dashed black line); Co PEDOS. Panel down: Fe PEDOS (the s, p and d PEDOS is presented with red, blue and green lines, respectively).

localized close to the Fe atoms.

In figure 6.17.(c) panel up, we report the total EDOS and Co PEDOS. Referring to the Co PEDOS we notice that Co-3d up electrons are enclosed between -5eV and the homo state, while Co 4s up are at lower energy levels between -7eV and -6eV. Co-3d down orbitals are shifted toward higher energy levels between -4.5eV and close to the homo state. Focusing on Fe fig.6.17.(c) panel down, Fe-3d up electrons are between -5eV and -1eV, while Fe-3d down electrons are between -3eV and next to the homo state. In addition, Fe 4s up and down orbitals occupy low energy levels around -7eV and -4.5eV. Finally, we observe no H-L gap in

the majority occupation, while a H-L gap of -0.2eV is shown in the minority charge, giving a half metallic character to this cluster.

In table 6.12, we present the majority (↑) and the minority (↓) Fe and Co electron population and the local atom MM (μ_B) of Fe and Co atoms.

Table 6.12: Spin up (↑), Spin Down (↓) Fe and Cu electron population and local atom MM (μ_B) of Fe_6Cu_{49} when Fe atoms are in the triangle cluster's face.

atom		VASP				SIESTA
		s	p	d	total	total
Fe(V)	Spin Up (↑)	0.26	0.14	4.55	4.95	
	Spin Down (↓)	0.23	0.14	1.64	2.01	
	(μ_B) (↑)-(↓)	0.03	0.00	2.91	2.94	3.31
Co(V_T)	Spin Up (↑)	0.25	0.14	4.57	4.96	
	Spin Down (↓)	0.24	0.12	2.70	3.06	
	μ_B (↑)-(↓)	0.01	0.02	1.87	1.90	2.07
Co(E_T)	Spin Up (↑)	0.24	0.17	4.55	4.97	
	Spin Down (↓)	0.24	0.21	2.71	3.17	
	μ_B (↑)-(↓)	0.00	-0.04	1.84	1.80	1.87
Co(I)S	Spin Up (↑)	0.26	0.28	4.55	5.09	
	Spin Down (↓)	0.27	0.33	2.77	3.37	
	μ_B (↑)-(↓)	-0.01	-0.05	1.78	1.72	1.78
Co(C)	Spin Up (↑)	0.27	0.32	4.48	5.06	
	Spin Down (↓)	0.30	0.35	2.86	3.50	
	μ_B (↑)-(↓)	-0.03	-0.03	1.62	1.56	1.79

Focusing on Fe(V) we observe that s and d majority orbitals are more occupied than the minority. However, the p orbitals exhibit the same amount of charge in both spin up and spin down states. For these reasons, we observe a lower Fe(V) atomic MM compared to the corresponding Fe(V_T) of the configuration Fe_6Co_{49}(II). Making a comparison between Fe_6Cu_{49}(III) and Fe_6Co_{49}(III), we notice that the Fe local MM of the first structure is larger compared to the second one. We discovered that the presence of the Cu atoms in the first neighborhood favours the imbalance between spin up and spin down occupation resulting in a larger Fe local atomic MM.

Referring to Co(V_T) and Co(E_T), the table 6.12 displays almost the same s and p orbitals occupation exhibited in table 6.11 for the Fe_6Co_{49}(II). In addition, the 3d states present a smaller imbalance between spin up and down occupation compared to it. As a result, we find a Co(V_T) and Co(E_T) local atomic MM lower than the Co(V_T) and Co(E_T) local atomic MM of Fe_6Co_{49}(II). Finally, we observe s and p minority orbitals more occupied than the majority in Co(I)S and Co(C), whereas the 3d majority is always more filled for both atoms. These results reflect the same behaviour of the Fe_6Co_{49}(II) structure and they are in line with the shell model presented by the by Billas et al. [20][37][40].

In conclusion, we investigated two different Fe_6Co_{49} configurations: (II) Fe atoms in the triangle clusters' surface and (III) Fe atoms in the clusters' vertex. We observed almost the same binding energy for both configurations, discovering that the Fe atoms positions do not affect the stability of the cluster. However, we found that Fe_6Co_{49}(II) shows a larger average cluster's MM compared to the Fe_6Co_{49}(III). In fact, we have noticed that the Co atomic MM contribution is lower in the Fe_6Co_{49}(III) structure than in the Fe_6Co_{49}(II), resulting in a larger average cluster's MM in the second one. Additionally, according to the experimentally results, [20][37][40], the Co local MM decreases from the outermost shell to the cluster's center in both configurations. This behaviour is mainly due to the fact that it is energetically favoured the minority orbitals occupation than the majority when the Co atoms occupy the inner shell.

6.2.3 Fe_xCo_{147-x}

In line with the FeCu clusters with 147 atoms, in this section we present: (a) $Fe_{10}Co_{137}$ where the Fe atoms are in the cluster's face, and (b) $Fe_{12}Co_{135}$ with the Fe atoms in the cluster's vertex.

(a) $Fe_{10}Co_{137}$ cluster: Fe in the cluster's triangle face

In figure 6.18.(a) we present the binding energy, the average cluster's MM and the Fe/Co local atom MM of $Fe_{10}Co_{137}$ cluster. We calculated a binding energy of -4.55eV and an average cluster's MM close to $1.80\mu_B$. In this structure the Fe and Co atoms display different local MM depending on the triangle surface position in the outermost shell. Specifically, we refer with V_T to the Fe/Co atom in the triangle's vertex, with E_T the Fe/Co atom in the edge, finally we use C_T for Fe/Co atom at the center. We found an Fe local MM of $2.94\mu_B$ for Fe(V_T) with VASP and $3.28\mu_B$ with SIESTA, while the Fe(E_T) local MM is $2.84\mu_B$ with VASP and $3.09\mu_B$ with SIESTA. Moreover, Fe(C_T) exhibits a local MM of $2.73\mu_B$ by VASP and $2.94\mu_B$ with SIESTA. Co(V_T) shows a MM of $1.86\mu_B$ with VASP and $2.03\mu_B$ with SIESTA, whereas the Co(E_T) displays a local MM of $1.80\mu_B$ with VASP and $1.82\mu_B$ with SIESTA. In addition, Co(C_T) atoms exhibit an atomic MM of $1.74\mu_B$ with VASP and $1.75\mu_B$ with SIESTA. Furthermore, Co atoms in the first shell display a local MM $\sim 1.55\mu_B$ and the Co atom in the center exhibits an atomic MM of $\sim 1.2\mu_B$ with VASP and $1.75\mu_B$ with SIESTA.

Figure 6.18.(b) displays the spin up and spin down WF at the homo level. Focusing in the spin up WF we observe 3d-electrons mainly localized on the center of the Fe and Co triangle face in the outermost shell. Specifically, we found Co-3d hybridizations situated in the middle of the Co triangle face. However, we see hybridizations between Fe-3d electrons located in the center of the Fe triangle surface. On the other hand, the spin down WF shows the charge close to the own Fe or Co atoms, resulting in the absence of hybridizations.

In fig.6.18.(c) in the panel up we report the total EDOS and Co PEDOS. First of all, it is interesting to notice the band like character of the total and partial EDOS. We find that the Co 3d-up electrons are between -5eV and -0.5eV, whereas the Co 3d-down are between -3.5eV and the homo state. Additionally, we observe Co 4s electrons a low energy close to -8eV and -7eV. Moving to Fe atoms, fig.6.18.(c) panel down, we see that

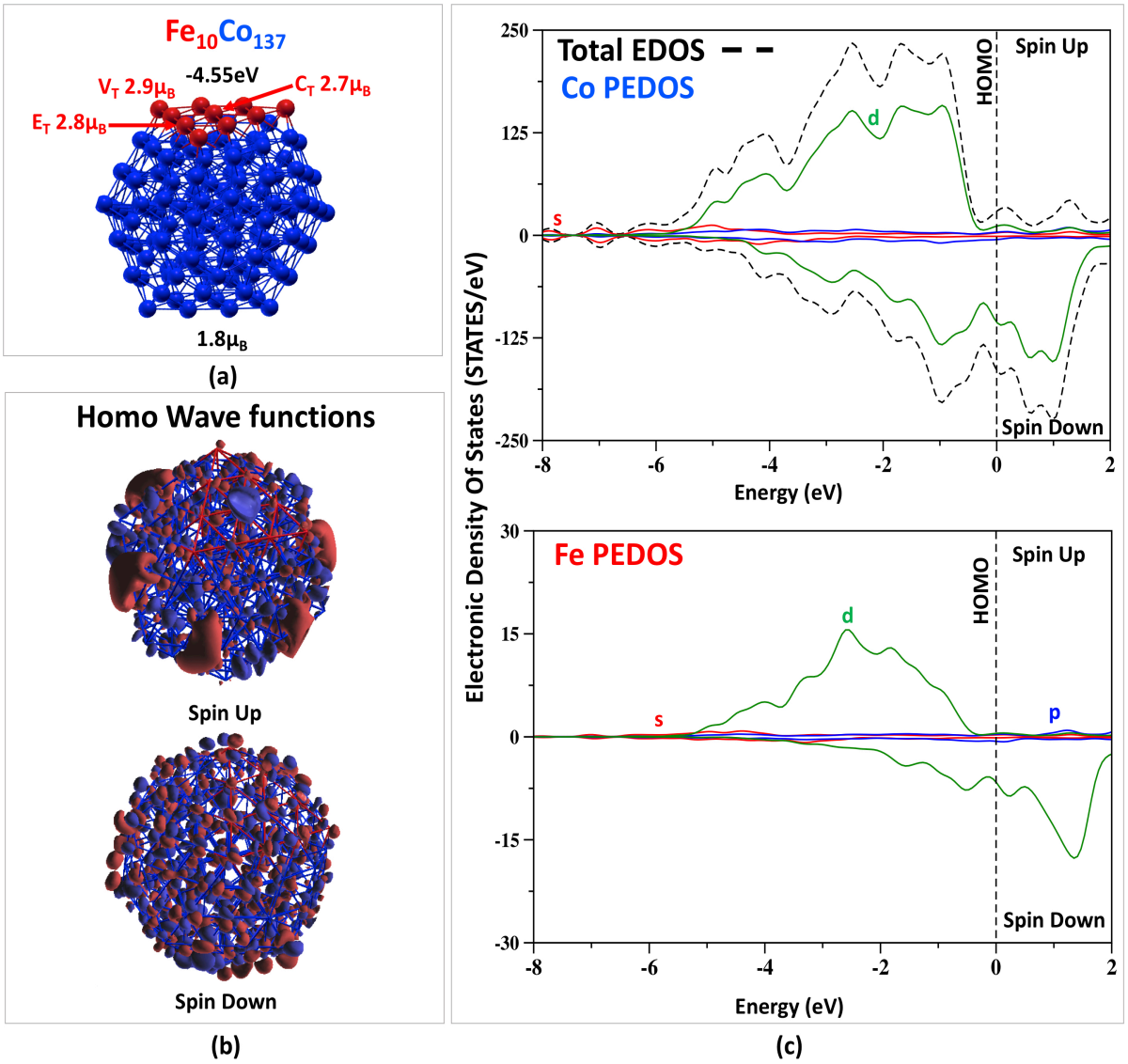

Figure 6.18: $Fe_{10}Co_{137}$: (a) magnetic and structural properties. (b) Spin up and Spin down Wave Functions (WF) at the homo level. Red and blue area stand for the negative and positive charge of the WF.(c) Panel up: Total cluster EDOS (dashed black line); Co PEDOS (the s, p and d PEDOS is presented with red, blue and green lines, respectively). Panel down: Fe PEDOS.

the Fe 3d-up electrons occupy the energy between -5eV and -0.5eV. Moreover, we found that the Fe 3d-down charge is enclosed by -2eV and the homo level. Finally, we do not observe any H-L gap in both majority and minority occupation resulting in a metallic character of this cluster.

In table 6.13 we present the majority (↑) and the minority (↓) Fe and Co electron population and the local atom MM (μ_B) of Fe and Co atoms. Additionally, the positive/negative sign of μ_B denotes its resulting up/down direction, respectively. Moreover, we name with Co(II) and Co(I) the Co atom in the second and

the first shell respectively, and Co(C) the Co atom in the cluster's center. In line with Fe_6Co_{49}(II) and

Table 6.13: Spin up (↑), Spin Down (↓) Fe and Cu electron population and local atom MM (μ_B) of Fe_6Cu_{49} when Fe atoms are in the triangle cluster's face.

atom		VASP				SIESTA
		s	p	d	total	total
Fe(V_T)	Spin Up (↑)	0.26	0.14	4.55	4.94	
	Spin Down (↓)	0.24	0.15	1.64	2.00	
	(μ_B) (↑)-(↓)	0.02	-0.01	2.91	2.94	3.28
Fe(E_T)	Spin Up (↑)	0.24	0.18	4.51	4.92	
	Spin Down (↓)	0.24	0.20	1.66	2.08	
	μ_B (↑)-(↓)	0.00	-0.02	2.85	2.84	3.09
Fe(C_T)	Spin Up (↑)	0.23	0.18	4.47	4.87	
	Spin Down (↓)	0.23	0.21	1.70	2.14	
	μ_B (↑)-(↓)	0.00	-0.03	2.77	2.73	2.94
Co(V_T)	Spin Up (↑)	0.24	0.21	4.55	5.00	
	Spin Down (↓)	0.23	0.20	2.70	3.13	
	μ_B (↑)-(↓)	0.01	0.01	1.85	1.86	2.03
Co(E_T)	Spin Up (↑)	0.24	0.17	4.54	4.95	
	Spin Down (↓)	0.25	0.20	2.70	3.15	
	μ_B (↑)-(↓)	-0.01	-0.03	1.84	1.80	1.82
Co(C_T)	Spin Up (↑)	0.23	0.18	4.52	4.93	
	Spin Down (↓)	0.24	0.23	2.72	3.20	
	μ_B (↑)-(↓)	-0.01	-0.05	1.80	1.73	1.75
Co(II)S	Spin Up (↑)	0.25	0.27	4.52	5.04	
	Spin Down (↓)	0.27	0.33	2.78	3.37	
	μ_B (↑)-(↓)	-0.02	-0.06	1.74	1.66	1.73
Co(I)S	Spin Up (↑)	0.26	0.27	4.45	4.98	
	Spin Down (↓)	0.27	0.32	2.88	3.47	
	μ_B (↑)-(↓)	-0.01	-0.05	1.57	1.51	1.66
Co(C)	Spin Up (↑)	0.30	0.36	4.33	4.98	
	Spin Down (↓)	0.31	0.41	3.09	3.81	
	μ_B (↑)-(↓)	-0.02	-0.05	1.24	1.17	1.48

Fe_6Cu_{49}(III), we observe that the Fe(V_T) shows an higher atomic MM than the Fe(E_T) and the Fe(C_T). In particular, we found that s and p majority Fe(V_T) orbitals are more occupied than the minority ones. On the contrary, Fe(E_T) and Fe(C_T) exhibit the minority orbitals more filled than the majority states. Moreover, the Fe(V_T) exhibits a larger imbalance between spin up and down 3d orbitals than Fe(E_T) and Fe(C_T), giving an higher Fe atomic MM. Focusing on Co(V_T), Co(E_T) and Co(C_T) we observe a lower Co local MM compared to the corresponding Co atoms in Fe_6Co_{49}(II). We can see that Co(V_T) displays a smaller imbalance in the s,

p and d occupation than in the Fe_6Co_{49}(II), resulting in a lower Co local MM. However, Co(E_T) and Co(C_T) exhibit s and p minority orbitals more occupied than the majority one, further lowering the local Co MM. In agreement with the previous sections, experimentally works [40] and theoretical calculation [42], the Co local atomic MM decreases from the outermost shell to the center. Specifically, we notice that Co(II), Co(I) and Co(C) show the s and p spin down orbitals more occupied than the majority ones.

(b) $Fe_{12}Co_{135}$: Fe at the cluster's vertex

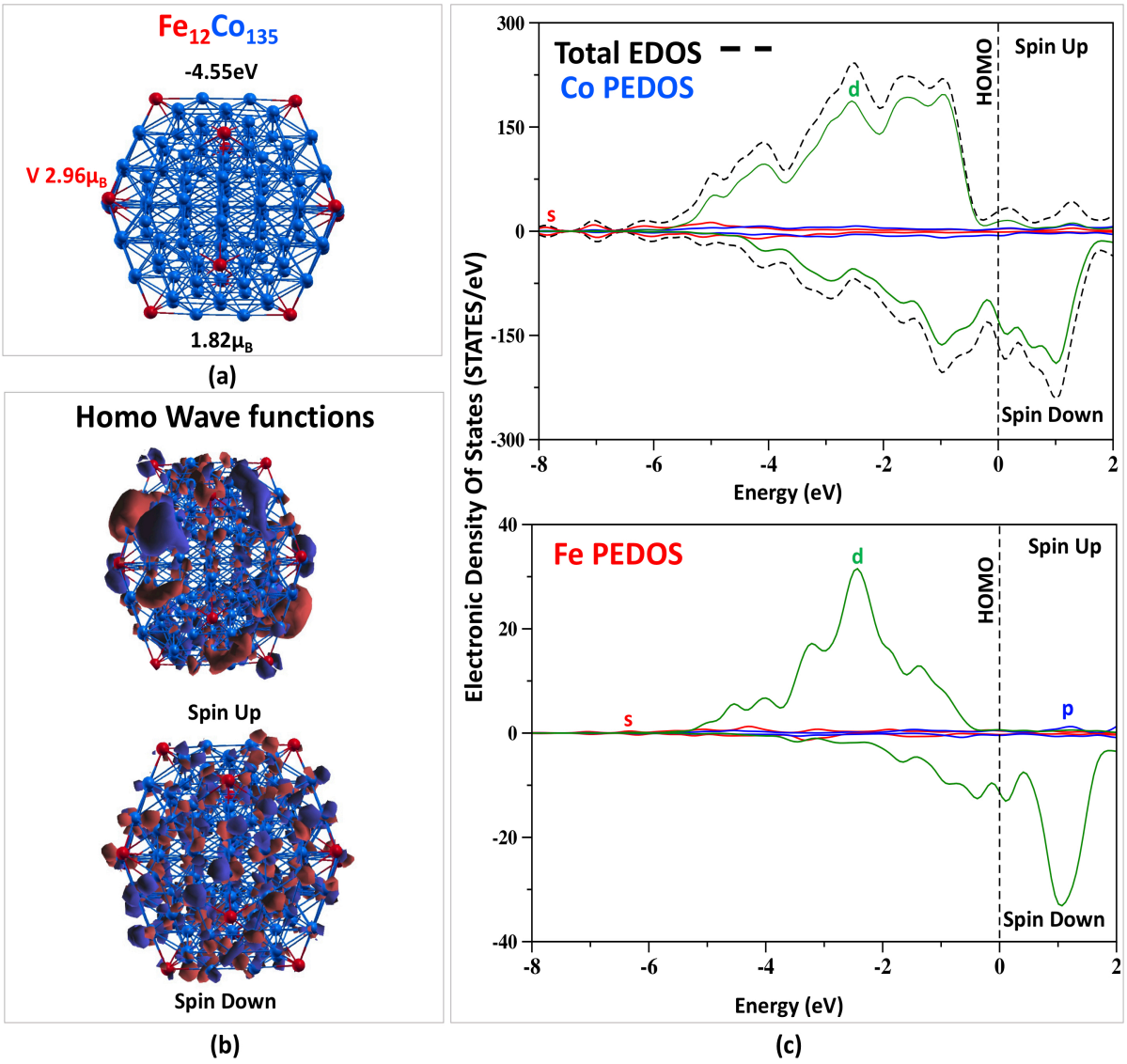

Figure 6.19: $Fe_{12}Co_{135}$: (a) magnetic and structural properties. (b) Spin up and Spin down Wave Functions (WF) at the homo level. Red and blue area stand for the negative and positive charge of the WF.(c) Panel up: Total cluster EDOS (dashed black line); Co PEDOS (the s, p and d PEDOS is presented with red, blue and green lines, respectively). Panel down: Fe PEDOS.

In figure 6.19.(a) we show the binding energy, the average cluster's MM and the Fe and Co local atomic MM. We found a binding energy of -4.55eV and an average cluster's MM of $1.82\mu_B$ that it is larger than the average cluster's MM of $Fe_{10}Co_{137}$ structure ($1.80\mu_B$).
Referring to the Fe atomic MM we observe a value of $2.96\mu_B$ with VASP and $3.29\mu_B$ with SIESTA that are higher than the values shown in the triangle surface case exhibited in the previous section. In addition, the same Fe atomic MM value is displayed in the corresponding $Fe_{12}Cu_{135}$ cluster. We see that when the number of atoms in the cluster increases the Fe local MM assumes almost the same value, no matter which is the first neighbour element. Moreover Co atoms in the outermost shell exhibit an atomic moment lower than the $Fe_{10}Co_{137}$, while the Co local MM of the Co atoms in the inner shell are almost the same.

Fig.6.19.(b) presents the spin up and spin down WF at the homo level. Focusing on the spin up WF, we observe a small amount of charge located on Co atoms, giving hybridizations between Co-3d orbitals. Furthermore, only a small amount or no charge is localized on the Fe atoms. Referring to the spin down, we see only a small amount of charge localized on both Co and Fe atoms without any hybridization between the atoms.

In figure 6.19.(c) in the panel up we display the total EDOS and Co PEDOS. We observe Co 3d-up electrons between -5.5eV and -0.5eV, while the Co 3d-down charge is among -4eV and the homo state. Furthermore, Co 4s electrons are close to -8eV and -7eV. Moving to the Fe atoms, fig.6.19.(c) panel down, we discover that the Fe 3d-up electrons are enclosed beteen -5eV and close to the -1eV. In addition, we found the Fe 3d-down charge between -2eV and the homo level. Finally, we do not observe any H-L gap in both majority and minority total EDOS resulting in a metallic character of this cluster.

The table 6.14 exhibits the majority ($\uparrow$) and the minority ($\downarrow$) Fe and Co electron population and the local atom MM (μ_B) of Fe and Co atoms. Additionally, the positive/negative sign of μ_B denotes its resulting up/down direction, respectively. Focusing on the Fe atoms, we found a local atomic MM close the Fe local atomic MM in the $Fe_{10}Co_{137}$ structure. Also in this case we observe that s, p and d majority orbitals are more occupied than the minority, contributing to increase the Fe local atomic MM. Moving to the Co(E_T), we notice a lower atomic MM compared to the corresponding value displayed in $Fe_{10}Co_{137}$ cluster. In particular, we observe an occupation of 4.94($\uparrow$) and 3.15($\downarrow$) in this configuration, while Co(E_T) in $Fe_{10}Co_{137}$ structure shows an occupation of 5.00($\uparrow$) and 3.13($\downarrow$), resulting in a higher Co atomic MM. On the contrary, Co(E_T) exhibits almost the same atomic MM value with the same spin up and spin down occupation. Conforming to the shell model, the Co local MM decreases from the outermost shell to the cluster's center. In line with $Fe_{10}Co_{137}$ orbitals, s and p minority states are more occupied than the majority lowering the Co local atomic MM.

In this paragraph we provided a comparison between two configurations: (a) Fe atoms in the clusters' triangle face $Fe_{10}Co_{137}$ and (b) Fe atoms in the clusters' vertex $Fe_{12}Co_{135}$. We observe that the Fe position does not affect the stability of the clusters and the average MM. Interestingly, we found a higher Fe local MM in the configuration b) than in the a), mainly due to the larger imbalance between spin up and down occupation in the first configuration than in the second ones. Referring to the Co atoms, in line with the shell model [37], we observe that the Co atoms in the inner shells show s and p minority states more occupied than the majority, lowering the Co atomic MM. Comparing with the corresponding FeCu clusters, we found that when

Table 6.14: Spin up (↑), Spin Down (↓) Fe and Co electron population and local atom MM (μ_B) of $Fe_{12}Co_{135}$ when Fe atoms are in the triangle cluster's face.

atom		VASP				SIESTA
		s	p	d	total	total
Fe(V)	Spin Up (↑)	0.26	0.14	4.55	4.97	
	Spin Down (↓)	0.23	0.14	1.62	2.01	
	(μ_B) (↑)-(↓)	0.03	0.00	2.93	2.96	3.29
Co(E_T)	Spin Up (↑)	0.24	0.17	4.54	4.94	
	Spin Down (↓)	0.25	0.20	2.71	3.15	
	μ_B (↑)-(↓)	-0.01	-0.04	1.83	1.79	1.83
Co(C_T)	Spin Up (↑)	0.23	0.18	4.51	4.92	
	Spin Down (↓)	0.24	0.23	2.74	3.21	
	μ_B (↑)-(↓)	-0.01	-0.05	1.77	1.71	1.73
Co(II)S	Spin Up (↑)	0.25	0.26	4.52	5.03	
	Spin Down (↓)	0.27	0.32	2.78	3.37	
	μ_B (↑)-(↓)	-0.02	-0.06	1.74	1.66	1.73
Co(I)S	Spin Up (↑)	0.26	0.27	4.41	4.99	
	Spin Down (↓)	0.27	0.32	2.82	3.47	
	μ_B (↑)-(↓)	-0.01	-0.05	1.58	1.52	1.67
Co(C)	Spin Up (↑)	0.29	0.35	4.33	4.98	
	Spin Down (↓)	0.31	0.40	3.10	3.81	
	μ_B (↑)-(↓)	-0.02	-0.05	1.23	1.17	1.47

Fe atoms are in the cluster's triangle face we observe an higher Fe atomic MM in the FeCo clusters while when the Fe atoms occupy the cluster's vertex the Fe atomic MM is found to be almost the same in both FeCo and FeCu systems. Finally, both configurations display a total EDOS with a band-like behaviour and a metallic character.

6.2.4 Fe_xCo_{309-x}

In this paragraph we present the structural, electronic and magnetic properties of: (a) $Fe_{15}Co_{294}$ where Fe atoms are in the cluster's face, and (b) $Fe_{12}Co_{297}$ with Fe atoms in the cluster's vertex.

(a) $Fe_{15}Co_{294}$ cluster: Fe at the cluster's face

In figure 6.20.(a) we display the binding energy, the average cluster's MM and the Fe and Co local atomic MM. We calculated a binding energy of -4.23eV and an average cluster's MM of 1.75μ_B. As we observed in the previous section, Fe and Co atoms display different local MM depending on the triangle surface position in the outermost shell. In particular, we name V_T the Fe/Co atoms that occupy the triangle's vertex, while

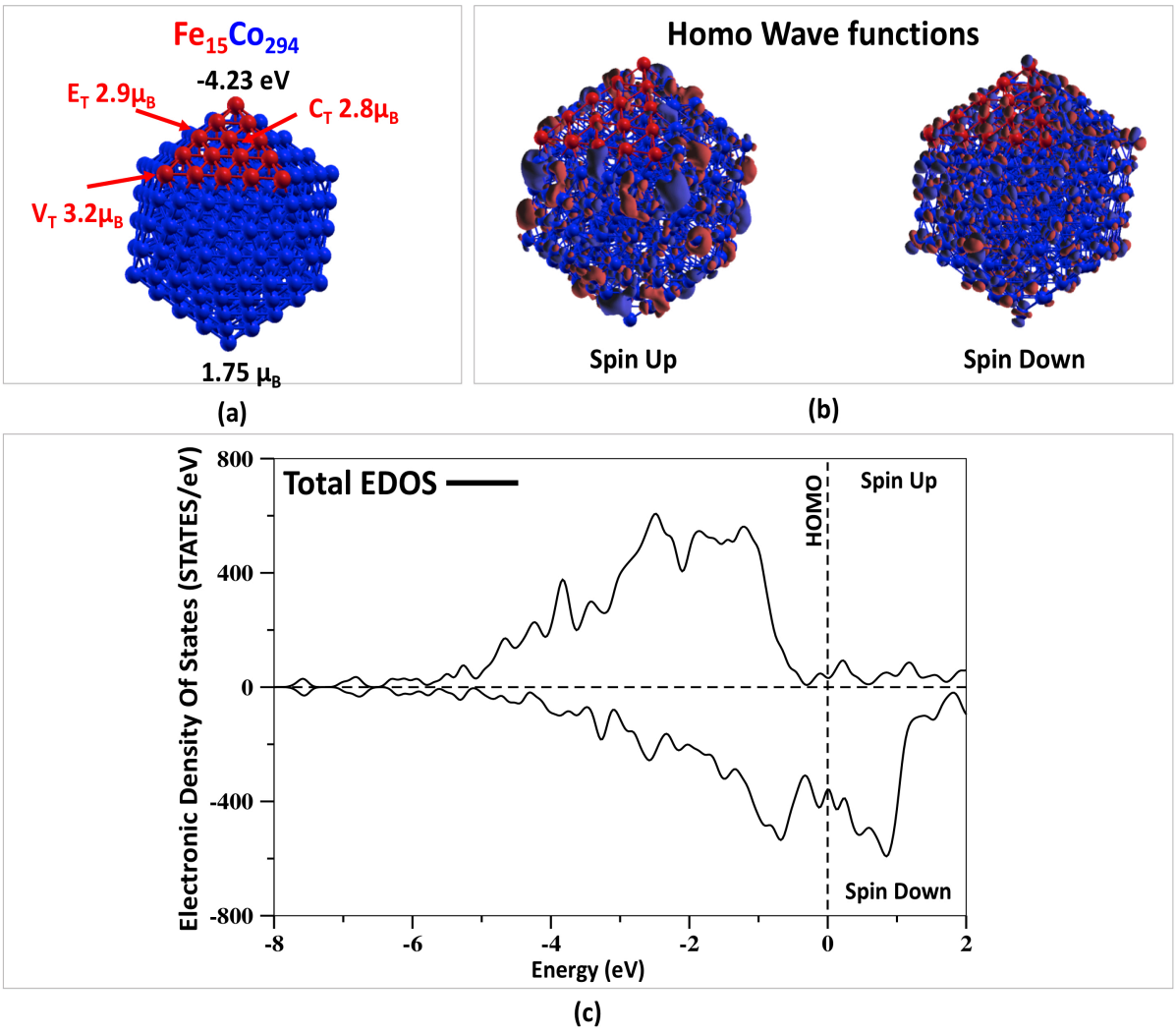

Figure 6.20: $Fe_{15}Co_{293}$: (a) magnetic and structural properties. (b) Spin up and Spin down Wave Functions (WF) at the homo level. Red and blue area stand for the negative and positive charge of the WF.(c) Total cluster EDOS (dashed black line)

we refer to E_T the atoms in the edge of the triangle surface, and finally with C_T for the Fe/Co atoms at the center. We found that both, Fe and Co atoms in the outermost shell exhibit the largest local atom MM when are placed in the vertex of the surface. Moreover, we can see that the lowest local atom MM is shown when they are at the center of the triangle surface. Additionally, the Co local MM decreases from the outermost shell to the inner ones, in line with the previous results.

Figure 6.20.(b) shows the spin up and spin down WF at the homo level. In the spin up WF, we can see a small amount of charge deposited mainly on the Co atoms, leaving the Fe atoms almost totally empty. On the contrary, spin down WF exhibits 3d electrons localised on both Fe and Co atoms.

In figure 6.20.(b) we present the total $Fe_{15}Co_{293}$ EDOS. First, we observe a different spin up and down

electronic distribution. Specifically, we found that the majority orbitals are enclosed by -5eV and -0.5eV, making the spin up state almost fully filled. Contrarily, the spin down electrons are between the -4eV and the homo state. Moreover, the spin down orbitals are shifted towards the homo states, leaving the minority states less occupied. Finally, we found a band like distribution and a metallic character of this cluster.

In table 6.15, we present the majority (↑) and the minority (↓) Fe and Co electron population and local atom MM (μ_B) of Fe and Co atoms. First of all, we observe that the triangle surface's vertex Co and Fe atoms

Table 6.15: Spin up (↑), Spin Down (↓) Fe and Co electron population and local atom MM (μ_B) of $Fe_{15}Co_{294}$ when Fe atoms are in the triangle cluster's face.

SIESTA			
atom	Spin Up (↑)	Spin Down (↓)	μ_B(↑)-(↓)
Fe(V_T)	8.62	5.41	3.21
Fe(E_T)	8.58	5.65	2.93
Fe(C_T)	8.55	5.76	2.78
Co(V_T)	8.50	6.54	1.96
Co(E_T)	8.49	6.70	1.79
Co(C_T)	8.48	6.80	1.68
Co(III)S	8.35	6.63	1.72
Co(II)S	8.01	6.36	1.65
Co(I)S	8.01	6.50	1.51
Co(C)	7.55	6.14	1.41

exhibit an higher local atom MM compared to the other atom positions in the triangle face. It seems that the vertex position favours an enlarged imbalance among majority and minority electrons. This behaviour can be attributed to the reduced coordination number of the atoms in the vertex triangle surface. Moreover, we note that the Fe atoms always show an higher local atom MM than the Co ones. Finally, we found that the Co atoms MM decreases from the outermost to the inner shells. This behaviour is mainly due to the increasing spin down occupation in the inner shell.

(b) $Fe_{12}Co_{297}$: Fe in the cluster's vertex

In figure 6.21.(a) we display the binding energy, the average cluster's MM and the Fe/Co local atomic MM. We found a binding energy of -4.24eV and an average cluster's MM of 1.74μ_B, that are almost the same compared with the corresponding value in the $Fe_{15}Co_{293}$ structure (-4.24eV and 1.75μ_B). Also in this case, we observe that the local atom MM decreases from the outermost to the inner shell.

Fig. 6.21.(b) exhibits the spin up and spin down WF at the homo level. The spin up WF exhibits a small amount of 3d charge localized on the Co atoms in the outermost shell, whereas no charge is found on the Fe atoms. On the contrary, the spin down WF displays 3d electrons located on both the Fe and Co atoms. In

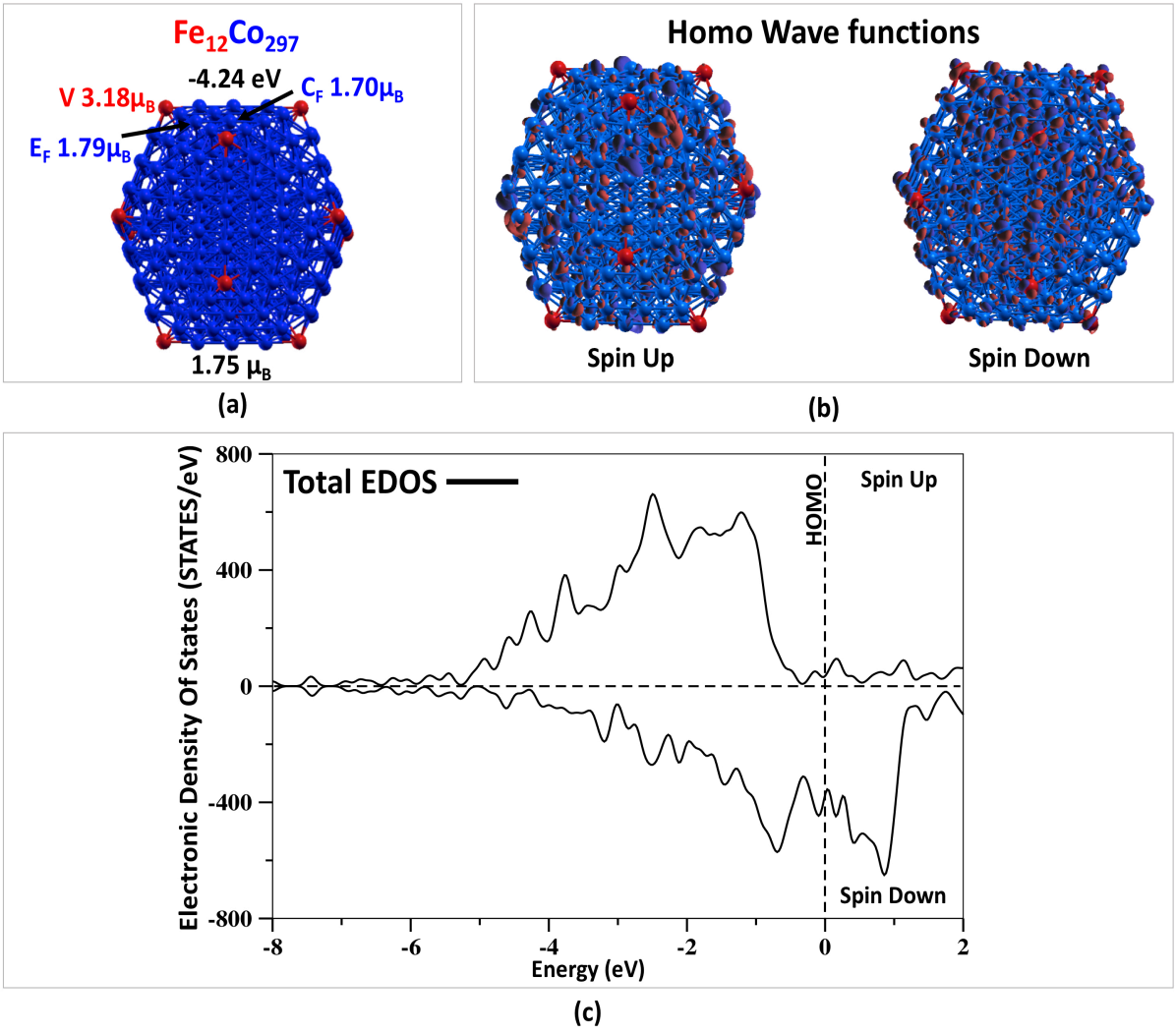

Figure 6.21: $Fe_{12}Co_{297}$: (a) magnetic and structural properties. (b) Spin up and Spin down Wave Functions (WF) at the homo level. Red and blue area stand for the negative and positive charge of the WF.(c)Total cluster EDOS (dashed black line).

addition, we observe a small amount of charge on the Co atoms in the inner shell.

In figure 6.21.(c) we display the total $Fe_{12}Co_{297}$ EDOS. We can see the majority electrons between -5eV and -1eV, on the contrary the minority charge is among -3eV and the homo state. In particular, the spin down orbitals are moved towards the homo state, leaving the minority states less occupied than the majority ones. In line with the $Fe_{15}Co_{293}$ configuration, the total EDOS display a band like behaviour. Moreover, it does not show any H-L gap, giving a metallic character to this cluster.

In table 6.16, we present the majority ($\uparrow$) and the minority ($\downarrow$) Fe and Co electron population and local atom MM (μ_B) of Fe and Co atoms. Concerning the Fe local MM, we can see a larger local atom MM compared to the corresponding value in $Fe_{15}Co_{293}$ cluster, while the Co atoms show a similar local atom

Table 6.16: Spin up (↑), Spin Down (↓) Fe and Co electron population and local atom MM (μ_B) of $Fe_{12}Co_{297}$ when Fe atoms are in the triangle cluster's face.

SIESTA			
atom	Spin Up (↑)	Spin Down (↓)	μ_B(↑)-(↓)
Fe(V)	8.59	5.41	3.18
Co(E_T)	8.48	6.68	1.79
Co(C_T)	8.46	6.78	1.70
Co(III)S	8.32	6.61	1.71
Co(II)S	8.02	6.36	1.67
Co(I)S	8.08	6.53	1.56
Co(C)	7.83	6.35	1.48

MM. Additionally, in line with the previous cluster configuration and the shell model presented by Billas et al. [37], the Co local atom MM decreases from the outermost shell to the inner ones.

In these two sections we presented: (a) $Fe_{15}Co_{294}$, Fe atoms in the clusters' triangle face, and (b) $Fe_{12}Co_{297}$, Fe atoms in the clusters' vertex. First, we have noted that the Fe atoms position does not affect the stability of the clusters and the average clusters' MM. We have observed a smaller enhancement of the Fe local MM in configuration (b), while the Co atoms exhibit almost the same local MM in both (a) and (b) structures. In addition, the total (a) and (b) EDOS reveal a band like behaviour and a metallic character. In agreement with other theoretical calculation [42] and experimental results [40], we found that the Fe and Co local MM and the average cluster's MM increases with the reduction of the structural dimension.

6.3 FeMn

In this section we present the FeMn icosahedral clusters. It is worth mentioning that Mn is the element that shows the highest MM in the table of elements. On the contrary, it displays fascinating magnetic properties when forming nanoclusters.

6.3.1 $FeMn_{12}$

In the next two paragraphs we display two configurations of the $FeMn_{12}$ icosahedral clusters with 13 atoms: (I) Fe atom in the center, (II) Fe atom in the shell.

(I) $FeMn_{12}$: Fe atom in the center

First of all, we analyze two different (I)$FeMn_{12}$ magnetic arrangements:

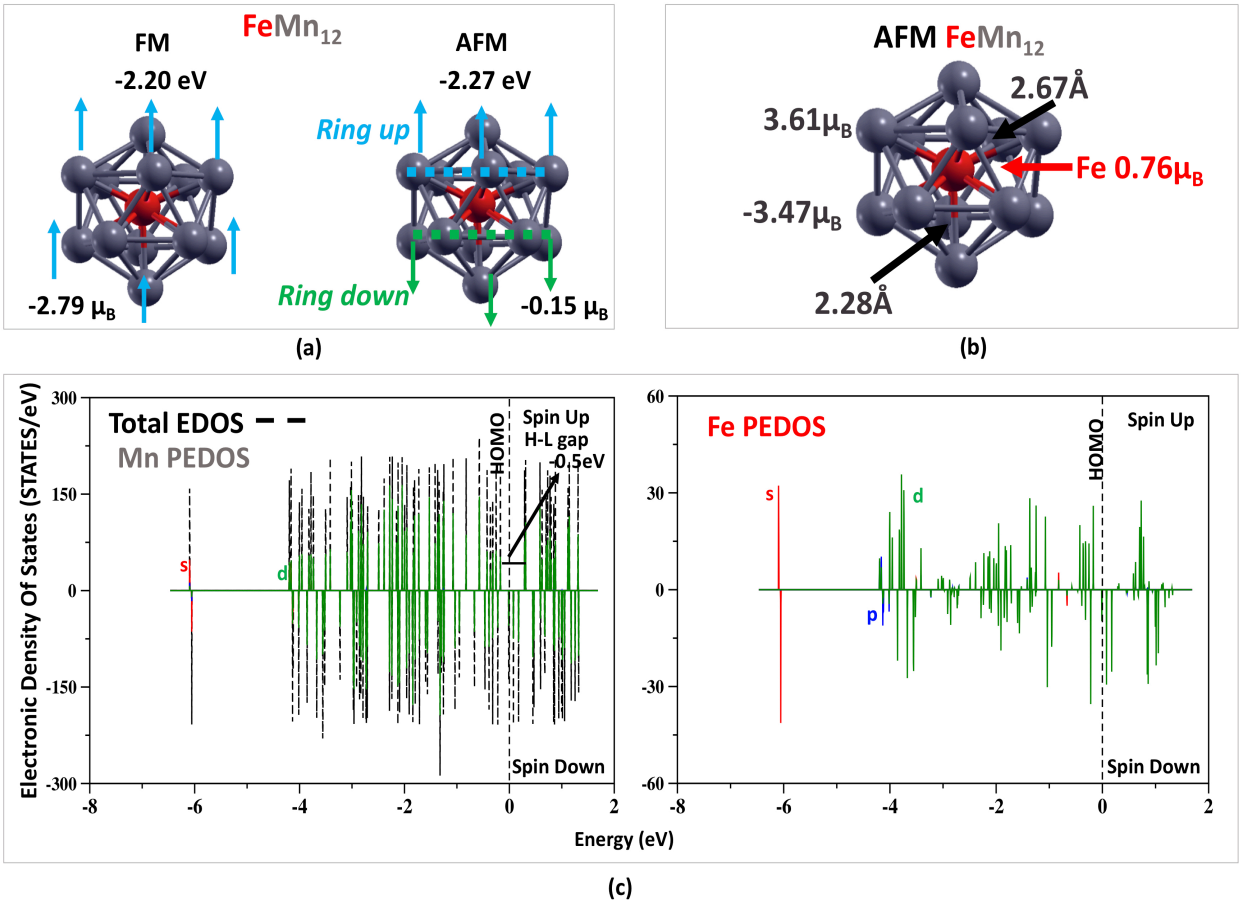

Figure 6.22: (I)$FeMn_{12}$: (a) FM and AFM arrangement and binding energy. (b) Magnetic properties. (c) Panel left: Total cluster EDOS (dashed black line); Mn PEDOS (the s, p and d PEDOS is presented with red, blue and green lines, respectively). Panel right: Fe PEDOS.

- FerroMagnetic (FM): all Mn spin atoms couple parallel;
- AntiFerroMagnetic (AFM): Mn spin atoms couple anti-parallel each others.

Figure 6.22.(a) left part exhibits the FM (I)$FeMn_{12}$ structure, while figure 6.22.(a) right part the AFM (I)$FeMn_{12}$ cluster. Referring to the AFM configuration, we can consider the $FeMn_{12}$ cluster as separated in two rings depending on the spin orientation of the Mn atoms. We name *ring up* the cluster's section where the Mn atoms' magnetic moment is oriented up, whereas we refer to the *ring down* that part of the cluster in which the Mn atoms' magnetic moment is aligned down. FM (I)$FeMn_{12}$ shows a binding energy of -2.20eV and an average cluster's MM of $2.98\mu_B$. On the contrary, the AFM (I)$FeMn_{12}$ displays a binding energy of -2.27eV and an average cluster's MM of $0.15\mu_B$, showing that is the most stable configuration. For this reason, we focus on the AFM (I)$FeMn_{12}$ system.

In figure 6.22.(b) we present the magnetic and structural properties of the AFM (I)$FeMn_{12}$. Moving to the Fe-Mn distances, we observe diverse distances in a range between 2.28$\AA$ and 2.67$\AA$, depending on the Mn

local MM. Concerning the Fe atom MM we found a value of $0.77\mu_B$, while Mn atoms show a local MM, spin up and down alignment, around $3.5\mu_B$.

Figure6.22.(c) panel left displays the total EDOS and Mn PEDOS. We can see that the Mn charge is symmetrically distributed in the spin up and down occupation, due to the AFM coupling among the Mn atoms. Moving to the Fe atom, fig.6.22.(b) panel right, we observe almost the same charge distribution in the majority and minority charge, resulting in a very small Fe atom MM. Concluding, we found a H-L gap of -0.5 eV in the total majority EDOS, while no gap is exhibited in the minority counterpart, giving a half-metallic character to this cluster.

The table 6.17 exhibits the majority (↑) and the minority (↓) Fe and Mn electron population and the local atom MM (μ_B) of Fe and Mn atoms. Additionally, the positive/negative sign of μ_B denotes its resulting up/down direction, respectively. We refer with Mn(U) to the Mn atoms in the ring up, while we name Mn(D) the Mn atoms in the ring down.
Focusing on Fe atom, we observe almost the same occupation in both spin up and down distribution, resulting

Table 6.17: Spin up (↑), Spin Down (↓) electron population and local atom MM (μ_B) of Fe and Mn in $FeMn_{12}$(I) with Fe in the center.

atom		VASP				REF
		s	p	d	total	
Fe	Spin Up (↑)	0.28	0.40	3.62	4.17	
	Spin Down (↓)	0.28	0.30	2.80	3.40	
	μ_B (↑)-(↓)	0.00	0.10	0.76	0.77	~ 0[92]
Mn(U)	Spin Up (↑)	0.22	0.10	4.26	4.59	
	Spin Down (↓)	0.16	0.09	0.73	0.98	
	μ_B (↑)-(↓)	0.06	0.01	3.54	3.61	~ 4[92]
Mn(D)	Spin Up (↑)	0.17	0.11	0.79	1.06	
	Spin Down (↓)	0.22	0.11	4.22	4.55	
	μ_B (↑)-(↓)	-0.05	0.00	-3.43	-3.49	$\sim$ -4[92]

in an almost zero Fe local MM. This behaviour is reported in fig.6.22.(b) panel right, where we can see that up and down s and d electrons occupy almost the same energy levels. On the contrary, Mn atoms show an AFM coupling which means that the spins are antiparallel aligned. Specifically, all Mn(U) atoms display majority orbitals more occupied than the minority. Conversely, Mn(D) atoms exhibit minority charge more filled than the majority. We observe that the majority and minority contributions from Mn(U) and Mn(D) are almost the same, resulting in a low average cluster's MM and in a symmetric spin up and down occupation in the Mn PEDOS, fig.6.22.(b) panel left.

(II)$FeMn_{12}$: Fe atom at the shell

Figure 6.23.(a) left part exhibits the FM (II)$FeMn_{12}$ structure, while figure 6.23.(a) right part the AFM (II)$FeMn_{12}$ cluster. Referring to the FM configuration, we found a binding energy of -2.25eV and an average

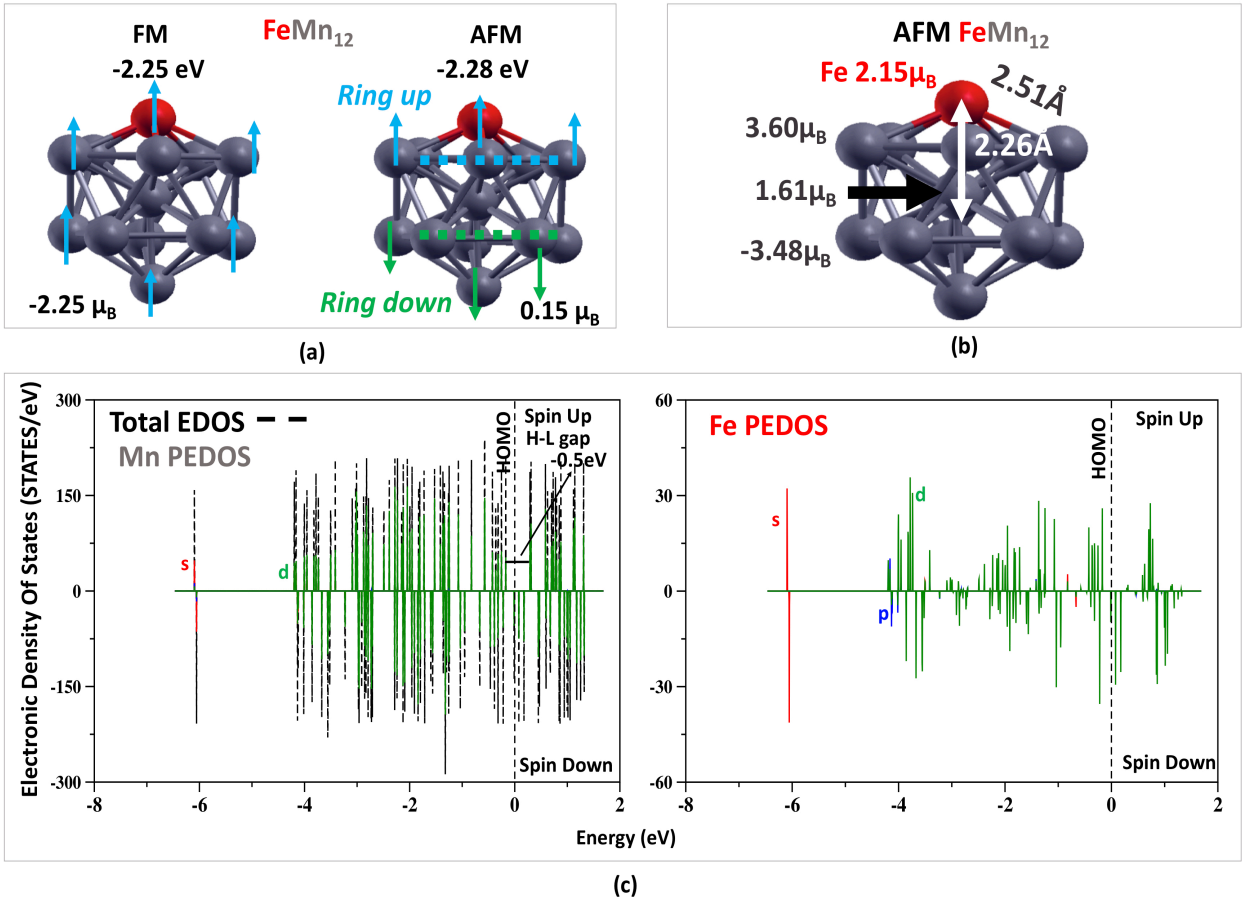

Figure 6.23: (II)$FeMn_{12}$: (a) FM and AFM arrangement and binding energy. (b) magnetic properties. (c) Panel left: Total cluster EDOS (dashed black line); Mn PEDOS (the s, p and d PEDOS is presented with red, blue and green lines, respectively). Panel right: Fe PEDOS.

cluster's MM of $2.16\mu_B$. Moving on the AFM arrangement, we observe a binding energy of -2.27 and an average cluster's MM of $0.15\mu_B$. In line with the previous paragraph we discover the AFM arrangement as the most stable configuration. Furthermore, we observe the same average cluster MM of the (I)$FeMn_{12}$ structure ($0.15\mu_B$), concluding that the position of the Fe atom does not affect the stability and the average MM of the clusters.

In figure 6.23.(b) we exhibit magnetic and structural properties of the AFM (II)$FeMn_{12}$. Focusing on the Fe atom MM, we found a value of $2.15\mu_B$, that is higher than the Fe local MM shown in (I)$FeMn_{12}$ configuration. In addition, the Mn atoms in the shell show an average local MM of $3.45\mu_B$, while Mn atom in the center reports a MM of $1.61\mu_B$. Concerning to the Fe and Mn distances, we find $2.26\mathring{A}$ between Fe and Mn in the center, whereas we observe a distance of $2.51\mathring{A}$ betwixt Fe and Mn in the shell.

Figure 6.23.(c) panel left exhibits the total EDOS and Mn PEDOS. In line with the previous case, we found the same symmetric distribution shown in the (I)$FeMn_{12}$, resulting in the same average cluster's MM. Referring to the Fe atom, fig.6.22.(b) panel right, we observe a similar electrons distribution exhibited in the

previous case. Uniformly with (I)$FeMn_{12}$, we find a H-L gap of -0.5eV in the majority total EDOS, on the contrary no H-L gap is displayed in the minority counterpart, revealing the half-metallic character of this cluster.

Table 6.18 exhibits the majority (↑) and the minority (↓) Fe and Mn electron population and the local atom MM (μ_B) of Fe and Mn atoms. Additionally, the positive/negative sign of μ_B denotes its resulting up/down direction, respectively. Concerning to the Fe atoms, we observe an higher Fe atom MM compared

Table 6.18: Spin up (↑), Spin Down (↓) electron population and local atom MM (μ_B) of Fe and Mn in $FeMn_{12}$(II) with Fe in the shell.

atom		VASP			
		s	p	d	total
Fe	Spin Up (↑)	0.27	0.15	4.23	4.65
	Spin Down (↓)	0.24	0.15	2.11	2.50
	μ_B (↑)-(↓)	0.03	0.00	2.12	2.15
Mn(C)	Spin Up (↑)	0.24	0.24	3.39	3.86
	Spin Down (↓)	0.21	0.23	1.81	2.25
	μ_B (↑)-(↓)	0.03	0.01	1.58	1.61
Mn(U)	Spin Up (↑)	0.22	0.11	4.29	4.62
	Spin Down (↓)	0.16	0.09	0.70	0.95
	μ_B (↑)-(↓)	0.06	0.02	3.59	3.67
Mn(D)	Spin Up (↑)	0.17	0.11	0.87	1.14
	Spin Down (↓)	0.22	0.11	4.17	4.49
	μ_B (↑)-(↓)	-0.04	0.00	-3.30	-3.35

with the value shown in (I)$FeMn_{12}$. In this configuration we found a larger imbalance between spin up and down occupation. This result is due to the lower coordination number of the Fe atom when it occupies the shell. In addition, we observe a Mn(U) atom MM of $3.67\mu_B$ that it is higher compared to the Mn(U) atom MM shown in the (I)$FeMn_{12}$ ($3.61\mu_B$), due to the larger imbalance between 3d spin up and down occupation. Furthermore, Mn(D) atomic MM displays a value of $-3.35\mu_B$ that it is lower than the value obtained in the (I)$FeMn_{12}$ counterpart ($-3.49\mu_B$), exhibiting a smaller imbalance between 3d minority and majority occupation. For these reasons the two configurations display the same average cluster's MM but diverse Fe and Mn atom MM.

Concluding, in these paragraphs we presented: (I)$FeMn_{12}$, Fe atom in the cluster's center, and (II)$FeMn_{12}$ Fe atom in the cluster's shell. We observed that the position of the Fe atom does not effect the stability and the average MM of the cluster. Interestingly, we found that when Fe occupies the center its atom MM drops to zero, whereas in the (II)$FeMn_{12}$ configuration exhibits a local MM of $2.215\mu_B$. Moreover, although Mn atoms show a large atom MM, because of the AFM coupling, the cluster's average MM is almost zero in both structures. These results are in a good agreement with experimental works and others theoretical calculations [91][90]

6.3.2 Fe_6Mn_{43}

Proceeding with icosahedral clusters with 55 atoms, in line with FeCu and FeCo systems in the next section we present two cases: (I)Fe_6Mn_{43} Fe atoms in the cluster's triangle face and (II)Fe_6Mn_{43} Fe atoms in the cluster's vertex.

(I) Fe_6Mn_{43}: Fe atoms at the cluster's triangle face

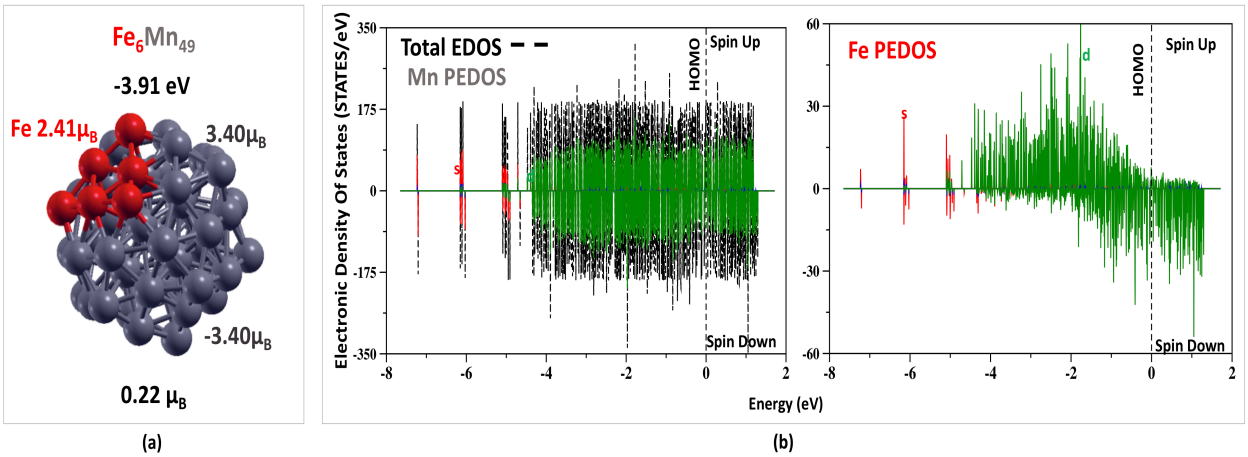

Figure 6.24: (I)Fe_6Mn_{43}: (a) magnetic and structural properties. (b) Panel left: Total cluster EDOS (dashed black line); Mn PEDOS (the s, p and d PEDOS is presented with red, blue and green lines, respectively). Panel right: Fe PEDOS.

In figure 6.24.(a) we present the structural and magnetic properties of the (I)Fe_6Mn_{43} structure, when Fe atoms occupy the triangle face in the outermost shell. First of all, it is worth to notice that not only Mn atoms coupled AFM in the same shell as reported previously, but also between the two consecutively shells in the first and second ones. For this reason we observe an average cluster's MM of $0.22\mu_B$. In addition, we calculate a binding energy of -3.91eV. Focusing on the Fe atom MM, we found a value enclosed by $2.11\mu_B$ and $2.72\mu_B$. Interestingly, Mn atoms show a local MM close to (+/-) $3.4\mu_B$ in the outermost shell, whereas we find a value close to (+/-)$1.00\mu_B$ in the first shell.

Figure 6.24.(b) panel left reports the total cluster's EDOS and the Mn PEDOS. In agreement with the small 13 atom cluster, we observe a symmetric distribution between spin up and spin down electrons, resulting in an almost zero average cluster's MM. In addition, the total EDOS exhibits a band like behaviour. Moving on the Fe PEDOS, fig.6.24.(b) panel right, we can see that Fe 3d spin up electrons are between -4.5eV and -0.5eV, whereas the Fe 3d spin down are shifted towards higher energy enclosed by -2.0eV and the homo state. Furthermore, s up and down orbitals are in the low energy levels between -7.0eV and -4.0eV. Finally, the total cluster's EDOS suggests a metallic character, due to the fact that no H-L gap is shown in both majority and minority occupation.

(II) Fe_6Mn_{49}: Fe atoms at the cluster's vertex.

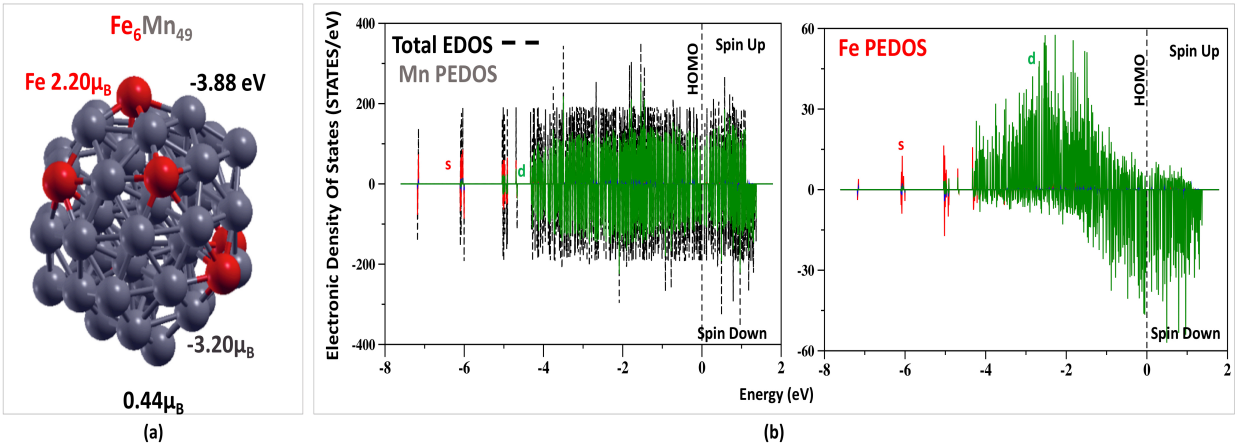

Figure 6.25: (II)Fe_6Mn_{43}: (a) magnetic and structural properties. (b) Panel left: Total cluster EDOS (dashed black line); Mn PEDOS (the s, p and d PEDOS is presented with red, blue and green lines, respectively). Panel right: Fe PEDOS.

In figure 6.25.(a) we report the structural and magnetic properties of the (II)Fe_6Mn_{43} structure, when the Fe atoms occupy the cluster's vertex. We calculated a binding energy of -3.88eV, that is larger than the binding energy of (I)Fe_6Mn_{43}(-3.91eV). Furthermore we found an average cluster's MM of $0.44\mu_B$ that is higher compared to the previous structure. Concerning to the Fe atom MM we observe an Fe atom MM between 1.84 μ_B and $2.56\mu_B$. In addition, we found a Mn atom MM of -0.218μ_B for the Mn in the center, while the Mn atoms in the first shell show an average value close to $1.00\mu_B$. Mn atoms in the outermost shell exhibit a local MM around $3.2\mu_B$ aligned spin up or spin down depending on the position.

Figure 6.25.(b) panel left reports the total cluster's EDOS and the Mn PEDOS. Also in this case, we found a symmetric occupation between majority and minority orbitals, reflecting the same magnetic properties of the (II)Fe_6Mn_{43} structure. Focusing on Fe, fig.6.25.(b) panel right shows Fe 3d spin up electrons between -4.5eV and -0.5eV, while the Fe 3d spin down are enclosed by -2.0eV and the homo state. Moreover, s up and down orbitals are between -7.0eV and -4.0eV. Finally, we found that the total cluster's EDOS displays a metallic character, caused by to the fact that no H-L gap is shown in both majority and minority occupation.

In conclusion, we presented: (I)Fe_6Mn_{43}, Fe atoms in the cluster's triangle face and (II)Fe_6Mn_{43} Fe atoms in the cluster's vertex. We discovered that configuration (I) is more stable than (II) while the second one show an higher average cluster's MM compared to the first one. Interestingly, we observe an AFM coupling between the Mn atoms in the same shell and between the two consecutively shells. Referring to the Fe atom MM we found that the (I)Fe_6Mn_{43} shows an Fe local MM higher than (II)Fe_6Mn_{43}. In addition, the Mn local MM remains almost the same in both configurations. Finally, both structure show a metallic character and a band like behaviour in the total EDOS. These results are in good agreement with literature [83][94].

6.4 Conclusion

In this chapter we analyzed the Fe-X (Cu, Co, Mn) clusters in order to understand the influence of Fe atoms in presence of traditional magnetic or no magnetic elements.

Focusing on the smallest icosahedral cluster of 13 atoms, we studied two possible configurations: (a) Fe in the shell and (b) Fe in the center. First, we observe that FeCu cluster prefers the Fe atoms to be on the shell ((a) arrangement), while the FeCo clusters favoured the (b) ones. Moreover, in the FeMn structure we found that the configuration (a) and (b) exhibit a similar binding energy, rendering equivalent probability for both configurations. Concerning the magnetic properties, we found a larger Fe local atom MM in configuration (a) than in the (b) one, for all Fe-X (Cu, Co, Mn) 13 atoms clusters. We discover the highest Fe local atom MM in the FeCu system (e.g. $3.18\mu_B$), while it decreases in the FeCo (e.g. $3.17\mu_B$) and in the FeMn (e.g. $2.15\mu_B$) structures. Our results show that in the FeCu clusters the presence of the Cu atoms favour the Fe-3d majority occupation in the Fe atom, leaving the minority states less occupied. On the contrary, in the FeCo and FeMn clusters the Fe charge distribution exhibits a smaller Fe-3d spin up-down imbalance compared to the Fe atom in the FeCu clusters, resulting in a lower Fe local atom MM. Focusing on the average cluster MM, it is relevant to observe that, because of the Cu's non magnetic character, the average FeCu MM is close to zero. Due to Co magnetic feature, the FeCo cluster displays the highest average cluster's MM. On the contrary, because of the AFM coupling, FeMn clusters show an average MM close to zero mimicking the FeCu trend. Finally, all Fe-X (Cu, Co, Mn) clusters exhibit discrete and localized states in the total EDOS and a half metallic character.

Furthermore, we analyzed the next icosahedral cluster with 55 atoms. We found two characteristic configurations: (a) Fe atoms in the clusters' triangle surface and (b) Fe atoms in the clusters' vertex positions. Interestingly, we have found that the FeCu system exhibits the largest Fe local MM in the configuration (b), while FeCo and FeMn display the highest Fe local MM in the configuration (a), when the Fe atom occupies the vertex of the triangle surface. Also in this case, due to the Co magnetic character the largest average cluster's MM is displayed in the CoFe clusters, whereas the FeCu and FeMn exhibit a value close to zero. On the contrary, the highest Fe local MM is found on the FeCu clusters. Moreover, for all systems under study the total EDOS exhibit discrete and localised states and a half metallic feature. Concluding, it is worth noting that all 55 atom clusters show a smaller Fe local MM compared to the corresponding 13 atom clusters.

Concerning the 147 atoms clusters, we replay the configurations: (a) Fe in the clusters' triangle surface and (b) Fe in the clusters vertex positions. First of all, we observe that due to the Co magnetic feature both (a) and (b) FeCo configurations display a larger average cluster's MM compared to the FeCu clusters that exhibit an average clusters MM almost zero. Focusing on the Fe local MM, we observed that (a) and (b) FeCo clusters show an higher Fe local atom MM than the FeCu structures. Moreover, both FeCu and FeCo structures exhibit a larger Fe local MM in configuration (b) than in (a). Additionally, the FeCo and the FeCu total EDOS exhibit a band like behaviour and reveal the metallic character of these two systems.

For the biggest understudy 309 clusters we analyzed the same configurations with the 147 ones: (a) Fe atoms cover the clusters' triangle surface and (b) Fe atoms in the clusters vertex positions, in order to compare with the previous results. As expected, we observed a larger average cluster MM in the FeCo clusters than the FeCu ones. In addition, the Fe local atom MM is found to be larger in the FeCu systems than in the FeCo clusters. Moreover, also in this case configuration (b) displays a higher Fe local MM compared to configuration (a). Finally, the FeCo and the FeCu total EDOS exhibit a band like behaviour and reveal the metallic character of these two systems.

In conclusion, we found that the Co and Fe cluster's atoms display a local MM larger than the corresponding value in the bulk dimension. Moreover, we observed that the Mn atoms display a great local atom MM, but when they are assembled in a cluster they assume a magnetic arrangement that minimise the average cluster MM. Interestingly, the FeCu clusters exhibit the highest Fe local MM. In addition, when the Fe atoms are placed at the cluster's vertex they exhibit the highest local MM. It seems that this position favours the occupation of the majority orbitals, leaving the minority states less occupied. Finally, the small clusters exhibit discrete and localized energy states and a half metallic character. On the contrary, the large systems show a band like EDOS and a metallic character.

Chapter 7

General Conclusion

Environmentally friendly and sustainable magnetic nano-clusters and coatings are currently under investigations aiming in answering specific technological demands, like superior magnetic properties, thus being promising for several applications such as drug delivery, high-density magnetic recording, catalysis, sensors and for the production of innovative nano-robotic platforms.

Transition metal clusters and coatings are interesting since their structural, electronic and magnetic properties depend on their size and composition, rendering them suitable candidates for various potential applications. In particular, the magnetic moment (MM) of Fe clusters with less than 100 atoms is around $3\mu_B$ much higher than the corresponding $2.2\mu_B$ bulk value while it decays as a function of clusters' size towards the bulk values. Extensive studies revealed that alloying the classical Fe ferromagnet with non-magnetic elements, like Cu, provides the possibility of tailoring the magnetic properties interplaying with the crystallographic structure, especially in systems with reduced dimensions like clusters and thin films.

In this thesis, we performed a systematic study on the Fe-X (X=Cu, Co, Mn) nano-clusters aiming in finding the optimum configuration and clusters' size exhibiting the highest MM. In addition, taking into account that the Fe and Fe-X monolayers on fcc Cu(111) have the same structure with the icosahedral cluster's faces, they could be considered as an infinite cluster's surface and therefore they were also studied in order to provided valuable information also when comparing with experimental data.

Starting with the smallest 13-atom nano-clusters we found that the configuration with the Fe atom at the center of the Fe-Cu nano-clusters is the energetically favoured whereas for the Fe-Co and Fe-Mn clusters the opposite is true. For all cases, the highest MM per Fe atom was found when the Fe atoms are located at the vertex sites of the surface shell having non-magnetic Cu first neighbours. The highest Fe local atom MM stands for the FeCu and the smallest in the FeMn clusters. The FeCu MM is related to the spin up - down EDOS's differences that are mainly situated close to the homo state. In particular, the Spin-up Fe 3d electronic density of states are fully occupied yielding wavefunctions with homogeneous change distribution while the Spin-down is almost unoccupied exhibiting dangling bonding states close to the homo state. The FeCo or FeMn clusters' electronic properties reveal that the Fe 3d states are strongly hybridized with the Co or Mn 3d for both spin up and spin down EDOS's while in the Fe-Cu clusters the Fe partial 3d spin down

EDOS is saturated close to the homo state.

As the radius of the cluster increases new configurations for Fe surface atoms exist (triangle and vertex sites) for the 55, 147 and 309 clusters. The FeCu exhibits the highest Fe local MM in the vertex sites while the FeCo and FeMn in the triangle positions. Due to the Co magnetic character the largest average cluster's MM is displayed in the CoFe clusters, whereas the FeCu and FeMn (AFM) are negligible. Moreover, the 55-atom total EDOS's exhibits discrete and localized states and a half metallic character similar to 13-atom clusters while in the 147 and 309 clusters the electronic states are broaden towards a band-like behaviour, exhibiting mainly metallic features, in line with the Fe clusters. In particular, the $FeCo_{12}$ and Fe_6Co_{49} clusters reveal a pseudo-gap at the homo state in the spin minority that is altered in the case of $Co_{135}Fe_{12}$ and Fe/Co/Cu(111).

In general for all cases, the nano-clusters exhibit larger MM than the Fe thin films and bulk systems, decreasing towards the value of Fe ML on Cu(111), to reach a plateau above 120 atoms. We found that the highest average cluster's MM is shown in the pure Fe clusters, while FeCu and FeMn exhibit a value close to zero. Concerning the FeCu clusters, we know that the Cu atoms do not contribute in the cluster's total magnetic moment. For this reason, the FeCu average clusters' MM drops to zero. On the contrary, the Mn atoms in the FeMn structures display a Mn local MM different from zero. Due to the AFM coupling exhibited between the Mn cluster's atoms, the FeMn clusters assume no magnetic character. In addition, the FeCo clusters show an average clusters' MM between the FeCu/FeMn and Fe pure clusters, resulting in the Fe-mixed clusters with the largest average cluster's MM.

Concerning the local atomic Fe MM, we found that it's highest value is for the $FeCu_{12}$ edge configuration ($3.18\mu_B$) compared to $3.10\mu_B$ in the pure Fe cluster. These results are in good agreement with experimental data of Billas et al. [37] who found MM of $3.00\mu_B$ for Fe clusters having from 25 up to 130 atoms while this value decreases towards the bulk value ($2.2\mu_B$) for bigger nano-clusters (close to 500 atoms). We found that when Fe is at the clusters' surface surrounded by non-magnetic elements (like Cu) it enhances its local MM is enhanced due to the larger majority-minority electronic occupation imbalance compared to the Fe-X, X = magnetic element like Co and Mn. Especially in the case of FeMn, due to its AFM character the resulting average MM is negligible and the Fe local MM is equivalent to Fe bcc.

Concluding, the FM Fe-Co clusters or Fe coating on Co/Cu(111) are suggested as the best candidate for Fe-based systems with equivalent total and local Fe MM compared to the corresponding Fe-Cu systems. On the contrary, because of the Mn-Mn AFM coupling, FeMn clusters exhibit an average MM close to zero mimicking the FeCu total MM trend. Nevertheless, although the Fe local MM is the highest in the shell of the $FeCu_{12}$ surrounded by non-magnetic Cu atoms, nowadays this tiny cluster is almost impossible to be experimentally achieved.

These results can contribute to future developments in the design of Fe-X (X=Cu, Co, Mn) environmentally sustainable smart magnetic clusters or coatings.

Bibliography

[1] C. Kittel. *Introduction to Solid State Physics*. John Wiley & Sons, Inc, 2005.

[2] K. Hermann X. Yin. Structural and magnetic properties of ultrathin fcc fe films on cu(001): Full-potential lapw studies. *Physical Review B*, 63(115417), 2001.

[3] P. Weinberger B. Újfalussy, L. Szunyogh. Magnetic anisotropy in fe/cu(001) overlayers and interlayers: The high-moment ferromagnetic phase. *Physical Review B*, 54(14), 1996.

[4] H. Kasai A. Okiji T. Kishi, H. Nakanishi. Magnetic properties of fe thin films on cu(111). *Journal of the Physical Society of Japan*, 71:2983–2985, 2002.

[5] Yong-Chae Chung Heechae Choi, Soon-Gun Lee. The role of structural variations in the magnetism of fe/cu(1 1 1): First-principles calculations. *Computational Materials Science*, 49:S291–S296, 2010.

[6] H. L. Skriver A. M. N. Niklasson, B. Johansson. Interface magnetism of 3d transition metals. *Physical Review B*, 59(9), 1999.

[7] A. Scholl C. Carbone W. Eberhardt D. Schmitz, C. Charton. Magnetic moments of fcc fe overlayers on cu(100) and co(100). *Physical Review B*, 59(6):4327–4333, 1999.

[8] W. Hübner X. Qian. First-principles calculation of structural and magnetic properties for fe monolayers and bilayers on w(110). *Physical Review B*, 60(23), 1999.

[9] J. Wang J. Chen W. Huang J. Yu, X. Lin. First-principles study of the relaxation and energy of bcc-fe, fcc-fe and aisi-304 stainless steel surfaces. *Applied Surface Science*, 255:9032–9039, 2009.

[10] W. Wurth M. Martins. Magnetic properties of supported metal atoms and clusters. *Journal Physics Condensed Matter*, 28, 2016.

[11] R. S. Varmab A. Moores R. Hudson, Y. Feng. Bare magnetic nanoparticles: sustainable synthesis and applications in catalytic organic transformations. *Green Chem*, 16:4493–4505, 2014.

[12] Rajender S. Varma R. B. Nasir, Baig. Magnetically retrievable catalysts for organic synthesis. *Chem. Commun*, 49:752–770, 2013.

[13] M. S. Serajia Z. Luoa G. E. Hoagb H. C. Genuinoa, N. Mazruia. Green synthesis of iron nanomaterials for oxidative catalysis of organic environmental pollutants. *Catalysis for Remediation and Environmental Concerns*, pages 41–61, 2018.

[14] I. M.C. Lo S. C.N. Tang. Magnetic nanoparticles: Essential factors for sustainable environmental applications. *Water research*, 47:2613–2632, 2013.

[15] E. M. Bringa S. Allende P. Sepuveda N. Arancibia-Miranda S. E.Baltazar J Rojas-Nunez, R. I. Gonzalez. Toward controlled morphology of fecu nanoparticles: Cu concentration and size effects. *J. Phys. Chem. C*, 122:8528–8534, 2018.

[16] Karrina McNamara Syed A. M. Tofail. Nanoparticles in biomedical applications. *Advances in Physics: X*, 2(1):54–88, 2017.

[17] Rumpf Klemens Granitzer, Petra. Magnetic nanoparticles embedded in a silicon matrix. *Materials*, 4(5):908–928, 2011.

[18] A. Ionescu C.H. Barnes J.Liandro, J.J. Palfreyman. Magnetic biosensor technologies for medical applications: a review. *Med Biol Comput*, 48:977–998, 2010.

[19] M. Avram M. Volmer, J. Neamtu. Magnetoresistance sensors with magnetic layers for high sensitivity measurement. *Jour of Optoel and Advanc Materials*, 10(1):104–109, 2008.

[20] A. Chatelain W. A. de Heer I. M. L. Billas, J. A. Becker. Magnetic moments of iron clusters with 25 to 700 atoms and their dependence on temperature. *Physical Review Letters*, 71(24), 1993.

[21] L. J. Gallego A. Vega F. Aguilera-Granja, R. C. Longo. Structural and magnetic properties of $x_{12}y$ (x, y=fe, co, ni, ru, rh, pd, and pt) nanoalloys. *The Journal of Chemical Physics*, 132(184507), 2010.

[22] K.G. Belay C.A. Weatherford L.G. Gutsev B.R. Ramachandran G.L. Gutsev, L.E. Johnson. Structure and magnetic properties of fe_{12}x clusters. *Chemical Physics*, 430:62–68, 2014.

[23] M. B. Knickelbein. Magnetic moments of small bimetallic clusters: $co_n mn_m$. *Physical Review B*, 75(014401), 2007.

[24] X. Xu W. A. de Heer S. Yin, R. Moro. Magnetic enhancement in cobalt-manganese alloy clusters. *Physical Review Letters*, 98(113401), 2007.

[25] G. Ghosh M. Asta J. Z. Liu, A. van de Walle. Structure, energetics, and mechanical stability of fe-cu bcc alloys from first-principles calculations. *Physical Review B*, 72(144109), 2005.

[26] S. C. Watson E. A. Carter V. Cocula, F. Starrost. Spin-dependent pseudopotentials in the solid-state environment: Applications to ferromagnetic and antiferromagnetic metals. *The Journal of Chemical Physics*, 119(15):7659–7671, 2003.

[27] D. E. Ellis D. Guenzburger. Magnetic and electronic properties of γ-fe and γ-fe/al particles in copper. *Physical Review B*, 52(18):390–398, 1995.

[28] J. Kiibler M. Uhl, L.M. Sandratskii. Electronic and magnetic states of γ fe. *Journal of Magnetism and Magnetic Materials*, 103:314–324, 1992.

[29] J. KUBLER. Magnetic moments of ferromagnetic and antiferromagnetic bcc and fcc iron. *Physics Letters*, 81A(1), 1981.

[30] B. X. Liu L. T. Kong. Correlation of magnetic moment versus spacing distance of metastable fcc structured iron. *Applied Physics Letters*, 84(18), 2004.

[31] H. Schiechl P. Varga M. Schmid A. Biedermann G. Rauchbauer, A. Buchsbaum. Ultra-thin fe films grown on cu by pulsed laser deposition: Intermixing and bcc-like structures. *Surface Science*, 602:1589–1598, 2008.

[32] J. Shen J. Barthel H. Jenniches J. Kirschner S. S. Manoharan, M. Klaua. Artificially ordered fe-cu alloy superlattices on cu(001) i. studies on the structural and magnetic properties. *Physical Review B*, 58(13), 1998.

[33] X. Gao M.T. Lin M. Klaua J. Barthel Ch. V. Mohan J. Kirschner W. Kuch, M. Salvietti. Artificially ordered fecu alloy superlattices on cu(001) ii. spin-resolved electronic properties and magnetic dichroism. *Physical Review B*, 58(13):8556–8565, 1998.

[34] F. J. Hirnpsel. Exchange splitting of epitaxial fcc fe/cu(100) versus bcc fe/ag(100). *Physical Review Letter*, 67(17), 1991.

[35] L. Pasquali C. Carbone W. Eberhardt A. Dallmeyer, K. Maiti O. Rader. Magnetism and interlayer coupling in fcc fe/co films. *Physical Review B*, 63(104413):1–5, 2001.

[36] J. Hafner D. Spišák. Magnetism of fe-co nanostructures on flat and stepped w(100) surfaces: Effects of dimensionality and substrate. *Physical Review B*, 70(014430):1–10, 2004.

[37] W. A.de Heer I. M. L.Bilas, A. Chatelain. Magnetism from the atom to the bulk in iron, cobalt, and nickel clusters. *SCIENCE*, 265:1682–1684, 1994.

[38] M.M.G. Alemany Y. Saad J. R. Chelikowsky M. L. Tiago, Y. Zhou. The evolution of magnetism in iron from the atom to the bulk. *PHYSICAL REVIEW LETTERS*, 97(147201):1–4, 2006.

[39] P. Weinberger B. Lazarovist, L. Szunyogh. Fully relativistic calculation of magnetic properties of fe, co, and ni adclusters on ag(100). *Physical Review B*, 65(104441), 2002.

[40] W. A.de Heer I. M. L.Bilas, A. Chatelain. Magnetism of fe, co and ni clusters in molecular beams. *Journal of Magnetism and Magnetic Materials*, 168:64–84, 1997.

[41] J.M. Soler A.V. Postnikov, P. Entel. Density functional simulation of small fe nanoparticles. *THE EUROPEAN PHYSICAL JOURNAL D*, 25:261–270, 2003.

[42] P. Kroll R. Singh. Structural, electronic, and magnetic properties of 13, 55, and 147 atom clusters of fe, co, and ni: A spin-polarized density functional study. *Physical Review B*, 78(245404), 2008.

[43] A. Vega F. Aguilera-Granja, A. García-Fuente. Comparative ab initio study of the structural, electronic, and magnetic trends of isoelectronic late 3d and 4d transition metal clusters. *Physical Review B*, 78(134425), 2008.

[44] A.W. Castleman Jr. P. Jena. Clusters: A bridge across the disciplines of physics and chemistry. *PNAS*, 103(28):10560–10569, 2006.

[45] Jr M. T. Kief, W. F. Egelhoff. Growth and structure of fe and co thin films on cu(111), cu(100), and cu(110): A comprehensive study of metastable film growth. *Physical Review B*, 47(16):10785–10814, 1993.

[46] C. J. Hirschmugl V. Fernandez K.-M. Schindler M. Polcik A. M. Bradshaw D. P. Woodruff A. Theobald, O. Schaff. Photoelectron diffraction study of ultrathin fe films on cu(111). *Physical Review B*, 59(3):2313–2319, 1999.

[47] G. Xing K. Jamison C. Rau, C. Schneider. Ferromagnetic order at surfaces of ultrathin epitaxial fcc γ-fe(lll)p(1x1) films on cu(lll). *PHYSICAL REVIEW LETTERS*, 57(25):3221–3224, 1986.

[48] M. Schmid P. Varga A. Biedermann, W. Rupp. Coexistence of fcc- and bcc-like crystal structures in ultrathin fe films grown on cu(111). *Physical Review B*, 73(165418):1–16, 2006.

[49] A. C. de Castro S. D. de Magalhães V. M. T. S. Barthem D. Givord P. E. V. de Miranda G. Clemente R. A. Simão A. Kazadi, M. Bantu. Structural and magnetic properties of electrodeposited copt and fecu nanowires embedded in polycarbonate membranes. *The African Review of Physics*, 9:487–496, 2015.

[50] Ch. V. Mohan S. Sundar Manoharan J. Barthel P. Ohresser M. Klaua J. Kirschner H. Jenniches, J. Shen. Structure and magnetism of pulsed-laser-deposited ultrathin films of fe on cu(100). *Physical Review B*, 59(2):1196–1208, 1999.

[51] J. Barthel M. Zheng Ch. V. Mohan M. Klaua J. Kirschner P. Ohresser, J. Shen. Growth, structure, and magnetism of fcc fe ultrathin films on cu(111) by pulsed laser deposition. *Physical Review B*, 59(5), 1999.

[52] M. Schmid P. Vargau A. Biedermann, R. Tscheliessnig. Local atomic structure of ultra-thin fe films grown on cu(100). *Applied Physics A*, 78:807–816, 2004.

[53] J. Hafner E. G. Moroni, G. Kresse. Coherent epitaxy and magnetism of face-centred-cubic fe films on cu(100). *Journal of Physics: Condensed Matter*, 11:35–42, 1999.

[54] D. Li R. E. Camley. Theoretical calculation of magnetic properties of ultrathin fe films on cu(100). *Physical Review Letter*, 84(20):4709–4712, 2000.

[55] J. Hafner D. Spisák. Complex reconstruction of γ-iron multilayers on cu(100): Ab initio local-spin-density investigations. *Physical Review B*, 61(23):129–136, 2000.

[56] F.J.Himpsel G.J.Mankey, R.F.Willis. Unoccupied electronic states of ultrathin films of co/cu(111) and fe/cu(111). *Physical Review B*, 47(1):190–196, 1993.

[57] M. Donath. Magnetic order and electronic structure in thin films. *Journal Physics: Condensed Matter*, 11:9421–9436, 1999.

[58] L. C. Balbás D. Sánchez-Portal Javier Junquera Emilio Artacho J. M. Soler Pablo Ordejón J. Izquierdo, A. Vega. Systematic ab initio study of the electronic and magnetic properties of different pure and mixed iron systems. *PHYSICAL REVIEW B*, 61(20):13639–13646, 2000.

[59] A. J. Freeman C. L. Fu. Electronic and magnetic properties of the fcc fe(001) thin films: Fe/cu(001) and cu/fe/cu(001). *Physical Review B Condensed Matter*, 35(3):925–932, 1986.

[60] H. L. Skriver N. M. Rosengaard B. Johansson M. Alden, S. Mirbt. Surface magnetism in iron, cobalt, and nickel. *Physical Review B*, 46(10):6303–6312, 1992.

[61] P. Weinberger L. Szunyogh, B. Újfalussy. Magnetic structure and anisotropy in fe/cu(001) over- and interlayers with antiferromagnetic interlayer coupling. *Physical Review B*, 55(21):392–396, 1997.

[62] . Sukiennicki R. Wojnecki. Peculiar properties of ultrathin fcc iron films epitaxially grown on cu(001). *ACTA PHYSICA POŁONICA A*, 97(4):705–712, 2000.

[63] S. Blügel T. Asada. Total energy spectra of complete sets of magnetic states for fcc-fe films on cu(100). *PHYSICAL REVIEW LETTERS*, 79(3), 1997.

[64] D. Errandonea. Tight-binding study of the electronic and magnetic properties of an $l1_0$ ordered fecu alloy. *Physics Letters A*, 233(139-142), 1997.

[65] Weinberger Újfalussy Lazarovits, Szunyogh. Magnetic properties of finite fe chains at fcc cu(001) and cu(111) surfaces. *Physical Review B*, 68(024433), 2003.

[66] L. Ma G.H. Wang Q.L. Lu, L.Z. Zhu. Magnetic properties of co/cu and co/pt bimetallic clusters. *Chemical Physics Letters*, 407:176–179, 2005.

[67] M Manninen S Valkealahti. Molecular dynamics simulation of crystallization of liquid copper clusters. *Journal of Physics: Condensed Matter*, 9:4041–4050, 1997.

[68] P.Tereshchuk K. E. A. Batista A. S. Chaves D. Guedes-Sobrinho J. L. F. Da Silva M. J. Piotrowski, C. G. Ungureanu. Theoretical study of the structural, energetic, and electronic properties of 55-atom metal nanoclusters: A dft investigation within van der waals corrections, spinorbit coupling, and pbe+u of 42 metal systems. *Journal of Physical Chemistry C*, 120:2884428856, 2016.

[69] P. Berthoud S. Valkealaht R. Monot D. Reinhard, B. D. Hall. Unsupported nanometer-sized copper clusters studied by electron diffraction and molecular dynamics. *Physical Review B*, 58(8):4917–4926, 1998.

[70] W. Shi-Jian Z. Zheng-Quan W. Ling, D. Dong. Geometrical, electronic, and magnetic properties of cu_nfe (n=1–12) clusters: A density functional study. *Journal of Physics and Chemistry of Solids*, 76:10–16, 2015.

[71] X.C. Niea H. Zhaia F. Wanga Q. Suna Yu. Jiaa S.F. Lia Z.X. Guo S.L. Hana, Xinlian Xuea. First-principles calculations on the role of ni-doping in cu_n clusters: From geometric and electronic structures to chemical activities towards co_2. *Physics Letters A*, 374:4324–4330, 2010.

[72] Q. Q. Zheng D. Y. Sun G. H. Wang Q. Sun, X.G. Gong. Local magnetic properties and electronic structures of 3d and 4d impurities in cu clusters. *Physical Review B*, 54(15):10896–10904, 1996.

[73] C. Carbone E. Vescovo S. Blügel R. Klässges W. Eberhardt M. Wuttig J. Redinger F. J. Himpsel O. Rader, W. Gudat. Electronic structure of two-dimensional magnetic alloys: c22... mn on cu100... and ni100... *Physical Review B*, 55(8):5404–5415, 1997.

[74] A. Roldán F. Illas V. A. de la Peña, O'Shea I. de P. R. Moreira. Electronic and magnetic structure of bulk cobalt: The α,β , and -phases from density functional theory calculations. *The Journal of Chemical Physics*, 133(024701), 2010.

[75] T. Saitoh O. Rader K.-S. An A. Kakizaki N. Kamakura, A. Kimura. Magnetism of fe films grown on co(100) studied by spin-resolved fe 3s photoemission. *Physical Review B*, 73(094437), 2006.

[76] Z.Q. Qiu. fcc fe films grown on a ferromagnetic fcc co(100) substrate. *Physical Review B*, 54(6), 1996.

[77] X. G. Gong C. D. Dong. Magnetism enhanced layer-like structure of small cobalt clusters. *Physical Review B*, 78(020409(R)), 2008.

[78] J.L. Vialle J. Lermé M. Broyer J. Miller A. Perez M. Pellarin, B. Baguenard. Evidence for icosahedral atomic shell structure in nickel and cobalt clusters. comparison with iron clusters. *Chemical Physics Letters*, 217(4), 1994.

[79] S. Ganguly B. Sanyal T. Saha-Dasgupta A. Mookerjee S. Datta, M. Kabir. Structure, bonding, and magnetism of cobalt clusters from first-principles calculations. *Physical Review B*, 76(014429), 2007.

[80] R. Moro W. A. de Hee X. Xu, S. Yin. Magnetic moments and adiabatic magnetization of free cobalt clusters. *Physical Review Letters*, 95(237209), 2005.

[81] M. B. Knickelbein. Magnetic moments of bare and benzene- capped cobalt clusters. *Journal of chemical physics*, 124(044308), 2006.

[82] A. Vega F. Aguilera-Granja. Stability, magnetic behavior, and chemical order of $(co_x fe_{1x})_n$ (n=5,13) nanoalloys. *Physical Review B*, 79(144423), 2009.

[83] D. Spisák D. Hobbs, J. Hafner. Understanding the complex metallic element mn. i. crystalline and noncollinear magnetic structure of α-mn. *Physical Review B*, 68(014407), 2003.

[84] Ru-qian Wu A.J. Freeman. Electronic structure theory of surface, interface and thin-film magnetism. *Journal of Magnetism and Magnetic Materials*, 100:497–514, 1991.

[85] B.P. Tonner W. L. O' Brien. Surface-enhanced magnetic moment and ferromagnetic ordering of mn ultrathin films on fcc co(001). *Physical Review B*, 50(5):2963–2969, 1994.

[86] Ph. Bauer H. Fischer K. Hricovini G. Krill M. Piecuch S. Andrieu, M. Finazzi. Growth, structure, and magnetic properties of thin mn films epitaxially grown on 001... bcc fe. *Physical Review B*, 57(3):1985–1991, 1998.

[87] A.J. Freeman R. Wu. Predicted c(2 x 2) buckling reconstruction of monolayer mn on fe(001) and its importance to the interfacial magnetic orderi. *Physical Review B*, 51(23):131–134, 1995.

[88] J. C. Zhang C. Jing, S. X. Cao. Lattice constant dependence of magnetic properties in bcc and fcc fexmn1àx alloys. *Physical Review B*, 68(224407), 2003.

[89] I. A. Abrikosov M. Ekholm. Structural and magnetic ground-state properties of γ-femn alloys from ab initio calculations. *Physical Review B*, 84(104423), 2011.

[90] V. Kumar Y. Kawazoe T. M. Briere, M. H. F. Sluiter. Atomic structures and magnetic behavior of mn clusters. *Physical Review B*, 66(064412), 2002.

[91] M. B. Knickelbein. Magnetic ordering in manganese clusters. *Physical Review B*, 70(014424), 2004.

[92] A. Mookerjee T. Saha-Dasgupta S. Datta, M. Kabir. Engineering the magnetic properties of the mn13 cluster by doping. *Physical Review B*, 83(075425), 2011.

[93] Ying Liu You-Cheng Li Bao-Ru Wang, Qing-Min Ma. Small fenmn clusters: Magnetic order and magnetic moment. *Solide State Communications*, 149:210–213, 2009.

[94] A. Hucht P. Entel G. Rollmann, S. Sahoo. Magnetism and chemical ordering in binary transition metal clusters. *Physical Review B*, 78(134404), 2008.

[95] G. Makov N. Argaman. Density functional theory. an introduction. *American Journal of Physics*, 68(69-79), 2000.

[96] E. Kaxiras. *Atomic and Electronic Structure of Solids*. CAMBRIDGE UNIVERSITY PRESS, 2003.

[97] K. Capelle. A bird's-eye view of density-functional theory. *cond-mat.mtrl-sci*, 2006.

[98] J.A. Steckel D.S. Sholl. *Density Functional Theory. A practical introduction*. WILEY, 2009.

[99] M.Y. Chou M.L. Cohen W.A. De Heer, W.D. Knight. *Elettronic Shell Structure and Metal Clusters*, volume 40. SOLID STATE PHYSICS, 1987.

[100] F. Jensen. *Introduction to Computational Chemistry*. John Wiley e Sons Ltd, 2006.

[101] K. Burke&friends. *The ABC of DFT*. http://chem.ps.uci.edu/kieron/dft/book/, 2007.

[102] W. Kohn. v-representability and density functional theory. *Physical Review Letter*, 51(17), 1983.

[103] W. Kohn P. Hohenberg. Inhomogeneous electron gas. *Physical Review*, 3B(136), 1964.

[104] L. J. Sham W. Kohn. Self-consistent equations including exchange and correlation effects. *Physical Review*, 4A(140), 1965.

[105] M.Marques C.Fiolhais, F.Nogueira. *A Primer in Density Functional Theory*. Springer, 2002.

[106] Nicholas Harrison. An introduction to density functional theory. 2014.

[107] Yue Wang John P. Perdew, Kieron Burke. Generalized gradient approximation for the exchange-correlation hole of a many-electron system. *Physical Review B*, 54(23):533–539, 1996.

[108] M. Ernzerhof K. Burke, J. P. Perdew. Why the generalized gradient approximation works and how to go beyond it. *International Journal of Quantum Chemistry*, 61, 1997.

[109] L. Kleinman J.C. Phillips. New method for calculating wave functions in crystals and molecules*. *Physical Review*, 116(2):287–294, 1959.

[110] D. M. Bylander L. Kleinman. Efficacious form for model pseudopotentials. *Physical Review Letters*, 48(20):1425–1428, 1982.

[111] P. E. Blöchl. Projector augmented-wave method. *Physical Review B*, 50(24):953–997, 1994.

[112] D. Joubert G. Kresse. From ultrasoft pseudopotentials to the projector augmented-wave method. *Physical Review B*, 59(3):1758–1775, 1999.

[113] Martijn Marsman. Vasp: Plane waves, the paw method, and the self consistency cycle. Computational Materials Physics, Faculty of Physics, University Vienna, and Center for Computational Materials Science, 2011.

[114] C.C.J. Roothan. New developments in molecular orbital theory. *Reviews of Modern Physics*, 23(2), 1951.

[115] D. Sánchez-Portal E. Artacho J. Junquera, Ó. Paz. Numerical atomic orbitals for linear-scaling calculations. *Physical Review B*, 64(235111), 2001.

[116] R. E. Stanton. Hellmann-feynman theorem and correlation energies. *The Journal of Chemical Physics*, 36(5), 1961.

[117] T. Berlin. Binding regions in diatomic molecules. *The Journal of Chemical Physics*, 19(2), 1951.

[118] R. P. Feynman. Forces in molecules. *Physical Review*, 56:340–343, 1939.

[119] J.D.Gale A.García J.Junquera P.Ordejón D.Sánchez-Portal J.M.Soler E Artacho, J. M. Cela. *User's Guide SIESTA 4.0*. The Siesta Group, http://www.uam.es/siesta, 1996-2016.

[120] P. Ordejón A. García J.M. Soler E. Artacho, D. Sánchez-Portal. Linear-scaling ab-initio calculations for large and complex systems. *Physica status solidi (b)*, 215(809), 1999.

[121] E. Artacho J. M. Soler D. Sanchez-Portal, P. Ordejón. Density-functional method for very large systems with lcao basis sets. *International Journal of Quantum Chemistry*, 65:453–461, 1997.

[122] J. D. Gale A. García J. Junquera P. Ordejón D. Sánchez-Portal J. M Soler, E. Artacho. The siesta method for ab initio order-n materials simulation. *Journal of Physics: Condensed Matter*, 14:2745–2779, 2002.

[123] Jürgen Furthmüller G. Kresse, M. Marsman. *VASP the GUIDE.* http://cms.mpi.univie.ac.at/vasp/vasp.pdf, 10 2018.

[124] J. L. F. Da Silva M. J. Piotrowski, P. Piquini. Density functional theory investigation of 3d, 4d, and 5d 13-atom metal clusters. *Physical Review B*, 81(155446), 2010.

[125] G. Ho Lee Y. T. Jeon. Magnetism of the fcc rh and pd nanoparticles. *Journal of Applied Physics*, 103(094313), 2008.

[126] M. Weissmann J. Guevara, A. Maria Llois. Large variations in the magnetization of co clusters induced by noble-metal coating. *Physical Review Letter*, 81(24), 1998.

[127] W. H. Woodward A. W. Castleman Jr. A. C. Reber S. N. Khanna P. J. Roach. Complementary active sites cause size-selective reactivity of aluminum cluster anions with water. *SCIENCE*, 323, 2009.

[128] A. S. Ahmed J. F. Zhang H. K. Yuan, H. Chen. Density-functional study of scn n=2–16... clusters: Lowest-energy structures, electronic structure, and magnetism. *Physical Review B*, 74(144434), 2006.

[129] A. L. Mackay. A dense non-crystallo ,raphic packing of equal spheres. *Acta Crystallogr*, 15(916), 1962.

[130] K. H. Kuo. Mackay, anti-mackay, double-mackay, pseudo-mackay, and related icosahedral shell clusters. *Structural Chemistry*, 13, 2002.

[131] M. Ernzerhof J. P. Perdew, K. Burke. Generalized gradient approximation made simple. *Physical Review Letters*, 77(18):3865–3868, 1996.

[132] B.X. Liu F. Pan, M. Zhang. Magnetic properties of fcc iron in fe fcc metal multilayers. *Thin Solid Films*, 334(196200), 1998.

[133] M. Kinzaa K. Fauthb G. Ballentine, M. Heßler. Superparamagnetism in small fe clusters on cu(111). *The European Phisical Journal D*, 45:535–537, 2007.

[134] J. Furthmiiller G. Kresse. Efficiency of ab-initio total energy calculations for metals and semiconductors using a plane-wave basis set. *Computational Materials Science*, 6:15–50, 1996.

[135] J. Furthmiiller G. Kresse. Efficient iterative schemes for ab initio total-energy calculations using a plane-wave basis set. *Physical Review B*, 54(16), 1996.

[136] J. L. Martins N. Troullier. Efficient pseudopotentials for plane-wave calculations. *Physical Review B*, 43(3):1993–2006, 1991.

[137] L. Zosiak. *Simulations of atomic and electronic structure of realistic Co and Pt based nanoalloy clusters. Materials and structures in mechanics.* PhD thesis, Université de Strasbourg, 2013.

[138] X. Cheng Zeng Y. Gao, S. Bulusu. Gold-caged metal clusters with large homo-lumo gap and high electron affinity. *Journal of the American Chemical Society*, 127:15680–15681, 2005.

[139] P. Sen D. Bandyopadhyay. Density functional investigation of structure and stability of gen and genni (n) 1-20) clusters: Validity of the electron counting rule. *Journal physical chemistry A*, 114:1835–1842, 2010.

[140] Jun ichi Aihara. Reduced homo-lumo gap as an index of kinetic stability for polycyclic aromatic hydrocarbons. *Journal Physical chemistry A*, 103:7487–7495, 1999.

[141] J. A. Alonso. Electronic and atomic structure, and magnetism of transition-metal clusters. *Chemical Reviews*, 100:637–677, 2000.

[142] T. Saha-Dasgupta A. Mookerjee S. Datta, M. Kabir. Structure, reactivity, and electronic properties of v-doped co clusters. *Physical Review B*, 80(085418), 2009.

[143] M. R. Pederson C. Ashman S. N. Khanna J. Kortus, T. Baruah. Magnetic moment and anisotropy in $fe_m co_n$ clusters. *Applied Physics Letters*, 80(22), 2002.

[144] T. Wieland P. Kroll, J. Theuerkauf. Iron nanoparticles embedded in silica glass: A computational study. *Mater. Res. Soc. Symp. Proc*, 959, 2009.

[145] C. M. Wei C. Cheng C.M. Chang J. P.Chou, C. R. Hsing. Ab initio random structure search for 13-atom clusters of fcc elements. *Journal of Physics: Condensed Matter*, 25(125305), 2013.

[146] Abhijit Mookerjee Mukul Kabir, D. G. Kanhere. Emergence of noncollinear magnetic ordering in small magnetic clusters: mn_n and as@mn_n. *Physical Review B*, 75(214433), 2007.

[147] K. Kwong R. Tang A. Ziegler K. Lee, J. Callaway. Electronic structure of small clusters of nickel and iron. *Physical Review B*, 31(4), 1985.

[148] H. Shin J. I. Lee K. Lee, C. Jo. Electronic structure and magnetism of the co13 cluster. *J. Korean Phys. Soc.*, (27):412, 1994.

[149] H. Zainuddin H KT Chan A Shuaibu A N. Bolandhemat, R. Md. Mahmudur. Density functional study of electronic, magnetic and chemical bonding properties of spinel cdcr2o4. *Journal of Material Sciences & Engineering*, 6, 2017.